The University Of Sheffield.

DESIGN AND ANALYSIS OF LOW PROFILE CIRCULARLY POLARISED ANTENNAS

Hassan M Al-Lawati

A Thesis Submitted to the University of Sheffield for the Degree of Doctor of Philosophy in Electronic and Electrical Engineering

May 2014

ABSTRACT

In the last decade, mobile communication has spread widely and become an essential tool in every day's life. A tremendous increase in the demand of small Personal Mobile Devices (PMD) has been observed with wide model ranges and applications. This necessitates the design of low profile and compact antennas that can be accommodated in the smaller PMD sizes. This thesis focuses on designing low profile Circularly Polarised (CP) antennas that can be incorporated with these devices. Two types of circularly polarised antennas have been considered; Dielectric Resonator Antennas (DRA) and planar open loop antennas backed by an Artificial Magnetic Conductor (AMC) ground plane. The Elliptical DRA has been considered owing to the simplicity of achieving CP radiation compared to a cylindrical DRA. Several EDRAs have been designed employing a simple conformal strip excitation mechanism. The designed antennas include single and dual band, as well as a wideband CP DRAs. In addition, a low profile elliptical dielectric resonator antenna has been designed using a dielectric constant of $\varepsilon_r = 25$. Extremely lower profile CP loop antennas have been designed by incorporating the Artificial Magnetic Conductor (AMC) as a ground plane. Two excitation mechanisms have been employed; the Co-Planar waveguide and the vertical probe feed. A total antenna's thickness of $\lambda_o/48$ has been achieved for the probe-fed loop antenna compared to $\lambda_o/21.2$ that has been reported in the literature and incorporated the square patch AMC. Two artificial magnetic conductor surfaces have been designed; the traditional square patch and a novel AMC. The novel AMC has reduced the antenna's size by $\sim 28\%$ compared to other antennas, incorporated the square patch AMC given the same thickness using a 4×4 unit cells' grid. Additionally, a reduction of $\sim 45\%$ has

been achieved using a 3×3 grid of the novel unit cell with sufficient matching and axial ratio bandwidths. Furthermore, a CP loop antenna backed by the novel AMC out-performs an identical counterpart placed above the traditional square patches AMC with simulated axial ratio bandwidth of ~10%. Moreover, two dual band AMCs are presented, that are suitable for the L_1 and L_2 GPS bands. Once more, a pronounced size reduction of $\sim 42\%$ has been attained using the novel dual band AMC unit cells compared to the double square dual band AMC. Several prototypes have been fabricated with close agreement between simulated and measured results. Some results have been verified using another commercial software, HFSS.

ACKNOWLEDGEMENTS

First and foremost, all praises to the Almighty Allah for bestowing me with patience and perseverance in completing this thesis. Special appreciation dedicated to my supervisor, Dr. Salam Khamas, for his guidance, encouragement and patience. His invaluable help and advices throughout the research have significantly contributed to the completion of this thesis. I would like to express my gratitude to Prof. Richard Langley for his leadership of the communication group and continues support. Special thanks to Dr. Jonathan Rigelsford for his help and guidance in completing the experimental work. My appreciation extends to Mr. Steve Marsden and Mr. Richard Savage for their continues technical support. Many thanks as well to my colleague Mohammed Ismeal for his help throughout my research. I would like to express my deepest thanks to Prof. Omar Ramahi and Mr. Ahmed Ashour from the University of Waterloo in Canada for verifying some designs using HFSS.

I am grateful to every single person who supported and helped me in my studying career and especially, in the PhD studies. There is no word, which can express my thanks and appreciations to my parents for their continues support and patience until I reached this moment. Special thanks as well to my wife for her priceless encouragement and moral support in all the difficult moments in my studies. Many thanks to my brother, sisters, uncles, untie, friends and colleagues. Finally, I would like to thank my sponsor, The Government of the Sultanate of Oman and my Employee Sultan Qaboos University for supporting me and giving me this opportunity to pursue my studies. Last but not least, I dedicate this thesis to the one who gave us all what he has so that we can live with dignity.. to the one I love.. to the one I adore.. to you.. Imam Hussain...

PUBLICATIONS

- H. M. Al-Lawati, S. K. Khamas, S.P. Kingsley, " A Low Profile Circularly Polarized Loop Antenna above a Novel Artificial Magnetic Conducting Surface", submitted to the IEEE Transactions on Antennas and Propagation, 2014
- H. M. Al-Lawati and S.K. Khamas, "Circularly Polarized Elliptical Dielectric Resonator Antenna with a Conformal Strip Excitation", The *6th European Conference on Antennas and Propagation (EUCAP),* Prague, 2012.
- H. M. Al-Lawati and S.K. Khamas, "Experimental and Theoretical Results of a Circularly Polarized Elliptical Dielectric Resonator Antenna with a Conformal Strip Excitation", *Loughborough Antennas and Propagation Conference (LAPC)*, Loughborough, UK, 2012.

TABLE OF CONTENTS

LIST OF FIGURES

LIST OF TABLES

LIST OF ACRONYMS

AMC	Artificial Magnetic Conducting
AR	Axial Ratio
CP	Circularly Polarized
CPW	Co-Planar Waveguide
DRA	Dielectric Resonator Antenna
E	Electric field
EBG	Electromagnetic Band Gap
EDRA	Elliptical Dielectric Resonator Antenna
GPS	Global Positioning System
H	Magnetic field
LHCP	Left-Hand Circularly Polarized
LP	Linearly Polarized
MAS	Method of Auxiliary Sources
MoM	Method of Moments
PEC	Perfect Electrical Conductor
PMC	Perfect Magnetic Conductor
PMD	Personal Mobile Device
RHCP	Right-Hand Circularly Polarized
SIE	Surface Integral Equation
TE	Transverse Electric
TEM	Transverse Electromagnetic
TM	Transverse Magnetic

CHAPTER 1

Introduction

1.1 Overview

An antenna is one of the essential components in wireless communication systems. It is defined as a means for radiating or receiving radio waves [1], and it is the last element at the transmission segment and the first element at the receiving end. Therefore, failure in designing an efficient antenna, which can firmly close the link between the end points, degrades the system performance. With the rapid increase of Personal Mobile Devices (PMD), antennas become more and more important. Engineers are required to design low profile and compact antennas to be accommodated by the miniaturised newly PMD devices. An antenna is usually called low profile if its total height is less than $\lambda_o/10$ [2]. In order to attain a PMD with less sensitivity to the environment, Circularly Polarised (CP) antennas are more suitable than their Linearly Polarised (LP) counterparts. There are numerous antenna configurations such as dipole, horn, microstrip and dielectric resonator antennas. In this work, two types of low profile circularly polarised antennas are considered; dielectric resonator antennas and CP loop antennas backed by Artificial Magnetic Conductors (AMC).

1.2 Circular Polarisation (CP)

1.2.1 *CP Theory*

In wireless communication, electromagnetic (EM) waves are the means of transferring information between the transmitter and receiver. A general Transverse Electromagnetic (TEM) wave has electric field $\mathbf{E}$ and magnetic field $\mathbf{H}$ components perpendicular to each other and perpendicular to the direction of propagation. Further, it can be characterised at an observation point by frequency, magnitude, phase and polarisation [3]. For example, consider a z-directed plane wave with $\mathbf{E}$ field components in x and y directions. The time-harmonic electric field at $z = 0$ is expressed as:

$$\mathbf{E} = E_x \cos(wt)\, \mathbf{a}_x + E_y \cos(wt + \delta)\, \mathbf{a}_y \tag{1.1}$$

where E_x and E_y are the peak values of the correspondent component, δ is the phase at which the y-directed component is leading the x-directed counterpart. The antenna's polarisation can be understood from equation (1.1); for example if $\delta = 0$, then $\boldsymbol{E}_x$ and $\boldsymbol{E}_y$ are in phase and the net vector change as a line and accordingly the

wave is defined as Linearly Polarised (LP). In the case when the two filed components, E_x and E_y are equal to each other, then the polarisation will be linear at angle of 45^0. Furthermore, when the magnitude of E_x is negligible, a vertical polarization is obtained. Similarly, a horizontal polarisation achieved when $E_y \approx 0$. If $E_x \neq E_y$, then the polarization is given at an angle of:

$$\gamma = \tan^{-1}\left[\frac{E_y}{E_x}\right] \tag{1.2}$$

A schematic illustration for a linearly polarised wave is shown in Figure 1.2.1.

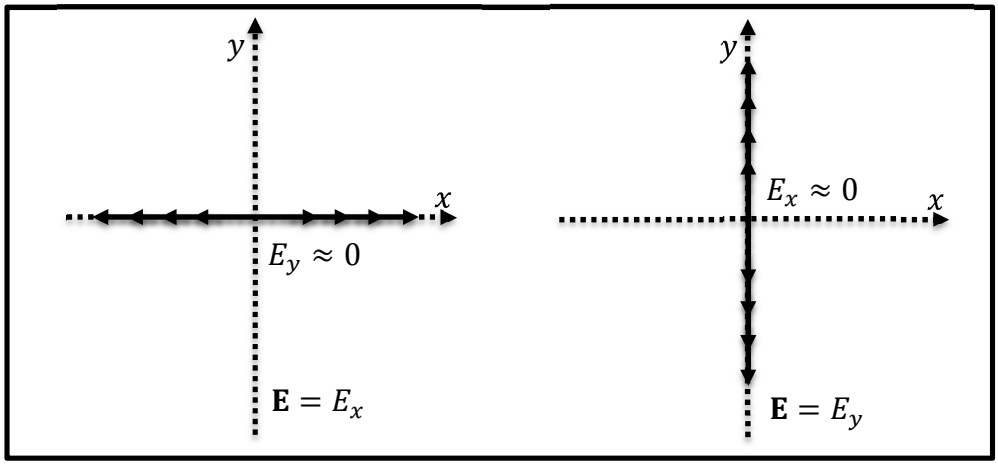

Figure 1.2.1: Horizontal and Vertical linear polarization

For a wave with a phase of $\delta = \pm 90^o$ and $E_x = E_y$, the field vector moves in a circular path as can be seen from Figure 1.2.2 and the polarisation is said to be circular. If however, $E_x \neq E_y$, which is more common, then the field vector rotates in elliptical path and the polarisation is said to be elliptical as illustrated in Figure 1.2.3. When the wave rotates in a clockwise direction, towards the observer, a Left Handed Circularly Polarised (LHCP) radiation is accomplished. On the other hand, if the wave rotates in an anti-clockwise direction, a Right Handed Circularly Polarised (RHCP) radiation is obtained.

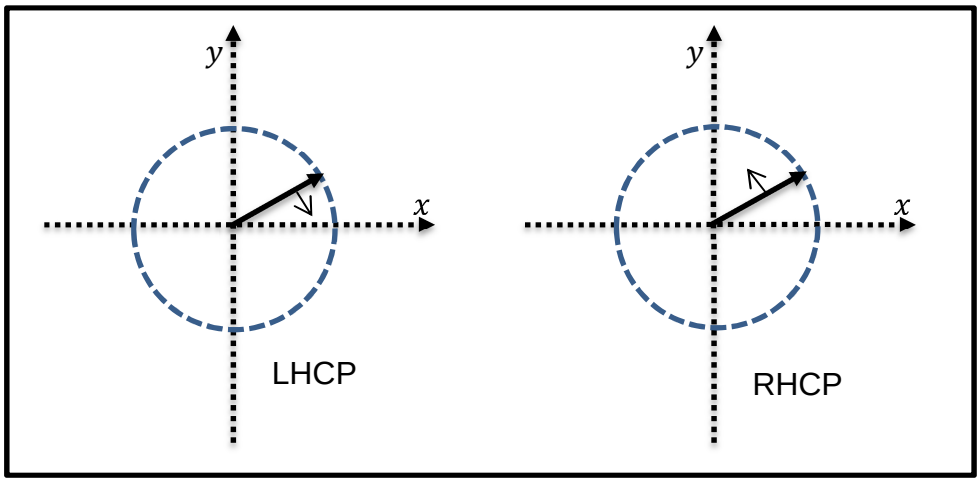

Figure 1.2.2: Left-handed and Right-handed circular polarisation

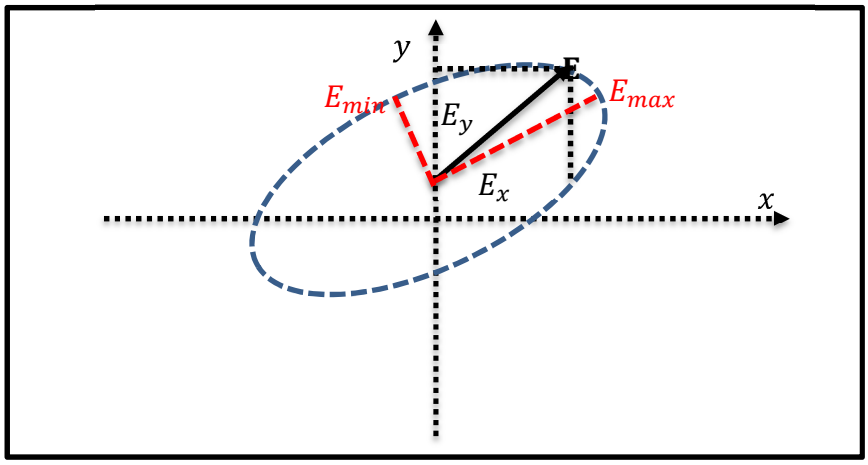

Figure 1.2.3: Elliptical polarisation

Circular polarisation is defined by the Axial Ratio (AR), which is the ratio of the maximum and minimum semi axes of the ellipse and is given in decibels by [4]:

$$\mathrm{AR} = 20\log_{10}\left[\frac{E_{max}}{E_{min}}\right] \tag{1.3}$$

from which it can be noticed that $1 \leq \mathrm{AR} \leq \infty$. A pure circular polarisation can be achieved when $\mathrm{AR} = 1$ or 0dB, which is difficult to achieve in practice. Therefore, a frequency range over which $\mathrm{AR} \leq 3\mathrm{dB}$ is considered, and defined as

$$\mathrm{AR}_{BW} = \frac{f_2 - f_1}{f_{min}} \tag{1.4}$$

where, f_2 and f_1 are the boundary frequencies for $\mathrm{AR} \leq 3\mathrm{dB}$ and f_{min} is the frequency of minimum value of AR.

1.2.2 *Comparison between Circular and Linear Polarizations*

Circularly Polarised (CP) antennas offer a distinct advantage over their Linearly Polarised (LP) counterpart. That is, there is no need to establish a similar orientation between the transmitter and the receiver. As a result, the probability of linking a transmitted CP wave is higher since it can be received in the horizontal, vertical as well as any plane in-between. In contrast, LP wave is capable of radiating in one plane only, which is particularly inefficient for mobile and satellite applications. Moreover, a CP wave that is transmitting in all planes is less susceptible to unwanted reflection and absorption. Reflecting surfaces may scatter the wave with a different phase, which results in a weak LP signal. However, a CP wave can be received regardless of the reflected plane. Additionally, CP antennas are capable of reducing the Faraday rotation effects, which means that a linearly polarized wave may be rotated by an unknown amount depending on the thickness and temperature of the ionosphere, as well as the frequency and therefore causes a reduction of 3dB in the signal strength of linearly polarised antennas [5, 6]. On the other hand, CP antennas tend to lose their polarisation and become elliptically polarised in the case of non-normal incident. In addition, CP waves lose their sense if reflected by a PEC, with 180^{o} reflection phase, which may change a Right Handed CP wave into a Left Handed CP wave or vice versa. Therefore, CP antennas are not recommended for indoor radio communications [6].

1.2.3 *Generation of CP waves*

CP waves can be generated by exciting two spatially orthogonal LP waves that are in phase quadrature and have equal amplitudes. Hence, the designs may require dual feeding or power divider, which increases the size and complexity. For example, a square patch can generate a CP wave by feeding two edges of the square as shown in Figure 1.2.4 [7]. Alternatively, a 90^{o} hybrid can be used in a conjunction with a single feeding for a circular patch at two orthogonal points as illustrated in Figure 1.2.5 [8]. For wide band CP radiation, four feeding ports may be used with $0^{o}, 90^{o}, 180^{o}$ and 270^{o} phase differences [9].

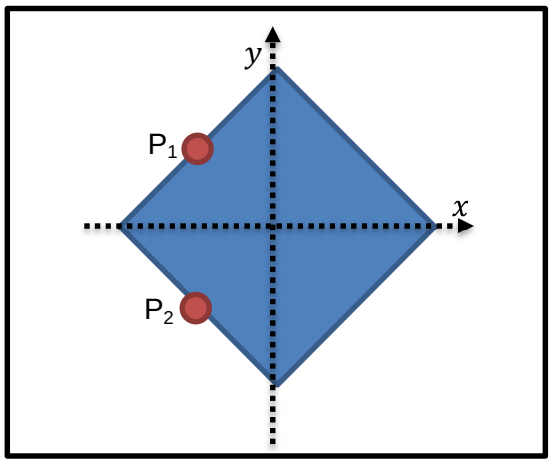

Figure 1.2.4: Dual-Feed CP square patch antenna

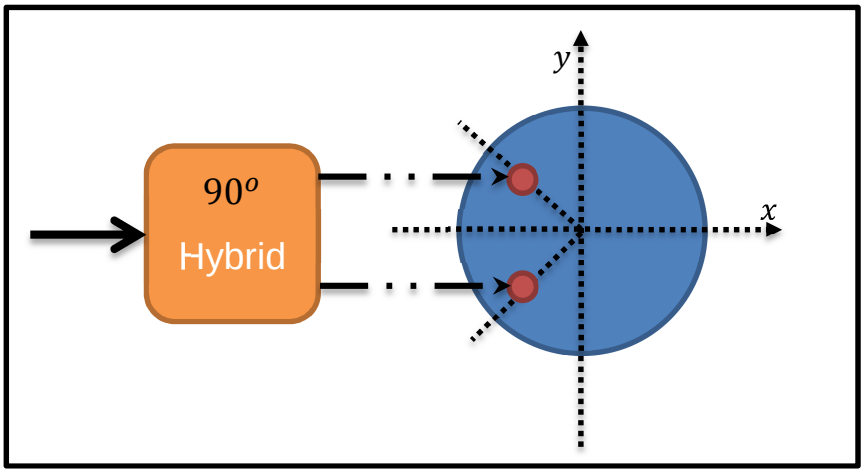

Figure 1.2.5: Singly fed CP circular patch antenna with a 90º hybrid.

Another method to generate CP waves is by introducing perturbation in the antenna. The small perturbation has to be with the right amount at the desired frequency to produce two orthogonally polarized components with the same amplitude and a 90^o phase difference. An example of such method is the truncated square patch shown in Figure 1.2.6(a) or a circular patch with two opposing edges with notches as can be seen in Figure 1.2.6(b) [10]. Alternatively, modifications can to be implemented on the feed itself rather than the antenna's geometry such as employing a cross-shaped slot feed as shown in Figure 1.2.7 [11]. The desired 90^o phase difference between the degenerate waves can be achieved by manipulating the cross's arms lengths l_1 and l_2.

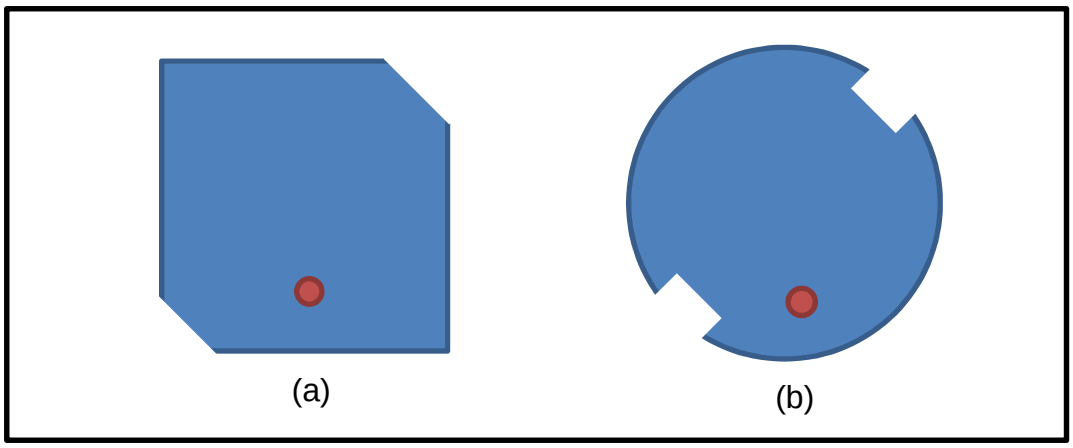

Figure 1.2.6: CP single feed square and circular patches

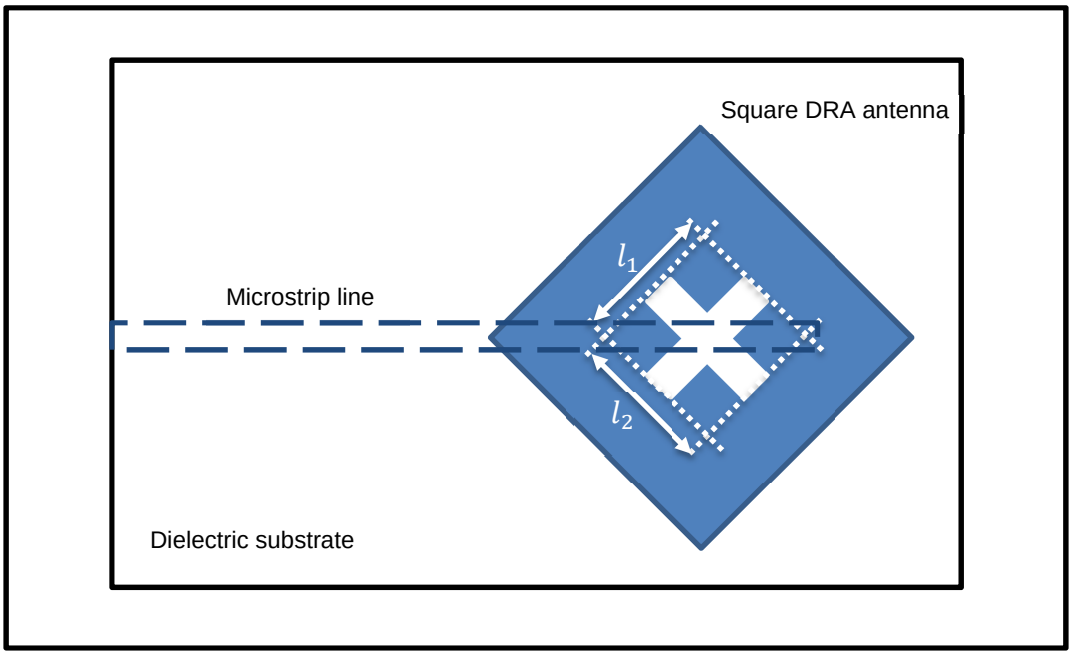

Figure 1.2.7: CP Square DRA antenna, fed by cross-slot and microstrip line

Another method of generating CP wave is by introducing a travelling wave current along the antenna surface. Antennas such as dipoles and closed loops are excited by standing wave current that is constructed by incident and reflected waves of equal amplitude and 180^o phase difference [1]. Therefore, the maxima and the minima repeat every integral number of half wavelengths. Such antennas are also called resonant antennas, which result in a narrow bandwidth of operation. In contrast, travelling wave antennas have uniform current patterns. Travelling wave can be achieved when the wave travelling from the feed point is absorbed at the end by a matched load causing no reflection or standing waves. Travelling wave antennas are

called non-resonant antennas and therefore, they operate over wider bandwidth. The travelling wave current distribution has a progressive, i.e. approximately linear, phase pattern. Curved wire antennas such as helix [12], curl [13], Archimedean spiral [3] and open, or c-figured, loops [14] are classified as travelling wave antennas. These antennas radiate CP waves when the circumference of their wire is in the order of a wave-length because points that are quarter-wavelength apart are 90^o out of phase and the currents are orthogonal in space with magnitudes nearly equal [3]. In this work, open loop antenna is employed for generating CP waves since it has a simple configuration, requires a single feeding and has pure resistance at resonance. In addition, it can provide wider bandwidth if a parasitic open loop is incorporated inside the main driven loop [15].

1.3 Dielectric Resonator Antennas (DRA)s

Dielectric Resonators that are fabricated with high dielectric constant materials (ε_r~ $20-100$) were commonly used as storage devices, with high Q-factor, in microwave-circuit applications [16]. Later, it was observed that these resonators can also be efficient radiators if they are placed in an open space with the proper excitation of the desired mode [17]. The authors of [16] insisted that this fact was realized as early as 1939 by Richtmyer. However, it can be said that the first systematic study of dielectric resonators as radiating elements was conducted by Long, McAllister and Shen in 1983 [18]. Since then, numerous investigations on what has been named as Dielectric Resonator Antennas (DRAs) have been carried out.

1.3.1 *DRA Advantages*

DRAs are available in different shapes, such as circular, rectangular, hemispherical, elliptical and others. The DRA size can be changed simply by varying the dielectric constant, ε_r of the material [16] since the dimensions are proportional to $\lambda_o/\sqrt{\varepsilon_r}$, where λ_o is the free-space wavelength. The only source of losses in DRA is the imperfect dielectric. Therefore, high radiation efficiency can be achieved even at high frequency bands, by selecting low-loss dielectric materials [17]. This is owing to the absence of conductor losses and surface waves. An important factor when designing a DRA is the field configuration of the various modes where they operate as a magnetic/electrical dipole, independent of their shapes [16, 17]. Applying the right

excitation mechanism at the proper location is crucial to excite the desired mode. Furthermore, investigation the plane of symmetry can enhance the design further. The plane of symmetry of the DRA modes can be classified as electric and magnetic walls [16]. Modes with electric walls can reduce the size of the DRA into half with the aid of metallic sheet at the plane of symmetry. Another advantage of DRAs is its wider impedance bandwidth compared to other antenna types such as a microstrip antenna. This is owing to the fact that the waves radiate through the entire DRA surface, except for the ground, in contrast with the limited radiation of waves through two narrow edges of the patch as in a microstrip antenna [17].

1.3.2 *DRA in the literature*

Numerous DRAs designs have been reported. A recent review quoted more than 800 publications and few DRA books as in 2010 [19]. Several excitation types, for different DRA shapes, of different applications have been reported. For example, a single probe feed has been utilized for single band LP radiation for cylindrical [18], Rectangular [20], hemispherical [21], and Hexagonal [22] DRAs. In addition, a microstrip slot coupled DRAs have also been reported for cylindrical [23], rectangle [24] and Triangle geometries [25]. Other DRA designs for Dual band LP radiation have also been reported, where a printed rectangular patch on the top of a rectangular dielectric resonator has been proposed in order to achieve a dual-band operation [26]. A DRA for Ultra Wide Band (UWB) applications has also been considered, where a probe-fed stacked rectangular DRA has been designed with a 10dB return loss range from $3.1 - 10.7\ \mathrm{GHz}$ [27]. Other important DRA configurations are those with the capability of radiating Circularly Polarised (CP) waves. Many CP DRAs that have been reported that can be classified into single and multiple feed CP DRAs. For example, a slot coupled rectangular DRA, which is fed by a microstrip line has been designed, with a 3dB axial ratio of 3% [28]. Moreover, a probe-fed, cylindrical DRA that is loaded with a set of longitudinal slots with limited depths for circular polarisation radiation has been reported with AR bandwidth of 4% [29] . For wider axial ratio bandwidth with single feed, travelling wave current antennas can be deployed such as spiral and open loops. For example, a single fed square spiral strip on rectangular DRA has been reported in [30, 31] where AR and S_{11} bandwidths of 7% and 11% respectively have been achieved. Other single feed wide-band CPDRA

incorporates complex designs with the used of arrays of single CPDRA or using 90^o phase shifter. For example, a $4\,x\,4$ element planar array of chamfered squares having uniform aperture distribution achieved an AR bandwidth of $\sim 15\%$ has been demonstrated using power divider [32]. Additionally, a pair of 90^o hybrid coupler have been used to excite four strips attached to a cylindrical DRA [33]. This complex design achieved AR and S_{11} bandwidths of 25.9% and 34.5% respectively. There are other CP DRAs designed using multiple feeds. For example, dual fed conformal strips have been deployed on cylindrical DRA to achieve a wide band axial ratio of 20% [34]. The same principle has been utilized in [35] to excite a hemispherical DRA with an axial ratio bandwidth of 21%. In this work, an Elliptical DRA is used for circular polarisation generation since it is provides a greater design flexibility compared to the circular cylindrical DRA. Several designs are presented including dual single and dual band CP.

1.4 Artificial Magnetic Conductor (AMC)

1.4.1 *AMC Theory*

In antenna design, a perfect electrical conductor (PEC) metal sheet is usually used as a ground plane to eliminate radiation into the lower hemi-sphere, which increases the gain. However, the antenna has to be placed at a distance of $\lambda_o/4$ from the PEC plane since radiation is disturbed by the image source. In addition, using a metal sheet introduces surface waves that exits between different materials. These surface waves, if scattered by bends or discontinuities, can cause interference with the antenna's radiation [36]. Moreover, if multiple antennas share the same ground plane, surface wave can cause unwanted mutual coupling. The image in a PEC ground plane reflects the incident wave with a phase of 180^0. Therefore, a ground plane surface that reflects the incident wave with 0^0 phase is needed. Such surface is known as Perfect Magnetic Conductor (PMC), which does not exist in nature [37]. However, it has been observed, that radio frequency electromagnetic properties of a PEC surface can be changed by introducing a repeated texture [36]. If the period of the texture is much smaller than λ, then the surface can be described using an effective medium model, the surface impedance [36]. A textured PEC surface offer high surface impedance at a particular frequency range unlike normal PEC surface, which offers extremely low impedance. The frequency range where the surface

impedance is high allows low tangential magnetic field [36], which results in an in-phase, rather than out-phase, image current and can be used as new ground plane for low profile antennas. Such surfaces has been first known as Electromagnetic band Gap (EBG) [36]. In EBG, the textured PEC is connected to a normal PEC sheet with the aid of small conductors, known as vias. Meanwhile, It has been found in other structures that vias can be removed, which reduces the design complexity while achieving remarkable results. Such structures are known as Artificial Magnetic Conductors [38-40]. Since then numerous AMC designs have been reported.

1.4.2 *AMC Reflection Phase*

While PEC and PMC surfaces exhibit 0^o and 180^o reflection phases, respectively, for incident waves, AMC introduces unique reflection phase that is varying from 180^o to -180^o as can be seen in Figure 1.4.1.

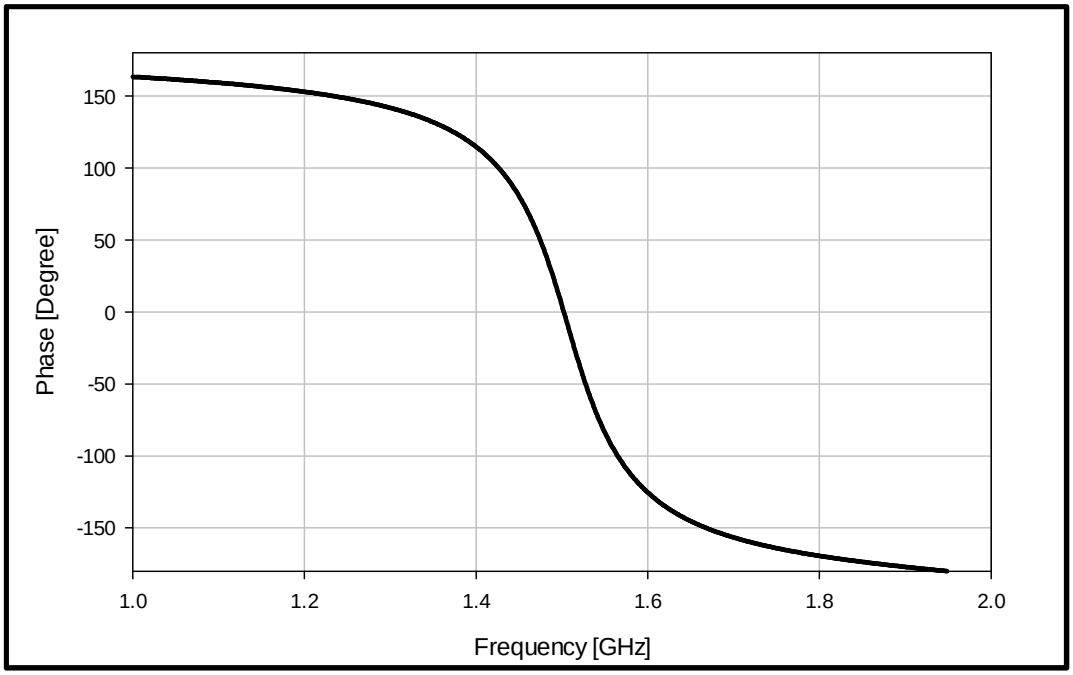

Figure 1.4.1: Typical reflection phase of AMC surface

The frequency range where the reflection phase is between 90^o and -90^o has a surface impedance larger than the free space impedance and hence, the image current is reflected in-phase when incident on the textured PEC surface [36]. On the other hand, it has been reported that the frequency range where the reflection phase lies within $90^o \pm 45^o$ achieves useful return losses for low profile wire antennas [37]. In this work, the operational bandwidth of an AMC surface is defined as

$$\mathrm{AMC}_{BW} = \frac{f_{-90} - f_{90}}{f_0} \tag{1.5}$$

where f_{-90}, f_{90} and f_0 are the frequencies at reflection phases of -90^0, 90^0 and 0^0 respectively [36].

1.4.3 *AMC Physical Interpretation*

The Physical interpretation of the mushroom-like structure introduced by Sievenpiper can be explained by modelling the surface impedance as a parallel resonant LC circuit as shown in Figure 1.4.2 [10].

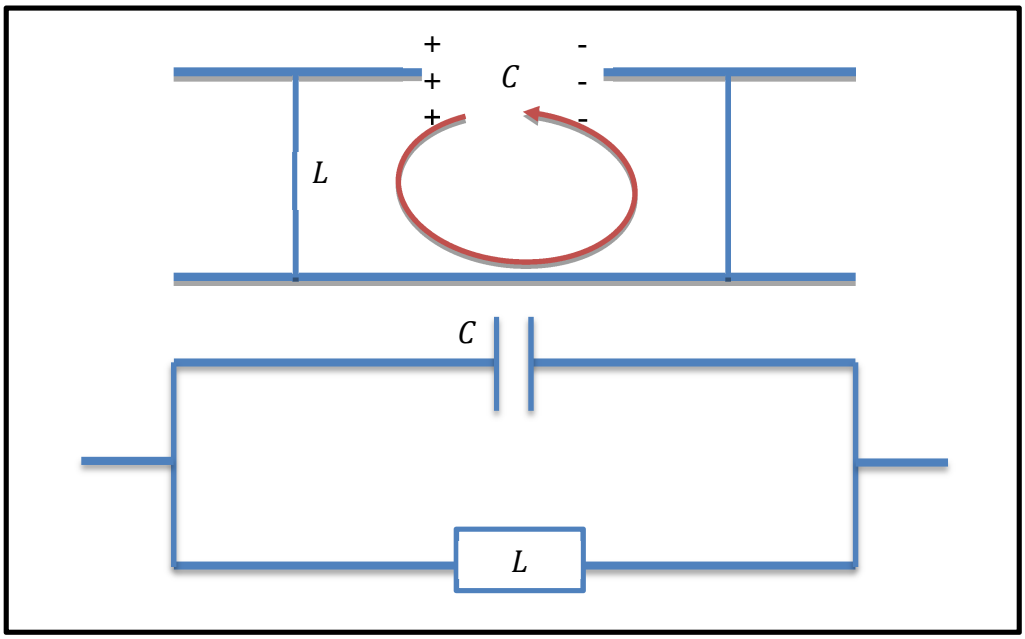

Figure 1.4.2: Equivalent LC circuit for the mushroom-like EBG

The structure can be seen as a resonant structure with a capacitance *C* and an inductance *L*. The capacitance is induced from the discontinuities and gaps between the conductors whereas the inductance is contributed by the current loops that are formed between the plates and the ground plane. The impedance of the surface can be expressed as [36]:

$$\mathrm{Z}_s = \frac{j\omega L}{1 - \omega^2 LC} \tag{1.6}$$

Therefore, the resonance frequency of the structure is given by:

$$\omega_o = \frac{1}{\sqrt{LC}} \tag{1.7}$$

and the relative operational bandwidth of the structure is given as:

$$\frac{\Delta\omega}{\omega} \propto \sqrt{\frac{L}{C}} \tag{1.8}$$

From equations (1.7) and (1.8), it can be seen that adding an inductance to the system results in reducing the resonance frequency and increasing the bandwidth, whereas adding more capacitance reduces both the resonance frequency and the bandwidth.

1.4.4 *AMC in the literature*

Several EBG/AMC structures have been reported. As mentioned earlier, the first detailed study on EBG structure has been reported by Sievenpiper in his pioneered Mushroom-like EBG [36]. During the same period, a similar concept has been presented by Yang *et. al.* with a structure known as Uniplanar Compact Photonic-Bandgap (UC-PBG), where it has been demonstrated that a 2D square lattice consisting of a metal pad and four connecting strips etched on the ground plane can provide stop-band for electromagnetic transmission [41]. A comprehensive study on the reflection phase of an EBG structure and its application for low profile wire antenna has been given [37]. A study of the AMC has been presented [39] and a design methodology for designing the mushroom-like EBG has been given [42]. Another study of the feasibility of using AMC structure as a ground plane for low profile antennas has been presented where the resonant cavity approach has been adopted to study the AMC using ray theory [40]. In a subsequent study, it has been shown that loading the AMC substrate with a magnetic material can enhance the bandwidth significantly [43]. This concept has also been cross validated with another study, which has shown that using magneto-dielectric substrate for EBG structure has resulted in in-phase reflection bandwidth of 70% [44]. A novel EBG structure has been designed using multiple non-grounded vias [45], where it has been shown that the unit cell size has been reduced by 81.6% compared to the mushroom-like EBG. However, the design is far complex. AMC structure has also been integrated with a 4 layer antenna for GPS and GALILEO Systems [46]. Several AMC structures can be found in the literature. For example, an AMC with width of $\lambda_o/4.49$ and thickness of

$\lambda_o/67.87$ with a dielectric constant of $\varepsilon_r = 3.28$ has been reported [47]. Another design using $\varepsilon_r = 4.4$ and achieving unit cell width and thickness of $\lambda_o/5.26$ and $\lambda_o/51.7$ respectively has been proposed [48]. Further, an AMC with width of $\lambda_o/8.9$ and thickness of $\lambda_o/38.7$ with dielectric constant of $\varepsilon_r = 6.15$ has been achieved [49]. For multiple band AMC structures, a design methodology based on Genetic Algorithm has been presented [50]. Similar principle has also been reported in [51]. Also, a dual square patch AMC for dual band operation has been demonstrated incorporating a wide band monopole antenna [52]. In the conventional AMC structure, the design relies on the physical size and shape to resonate at a particular frequency. In addition, it requires periodicity to work effectively, which increases the size of the antenna. Recently, a FSS structure associated with lumped reactive elements has been reported so that resonance relies on the lumped elements rather than the physical size [53], where a unit cell size of $\lambda_o/115$ has been achieved using lumped capacitor and inductor. Later, a design methodology has been reported for FSS/AMC design, which showed that resonant frequency has been controlled by the values of the lumped elements and the distance between them [54]. In a later study, a dual band AMC with lumped capacitors has been reported, where two capacitors have been used to tune the AMC to two different frequencies [55]. So far, the entire antennas reported with these active AMCs have been Linearly Polarised antennas (LP). A further investigation could be associating the active AMC with circularly polarised antenna, which can have a larger periodicity than 4×4 but smaller ground plane. In this work, the square patch AMC and a novel single and dual band AMCs are utilized as ground planes for low profile circularly polarised open loop antennas.

1.5 Computational Electromagnetic Techniques

The process of designing an efficient antenna with desired configuration demands good understanding of electromagnetic theory. Closed form analytic solutions are available for a few simple examples given some particular ideal conditions, which are hardly applicable for current systems. Another method includes experimental investigation of an antenna, which is expensive and time consuming. A preferred method is to use numerical techniques in conjunction with modern computers to simulate the behaviour of an antenna with variety of conditions and configurations. Numerical techniques refers to the process of solving relevant Maxwell's equations

by converting them into chain or matrix equations which can be solved either by matrix inversion or by iteration. They are mainly classified based on the type of Maxwell's equations used; Integral Equation methods and Differential Equation methods [3]. These methods are classified further into two types; Time Domain (TD) and Frequency Domain (FD). An example of Frequency Domain Integral Method is the Method of Moment whereas an example of Time Domain Differential Equation is the Finite Difference Time Domain (FDTD) method. Each method has its own capabilities and limitations. It is more convenient to use the most efficient technique for a specific problem. In this chapter, four main numerical methods are described briefly.

1.5.1 *The Method of Moments (MOM)*

This method is classified as a Frequency Domain (FD) method, based on solving boundary value problems with the aid of Maxwell's Integral Equations (IE). It has been first introduced by Harrington in his 1967 paper [56]. It involves transforming an integral equation into a set of linear equations in matrix format and then finding the solution by inverting the unknown matrix. This technique works efficiently for wires and flat plates or planar structures in general and resonators [57]. However, it is inadequate for applications that include pulse excitations. Examples of widely used MOM based commercial software are FEKO [58], NEC [59].

1.5.2 *Finite Difference Time Domain (FDTD)*

This method is classified as a Time Domain (TD) method, based in Maxwell's Differential Equation (DE). The solution method involves dividing the domain into a grid of nodes. Then, the differential equation and the boundary conditions are approximated by a set of linear equations on the grid points [60]. Advantages of FDTD includes broadband response with a single excitation and solving arbitrarily 3D geometries [3]. It is recommended for structures with small number of ports. However, FDTD is less efficient for the modelling of long, thin structures such as wires. Examples of commercial software based on FDTD include Apsim FDTD [61] and Remcom XFDTD [62].

1.5.3 *Finite Element Method (FEM)*

This method is classified as a Frequency Domain (FD) method, based on Maxwell's Differential Equations. It is has the advantage of solving any arbitrarily shape structure. This can be achieved by discretizing the solution region into a set of small sub regions or elopements. Then, the governing equations for each element are derived. After that, all the equations are assembled in the solution regions as a matrix [60]. FEM is recommended for structures with large number of ports such as ICs. Ansoft HFSS [63] is considered as the main commercial software based on FEM. It has been used in this this work to simulate some antenna designs.

1.5.4 *Finite Integral Technique (FIT)*

This method is classified as a Time Domain (TD) method, based on Maxwell's Integral Equation. The same principle of dividing the domain into nodes as given in FDTD is performed. To apply the method to the full set of Maxwell's equations in integral form, FIT uses all six vector components of electric field strength and magnetic flux density on a dual grid system; space and time which yield discrete grid equations [64]. The CST microwave studio [65] is considered as the main commercial software that is based on FIT, which is the main simulator in this work.

1.5.5 *Method of Auxiliary Sources (MAS)*

It is a numerical technique can be used to solve the boundary-value problem [66]. It provides an alternative to the standard Surface Integral Equation (SIE) formulation technique, in which the unknown currents are assumed to be distributed on the scatterer surface and obtained using the Method of Moment (MOM) [67]. In MAS, the main idea is to eliminate the singularity in the integral equation by shifting the contour of sources with respect to the integration contour[68]. This is achieved by representing the unknown scattered field with the aid of fictitious, or auxiliary, sources that are placed on an auxiliary surface, which is situated in the non-physical area of the problem [66, 69-71]. The auxiliary sources are chosen such that their fields are elementary analytical solutions to the boundary-value problem. Then, the actual EM field is expressed as weighted superposition of the analytical solutions. The resultant matrix has unknown expansion coefficients to be determined by point-matching the relevant boundary conditions at a discrete set of observation points,

known as collocation points or Test Points (TP) on the physical boundary [69]. The main disadvantage of this method is the ambiguity of the location of the auxiliary sources, which yields unpredicted results in some cases or complete failure of the method without clear explanation as suggested by other authors [72].

1.6 Thesis Layout

Following this introduction, several Circularly Polarised-Elliptical Dielectric Resonator Antennas (CP-EDRA) are presented in Chapter 2. The first is a conformal strip excited EDRA, followed by a wideband CP-EDRA. The wideband has been achieved using a half-open loop conformal antenna in conjunction with an inner parasitic open-loop. Then a dual band CP-EDRA is presented with simulated and experimental results. The last design is a low profile conformal strip excited CP-EDRA. In Chapter 3, two extremely low profile circularly polarised open loop antennas backed by a square patch AMC are studied for the L_1 frequency band. A coplanar waveguide, CPW, as well as a probe fed, loops have been considered theoretically and experimentally, with good agreement between measurements and simulations. In order to reduce the structure size, a design of a smaller novel AMC unit cell is proposed in Chapter 4. Once more, CPW and probe-fed CP loops have been placed above the novel AMC with good agreement between predicted and measured results. In Chapter 5, a novel dual band AMC is presented, which is suitable for both the L_1 and L_2 GPS signals. Finally, conclusions and future work recommendation are presented in Chapter 6.

CHAPTER 2

Circularly Polarized-Elliptical Dielectric Resonator Antenna (CP-EDRA)

2.1 Introduction

An Elliptical Dielectric Resonator Antenna (EDRA) is shown in Figure 2.1.1. The main parameters to be considered are: the major and the minor semi axes a and b respectively, the height h, and the dielectric constant ε_r.

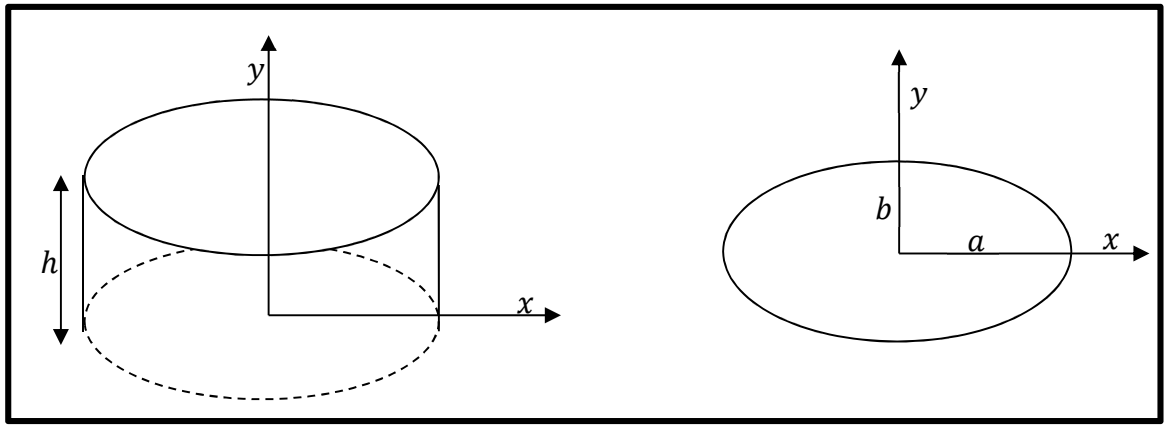

Figure 2.1.1: Elliptical Dielectric Resonator Antenna

Elliptical antennas have been used in different configurations. For example, a wide band planar elliptical monopole has been reported in [73]. Also, a low profile, ultra wideband single ended elliptical antenna has been suggested in [74] and a low profile differential elliptical antenna has been reported in [75]. The main advantage of an elliptical shape is that it can be considered as an overlap of two cylinders with different radii [76]. Therefore, it is expected that more modes are propagating in the elliptical DRA compared to the cylindrical DRA, which gives more flexibility to the designer. In this chapter, it will be demonstrated that by selecting the right feeding mechanism at the proper location, single, dual, and wide, band(s) circularly polarised antennas can be designed. First, a literature review on the EDRA is given. This is followed by an analysis of the resonance modes in addition to explanation of the measurements procedures followed in this work. Finally, simulation and experimental results are presented for several CP EDRA designs.

2.2 EDRA Literature Review

The first study on an elliptical DRA has been reported in 1999 [76], where a coaxial probe feed has been used to excite an EDRA for circular polarisation. The a/b axial ratio used was 1.14 with $\varepsilon_r = 45$. The results demonstrated the feasibility of generating a CP signal but no information was provided for the axial ratio AR or for

the reflection coefficient, $S_{11,}$ bandwidths. Later, in 2003, Kishk has used a coaxial probe to excite EDRAs of different geometries [77], where respective bandwidths of 3.5% and 14% for AR and S_{11} have been reported for $a/b = 1.5$ with a relative permittivity $\varepsilon_r = 12$. It has also been mentioned that when $a/b \approx 1$, poor results are expected. The best result has been achieved when the probe was placed inside the EDRA at an angle of 33.7^o from the major x-axis. In 2004, Chen*, et al.* have used EDRA for dual band applications [78], where two $HEM_{11\delta}$ modes have been excited using two different probe feeds. The a/b ratio was 3.26 and the dielectric constant was $\varepsilon_r = 37$. In the same year, Sharkawy*, et al.* have used stacked EDRA for wideband applications [79], by placing two EDRAs of different relative permittivities ($\varepsilon_r = 15$ and 2.5) and radii on top of each other. The stacked configuration has provided an impedance matching bandwidth of 61.5%. Additionally, Tadjalli*, et al.* have reported the cross-section field patterns and the cut off frequencies for the EDRA [80]. In 2005, Chair*, et al.* have designed an eye shaped DRA, which consists of a circular cylinder inside an elliptical resonator with different ε_r [81]. The structure has provided an impedance matching bandwidth of 27.7%. Later in 2006, Yang*, et al.* have used two different excitation mechanisms for an EDRA with $\varepsilon_r = 10.2$ for circular polarisation radiation [82]. The first feeding method was a microstrip line etched on a substrate of $\varepsilon_r = 3.38$, where respective measured AR and S_{11} bandwidths of 5.2% and 17.3% have been reported. Secondly, the EDRA has been rotated to $\varphi_x = 45^o$ and excited using a microstrip line through a narrow rectangular slot. The reported measured AR and S_{11} bandwidths were 4.2% and 26.5%, respectively. In the same year, Tadjalli and Sebak have provided a detailed analytical approach to determine the resonance frequencies and far field patterns for EDRAs using the Mathieu and Modified Mathieu functions to expand the fields inside the EDRA [83]. In 2007, Yang*, et al.* have designed a 2×2 EDRAs array in which the elements have been excited sequentially using a different feeding network [84]. Respective axial ratio and impedance matching bandwidths of up to 26% and 44% have been reported in that study. Moreover in 2007, Tadjalli*, et al.* have used Genetic Algorithm to optimize the dimensions of an EDRA that is excited by a microstrip line through a narrow rectangular slot [85]. In order to generate a CP wave at $3\ \mathrm{GHz}$, the even TE_{020} mode has been excited at $2.95\ \mathrm{GHz}$, while the odd TE_{110} mode has been excited at $3.05\ \mathrm{GHz}$. This structure has generated an AR bandwidth

of 2.7%. In a more recent article that has been published in 2010, Kejani and Neshati have designed an EDRA that is fed using a Direct Image Line (DIL) [86]. For the single EDRA element of $\varepsilon_r = 10.2$ and placed at $\varphi_x = 45^o$, an AR bandwidth of 4.5% has been achieved.

In this work, a simpler feeding method is employed that is based on using conformal strip(s) to design a number of singly fed elliptical DRAs with CP radiation. The first EDRA has been fed using a single conformal strip, while the second has been excited by a conformal half-open loop for a wide band circular polarisation radiation. Additionally, a dual band EDRA has been designed and measured. Finally, a low profile circularly polarised EDRA is presented.

2.3 EDRA Resonance Modes

In the DRA design, power has to be coupled efficiently from the feeding source to the antenna. As a result, it is essential to understand the resonance modes' electromagnetic fields distributions inside the DRA. When coupled to a DRA, the feeding source can be modelled either as an electric or magnetic current source [87]. In order to have an optimum coupling using an electric current source such as a probe, it should be located at a strong electric field point. On the contrary, in case of using a magnetic current source such as an aperture, it has to be located at a strong magnetic field point in the DRA [87]. Therefore, understanding the fields' configuration facilitates the employment of different excitation means depending on the requirements and application. Consider an elliptical DRA placed on a ground plane as shown in Figure 2.1.1, which has a dielectric permittivity ε_r, height h, and respective semi-major/minor axes of a and b. With the aid of image theory, the Electromagnetic fields inside an elliptical DRA mounted on a perfect electrically conducting (PEC) ground plane are assumed to be equivalent to those of an isolated elliptical dielectric waveguide having similar dimensions of a, b, ε_r and a height of $2h$ [16, 83]. Then, the perfect magnetic wall boundary condition is applied, which state that the total tangential magnetic field vanish on the surface of the EDRA [88]. In order to solve for the fields inside the EDRA, the scalar Helmholtz equation, given by equation (2.1) needs to be solved in elliptical coordinates [80].

$$\frac{2}{f_0^2(\cosh 2\xi - \cos 2\eta)}\left(\frac{\partial^2}{\partial \xi^2} + \frac{\partial^2}{\partial \eta^2}\right).\begin{Bmatrix} E_z \\ H_z \end{Bmatrix} + (k^2 - k_z^2)\begin{Bmatrix} E_z \\ H_z \end{Bmatrix} = 0 \qquad (2.1)$$

where:

f_0 is the semi-focal distance of the ellipse

ξ is the radial component in the elliptical coordinate

η is the angular component in the elliptical coordinate

k is cavity wavenumber and k_z is the longitude wavenumber

Solving the Helmholtz equation in elliptical coordinate using the separation of variables method yields Mathieu equations, which are linear second-order differential equations with periodic coefficients that have solutions, known as Mathieu functions, named after a French mathematician E. L. Mathieu [89, 90]. After a long procedure and derivations, which can be found in [83] and will not be repeated here, it has been found that except for the first harmonic, all the other modes can be either odd or even. Therefore, the elliptical cylinder has an advantage over the circular cylinder in terms of modes number. An isolated elliptical DRA can support TE (Transverse Electrical field), TM (Transverse Magnetic) and hybrid modes; HE and EH. The TE and TM modes are symmetrical around the axis and do not have azimuthal variation. However, the hybrid modes are azimuthally dependent. There are different ways for mode nomenclatures that have been used in the literature. In this thesis, the nomenclatures used by Kobayashi *et. al.* is employed [91]. Each mode has three indices, $nmp + \delta$, which, denote the field's variation in the azimuthal, radial, and z directions, respectively. Since TE and TM fields have no azimuthal variation, they are denoted as $TE_{0mp+\delta}$ and $TM_{0mp+\delta}$. The lowest orders TE mode TM modes are denoted as $TE_{01\delta}$ and $TM_{01\delta}$, respectively. The radiation patterns of the $TE_{01\delta}$ and $TM_{01\delta}$ modes for an isolated resonator are the same as a those of vertical magnetic and electric dipoles, respectively. Hybrid modes are classified as EH and HE depending on the strength of the electrical and magnetic fields along the z-axis. For the EH field, the H-field is dominant in the z-direction whereas for the HE field, the E-field is dominant in the z-direction. Since they have azimuthal variations, they are denoted as $HE_{nmp+\delta}$ and $EH_{nmp+\delta}$. The lowest order for the HE and EH modes are $HE_{11\delta}$ and $EH_{11\delta}$, respectively. The radiation fields for the $HE_{11\delta}$ and $EH_{11\delta}$ modes of an isolated resonators are the same as those of horizontal oriented magnetic and electrical dipoles, respectively. The hybrid HE and EH modes are degenerate for symmetrical structures such as circular resonators [76]. This results in having a multipole corresponding to each degenerate hybrid mode [16]. That is, for example,

for $HE_{11\delta}$ mode, there will be a 90^o magnetic dipole associated with every radiating 0^o magnetic dipole. Owing to the fact that the EDRA is not symmetrical around the axis, it is expected to have these two orthogonal modes, with a slight shift in the frequency. In this work, the $HE_{11\delta}$ mode will be utilized for circularly polarised EDRA, which can be classified as; odd and even. This behaviour can be understood from the electric and magnetic field distribution given in Figure 2.3.1-Figure 2.3.4, where the shortest dipole (y-directed, even mode) generates the lower frequency and the longest dipole (x-oriented, odd mode) generates the higher frequency. As a result, circularly polarised radiation can be achieved if these two modes are generated.

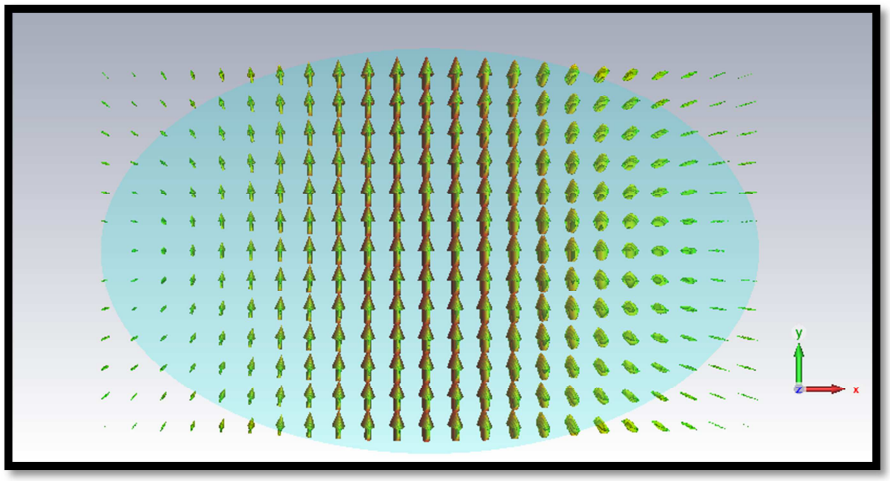

Figure 2.3.1: H-field for the y-oriented magnetic dipole for the $HE_{11\delta}$ even mode

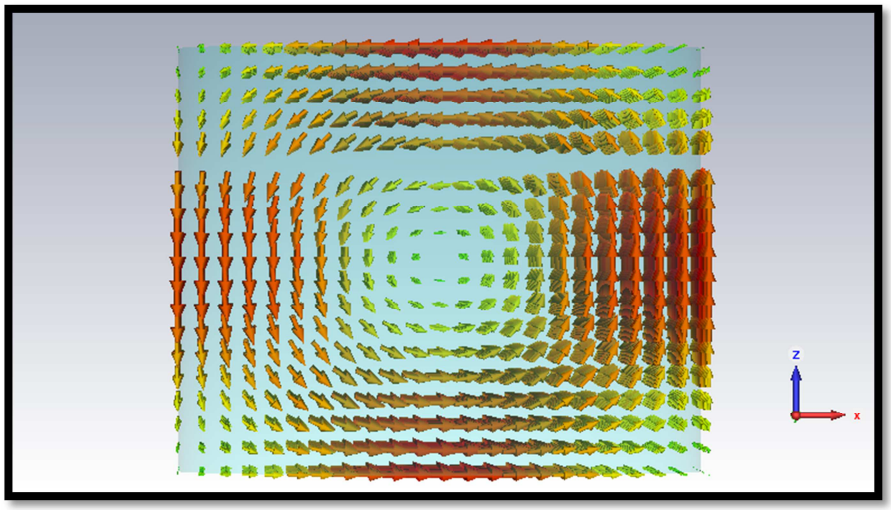

Figure 2.3.2: E-field for the y-oriented magnetic dipole for the $HE_{11\delta}$ even mode

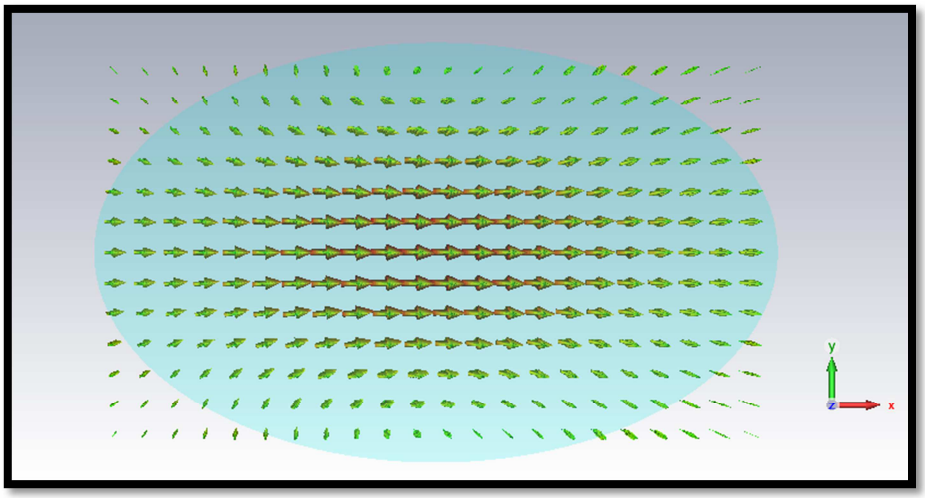

Figure 2.3.3: H-field for the x-oriented magnetic dipole for the $HE_{11\delta}$ odd mode

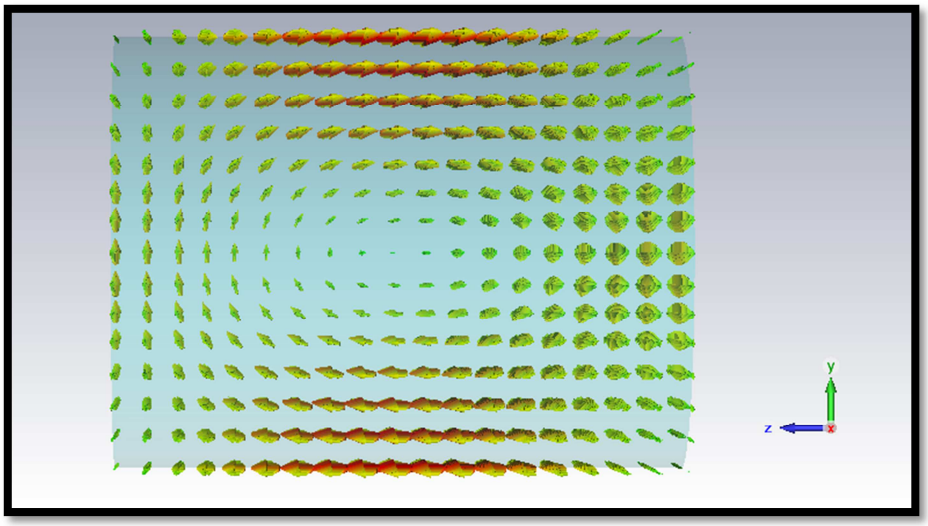

Figure 2.3.4: E-field for the x-oriented magnetic dipole for the $HE_{11\delta}$ odd mode

2.4 Measurements Procedures

In this work, the following antenna parameters have been measured; the reflection coefficient S_{11} the axial ratio, the gain and the radiation pattern. In this section, the procedures followed to measure these parameters are presented.

2.4.1 S_{11} Measurements

For S_{11}, the antenna has been connected to an HP8720D Vector Network Analyser (VNA) using a RF cable. To use the VNA effectively, the desired frequency range needs to be set first and calibration procedure using a safe calibration kit has to be done before using it for measurement.

2.4.2 *AR Measurements*

For the far-fields' measurements, the EDRA has been placed at the receiving terminal inside an anechoic chamber as shown in Figure 2.4.1, where it can be observed that a standard horn has been used as a transmitting antenna.

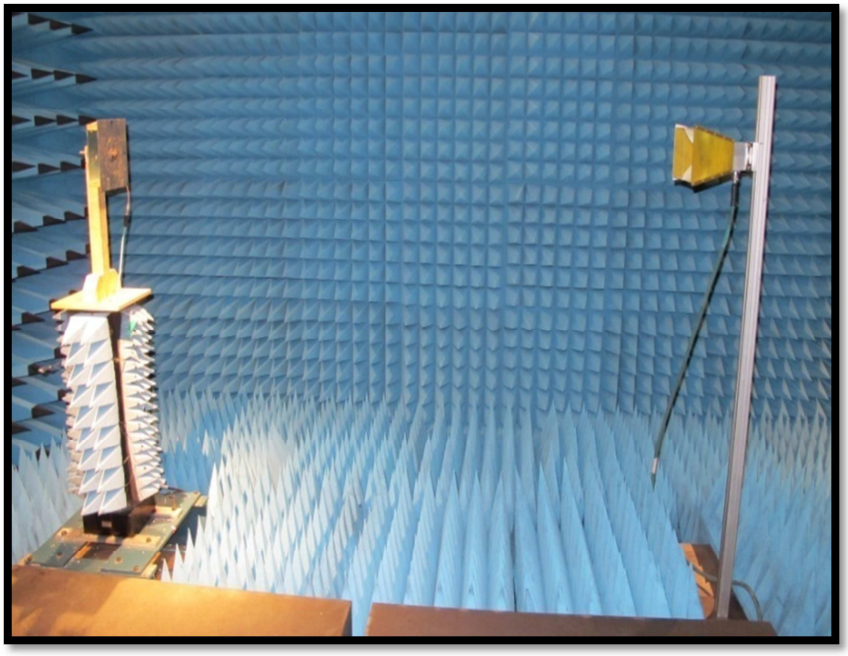

Figure 2.4.1: EDRA in the anechoic chamber

Then, two orthogonal cuts for the fields are measured; horizontal E_H and vertical E_V components, which correspond to E_φ and E_θ respectively. This has been implemented by measuring the received signal with the horn antenna rotated at 0^o and 90^o, respectively. Then, the axial ratio has been determined by calculating the right and left handed electric field components E_R and E_L given as [92]

$$E_R = \frac{1}{\sqrt{2}}(E_H + jE_V) \tag{2.2}$$

$$E_L = \frac{1}{\sqrt{2}}(E_H - jE_V) \tag{2.3}$$

Finally, the AR can be determined as [10]

$$AR = 20\log_{10}\left[\frac{|E_R| + |E_L|}{|E_R| - |E_L|}\right] \tag{2.4}$$

2.4.3 *Gain Measurements*

There are two popular methods for gain measurements; absolute-gain and gain-transfer, or gain-comparison, methods [1]. The first method is used to calibrate antennas that can be used later as standards for gain measurements. While in the second method, the antenna under test is compared with a standard antenna with known gain. There are two common standard antennas; the $\lambda/2$ dipole antenna and the pyramidal horn antenna. In this work, the horn antenna has been employed as a reference. The gain of the EDRA, G_{EDRA}, can be calculated from the known gain of the reference horn, G_{Horn} using [93]:

$$G_{EDRA}[dB] = G_{Horn}[dB] + 10\log_{10}\left[\frac{P_{EDRA}}{P_{Horn}}\right] - 20\log_{10}\left[\frac{1-|S_{11EDRA}|}{1+|S_{11Horn}|}\right] \quad (2.5)$$

Where P_{EDRA} and P_{Horn} are the powers received for the EDRA and the Horn antennas, respectively. The reflection coefficients S_{11EDRA} and S_{11Horn} are for the EDRA and the horn antennas, respectively. The last term in equation (2.5) takes account of the possible impedance and polarisation mismatches.

2.5 Conformal Strip Excited EDRA

2.5.1 *Introduction*

In any system design, a trade-off between the design complexity and outcome is needed. For a probe fed EDRA, the best achieved 3dB Axial Ratio bandwidth mentioned in literature is 3.5% [77]. In that design, the probe has been placed inside the dielectric, which means that in practice, the dielectric must be drilled to create a gap and then, the probe is inserted in that gap. This is usually associated with air gaps that affect the input impedance, resonance frequency and the bandwidth [94]. Therefore, it is more convenient to use a feeding mechanism that avoids this complexity. In this work, a conformal strip excitation mechanism is proposed [95] that is deployed on the surface of the EDRA. This results in a simpler design and a predictable performance.

2.5.2 *Design Procedures*

The conformal strip excited EDRA has several design parameters; a, b, h and ε_r in addition to the size and location of the conformal strip. As a starting point, the material of the EDRA has been chosen as Aluminium Dynallox with $\varepsilon_r = 9.8$. The

primarily aim is to design an antenna suitable for the L_1 GPS band $(1.575\,\mathrm{GHz})$. However, at this stage, it is only desired to show the feasibility of using a conformal strip to have circularly polarised EDRA antenna without any specific frequency range. Therefore, the antenna has been designed to work at $2\,\mathrm{GHz}$. The initial values of the EDRA parameters have been used with those given in [77] at $10\mathrm{GHz}$. A simple algebraic equation has been used to scale the dimensions so that the EDRA resonates at $2\mathrm{GHz}$, which is given by:

$$a_{new} = a_{old} \times \frac{f_{old}}{f_{new}} \tag{2.6}$$

CST Microwave Studio [65] has been used to simulate the elliptical DRA for optimum performance as discussed next. The discrete port of CST has been used to excite the EDRA, located at the bottom of the strip as shown in Figure 2.5.2. The width of the conformal strip has been chosen to be $3\,\mathrm{mm}$ as a starting size. The height of the strip l_w has been chosen to be equal the height of the EDRA. As mentioned earlier, the feeding strip needs to be located at the vicinity of a strong electric field. Examining the fields of the two $HE_{11\delta}$ modes given by Figure 2.3.1-Figure 2.3.4, demonstrates that locating the strip at $\varphi = 0, 180^o$ should excite the $HE_{11\delta}$ even mode, whereas locating the strip at $\varphi = 90, 270^o$ will excite the $HE_{11\delta}$ odd mode. Therefore, the ideal strip position to excite these two modes is somewhere between the two orthogonal points. As a result, the strip has been located at $\varphi = 135^o$ as shown in Figure 2.5.1 and Figure 2.5.2. The parametric sweep of CST Microsoft Studio has been used to vary the a/b ratio of the EDRA while keeping the height constant and vice-verse. For the first test, the effect of varying the a/b ratio on the reflection coefficient and the axial ratio AR are shown in Figure 2.5.3 and Figure 2.5.4, respectively.

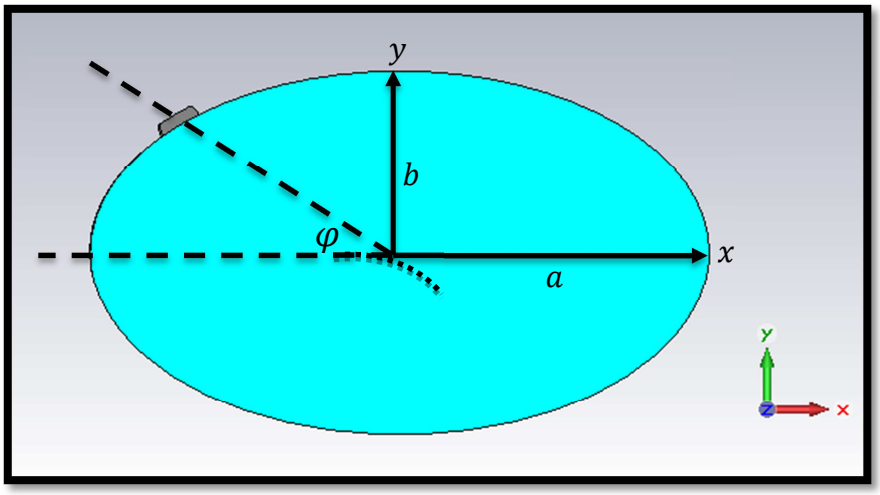

Figure 2.5.1: Conformal Strip Excited EDRA, top view

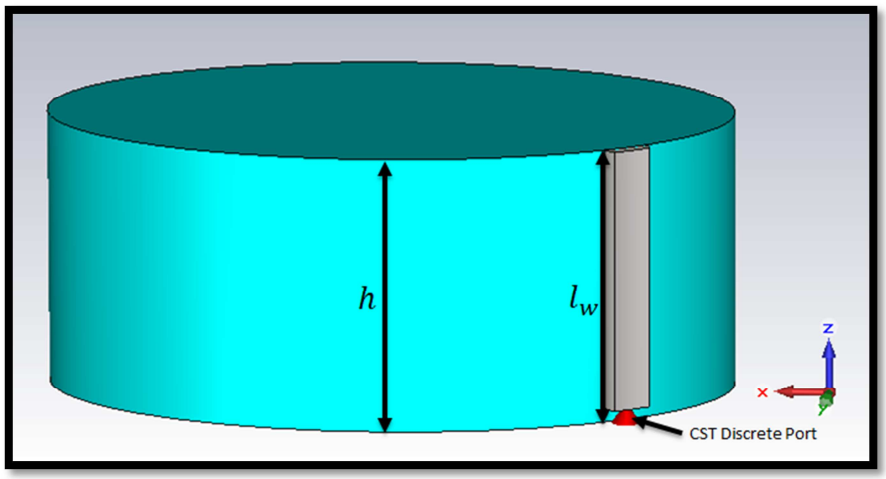

Figure 2.5.2: Conformal Strip Excited EDRA, side view

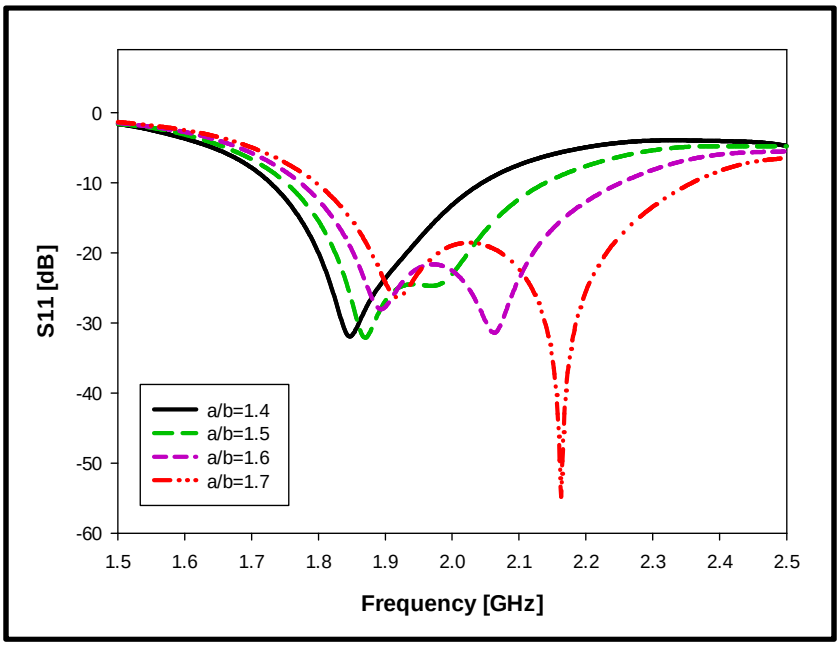

Figure 2.5.3: Reflection coefficient for different a/b ratios of the EDRA

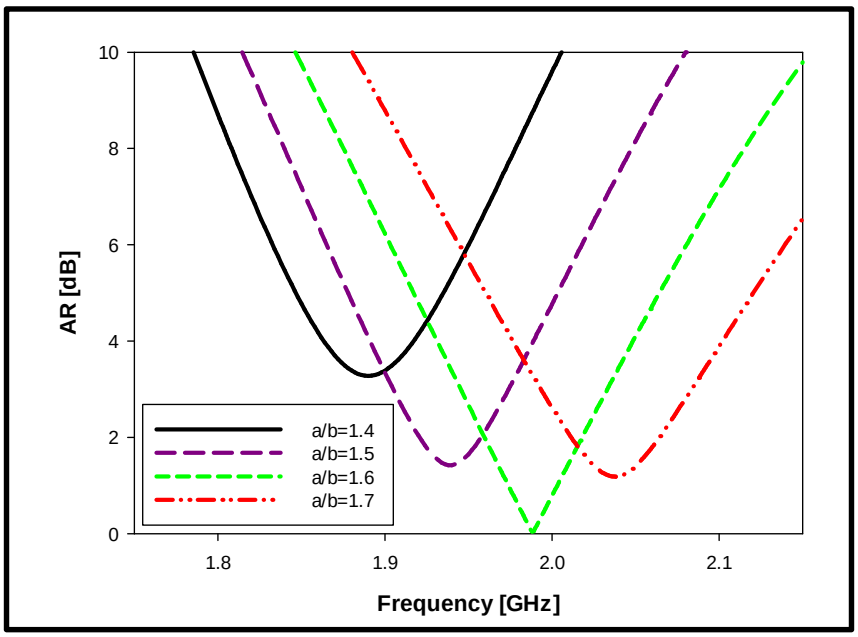

Figure 2.5.4: Axial ratio for different a/b ratios of the EDRA

It can be noticed from these results that varying the a/b ratio for this specific height alters the distance between the two excited modes. When the ratio is 1.4, the second mode starts to be excited and therefore an axial ratio can be achieved. As the a/b ratio increases, the axial ratio get closer to 0dB and two modes are excited strongly. However, further increment in the a/b ratio degrades the axial ratio because the two excited modes are displaced further from each other. The second test has been implemented by fixing the a/b ratio while the height h is varied. The results are presented in Figure 2.5.5 and Figure 2.5.6, where it can be noticed that changing the height from $17-23\text{mm}$ results in shifting the resonance frequency. However, two modes have been excited for all heights. A strong coupling has been achieved when the height is $21\ \text{mm}$ with the minimum axial ratio has been achieved at the required frequency of 2GHz.

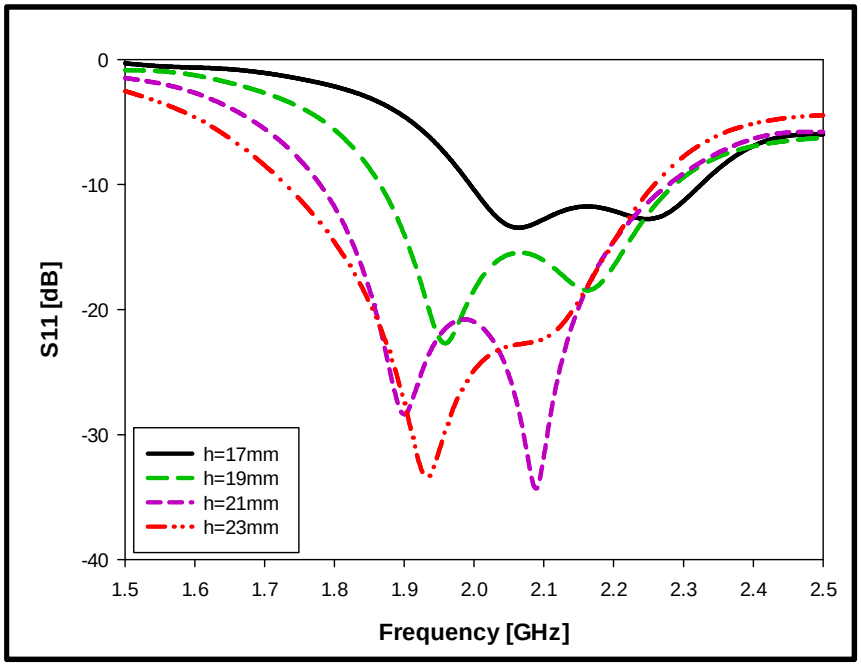

Figure 2.5.5: Reflection coefficient for different heights of the EDRA

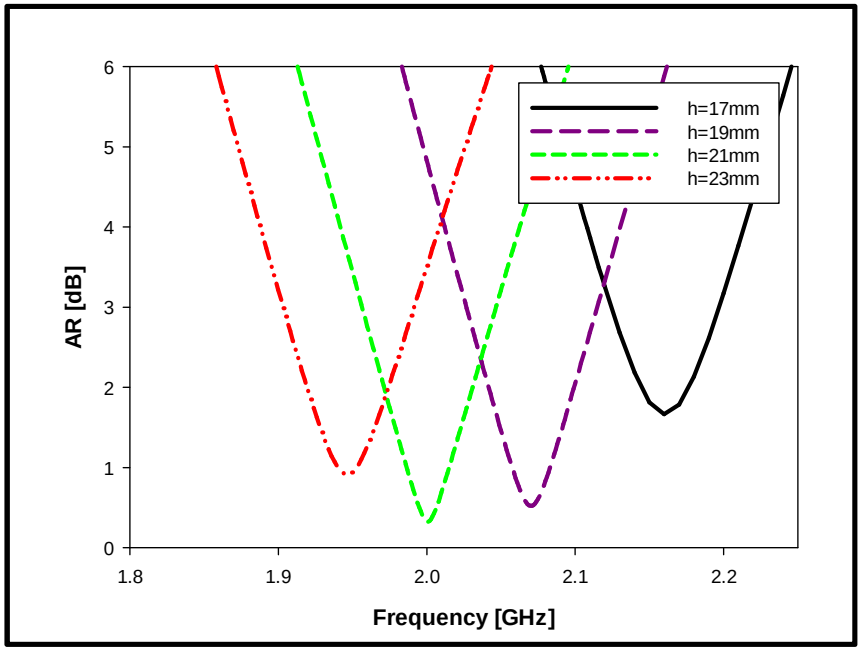

Figure 2.5.6: Axial ratio for different heights of the EDRA

As a result, The optimum a/b ratio has been determined as 1.625, with $a = 26\text{mm}$ and $b = 16\text{mm}$. The height of the EDRA has been chosen as $h = 21\text{mm}$, which corresponds to $\lambda_o/7.14$ at $2\ \text{GHz}$. Two more tests have been carried out for further understanding: First the strip length has been varied from $5 - 21\text{mm}$ and the AR and S_{11} have been studied as shown in Figure 2.5.7 and Figure 2.5.8, respectively.

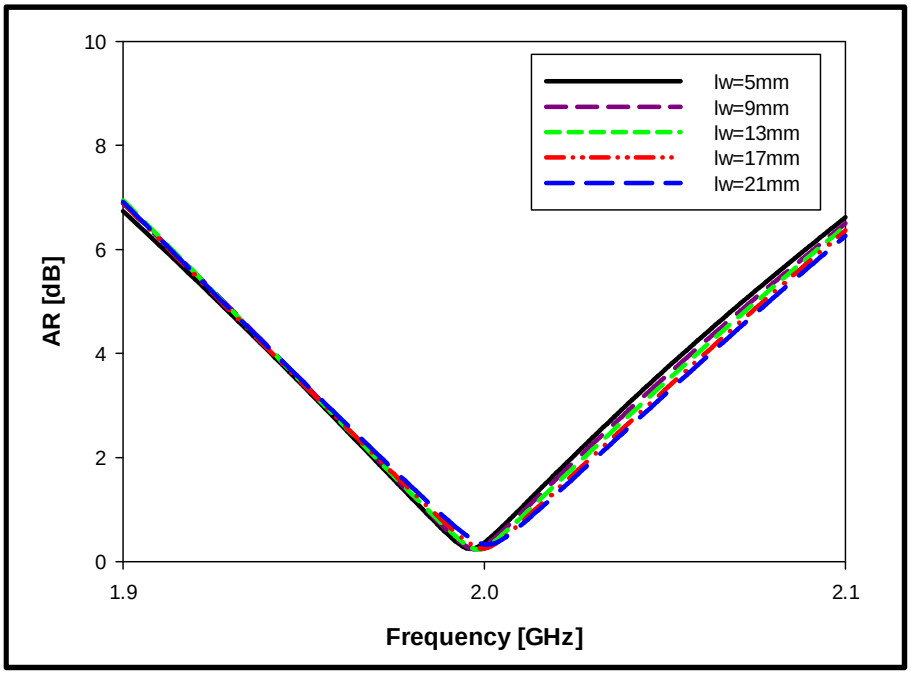

Figure 2.5.7: Axial ratio for different strip heights

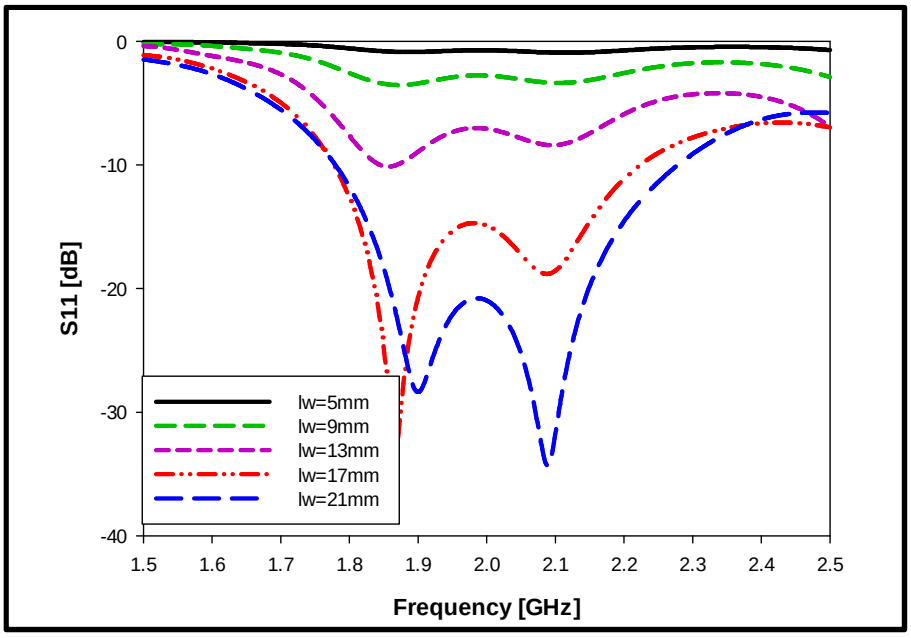

Figure 2.5.8: S_{11} for different strip heights

It can be observed that varying the strip length has marginal effects on the axial ratio since two modes are excited for all lengths. However, the reflection coefficient has been affected considerably with the length's variation. This is expected as the S_{11} is linked to the input impedance of the antenna, which is illustrated in Figure 2.5.9 and Figure 2.5.10 for different strip lengths.

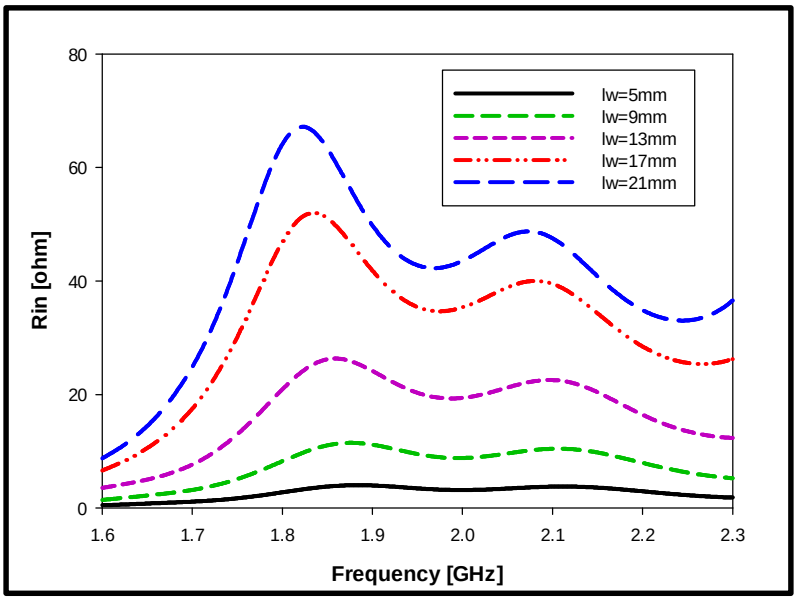

Figure 2.5.9: Input resistance for different strip heights

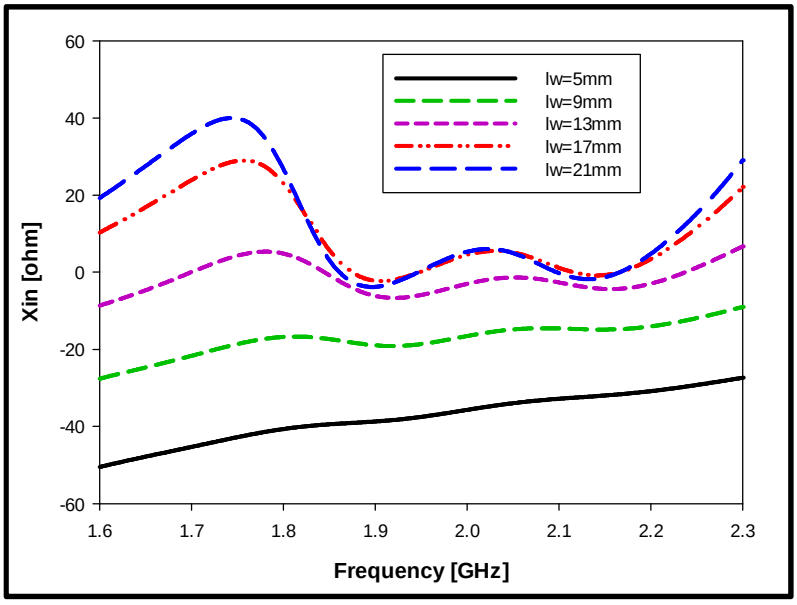

Figure 2.5.10: Input reactance for different strip heights

From these results, it can be seen that when the height is $5\ \mathrm{mm}$, the antenna offers a small input resistance in conjunction with a capacitive reactance. As the height increases, the input resistance becomes larger and the reactance is reduced. A strip length of $l_w = 21\mathrm{mm}$ provides, ~50Ω resistance and therefore an improved S_{11} could be achieved. Similar behaviour of the input impedance of variable probe lengths has also been observed by Long in his work for the cylindrical DRA [18]. Finally, the strip location has been varied. As explained earlier, in order to excite the two orthogonal $HE_{11\delta}$ modes, the strip has to be located in a position, where both modes have equal fields' strengths. Therefore the strip has been located initially at $\varphi = 135^o$, then, it

has been varied for several steps from $\varphi = 90 - 180^o$. The S_{11} and AR have been studied as shown in Figure 2.5.11and Figure 2.5.12, respectively.

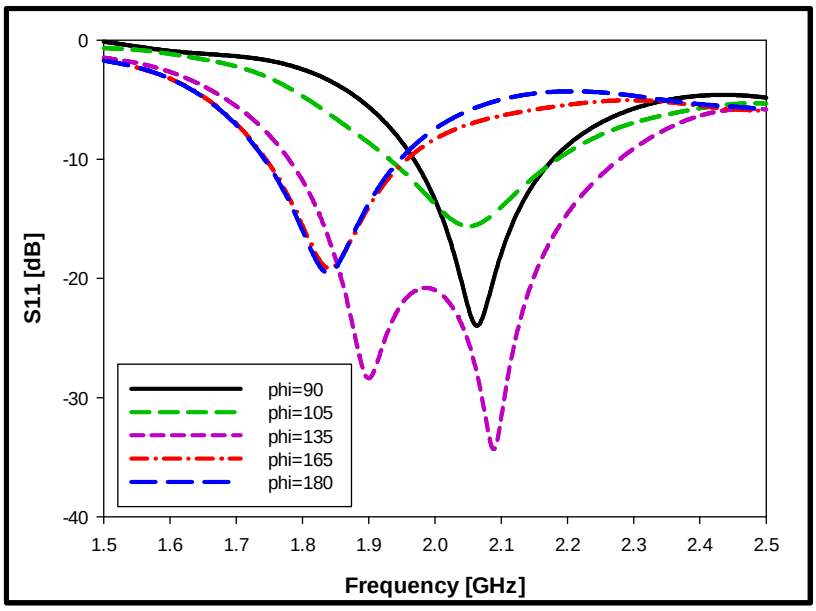

Figure 2.5.11: S_{11} for different strip locations

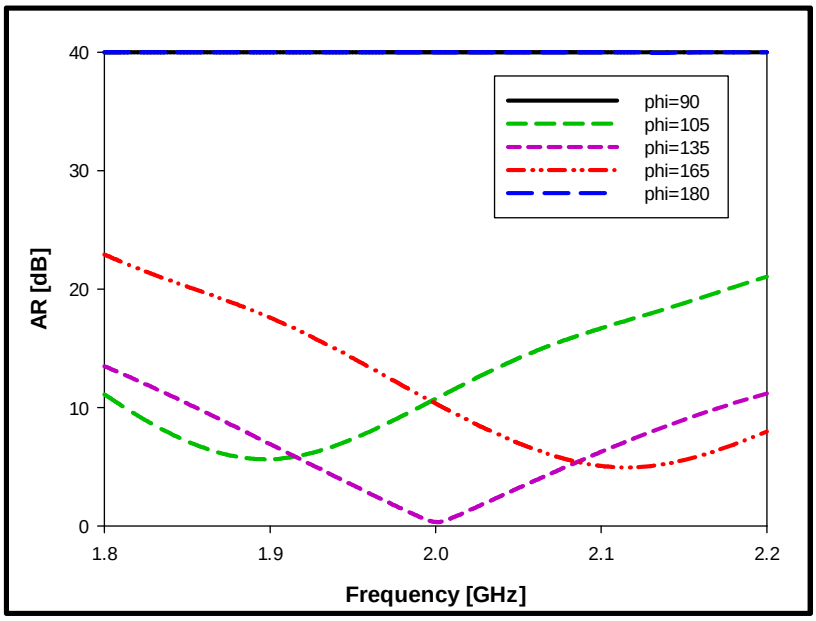

Figure 2.5.12: AR for different strip locations

These results demonstrate that when the strip is located at $\varphi = 90^o$ and 180^o, only single $HE_{11\delta}$ even and odd modes has been excited, respectively, since strong electrical fields can be found for the corresponding mode and zero field for the other mode as shown in Figure 2.5.13 and Figure 2.5.14. Therefore, the radiation is linearly polarised. As the strip moves away from the corners, the strength of the first field gets weaker and the strength of the second field becomes stronger. Therefore,

a better axial ratio has been achieved. Finally at $\varphi = 135^o$, the strength of the two fields are close to each other, which results in a lower axial ratio.

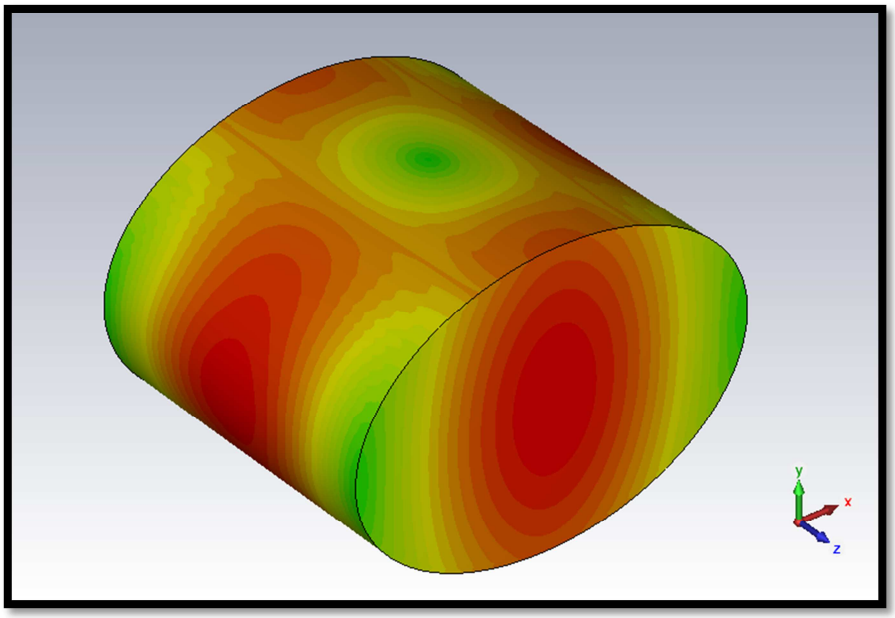

Figure 2.5.13: Electrical field distribution for the $HE_{11\delta}$ even mode

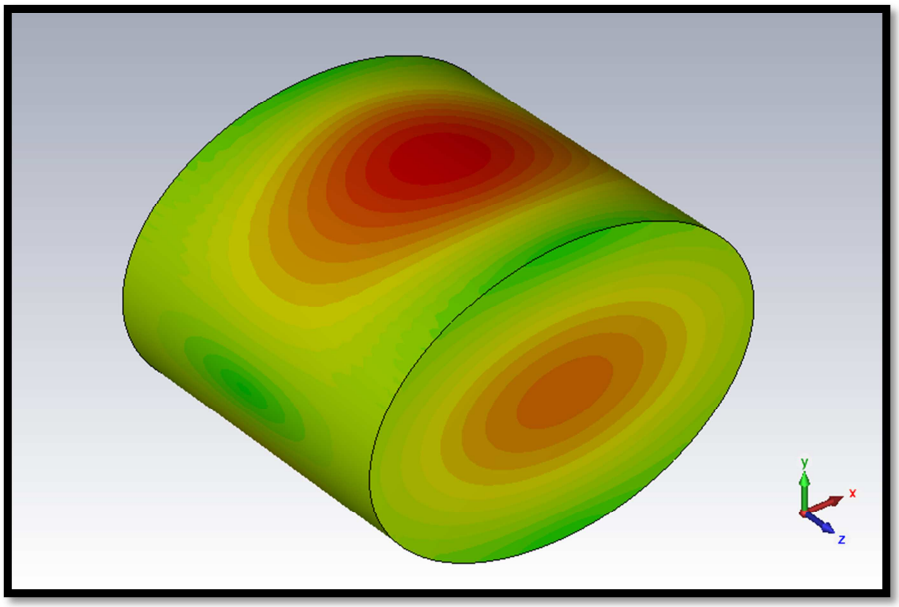

Figure 2.5.14: Electrical field distribution for the $HE_{11\delta}$ odd mode

2.5.3 *Results and Discussions*

The conformal strip excited EDRA has been fabricated and measured. Figure 2.5.15 illustrates a prototype of the EDRA that has been built using Dynallox material with a relative permittivity of $\varepsilon_r = 9.8$. The conformal strip has been connected to the ground plane using a conductive silver paint. Adhesive-backed copper strip has been

employed since it can be mounted easily on the surface of the DRA. An aluminium square ground plane, with a size of $40\,\mathrm{cm}$, has been employed and the measurements have been implemented using an HP8720D Vector Network Analyser (VNA). Feeding has been achieved by soldering one end of the feeding strip to an SMA connector that is connected to the network analyser using a $50\,\Omega$ coaxial cable. The procedure proposed in [95] has been followed to eliminate the potential air gaps between the DRA and the ground plane.

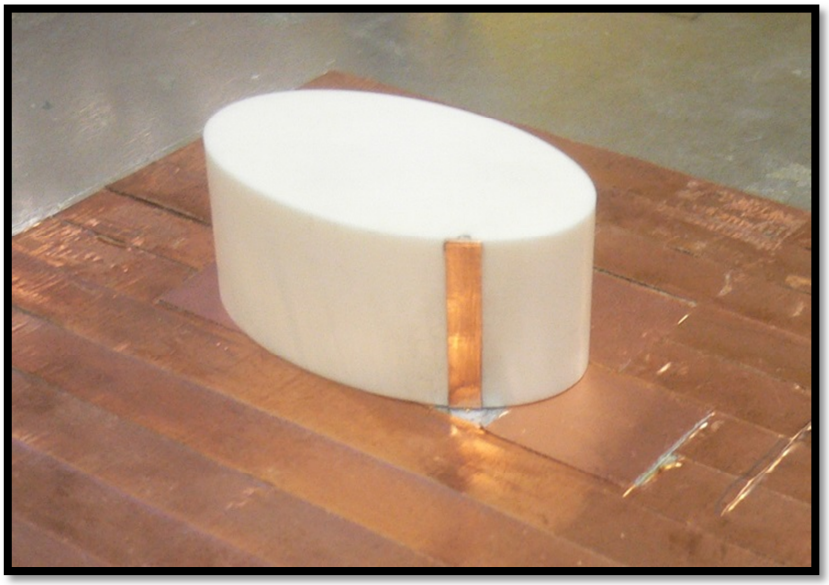

Figure 2.5.15: Prototype of the conformal strip excited EDRA

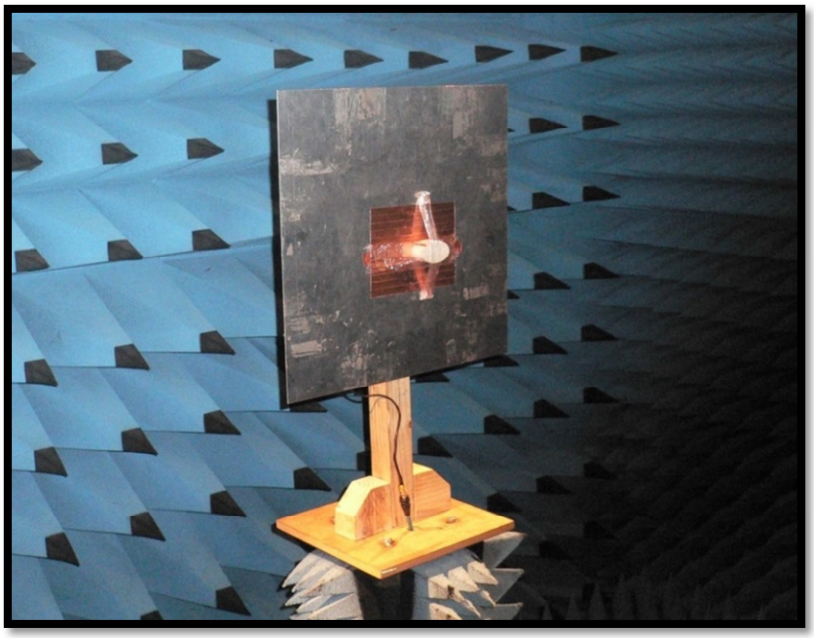

Figure 2.5.16: EDRA in the anechoic chamber

The experimental results have shown good agreement with the simulated ones as illustrated in Figure 2.5.17 for the reflection coefficient, where it can be seen that two closely spaced modes have been excited, which generates the circular polarisation radiation.

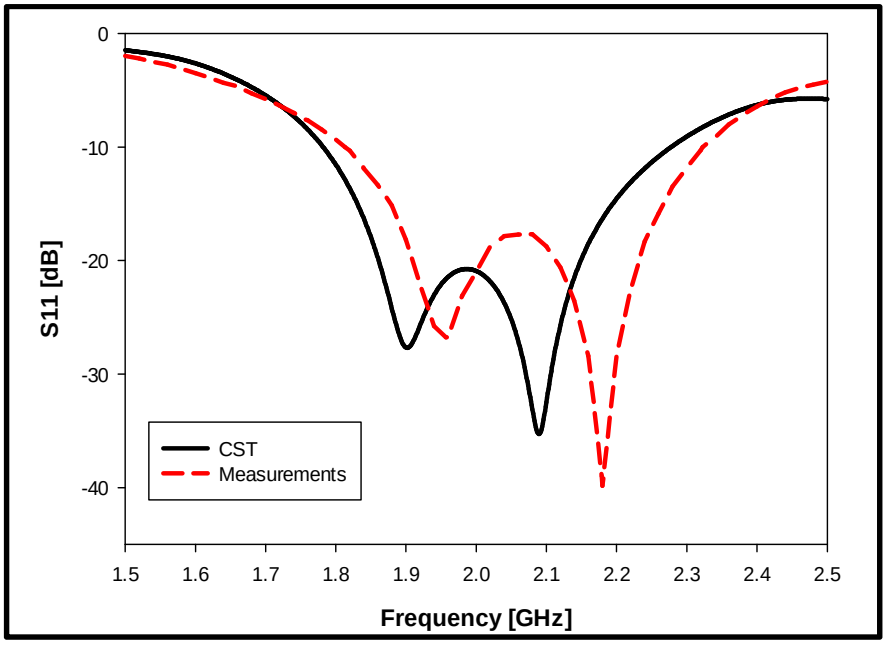

Figure 2.5.17: Reflection coefficient for the conformal strip excited EDRA

The simulated -10dB bandwidth is centred at $1.9\ \mathrm{GHz}$ with a percentage bandwidth of 25.8%. On the other hand, the measured S_{11} is centred at $1.96\ \mathrm{GHz}$ with a percentage bandwidth of 26%. There is a slight shift in the frequency, which might be due to the tolerance of the material and fabrication. Additionally, it can be seen from Figure 2.5.18 that the input resistance is ~50Ω and the reactance is close to zero for the required frequency range.

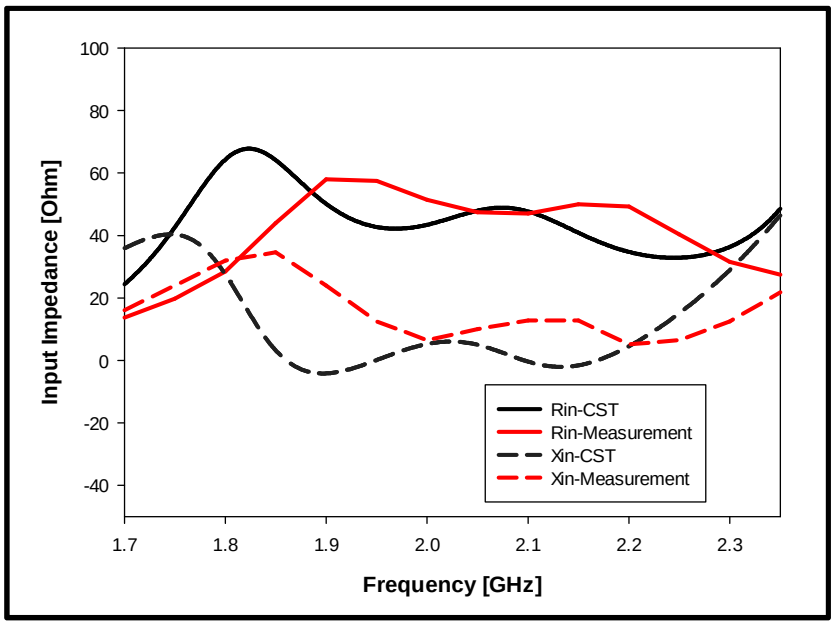

Figure 2.5.18: Input Impedance for the conformal excited EDRA

The axial ratio has been measured as shown in Figure 2.5.19, where the simulated 3dB axial ratio is centred at 2GHz with a percentage bandwidth of 4.5% whereas the measured axial ratio is, centred at 2.06GHz with a percentage bandwidth of 4.8%. The beamwidth bandwidth is given in Figure 2.5.20, where it can be seen that a wide angle of $\sim 80\%$ below 3dB has been achieved. The gain of the antenna has been measured in Figure 2.5.21, where it can be noticed that the antenna offers useful gain of 5dBi as simulated or 3.5dBi as measured. This discrepancy can be attributed to the finite ground plane as well as experimental and manufacturing tolerances.

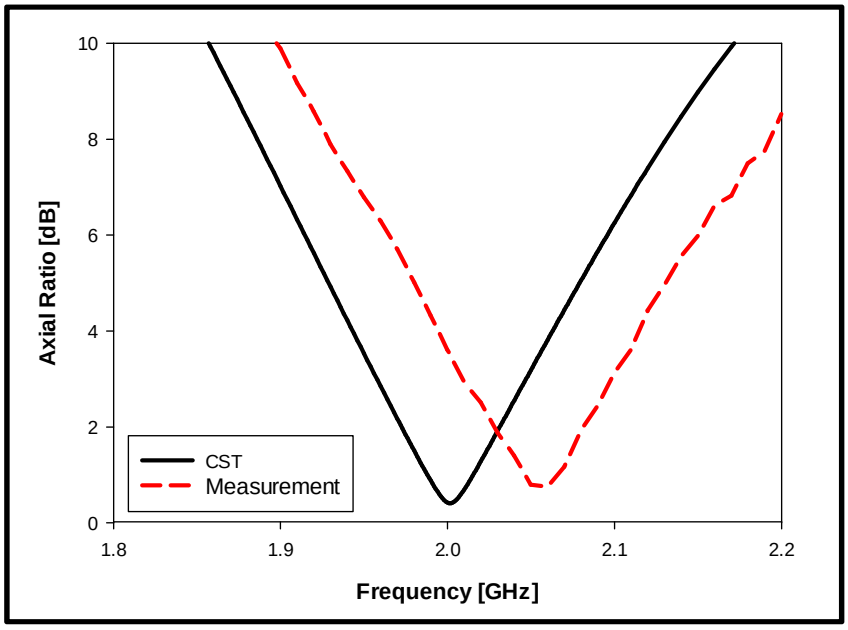

Figure 2.5.19: Axial Ratio for the conformal excited EDRA

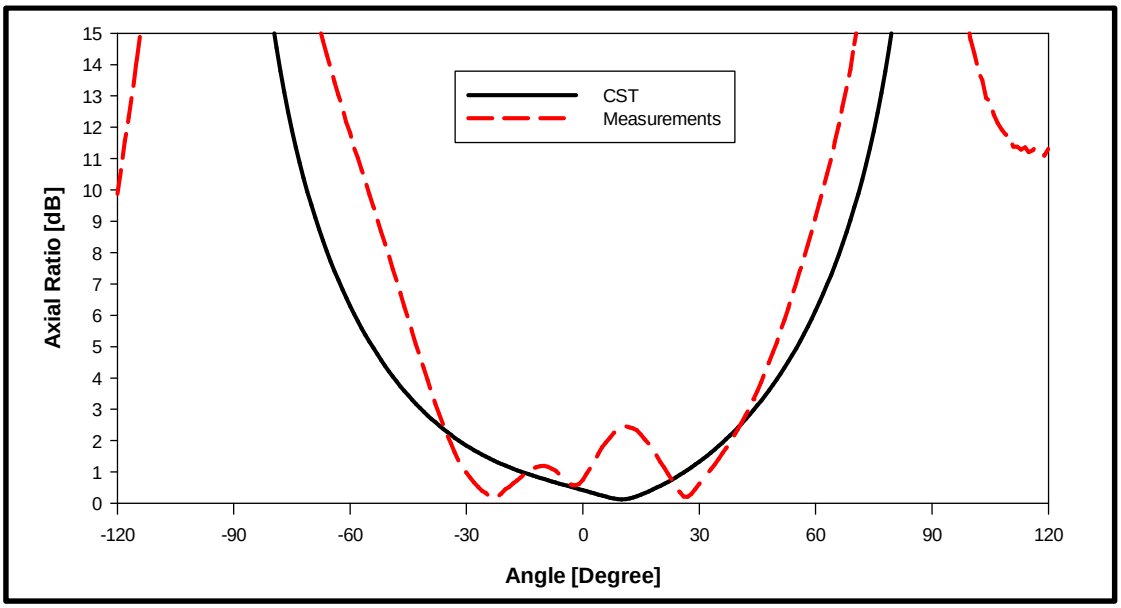

Figure 2.5.20: Beamwidth of the conformal excited EDRA

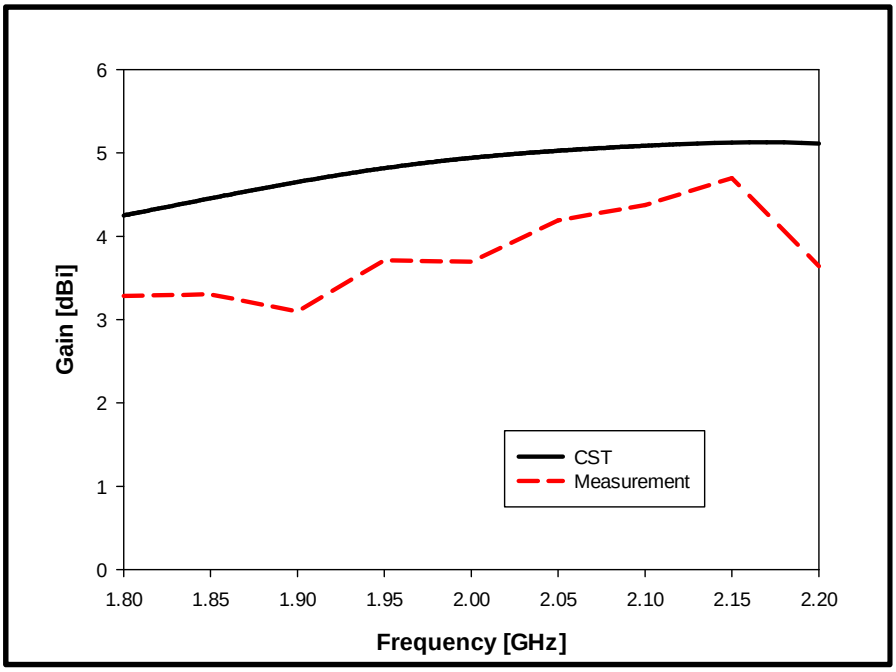

Figure 2.5.21: Gain for the conformal excited EDRA

This is a Left Handed Circularly Polarised (LHCP) antenna as can be seen from the radiation pattern in Figure 2.5.22 and Figure 2.5.23, in which the bore-sight E_R is approximately 30dB lower than the E_L.

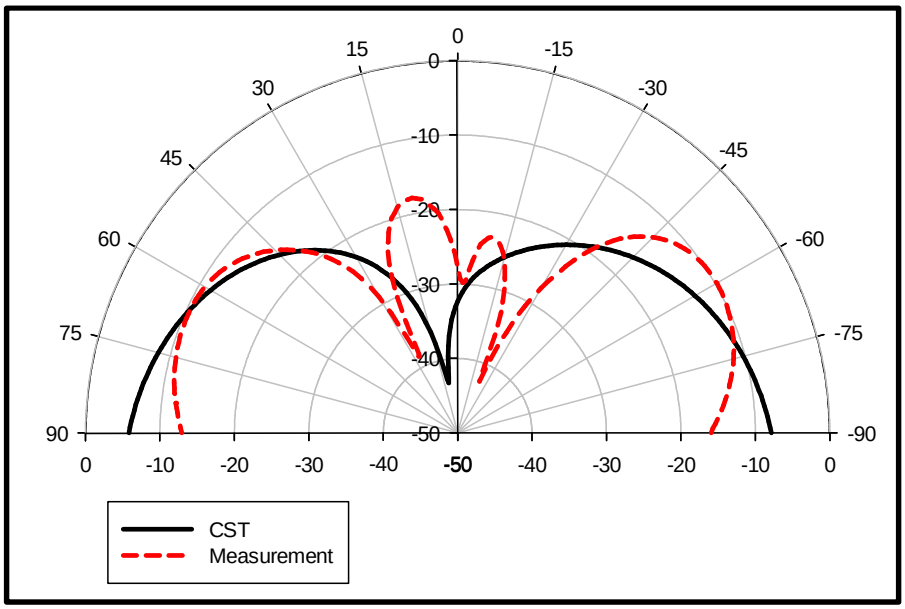

Figure 2.5.22: E_R for the conformal excited EDRA

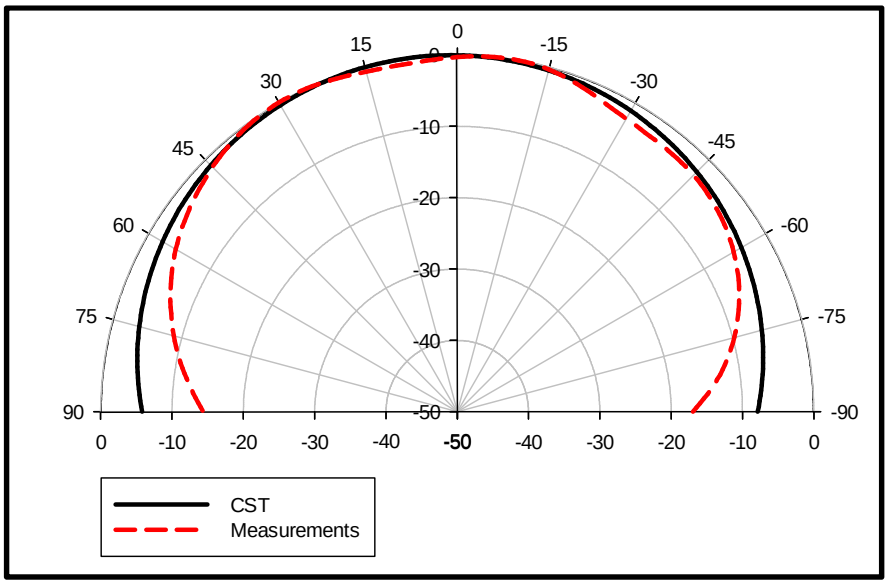

Figure 2.5.23: E_L for the conformal strip excited EDRA

2.6 Wide-band Circularly Polarised Elliptical DRA

2.6.1 *Introduction*

The next objective is to enhance the AR bandwidth by changing the feeding mechanism. As stated earlier, an open loop antenna with a circumference of approximately one wavelength can radiate a circularly polarised wave due to the generation of travelling current along its length [14, 96]. This concept has been employed, along with an internal parasitic open loop, which can enhance the

bandwidth further [15]. The detailed design procedures are presented in the next section.

2.6.2 *Design Procedures*

The Eigen mode CST solver has been used to study the resonance modes of the designed EDRA. Recall that the EDRA has a relative permittivity of $\varepsilon_r = 9.8$ and dimensions of $a = 26\text{mm}$, $b = 16\text{mm}$ and $h = 21\text{mm}$. It has been observed that two hybrid modes exists with similar H_z fields distributions of the even TE_{012} and odd TE_{021} modes [97], at 3.4GHz and 3.5GHz with strong electric fields at the same wall side of the EDRA as shown in Figure 2.6.1-Figure 2.6.4. Therefore, an attempt has been made to excite these modes using a single feed to design a wider band circularly polarised EDRA.

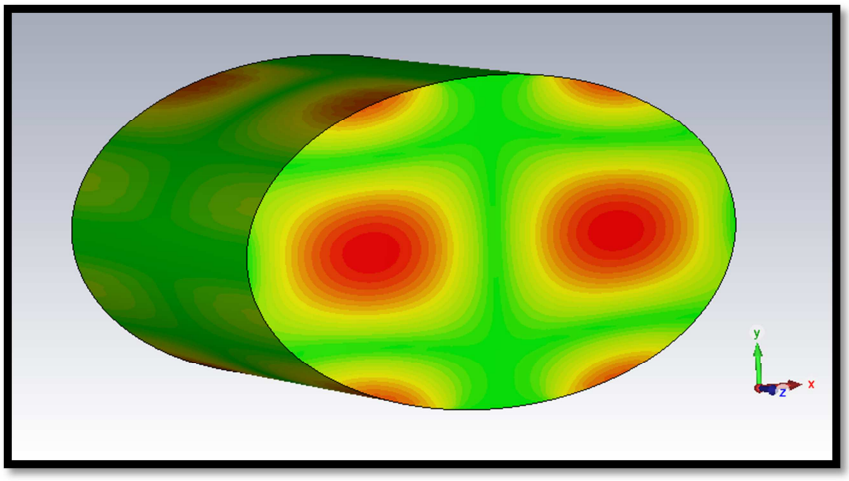

Figure 2.6.1: H_z-Field for the first hybrid mode, similar to the even TE_{012}

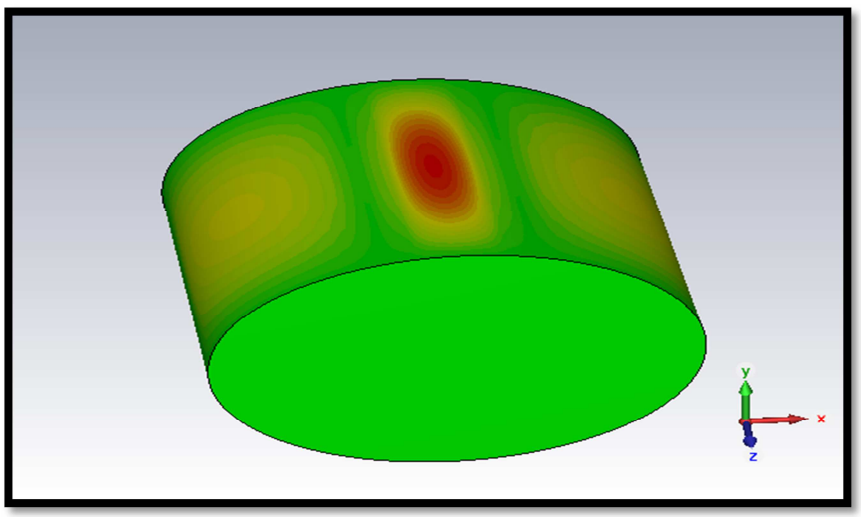

Figure 2.6.2: E_z-Field for the first hybrid mode, similar to the even TE_{012}

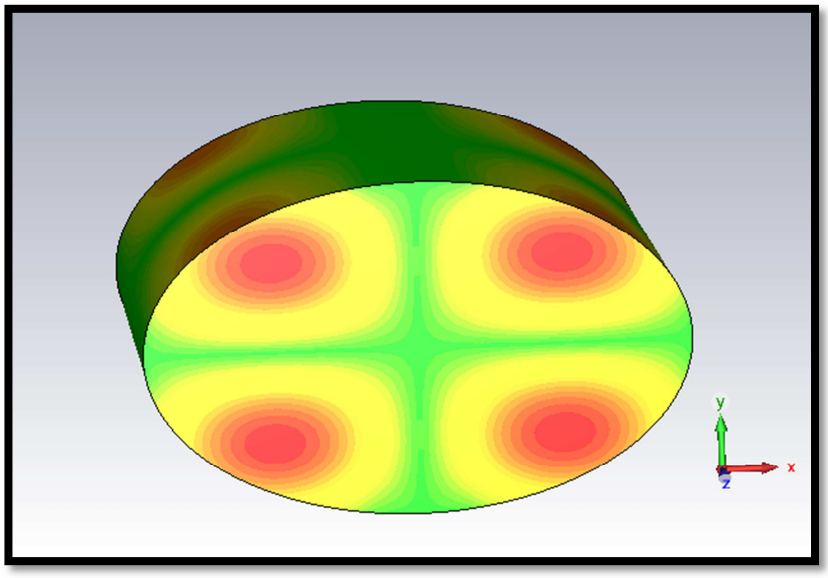

Figure 2.6.3: H_z-Field for the second hybrid mode, similar to the odd TE_{021}

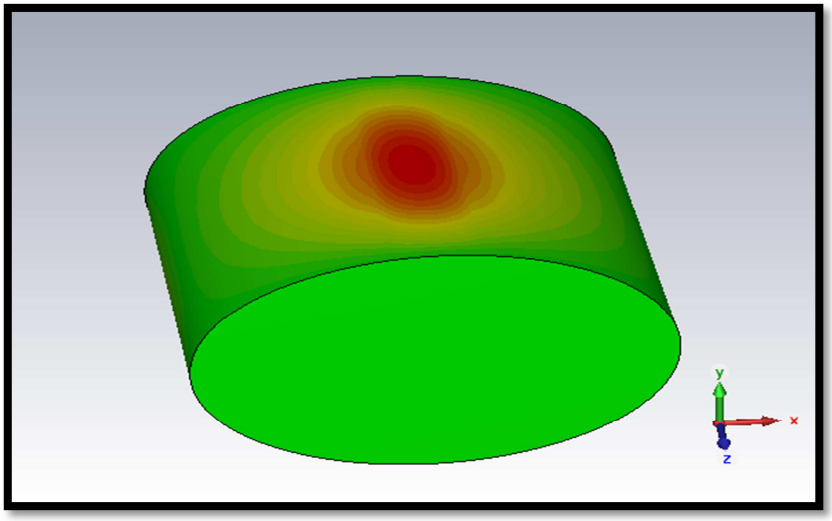

Figure 2.6.4: E_z-Field for the second hybrid mode, similar to the odd TE_{021}

A half rectangular open loop antenna has been deployed as shown in Figure 2.6.5 and Figure 2.6.6 so that the feeding strip of the half-loop is located at the strong electric field position, which is at $\varphi = 90^o$. The schematic of the half rectangular open loop is illustrated in Figure 2.6.7. The antenna has 3 main arms l_1, l_2 and l_3 with a gap g_1 in the loop. An iterative design procedure has been followed to find the optimum dimensions of the arm lengths and gap in order to generate the travelling current and therefore, the circularly polarised radiation.

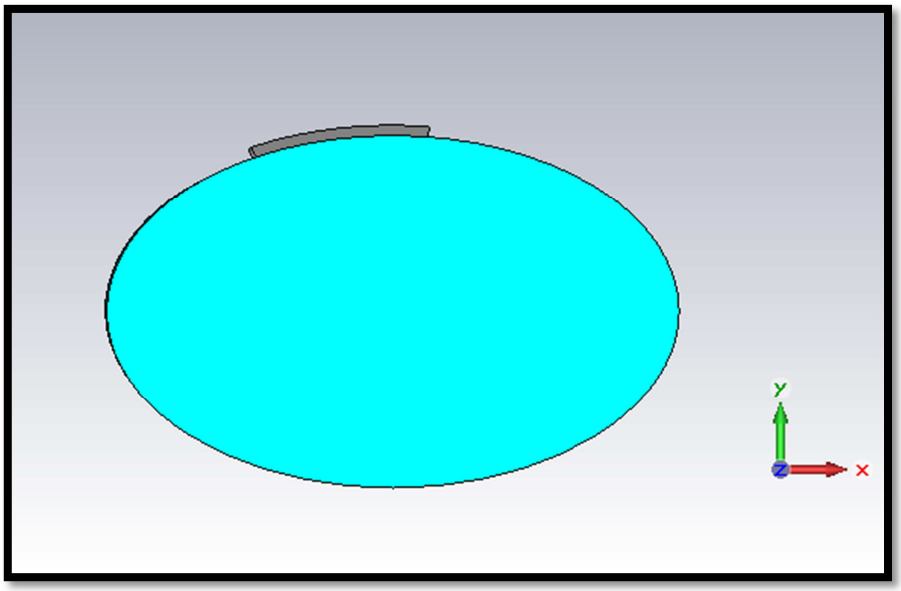

Figure 2.6.5: The wideband EDRA, Top view

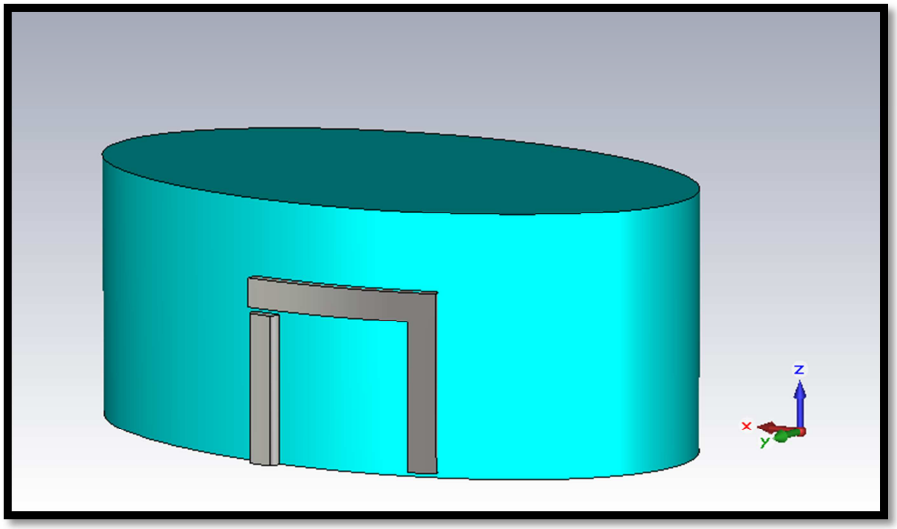

Figure 2.6.6: The wideband EDRA, side view

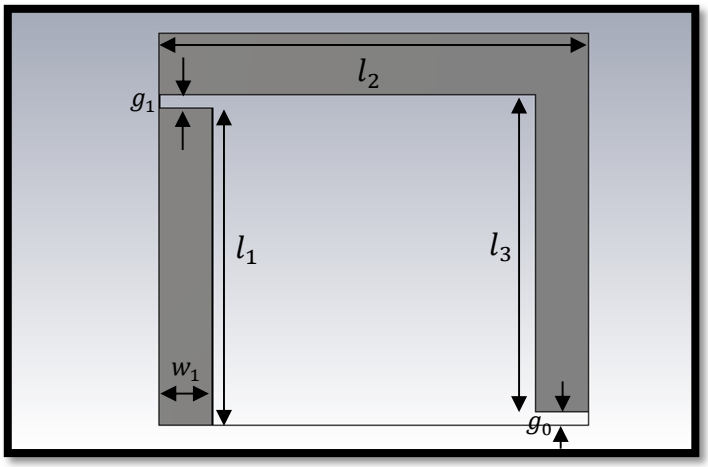

Figure 2.6.7: Schematic for the half-open loop antenna for wideband EDRA

At 3.5 GHz, $\lambda_o = 85.7\text{mm}$, $\lambda_g = 27.4\text{mm}$, and the effective wavelength $\lambda_{eff} = 36.9\text{mm}$ for the used dielectric substrate. As mentioned earlier, the size of the loop needs to be approximately one effective wavelength. Therefore, the initial values of the l_1, l_2 and l_3 arms have been chosen as $12\ \text{mm}$, $13\ \text{mm}$ and $12\ \text{mm}$ respectively. Then, a gap has been introduced at the l_1- l_2 junction. After a series of iterations, the optimum dimensions that provide the widest AR bandwidth have been obtained as shown in Table 2.6.1. These dimensions provide a $40.2\ \text{mm}$ loop circumference, which corresponds to $1.09\lambda_{eff}$ as expected.

Parameter	Value [mm]
$\boldsymbol{l_1}$	12.0
$\boldsymbol{l_2}$	16.2
$\boldsymbol{l_3}$	12.0
$\boldsymbol{w_1}$	2.0
$\boldsymbol{g_1}$	0.5
$\boldsymbol{g_0}$	0.5

Table 2.6.1: Optimum parameter values for the half-open loop antenna

The CP AR bandwidth can be improved further by introducing a parasitic open loop inside the driven loop, which generates an additional AR minimum point. Therefore, a wider axial ratio bandwidth can be achieved by merging those two AR minima [15]. Therefore, an inner loop has been incorporated in the structure as illustrated in Figure 2.6.8.

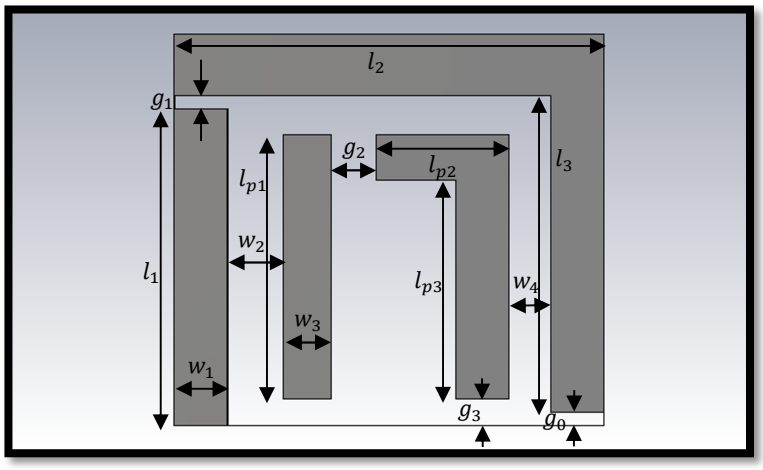

Figure 2.6.8: Schematic for the half-open loop antenna with inner loop

Once more, an iterative design procedure has been followed by studying the effects the parameter given by Figure 2.6.8. The key parameters that have considerable impact on the axial ratio are: g_2, w_4 and g_3. Finally, the optimum values of the parameters are given in Table 2.6.2.

Parameter	Value [mm]
$\boldsymbol{l_1}$	12.0
$\boldsymbol{l_2}$	16.2
$\boldsymbol{l_3}$	12.0
$\boldsymbol{l_{p1}}$	10.0
$\boldsymbol{l_{p2}}$	5.0
$\boldsymbol{l_{p3}}$	10.0
$\boldsymbol{w_1}$ and $\boldsymbol{w_2}$	2.0
$\boldsymbol{w_3}$	1.8
$\boldsymbol{w_4}$	1.2
$\boldsymbol{g_0}$ and $\boldsymbol{g_1}$	0.5
$\boldsymbol{g_2}$	1.9
$\boldsymbol{g_3}$	1.0

Table 2.6.2: Optimum parameter values for the half-open loop antenna with inner loop

2.6.3 *Results and Discussion*

The wideband EDRA has been designed and simulated in CST and verified using Ansoft High Frequency Structural Simulator (HFSS) commercial software. The reflection coefficients of a structure with and without the inner parasitic loop are presented in Figure 2.6.9, where it can be noticed that introducing the parasitic loop caused a stronger excitation for the two modes at $3.4\ \mathrm{GHz}$ and $3.5\ \mathrm{GHz}$ as suggested earlier and therefore has marginally improved the S_{11} bandwidth. For example, in the absence of the parasitic loop, the -10dB S_{11} bandwidth is 22%, compare to 22.8% when the parasitic loop is incorporated. The axial ratio is shown in Figure 2.6.10, where the 3dB AR bandwidth for the structure without the parasitic loop is ranging from $3.38 - 3.6\ \mathrm{GHz}$, and centred at $3.5\ \mathrm{GHz}$ with a percentage bandwidth of 7%, whereas at the presence of the inner loop, the percentage bandwidth has increased to 11.7% due to the generation of an extra AR minima.

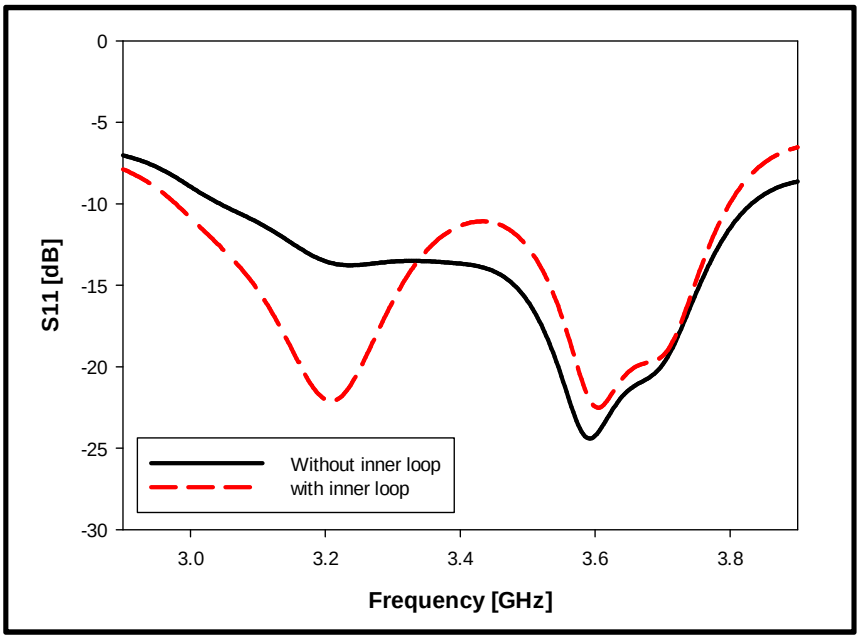

Figure 2.6.9: Reflection coefficient for the wideband antenna, with and without the inner loop

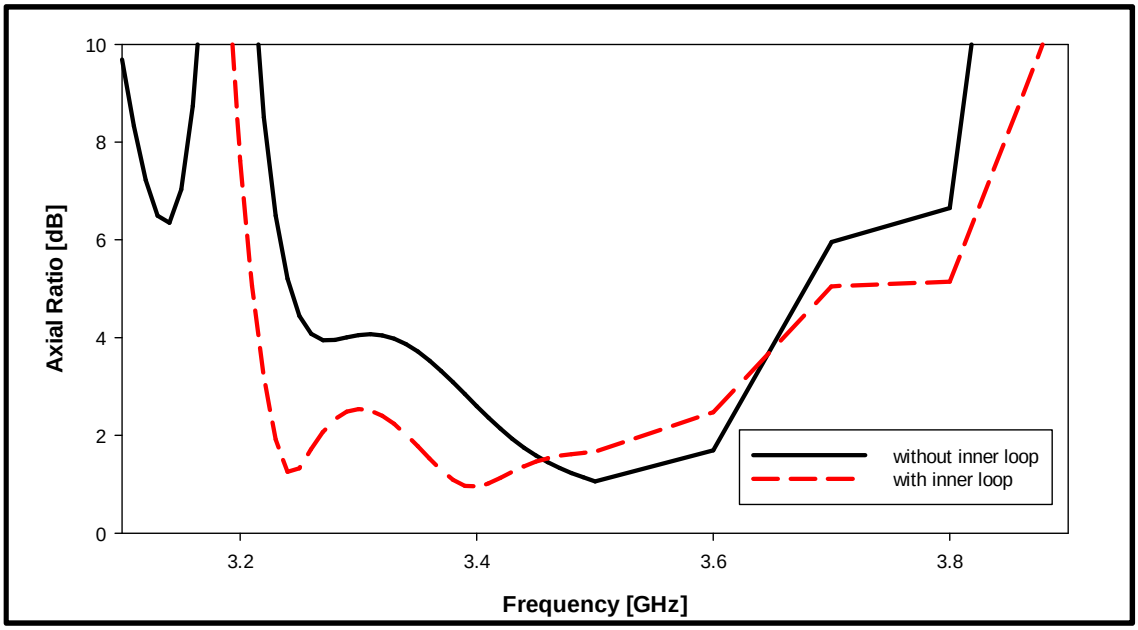

Figure 2.6.10: Axial ratio for the wideband EDRA, with and without inner loop

These results have been cross validated with HFSS, where it can be seen in Figure 2.6.11 that the reflection coefficients using the both software packages are in good agreement. The -10dB bandwidth from CST is 22.8% whereas for HFSS the bandwidth has been calculated as 24.4%.

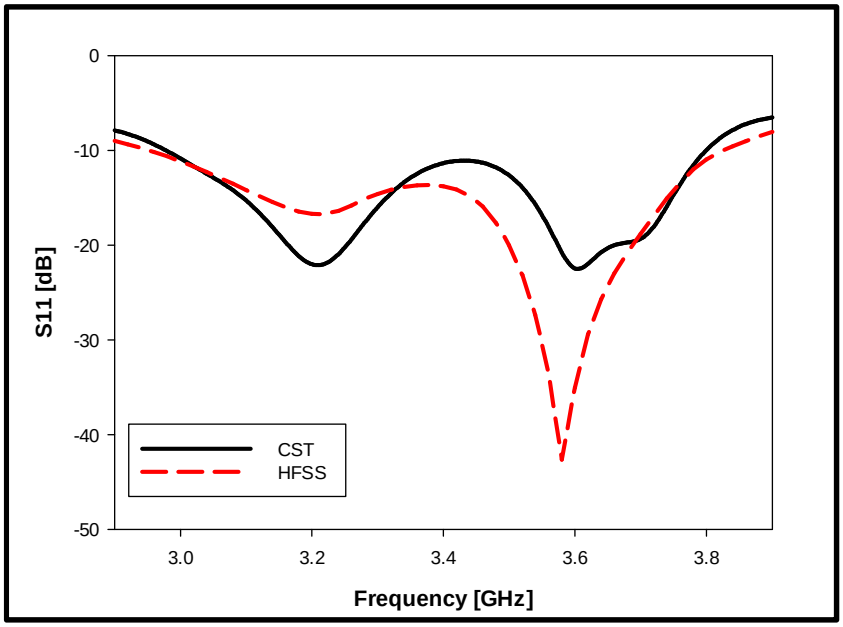

Figure 2.6.11: Reflection coefficient for the wideband EDRA using CST and HFSS

This good matching can be observed from the input impedance results shown in Figure 2.6.12, where it can be seen an almost pure resistance achieved over the desired frequency range.

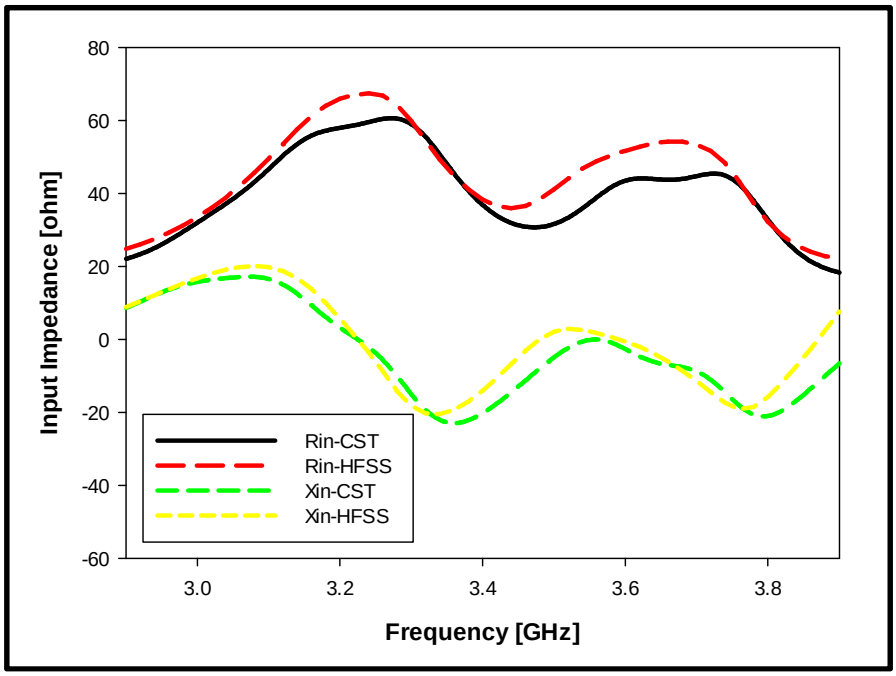

Figure 2.6.12: Input impedance for the wideband EDRA using CST and HFSS

The CST simulation result has provided a wide 3dB AR bandwidth of 11.7%. On the other hand, HFSS result provided even wider bandwidth of 12.6% ranging from $3.3 - 3.7\ \mathrm{GHz}$, centred at $3.4\ \mathrm{GHz}$ as can be seen from Figure 2.6.13. Moreover, the

gain is presented in Figure 2.6.14 with agreement between the two sets of results. However, not all the frequency band has a positive gain due to the shift of the main beam to $phi = 90^o$ as shown in Figure 2.6.15. The effective axial ratio bandwidth with positive gain is 8.7%, which is still $\sim 90\%$ wider than the axial ratio bandwidth of the conformal strip excited EDRA or any reported singly fed EDRA in the literature. The beamwidth of the antenna is presented in Figure 2.6.16 with good agreement between both sets of results. The antenna is Right Handed Circularly Polarised (RHCP) as can be seen from the results shown in Figure 2.6.17. The bore-sight E_R is almost 20dB higher than E_L. Good agreement between CST and HFSS results have been observed.

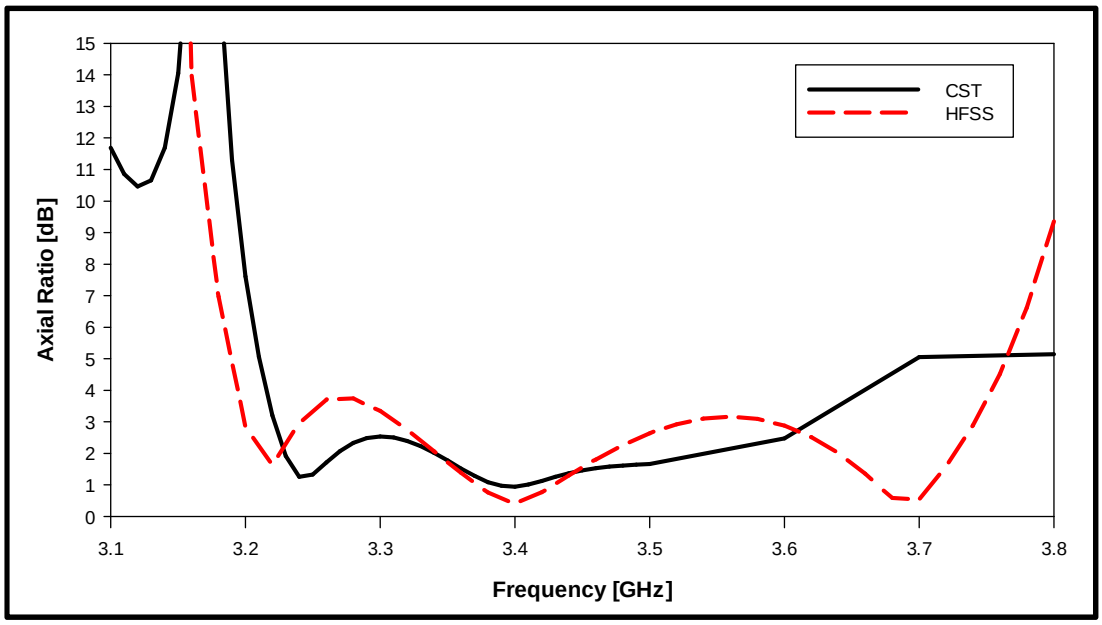

Figure 2.6.13: Axial ratio for the wideband EDRA using CST and HFSS

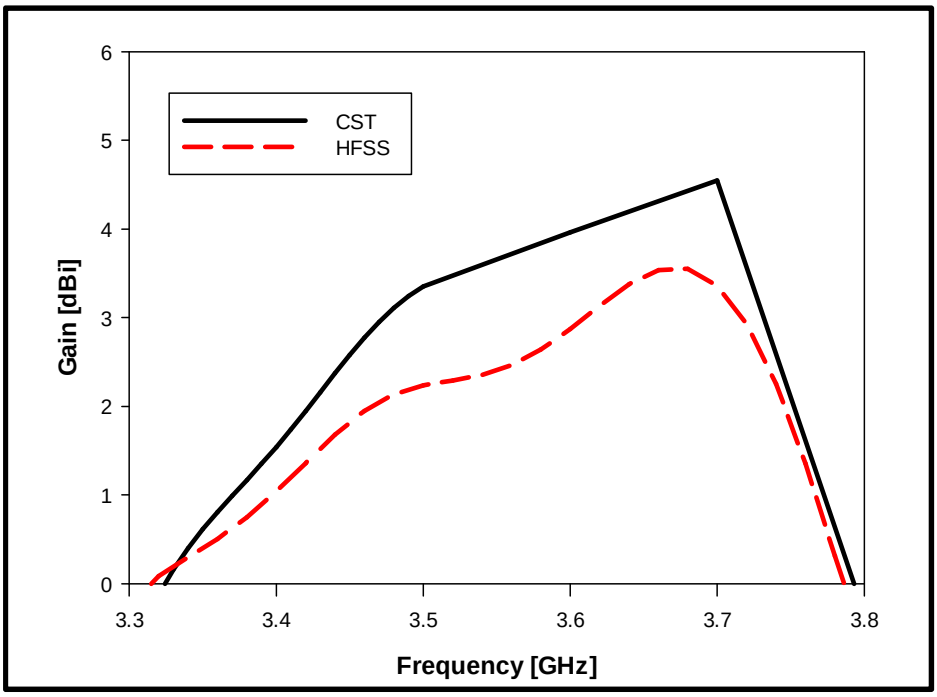

Figure 2.6.14: Gain of the wideband EDRA using CST and HFSS

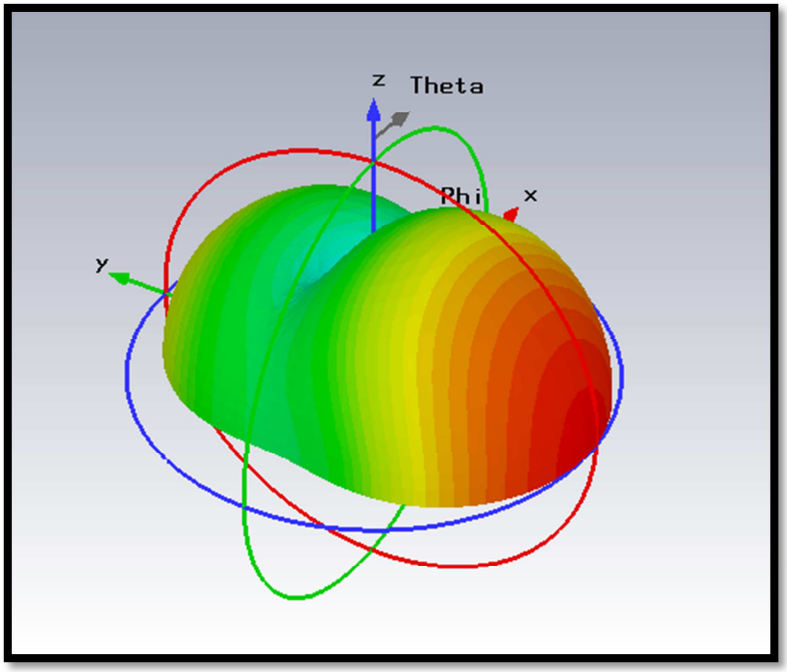

Figure 2.6.15: 3D radiation pattern for the wide band EDRA for $\varphi = 90^{o}$ at 3 GHz

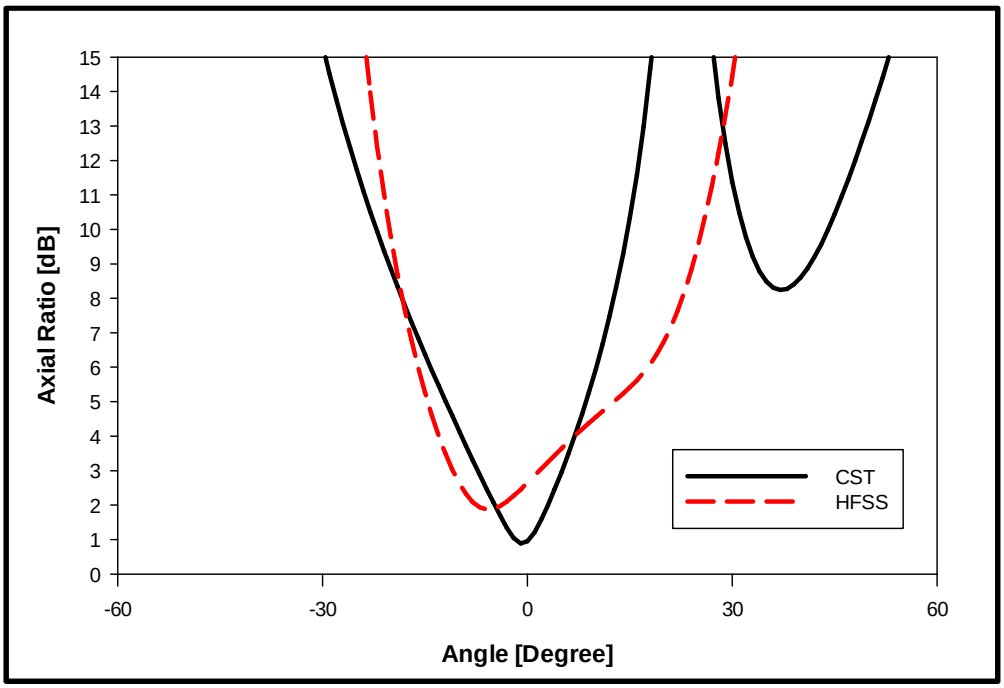

Figure 2.6.16: Beamwidth of the wideband EDRA

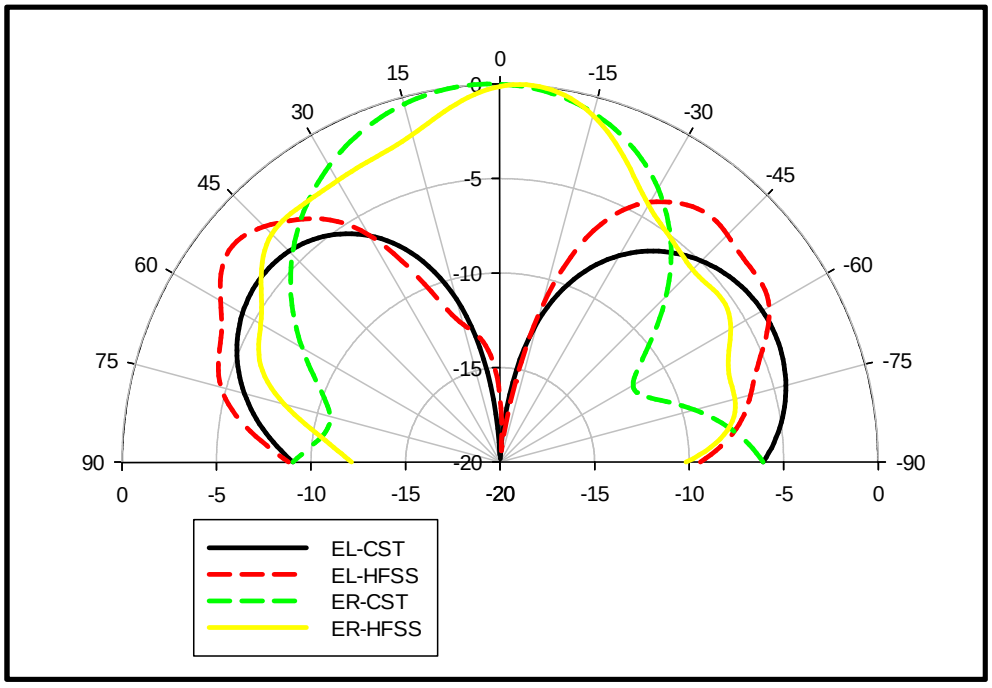

Figure 2.6.17: E_R and E_L for the wideband EDRA using CST and HFSS

2.7 Dual Band CP EDRA

2.7.1 *Introduction*

There are many designs available of DRAs radiating linearly and circularly polarised waves that are focused on single frequency bands. At the same time, few DRA designs that are suitable for multi frequency applications have been reported. Examples of dual band, linearly polarised antennas include a dual band linearly polarised elliptical DRA that has been designed in [78]. Additionally, a dual band rectangular DRA that is fed using a coaxial probe has been reported in [26] and an embedded dual band cylindrical DRA has been investigated in [98]. Moreover, a dual band split DRA has been suggested [99].

A further step in the dual band DRA design is the design of a multi band, multi-mode antenna. This yields the combination of circularly and linearly polarised radiations for the same antenna. Therefore, one band will radiate a circularly polarised wave and the other, a linearly polarised wave. Such designs have been investigated in [100-102]. However, a more desirable and challenging task is to design a dual band CP DRA. That is, a circularly polarised radiation is achieved in both bands. A number of studies have been conducted that are focused on the design of a dual band CP DRAs. For instance, a stacked cylindrical DRA, with a circular microstrip antenna for dual frequency operation, has been proposed [103], where four coaxial feeds have been used in conjunction with a phase quadrature to achieve the CP radiation. Another design is based on using a DRA on top of an L-probe-fed slotted cavity to form a circularly polarised hybrid antenna [104]. Recently, a new design of a cylindrical DRA has been suggested for dual band operation [105], in which the circularly polarised operation has been achieved using a quadrature strip-fed method. This is has been achieved by placing two feeding strips, which are angularly displaced at 90^o from each other and placed on the side of the DRA. A matching slot has been used for each excitation strip. In order to attain two quadrature signals, a dual band 90^o coupler was reported as well, increasing the complexity of the design. In addition, a dual band slot-coupled DRA has been designed using higher order mode [106], where two pairs of degenerate orthogonal modes of the rectangular DRA were excited by truncating two corners of the DRA at 45^o. Furthermore, a rectangular DRA, fed by a cross-slot has been designed for circularly polarised dual band operation [107, 108].

In this work, a simple singly fed dual band EDRA that is excited using a conformal open loop is proposed. The available dual band circularly polarised DRAs in the literature have used cylindrical and rectangular DRAs only but the elliptical DRA has not been used. The advantage of this design is the simple circuitry to achieve the dual band operation where the antenna is excited by a conformal strip, which is easy to fabricate and no additional complex circuitry is needed. Additionally, the dual band can be achieved with a single feed, neglecting the need of multi feeds and phase quadrature circuits. Compared to other excitation mechanism used for dual band such as cross slot reported in [108], using conformal strip mechanism is easier than aligning the DRA correctly above the feeding slot. Moreover, this antenna has a reasonably low profile thickness with an overall height of is $0.14\lambda_o$ at the lower frequency, which is close to $0.12\lambda_o$ reported in [108] and lower than those of $0.27\lambda_o$ [104], $0.26\lambda_o$ [105] and $0.19\lambda_o$ [106].

2.7.2 *Design Procedures*

Once more, the half open loop has been used for excitation. The same EDRA of $\varepsilon_r = 9.8$ has been considered with the major/minor semi axes a and b given as 26mm and 16mm respectively, with a DRA height of 21mm. The earlier results in this chapter demonstrated the potential of designing a dual band EDRA at 2GHz and 3.5GHz, which necessitates the excitation of the modes associated with these bands. That is, it is evident that the half open loop can generate a circularly polarised radiation at 3.5GHz. Additionally, if the first loop's strip is located close to $\varphi = 135^o$, then odd and even $HE_{11\delta}$ modes will be excited, which generates a CP radiation at 2GHz. Initially, a conformal half open loop strip has been deployed as shown in Figure 2.7.1. An iterative design procedure has been applied to have dual band circularly polarised EDRA at 2GHz and 3.5GHz. The achieved reflection coefficient and axial ratio are presented in Figure 2.7.2 and Figure 2.7.3 respectively, where it can be noticed that CP waves have been generated at $2\ \text{GHz}$ and $3.5\ \text{GHz}$. However, a narrow AR bandwidth has been achieved for the first band. Additionally, it can be observed from Figure 2.7.2, that the antenna is poorly matched at the intended frequency range. Consequently, a matching stub of width w_x and height w_y has been incorporated in the configuration as shown in Figure 2.7.4, and the loop's gap has

been adjusted and varied for optimum results. The final open loop strip is illustrated in Figure 2.7.5 with the optimum design parameters given in Table 2.7.1.

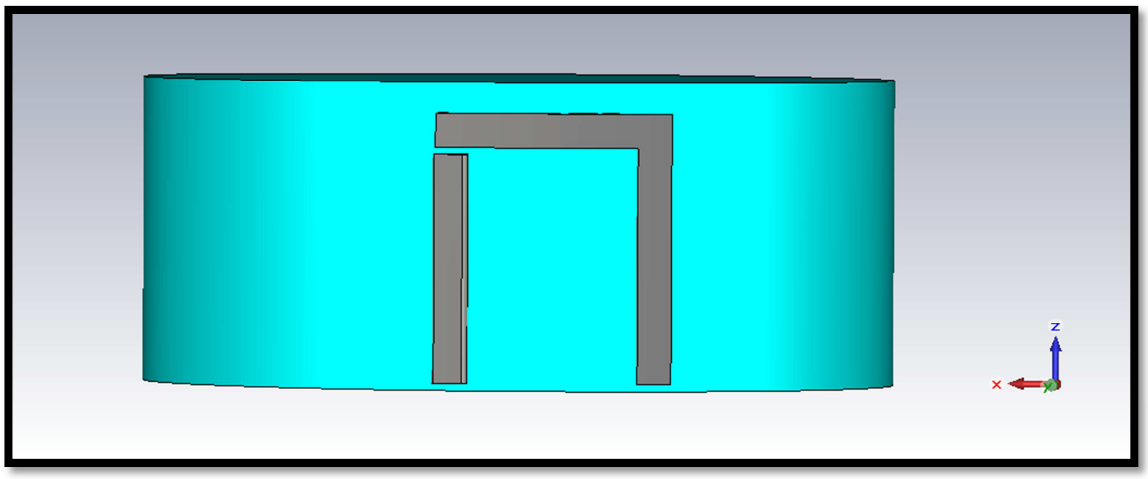

Figure 2.7.1: EDRA with conformal open loop strip

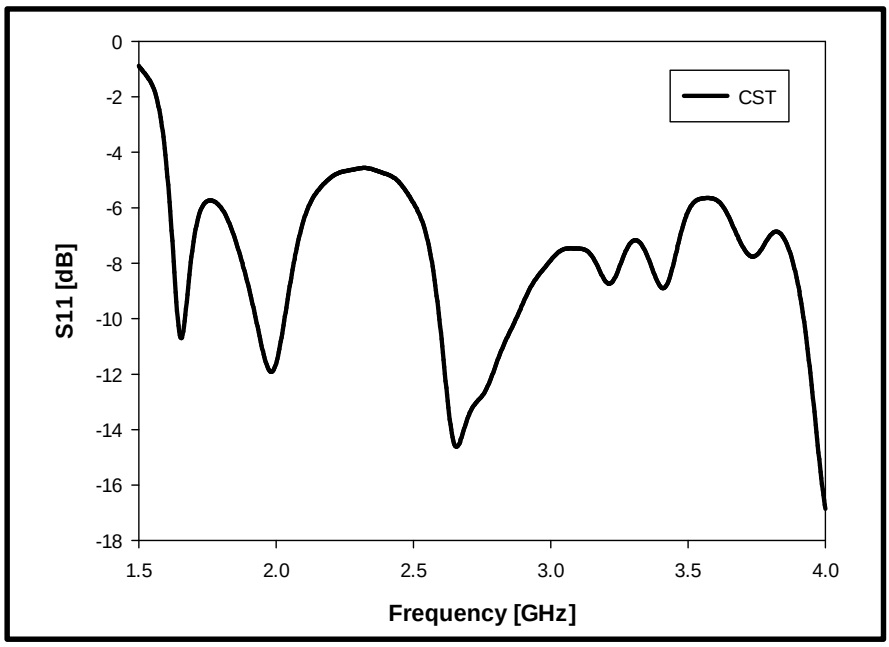

Figure 2.7.2: Reflection coefficient for the half-open loop antenna on EDRA

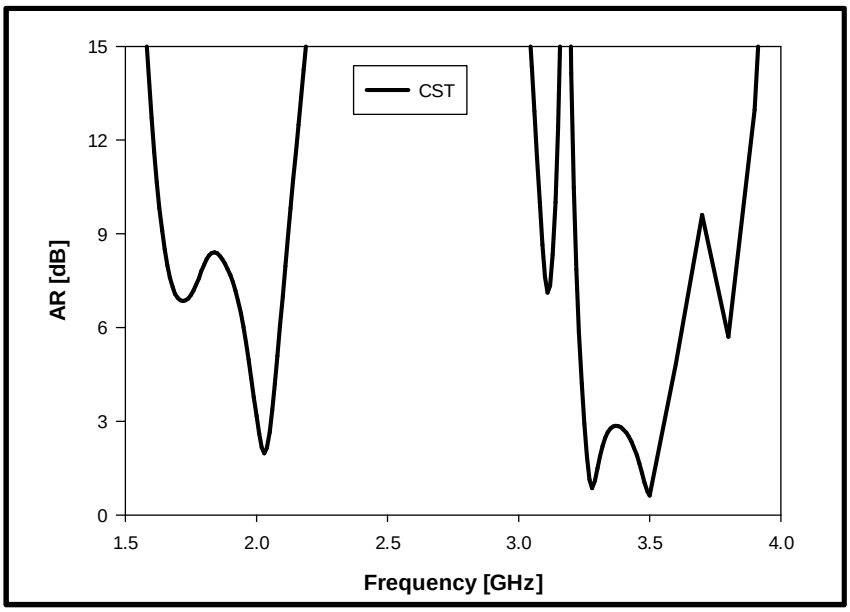

Figure 2.7.3: Axial ratio for the half-open loop antenna on EDRA

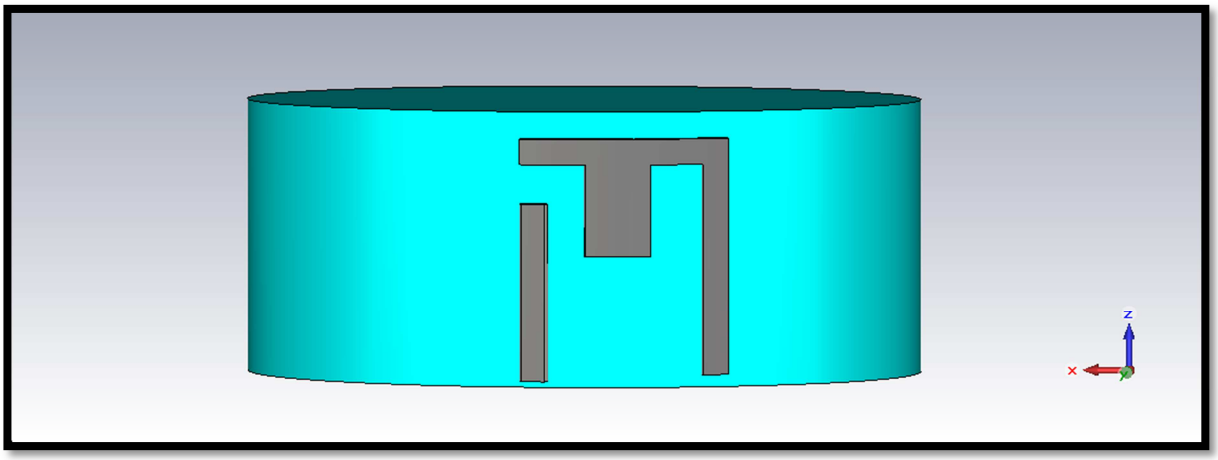

Figure 2.7.4: The dual band circularly polarised EDRA

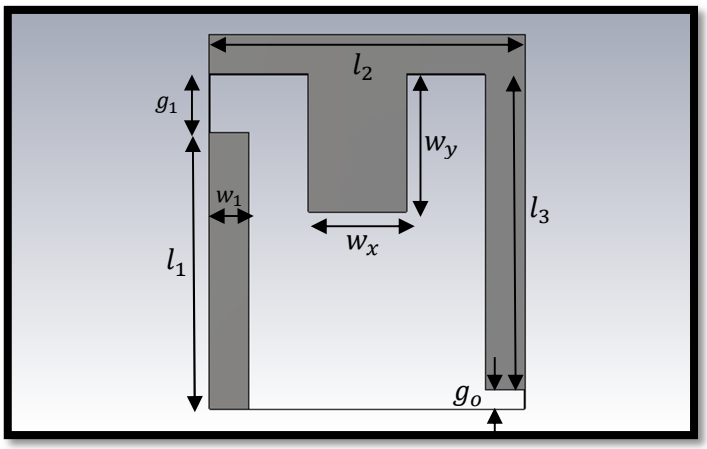

Figure 2.7.5: half Open loop strip for the dual band EDRA

Parameter	Value [mm]
l_1	14
l_2	16
l_3	16
w_x	5
w_y	7
w_1	2
g_o	1
g_1	3

Table 2.7.1: Optimum dimensions for the half open loop strip

2.7.3 *Results and Discussions*

The fabricated dual band EDRA is presented in Figure 2.7.6 with total loop's strip circumference of 46 mm, which corresponds to $1.24\lambda_{eff}$.

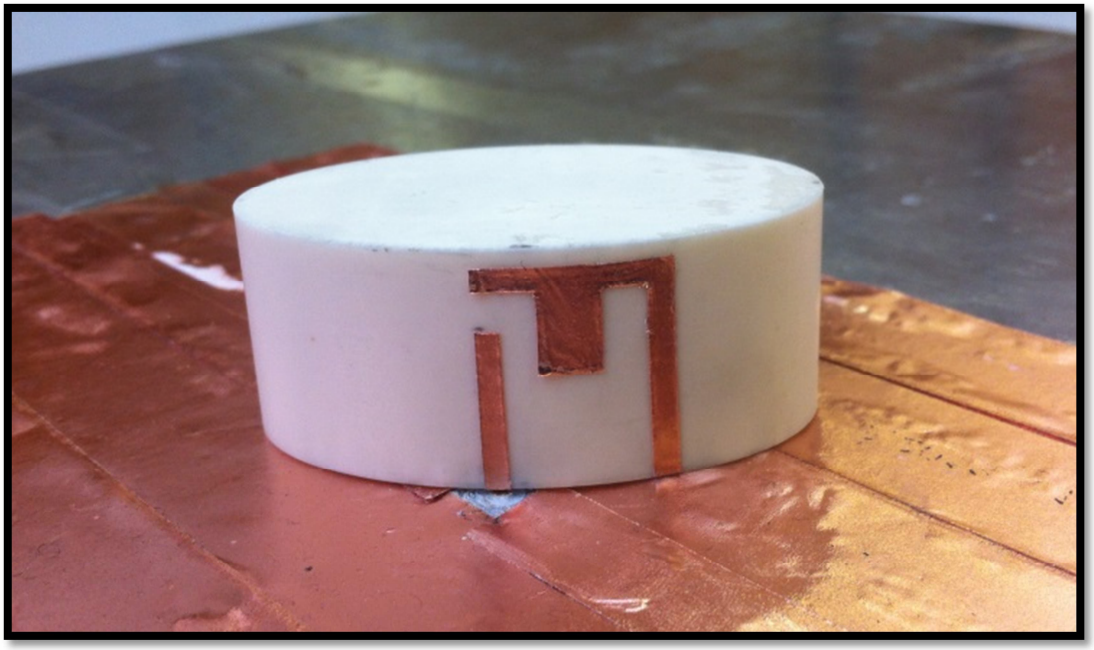

Figure 2.7.6: Fabricated Dual band EDRA

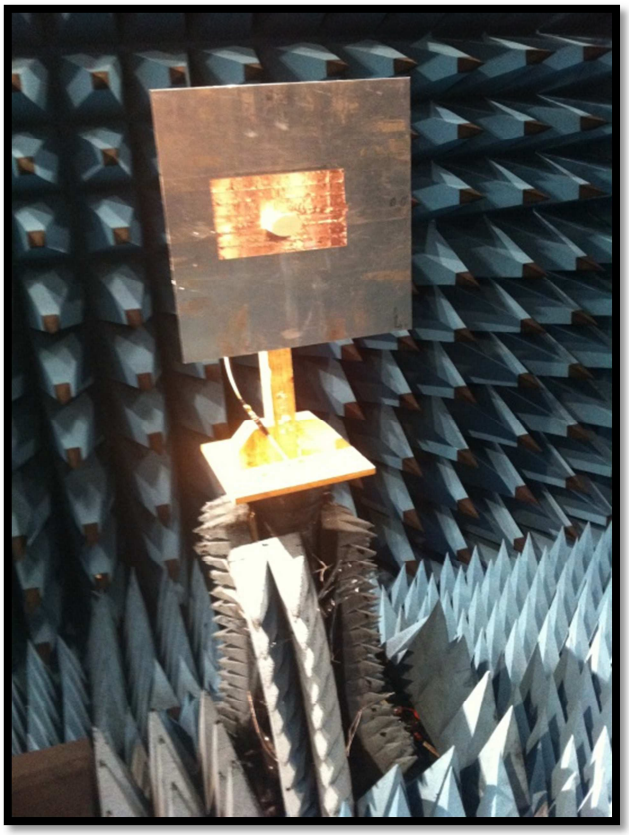

Figure 2.7.7: Fabricated dual band EDRA in the anechoic chamber

The simulated and measured reflection coefficients of the dual band EDRA are presented in Figure 2.7.8, where it can be seen that this antenna achieves two operation bands at $2\ \mathrm{GHz}$ and $3.5\ \mathrm{GHz}$. For the first band, the simulated -10dB S_{11} bandwidth is 10.65% compared to a measured bandwidth of 16.8%. This is in conjunction with a marginal shift in the resonance frequency that can be attributed to the experimental and fabrication tolerances. For the second band, the simulated -10dB S_{11} bandwidth is 29%, which agrees well with the measured bandwidth of 27.4%. The accomplished simulated and measured axial ratios are given in Figure 2.7.9.

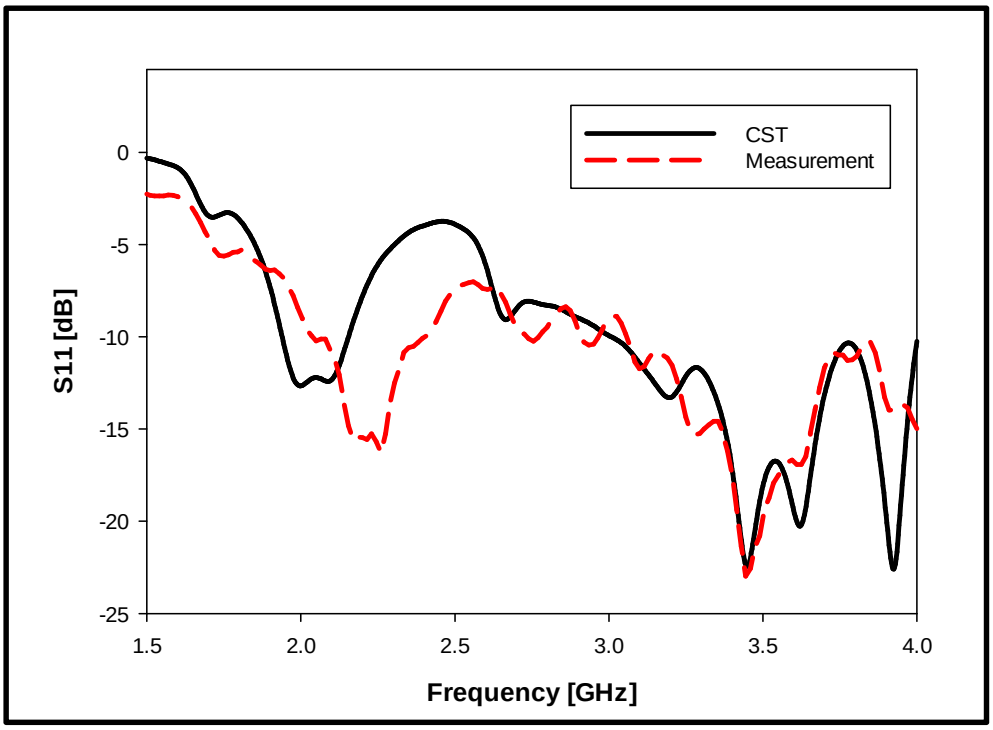

Figure 2.7.8: S_{11} for the dual band EDRA

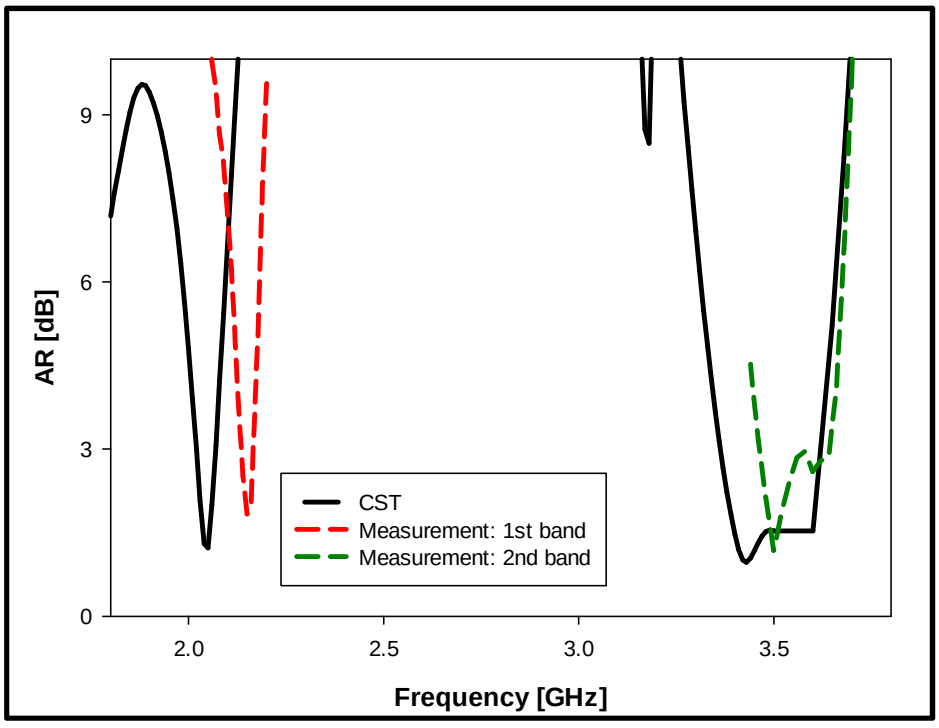

Figure 2.7.9: Axial Ratio for the dual band EDRA

For the first band, the simulated 3dB AR bandwidth range is $2.02 - 2.07\text{GHz}$, cantered at 2.05GHz, which corresponds to a percentage bandwidth of 2.44%. On the other hand, the measured 3dB AR bandwidth is $2.14 - 2.17\text{GHz}$, cantered at 2.15GHz, which corresponds to 1.4%. Again, there is a marginal shift in the

resonance frequency has been observed. For the second band, the simulated 3dB AR bandwidth is $3.363 - 3.619\text{GHz}$, cantered at 3.45GHz, which corresponds to 7.42%. The measured 3dB AR bandwidth is $3.464 - 3.642\text{GHz}$, cantered at 3.5GHz, which corresponds to a percentage bandwidth of 5.09%. The beamwidth bandwidths for both bands have also been found and are given in Figure 2.7.10 and Figure 2.7.11, with close agreement between both sets of results. For the first band, the 3dB bandwidth is $\sim 90^o$ whereas for the second band, the bandwidth is 18^o. The achieved gain of the antenna can be seen in Figure 2.7.12 and Figure 2.7.13, where it can be seen that for the first band, the gain is ~5dBi. On the other hand, for the second band, the simulated gain ranges between 2 and 3dBi whereas the measured gain is ranging between 0 and 2dBi. The far field patterns of the first band are illustrated in Figure 2.7.14 and Figure 2.7.15, where it can be seen that E_R is ~25dB less than E_L at bore-sight. Therefore, the first band is Left-Handed-Circularly-Polarised (LHCP). On the other hand, it can be seen from Figure 2.7.16 and Figure 2.7.17, that E_L is ~20dB less than E_R at bore-sight for the second band, and therefore the DRA is Right-Handed-Circularly-Polarised (RHCP) in this band. AS a result, this antenna offers a dual CP sense as well.

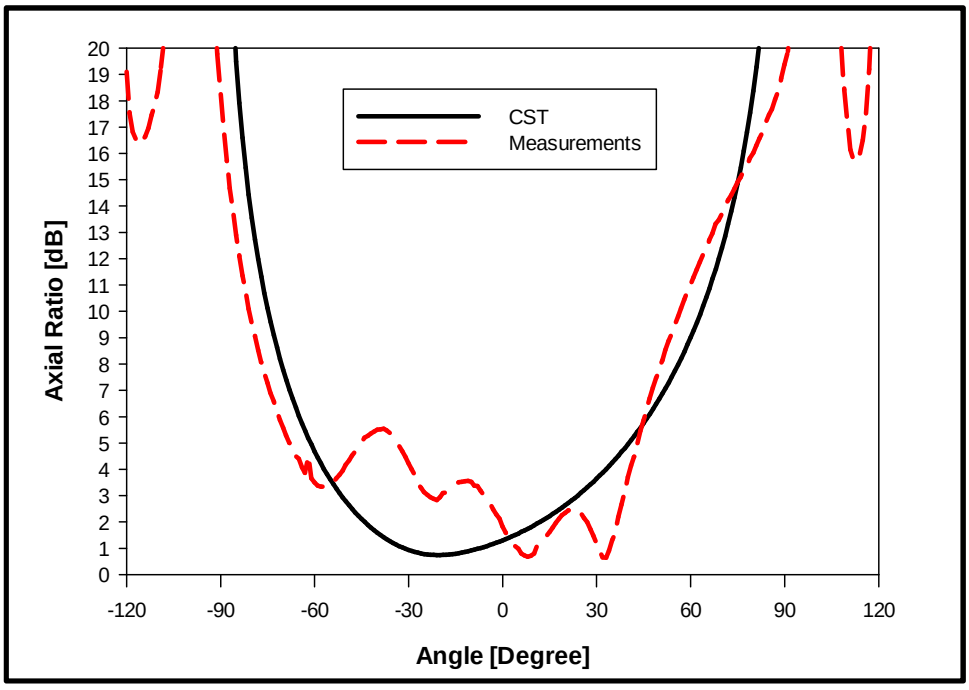

Figure 2.7.10: Beamwidth of the first band of DB-EDRA

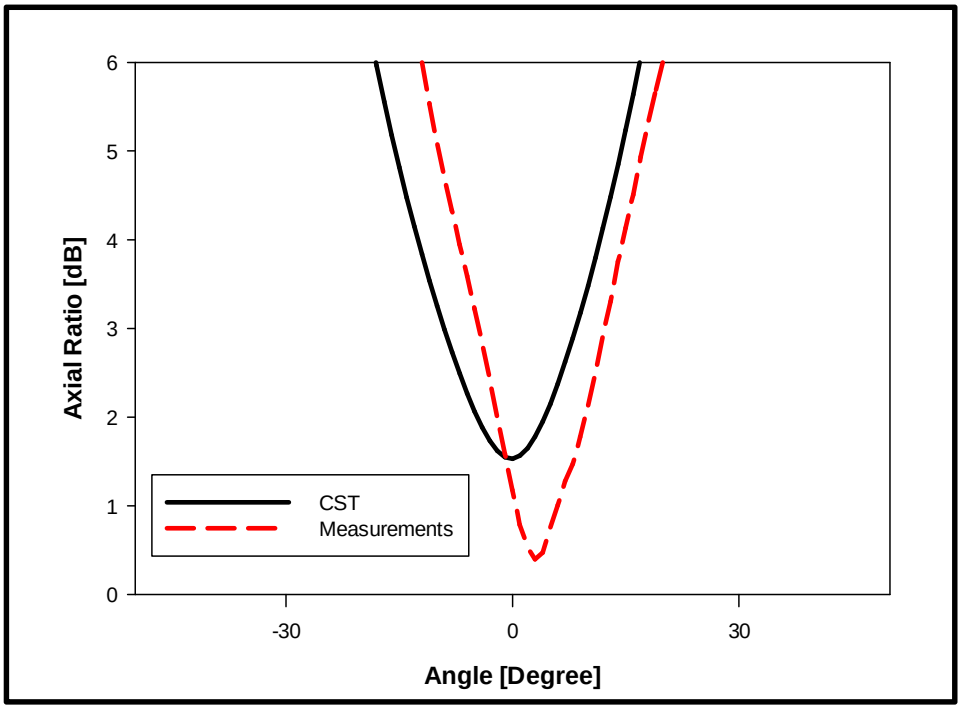

Figure 2.7.11: Beamwidth of the second band of the DB-EDRA

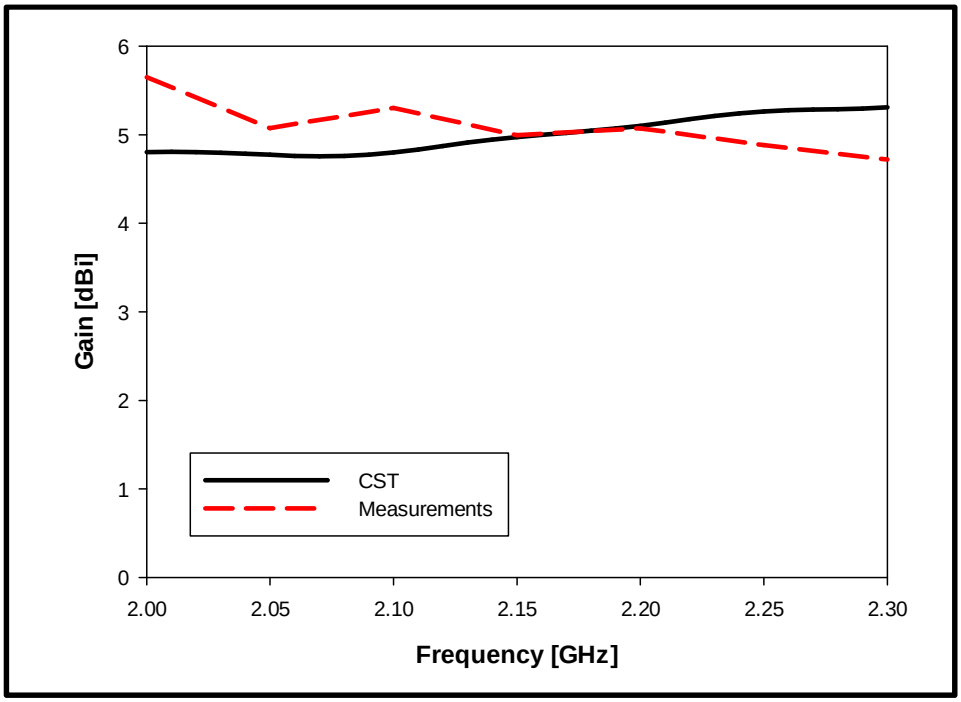

Figure 2.7.12: First band Gain of the dual band EDRA

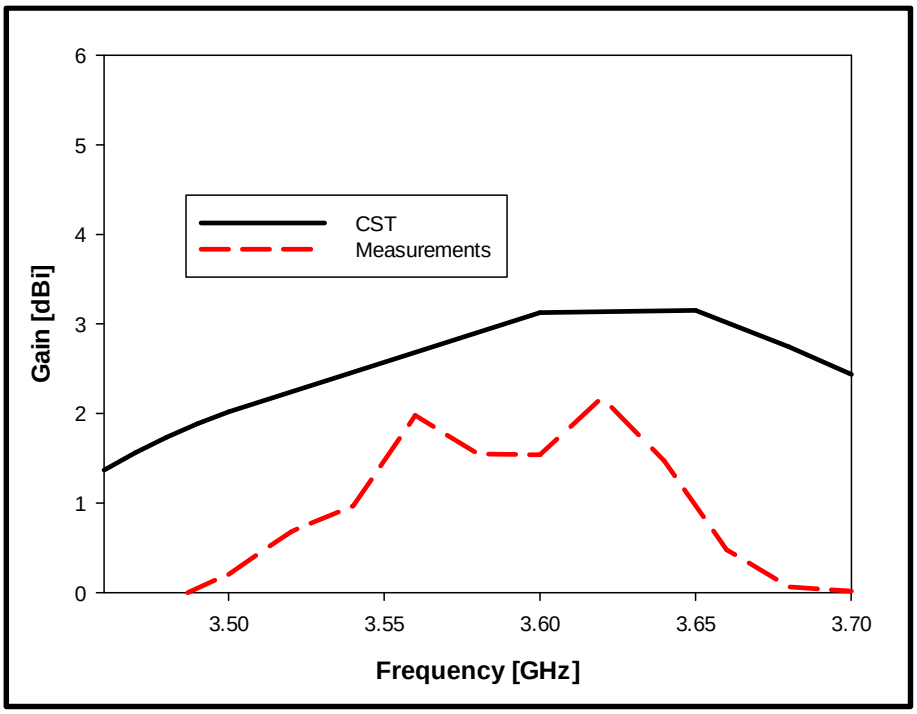

Figure 2.7.13: Second band gain of the dual band EDRA

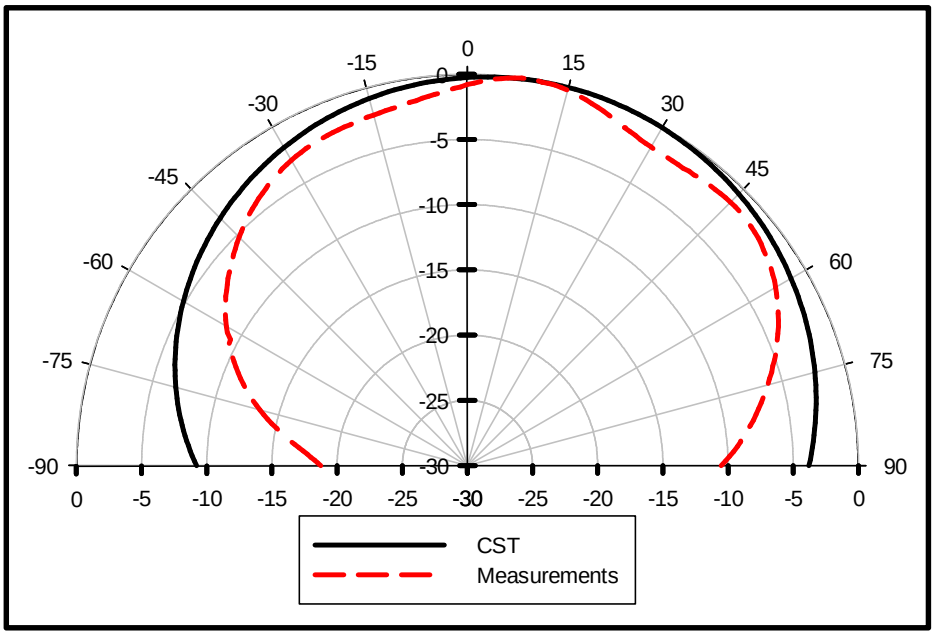

Figure 2.7.14: E_L for the first band of the dual band EDRA

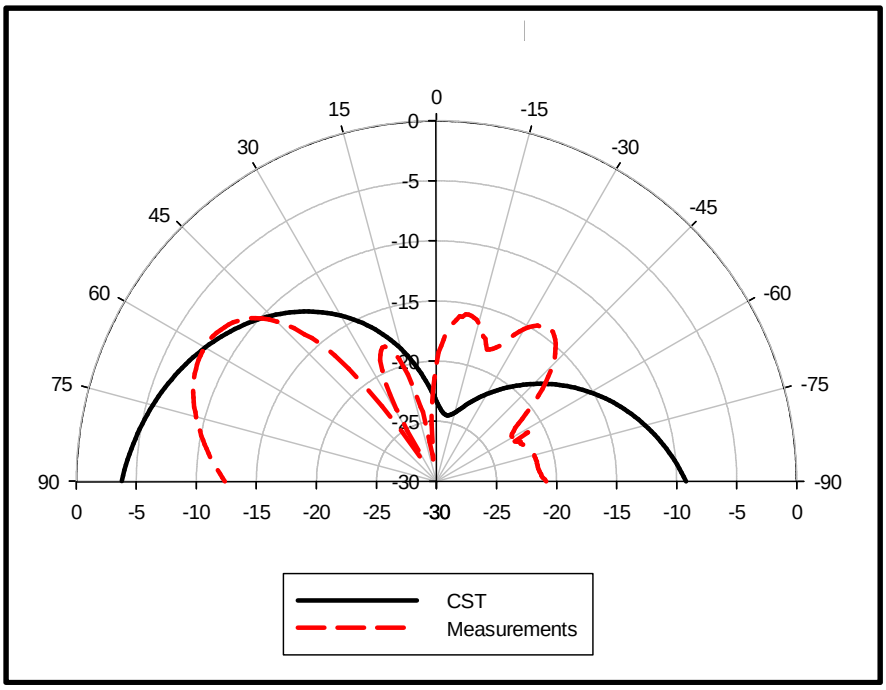

Figure 2.7.15: E_R for the first band of the dual band EDRA

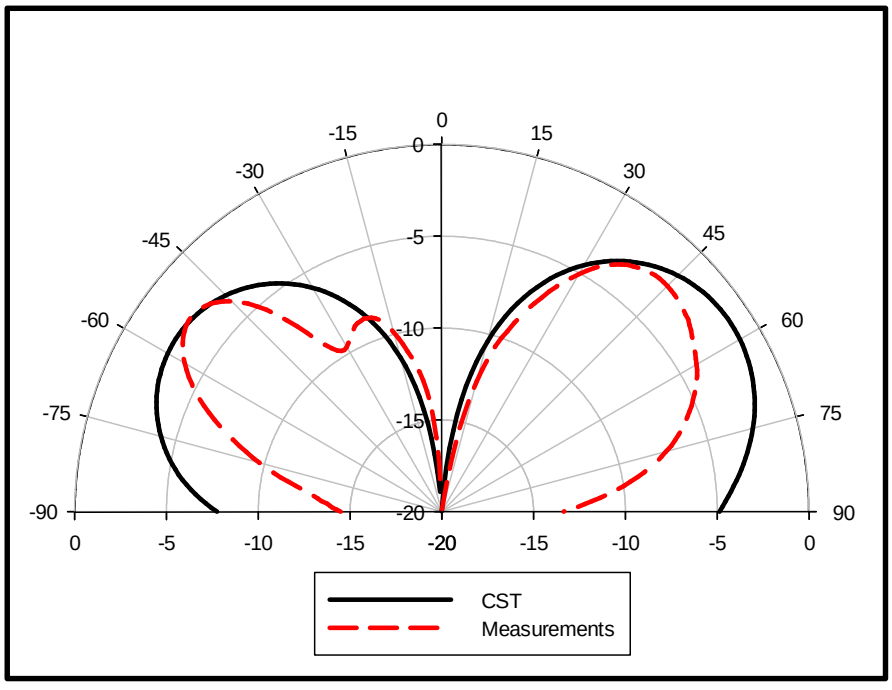

Figure 2.7.16: E_L for the second band of the dual band EDRA

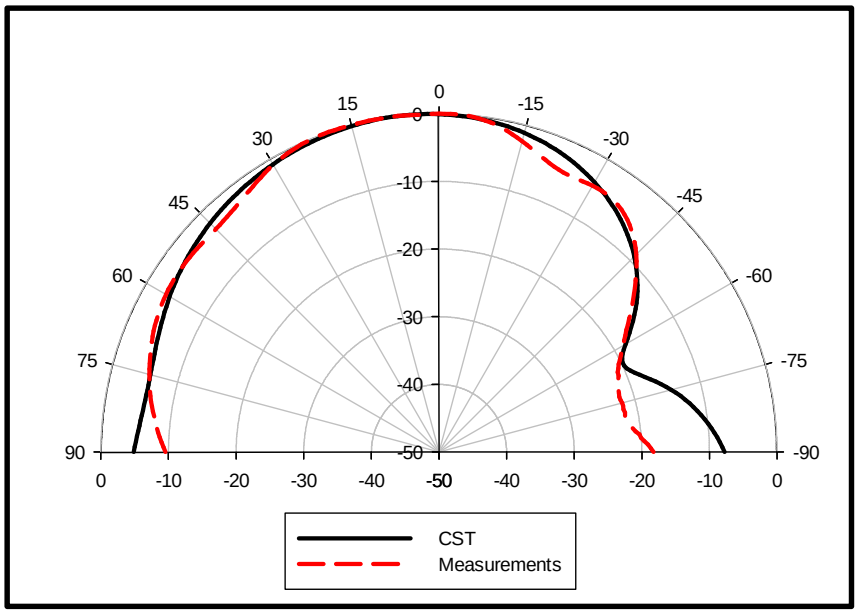

Figure 2.7.17: E_R for the second band of the dual band EDRA

2.8 Low Profile EDRA

2.8.1 *Introduction*

As demonstrated earlier, a conformal strip excited CP EDRA has been designed with a relative permittivity of $\varepsilon_r = 9.8$ and aspect ratio $(2a/h)$ of 2.48. The corresponding electrical dimensions of the major semi axes a and height h are shown in Table 2.8.1, where λ_o denotes wavelength in free space at 2GHz, λ_g denotes wavelength in the dielectric given by $\lambda_o/\sqrt{\varepsilon_r}$ and λ_{eff} denotes the effective wavelength given by $\lambda_o/\sqrt{(\varepsilon_r+1)/2}$. Usually, the dimensions of a dielectric resonator are given in order of the λ_g [16]. Therefore, increasing the relative permittivity should result in decreasing the size of the EDRA. Using this principal and by exciting the orthogonal odd and even $HE_{11\delta}$ modes, a low profile, circularly polarised EDRA has been designed.

Parameter (p)	Value [mm]	λ_o/p	λ_g/p	λ_{eff}/p
a	26	5.8	1.84	2.48
h	21	7.14	2.28	3.07

Table 2.8.1: Electrical dimensions for the conformal excited EDRA of $\varepsilon_r = 9.8$

2.8.2 *Design Procedures*

As a starting point, the values of a and h for $\varepsilon_r = 9.8$ have been calculated in terms of λ_g, so that varying the relative permittivity should be associated with changing a and h in order to maintain the same electrical λ_g dimensions. The strip has been located at $\varphi = 135^o$ with same width and the minor semi axis b has been given as $a/1.625$. The variables a and h can be expressed as:

$$a = \frac{0.5426 \times 0.15}{\sqrt{\varepsilon_r}} \text{ and } h = \frac{0.4383 \times 0.15}{\sqrt{\varepsilon_r}} \tag{2.7}$$

The dielectric constant ε_r has been varied from $9.8 - 20$ and the resultant reflection coefficient and axial ratio are presented in Figure 2.8.1and Figure 2.8.2, respectively, using a strip length of h.

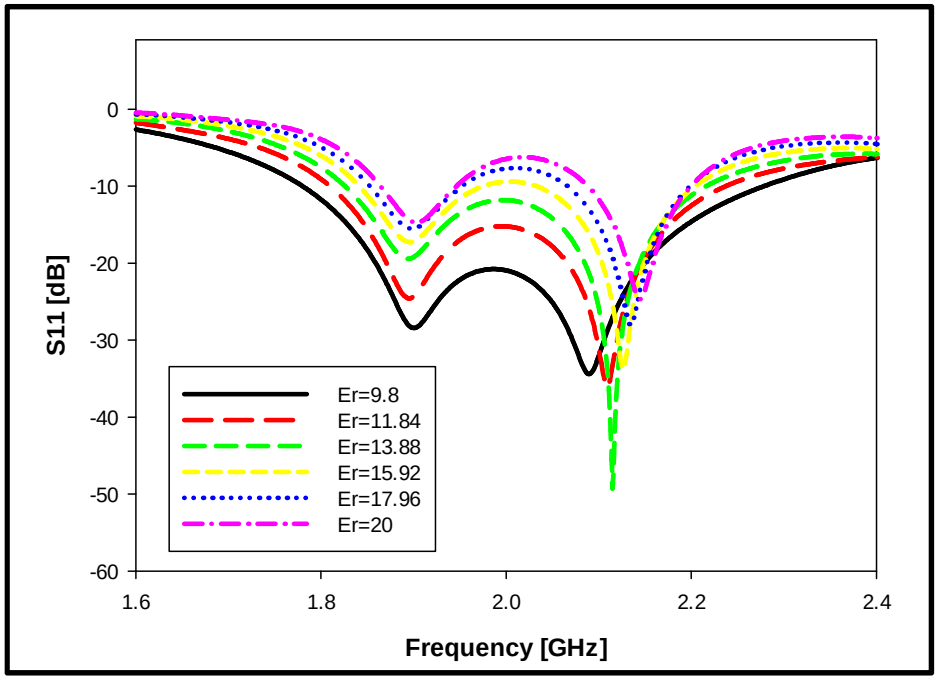

Figure 2.8.1: Reflection coefficient of conformal excited EDRA with different values of ε_r

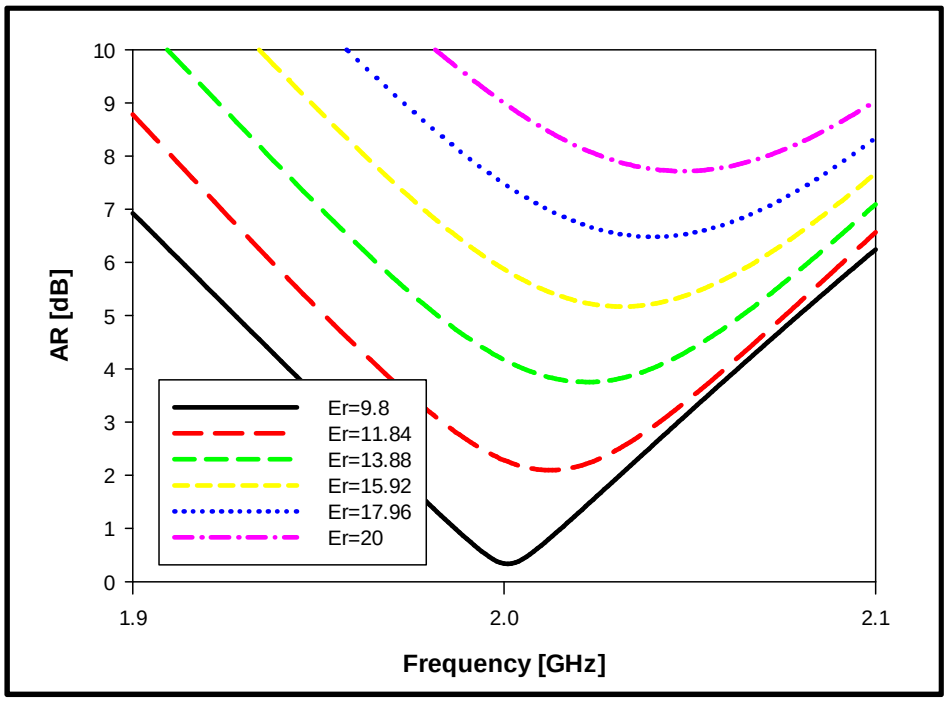

Figure 2.8.2: Axial ratio of conformal excited EDRA with different values of ε_r

It can be seen from these results that although for each ε_r, the EDRAs have the same λ_g dimensions, the reflection coefficient and the axial ratio have been changed significantly. From the analysis presented in section 3.5, it has been noticed that varying the a/b can also alter the results and therefore, the values of a and h have been set as for $\varepsilon_r = 20$ and the value of minor axes b has been varied. Good results have been achieved for $a/b = 1.25$, which will be shown next.

2.8.3 *Results and Discussion*

The low profile EDRA has been simulated using Microwave studio CST and cross validated with HFSS. As mentioned earlier, the dielectric constant has been fixed as $\varepsilon_r = 20$. The new dimensions of the EDRA has been determined as $a = 16.9\,\text{mm}$, $b = 13.55\text{mm}$ and $h = 13.7\text{mm}$, which corresponds to $a/b = 1.25$. The reflection coefficient is shown in Figure 2.8.3 with good agreement between the two sets of results. The achieved -10 dB bandwidths are 7.8% and 7% from CST and HFSS, respectively. The axial ratio is presented in Figure 2.8.4 with respective CST and HFSS bandwidths of 2% and 1.8%. Both CST and HFSS results show that this antenna offers a useful gain of ~5dBi over the CP bandwidth as can be seen from Figure 2.8.5.

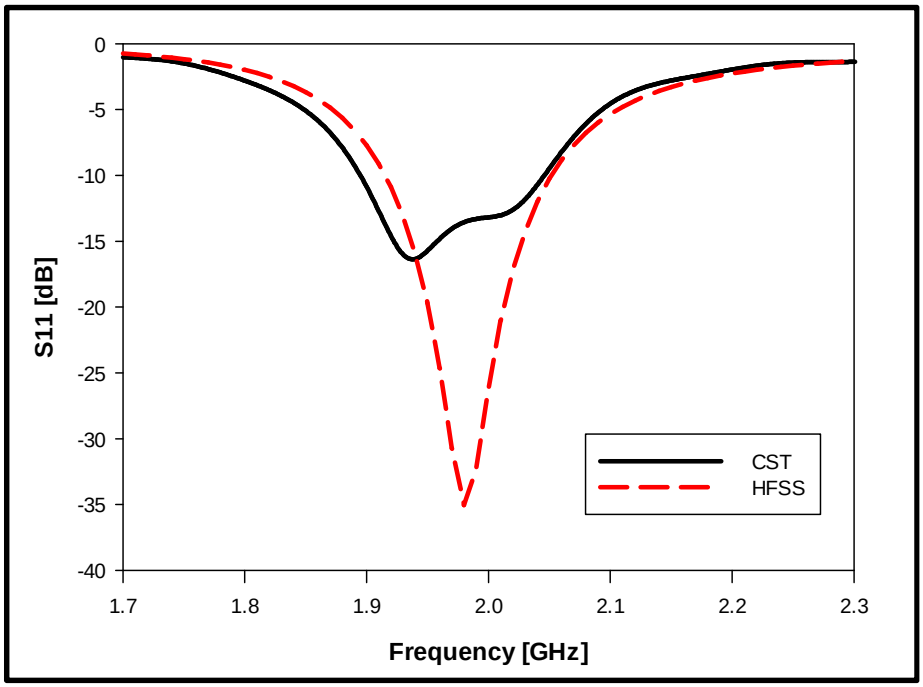

Figure 2.8.3: Reflection coefficient for the low profile EDRA

.

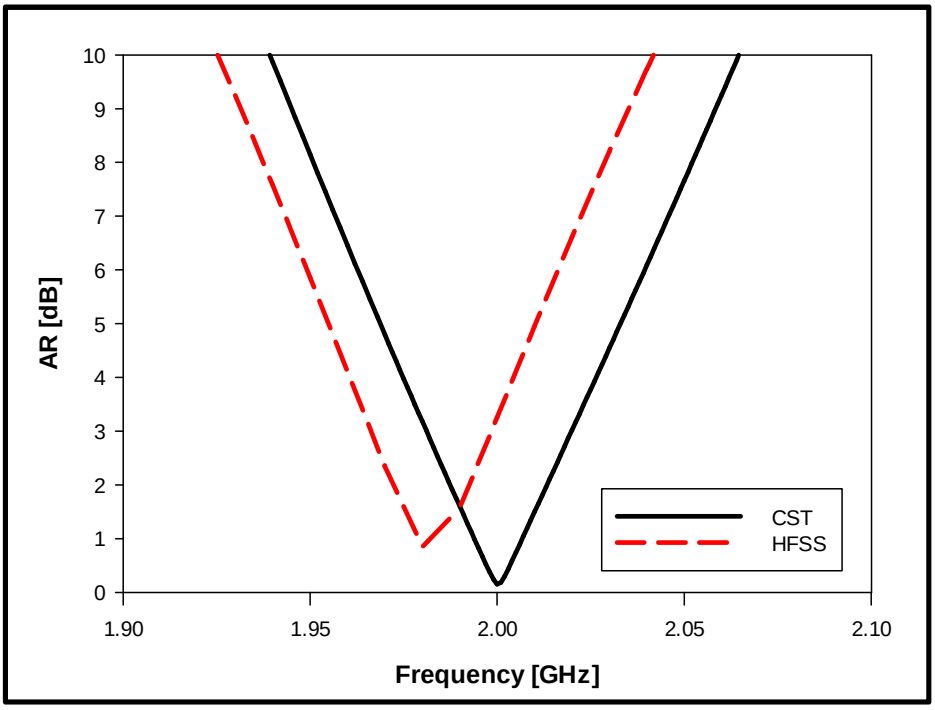

Figure 2.8.4: Axial ratio for the low profile EDRA

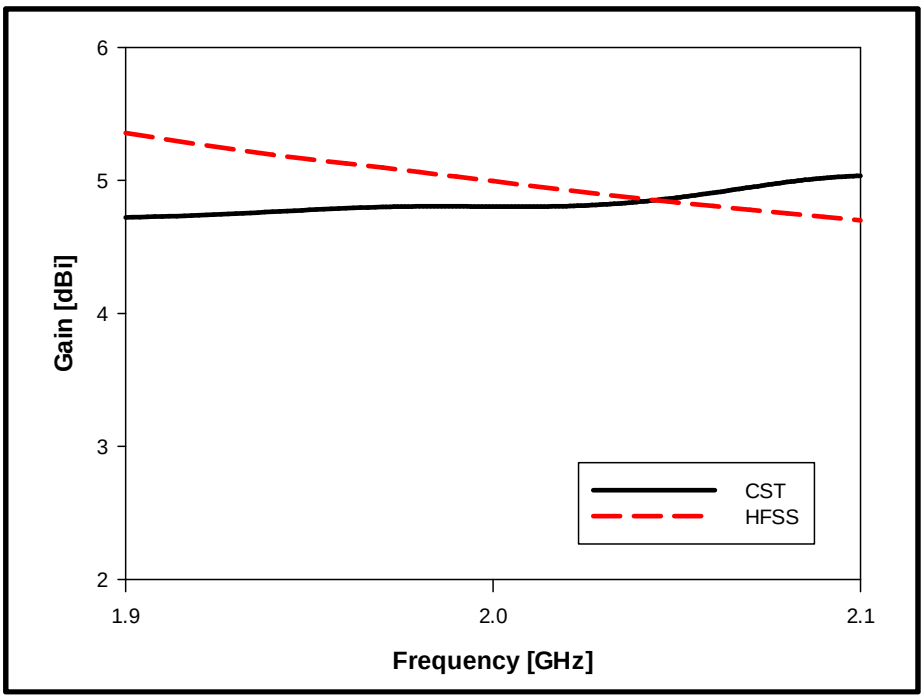

Figure 2.8.5: Gain for the low profile EDRA

Using the same principal, the dielectric constant has been increased further and the a/b ratio has been adjusted accordingly. The height of the EDRA has been reduced further. Table 2.8.2 summarizes the dimensions for the three designed conformal excited EDRA.

ε_r	a [mm]	$[a/\lambda_o]$	b[mm]	$[b/\lambda_o]$	a/b	h[mm]	$[h/\lambda_o]$	$2a/h$
9.8	26	5.8	16	9.4	1.625	21	7.1	2.48
20	16.9	8.9	13.6	11.1	1.25	13.7	11	2.47
25	15.1	10	12.6	12	1.20	12.2	12.3	2.48

Table 2.8.2: Geometry summary for the three designed conformal excited EDRA

A comparison of the achieved reflection coefficients and axial ratios for the three antennas are shown in Figure 2.8.6 and Figure 2.8.7 with a summary presented in Table 2.8.3.

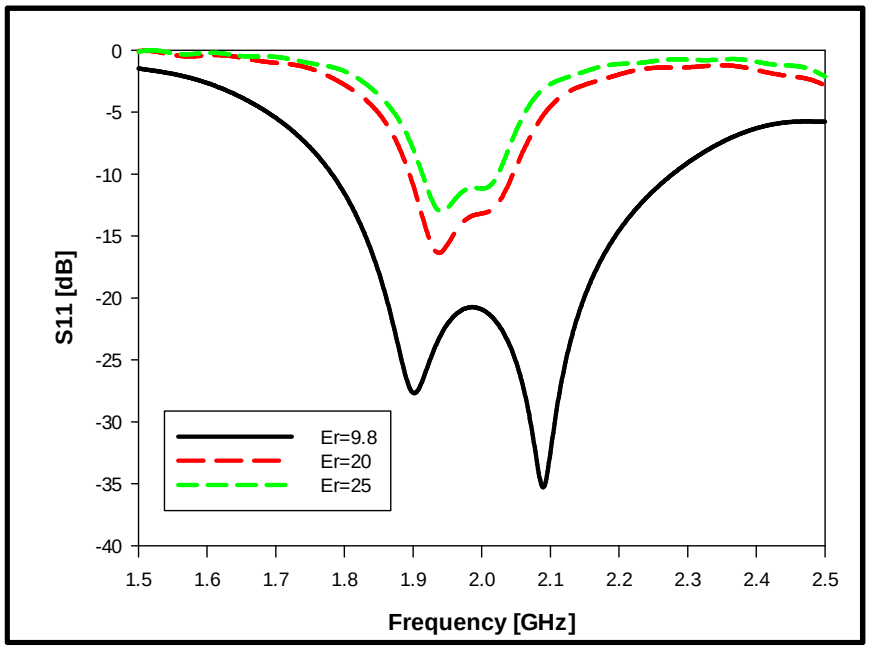

Figure 2.8.6: Reflection coefficients for three designed conformal excited EDRA

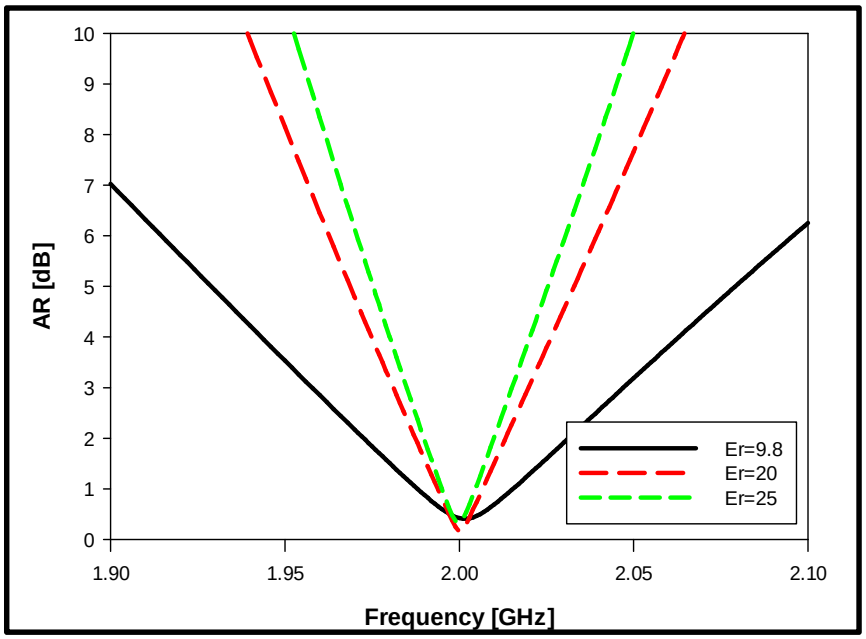

Figure 2.8.7: Axial ratios for the three designed conformal excited EDRA

ε_r	S_{11} [%]	AR [%]
9.8	25.8	4.8
20	7.8	2
25	5.7	1.5

Table 2.8.3: S_{11} and AR bandwidths for the three conformal excited EDRAs

From these results, it can be observed that all the three antennas resonate at 2GHz using the same aspect ratio $2a/h$ of 2.48. Also, it can be seen that changing the dielectric constant from 9.8 to 25 decreases the height of the EDRA by $\sim 42\%$ from 21mm to 12.2mm. However, increasing the dielectric constant results in a sharp deterioration the performance of the EDRA. For example, the reflection coefficient bandwidth has been reduced from 25.8% to 5.7% and the axial ratio from 4.5% to 1.5%. Increasing the dielectric constant can reduce the size of the EDRA further but this will degrade the bandwidth more and results in an inefficient EDRA. Since it is aimed to design a low profile CP antenna with a reduced size, another method will be deployed that employs an Artificial Magnetic Conductor (AMC), which will be discussed next chapter.

2.9 Conclusion

In this chapter, four designs of singly fed Elliptical DRAs have been presented using conformal strip excitation for simplicity. In the first design, it has been demonstrated that a single strip located at $\varphi = 135^o$ generates circularly polarised radiation with an axial ratio 3dB bandwidth of 4.8%. In the second design, a wide band CP radiation has been accomplished using a half open loop antenna associated with a parasitic inner loop, where a 3dB simulated axial ratio bandwidth of $\sim 11.7\%$ has been achieved. In the third design, a singly fed dual band circularly polarised EDRA has been designed at 2GHz and 3.5GHz. A half open loop with a matching strip has been used and good agreement between simulated and measured results has been achieved. Finally, a low profile EDRA has been proposed with $\varepsilon_r = 25$. As expected, increasing the dielectric constant reduces the DRA size. However, there is a limit in the increment as the antenna performance degrades considerably when ε_r exceed 25. Therefore, another method will be employed to design a low profile circularly polarised antenna using an Artificial Magnetic Conductor (AMC), which is presented in the next chapter.

CHAPTER 3

Circularly Polarized Antenna backed by a Square Patch Artificial Magnetic Conductor (AMC) Ground Plane

3.1 Introduction

The main objective of this chapter is to employ the concept of Artificial Magnetic Conductor (AMC) to design low profile circularly polarised antenna. Such designs have been achieved in the literature but it is desired here to design a CP antenna with a lower thickness and/or reduced size. For example, Fan Yang has used the curl antenna on top of the well-known mushroom-like EBG surface [109]. In that design, the total thickness of the antenna has been calculated as $\lambda_o/8.57$ and the total ground plane size is $0.82\lambda_o \times 0.82\lambda_o$. Additionally, H. Farahani *et al.* have used the curl antenna on a rectangular patches AMC [110], where the total thickness and the ground plane size have been calculated as $\lambda_o/10.2$ and $1.62\lambda_o \times 1.56\lambda_o$, respectively. Also, a rectangle AMC has been used to support dipole antenna radiating CP wave has been reported in [111]. In a subsequent study, the same antenna has been placed on square patch AMC [112], where the total thickness has been reduced to $\lambda_o/21.23$ with a total ground plane size of $0.84\lambda_o \times 0.84\lambda_o$. A simulated 3dB axial ratio bandwidth of 11% has been reported. However, the measured AR is greater than 3dB for the entire simulated bandwidth. The main drawback of the curl antenna is the high input reactance, which is in the order of $\sim -100\Omega$. In another study, X. Bao *et al.* have used a circularly polarised open loop antenna over a novel AMC shape for [113], where a dielectric substrate with a relative permittivity of $\varepsilon_r = 11.9$ has been used. The ground plane size has been reduced to $0.36\lambda_o \times 0.36\lambda_o$ but with a relatively high thickness of $\lambda_o/16.6$. Although the gain has been improved by introducing the AMC, the overall gain is negative.

In this chapter, a design of a low profile open loop antenna above the square patch AMC is presented. As a starting point, the aim is to reduce the antenna height. Two feeding mechanism are employed; the co-planar waveguide and the vertical probe. Compared to the curl antenna, the loop offers an input impedance of $\sim 50\Omega$, which simplifies the design and improve the total efficiency significantly.

3.2 A Circularly Polarized Open Loop Antenna Fed by a Co-Planar Waveguide (CPW)

3.2.1 *Unit Cell Design Procedures*

Square patches AMC unit cells have been reported in the literature [39], where each cell consists of a square patch of width w in conjunction with a gap, g, that separates

each two adjacent patches. The patch is shown in Figure 3.2.1and it is printed on a dielectric substrate of a relative permittivity ε_r and thickness of h_1. The square patch AMC offers four design parameters, w, g, ε_r and h_1, which can be altered to achieve the desired reflection's phase. In fact, designers usually use the available materials in the laboratory, which also come in specific thicknesses. In this case, the FR4 substrate of $\varepsilon_r \approx 4.3$ has been used, which comes with specific thicknesses as a multiple of 0.8mm. Therefore, the available sizes of h_1 are $0.8, 1.6, 2.4\text{mm}$.... This means that the most important parameters when designing the square patch AMC are w and g. The unit cell has been simulated using the CST Microwave Studio [65], where the square patch has been placed on a lossy grounded FR4 substrate. The reflection phase can be obtained by simulating the infinite structure of a single unit AMC by applying mirror boundary conditions at the side walls of a unit cell [39]. For example, to simulate the AMC cell shown in Figure 3.2.1 as infinite pattern, the boundary condition *unit cell* has been applied in all x and y boundaries, while the minimum z wall has been defined using the PEC boundary condition, and the z maximum wall is kept open as free space as illustrated in Figure 3.2.2 [65].

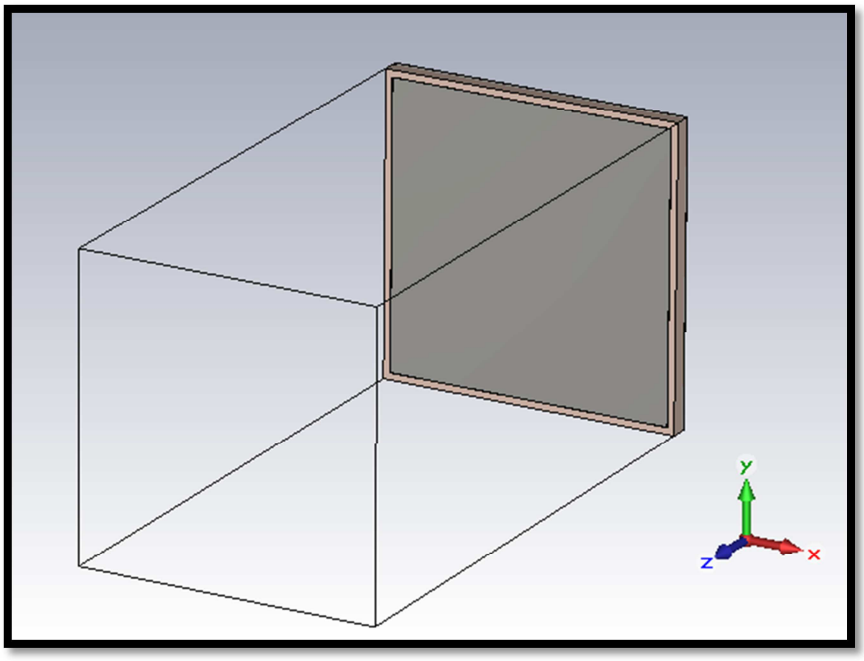

Figure 3.2.1: An AMC Unit Cell simulated in CST

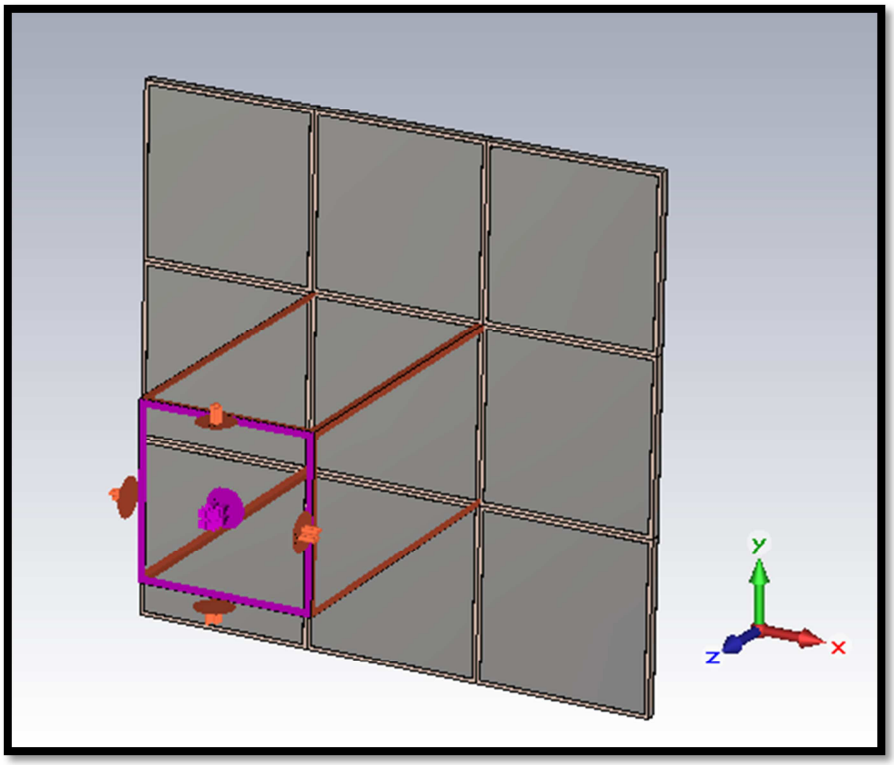

Figure 3.2.2: An AMC Unit Cell simulation in CST using *unit cell* boundary condition

Initially, the effects of the design parameters on the reflection phase have been investigated. The square's width w has been varied while g and h are kept constant and the resultant reflection phase is presented in Figure 3.2.4, where it can be seen that as the width increases, the resonance frequency decreases with a slight decrease in the bandwidth. Detailed results of the width effects are presented in Table 3.2.1 and Figure 3.2.5, where f_2 and f_1 represent the frequencies at reflection phases of -90^o and $+90^o$, respectively, and f_{res} represents the 0^o-reflection phase.

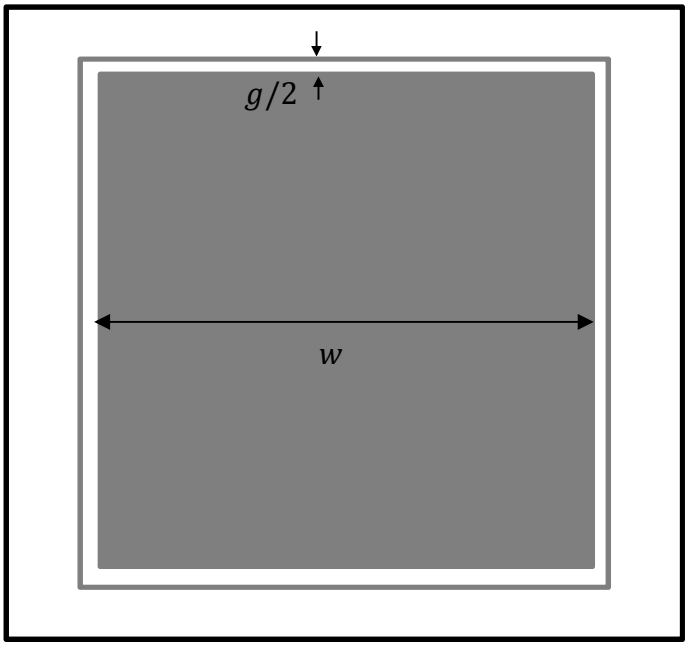

Figure 3.2.3: Square patch unit cell

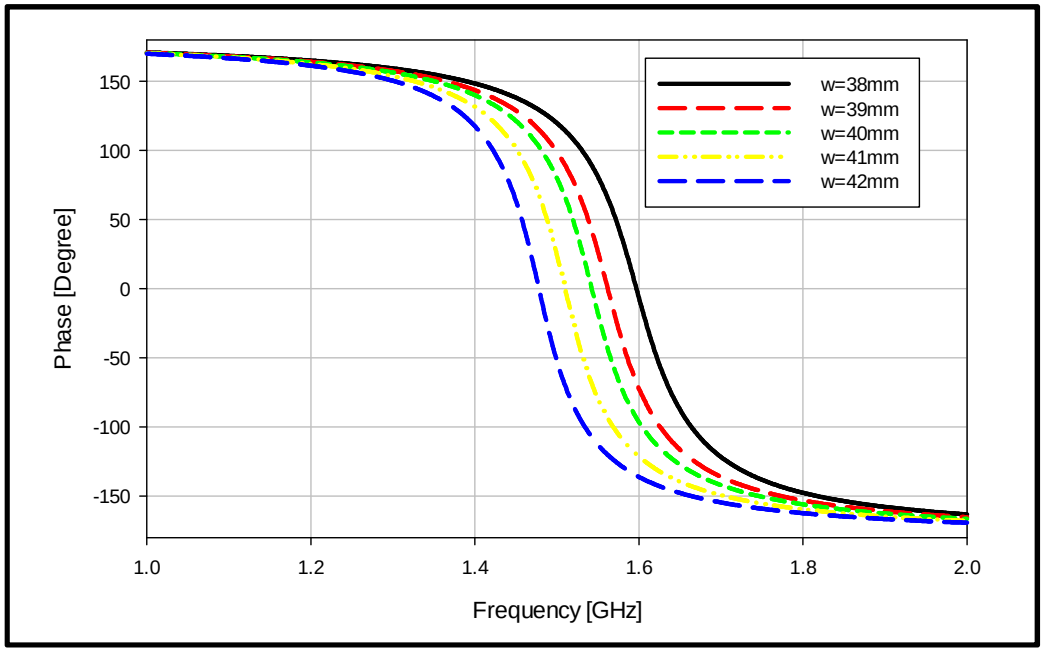

Figure 3.2.4: Reflection phase of various unit cell widths

$w[mm]$	f_2[GHz]	f_1[GHz]	f_{res}[GHz]	BW [%]
38	1.6526	1.5416	1.5969	6.95
39	1.6152	1.5095	1.5622	6.77
40	1.5937	1.4916	1.5426	6.62
41	1.5588	1.4614	1.51	6.45
42	1.5247	1.4319	1.4782	6.28

Table 3.2.1: Detailed results of reflection phase for various size of w

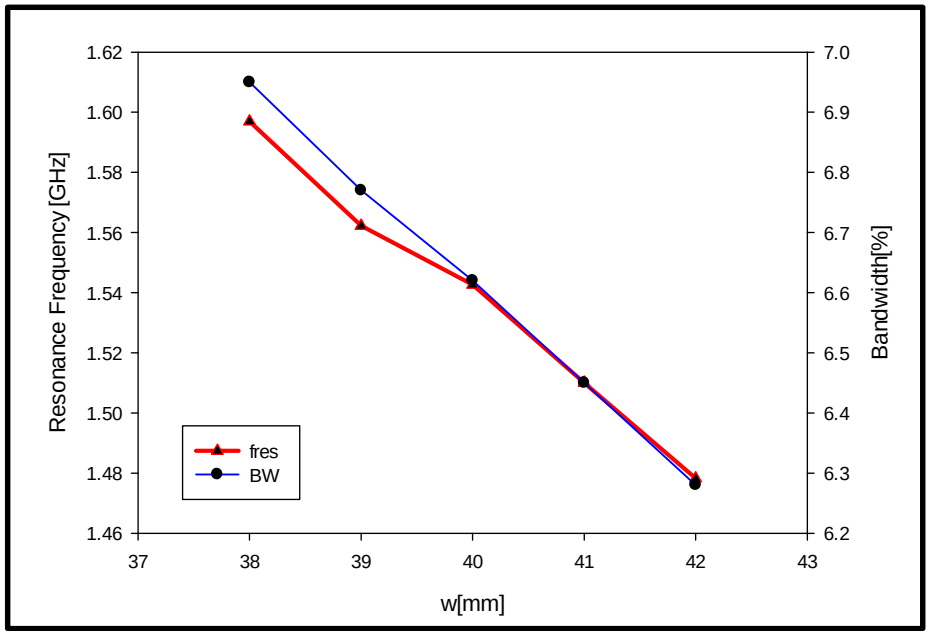

Figure 3.2.5: Resonance frequency and AMC bandwidth for various unit cell widths

It needs to be mentioned that the patch itself contributes to the inductance *L* of the AMC. The second investigated parameter is the gap g, which represents the major contribution to the capacitance in the system. The gap has been varied while the other parameters are kept constant and the resultant reflection phase is illustrated in Figure 3.2.6. It can be noticed from these as *g* increases, the 0^o-phase shifts to a higher frequency with a slight change in the operating bandwidth as illustrated in Table 3.2.2 and Figure 3.2.7. This result is in agreement with the proportionality of the resonance frequency of the AMC given by [36]:

$$f_{resonance} \propto \frac{1}{\sqrt{LC}} \tag{3.1}$$

The capacitance is inversely proportional to the distance between the two conductors of the adjacent cells. Therefore, as g increases, the capacitance reduces, which increases the resonance frequency.

$g[mm]$	f_2[GHz]	f_1[GHz]	$f_{resonance}$[GHz]	BW [%]
0.5	1.4513	1.3624	1.4066	6.32
1	1.5556	1.4565	1.5059	6.58
1.5	1.5937	1.4916	1.5426	6.62
2	1.6142	1.5111	1.5627	6.60
2.5	1.6277	1.5244	1.5761	6.55

Table 3.2.2: Reflection phase for various size gap g

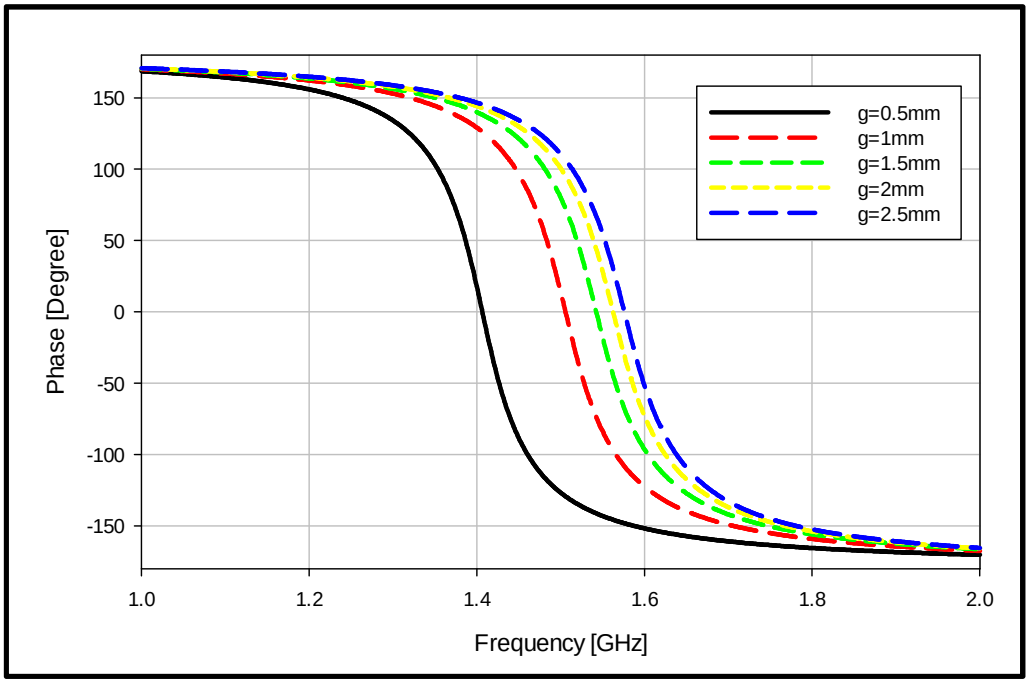

Figure 3.2.6: Reflection phase for various values of g

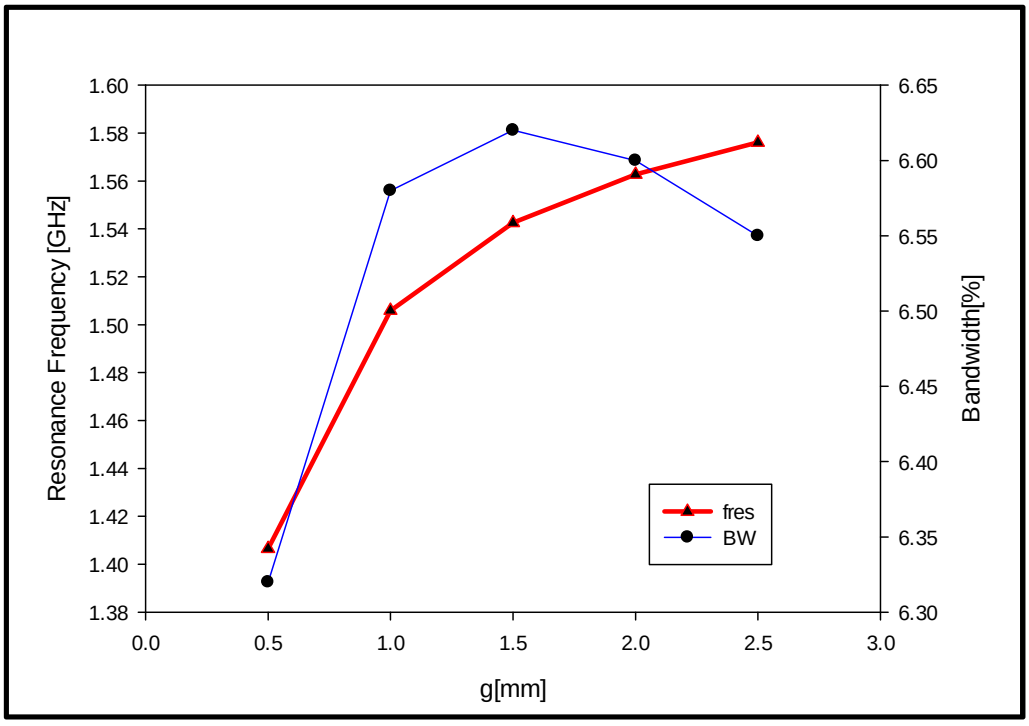

Figure 3.2.7: Resonance frequency and AMC bandwidth for various separation distances between the unit cells

Next, the substrate thickness, h_1, has been investigated while w and g were kept constants. The results are presented in Figure 3.2.8, where it can be observed that both the resonance frequency and bandwidth depend on the thickness. For example,

the bandwidth has changed from 0.19% for $h_1 = 0.8\text{mm}$ to 10.51% for $h_1 = 4\text{mm}$. This is owing to the fact that the substrate thickness contributes significantly to the overall inductance. As a result, using the proportionality of (3.2), any additional inductance increases the bandwidth [36].

$$BW \propto \sqrt{\frac{L}{C}} \tag{3.2}$$

Additional results are given in Figure 3.2.9 and Table 3.2.3.

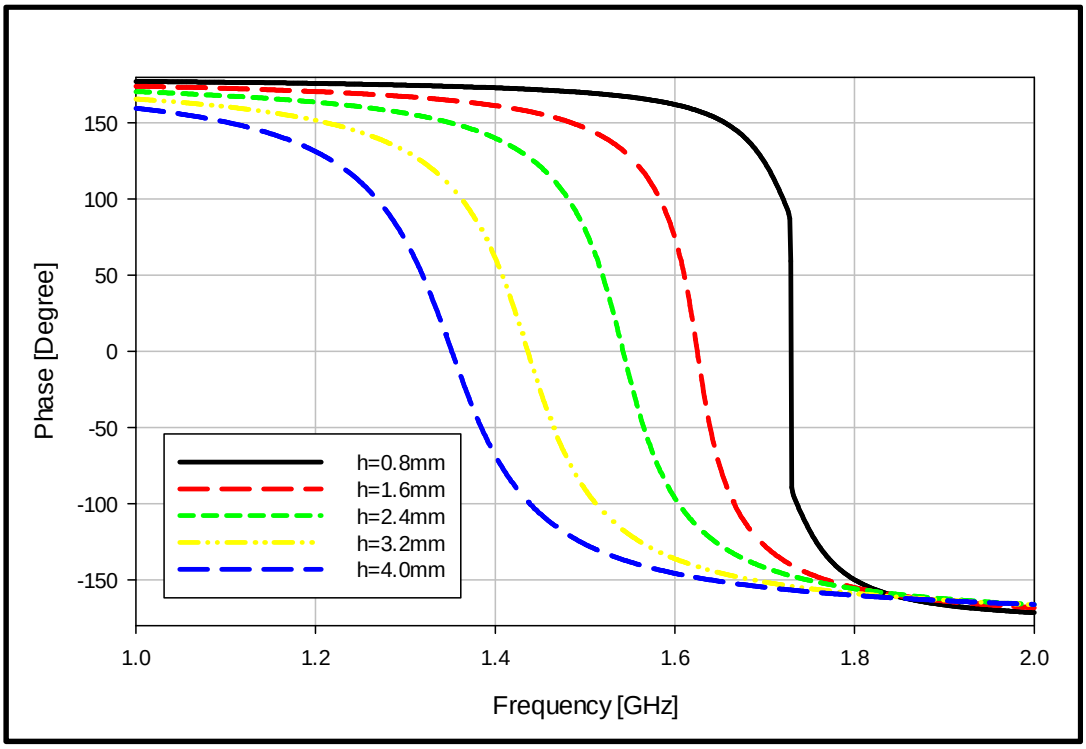

Figure 3.2.8: Reflection phase for various substrate thicknesses

$h_1[mm]$	$f_2[\text{GHz}]$	$f_1[\text{GHz}]$	$f_{resonance}[\text{GHz}]$	BW [%]
0.8	1.7302	1.727	1.7294	0.19
1.6	1.6586	1.591	1.6251	4.16
2.4	1.5937	1.4916	1.5426	6.62
3.2	1.4994	1.3747	1.4364	8.68
4	1.4240	1.2819	1.3518	10.51

Table 3.2.3: The resonance frequency and bandwidth for various substrate thicknesses

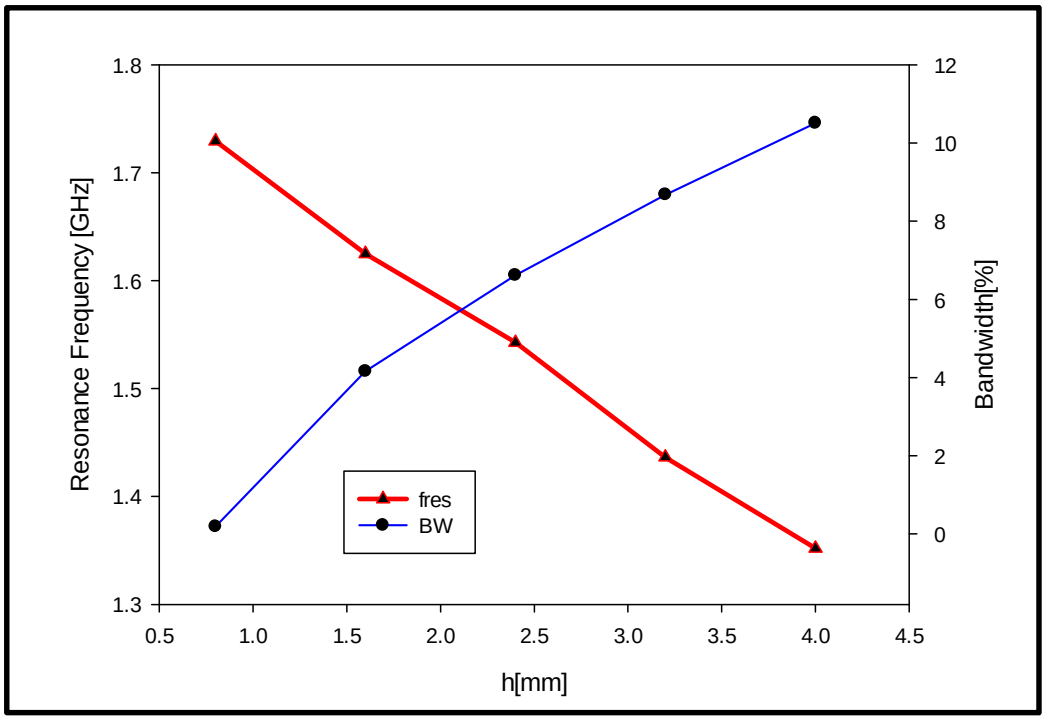

Figure 3.2.9: Resonance frequency and AMC bandwidth for various substrate thicknesses

Based on this analysis, the optimum values for the design parameters have been selected as $w = 40\text{mm}$, $g = 1.5\text{mm}$, with a total cell size of $x = 41.5\text{mm}$, which corresponds to $\lambda_o/4.6$ at the desired frequency of 1.57GHz. This square patch has been printed on a grounded FR4 substrate with a relative permittivity of $\varepsilon_r \approx 4.3$ and a thickness of $h_1 = 2.4\text{mm}$, which corresponds to $\lambda_o/79.6$. The reflection phase of this AMC unit cell is shown in Figure 3.2.10.

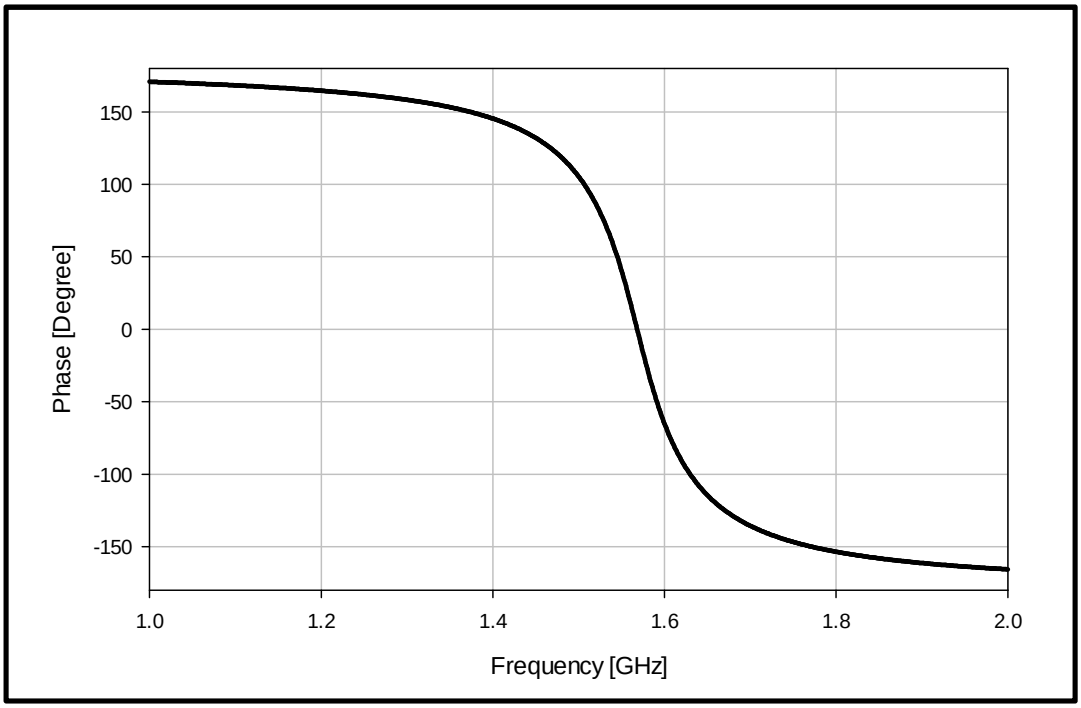

Figure 3.2.10: Reflection Phase for square patch AMC for the open loop antenna fed by co-planar waveguide

The square patch has been designed so that the 0 ± 90^{o} reflection phase covers the L_1 GPS bandwidth. The simulation result shows that the 0 ± 90^{o} bandwidth extends from 1.5168 to 1.6193GHz and centred at 1.5681GHz with a bandwidth of 6.54%. For testing purposes, a centre-fed dipole antenna has been placed at a height of 1mm above a 4×4 AMC grid that has been positioned at 3.4mm above the PEC ground plane as shown in Figure 3.2.11. This antenna has been compared with an identical counterpart that is placed at the same height above the PEC ground plane in the absence of the AMC. The reflection coefficients, S_{11}, for the two structures are given in Figure 3.2.12, where it can be observed that introducing the AMC has significantly improved the S_{11} at the desired frequency range as expected.

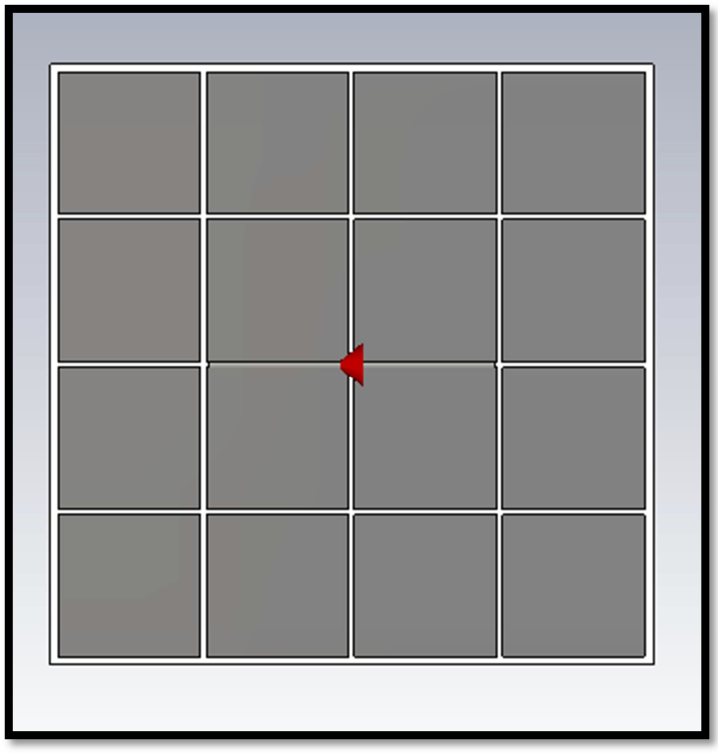

Figure 3.2.11: A dipole antenna positioned at $1mm$ above the square patches AMC

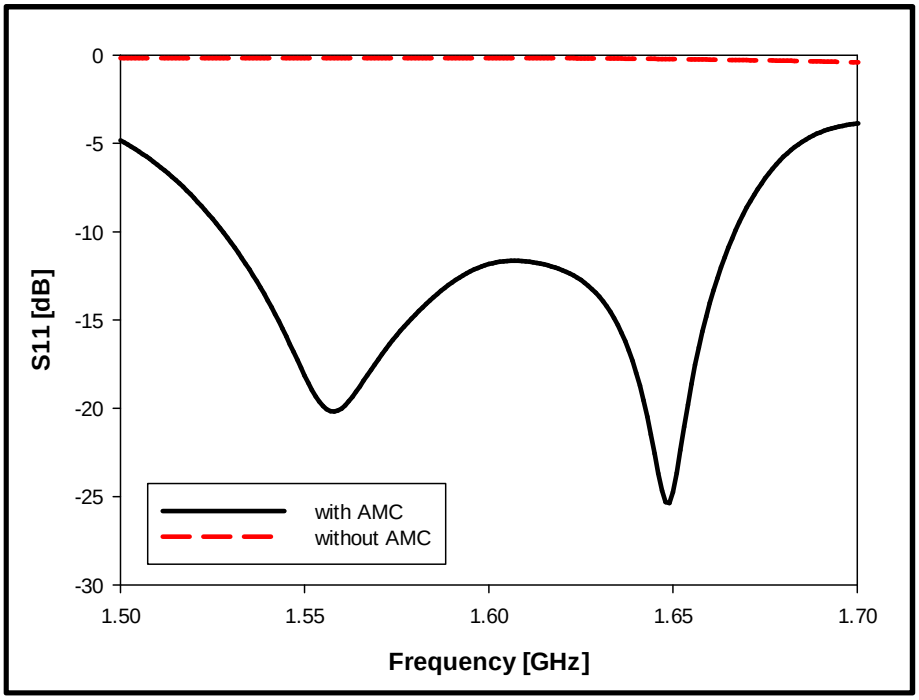

Figure 3.2.12: S_{11} of a dipole antenna at $3.4mm$ height above the PEC ground plane, with and without AMC

3.2.2 *Open Loop Antenna Design*

A planar open loop antenna that is fed by a co-planar waveguide and printed on a grounded dielectric substrate has been designed for circularly polarised radiation as shown in Figure 3.2.13. As mentioned earlier a lossy FR4 with $\varepsilon_r \approx 4.3$ and a thickness of $h_2 = 1.6\text{mm}$ has been employed.

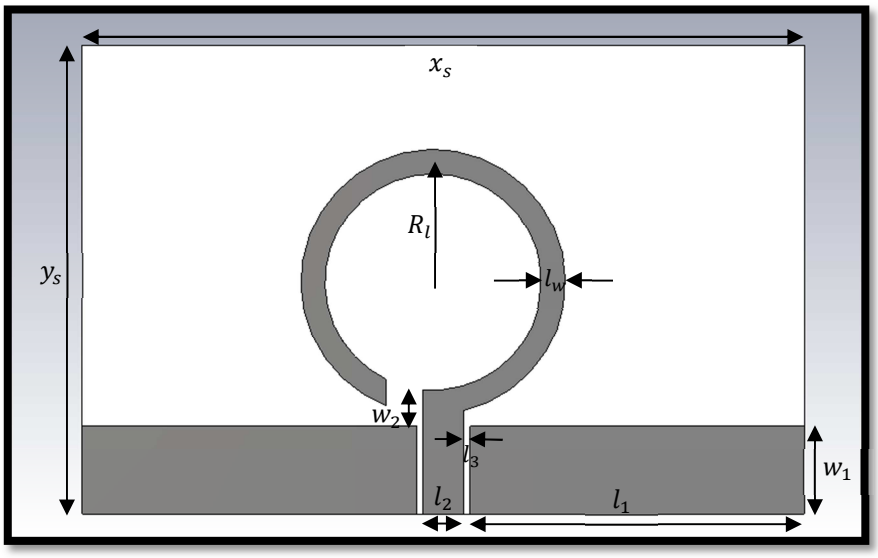

Figure 3.2.13: Open loop antenna fed by co-planar waveguide

In order to achieve a CP radiation, the loop circumference needs to be approximately one wavelength [96]. This is because travelling wave current is excited along the loop, which is the main cause of generating the circularly polarised wave. The width of the feed,l_2, and the gap between the feed and the rectangular ground, l_3, have been selected so that the input resistance is $\sim 50\Omega$. Additionally, the width of the loop has been varied in order to achieve matching. Since the interaction between the antenna and the AMC is considerably strong, the dimensions of the antenna had to be optimized for improved results.

When designing the full antenna, there are some parameters that play a vital role in the design, which are the loop radius and the gap between the two layers; that is, the AMC layer and the antenna layer. The loop radius is important because it introduces the axial ratio to the system as explained earlier. The radius has been varied from $11 - 17\text{mm}$ and the results of the reflection coefficient, S_{11}, and the axial ratio, AR, are given in Figure 3.2.14 and Figure 3.2.15, respectively.

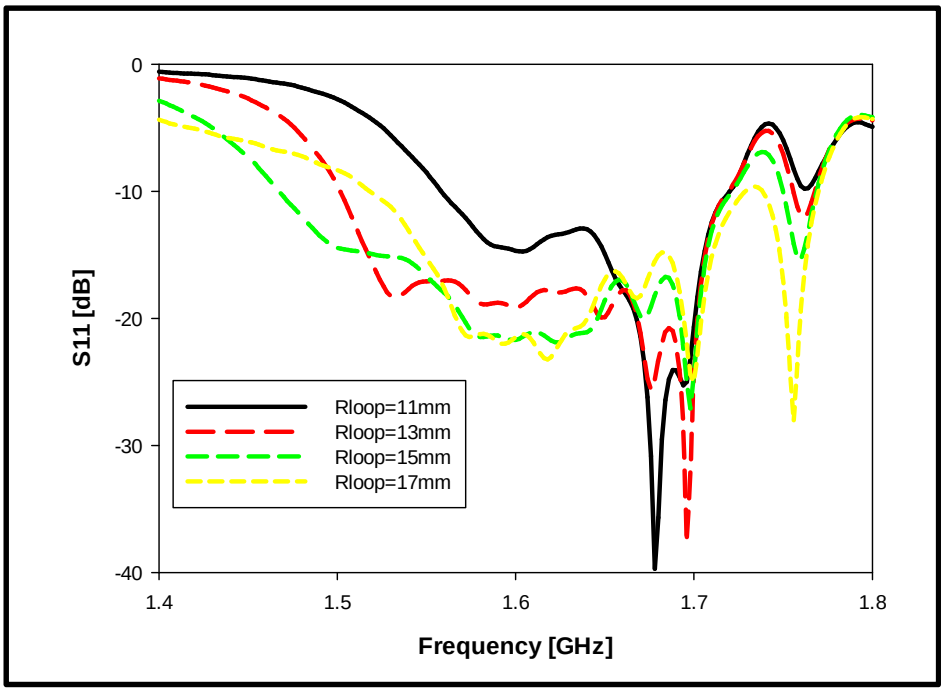

Figure 3.2.14: S_{11} for variable loop radii

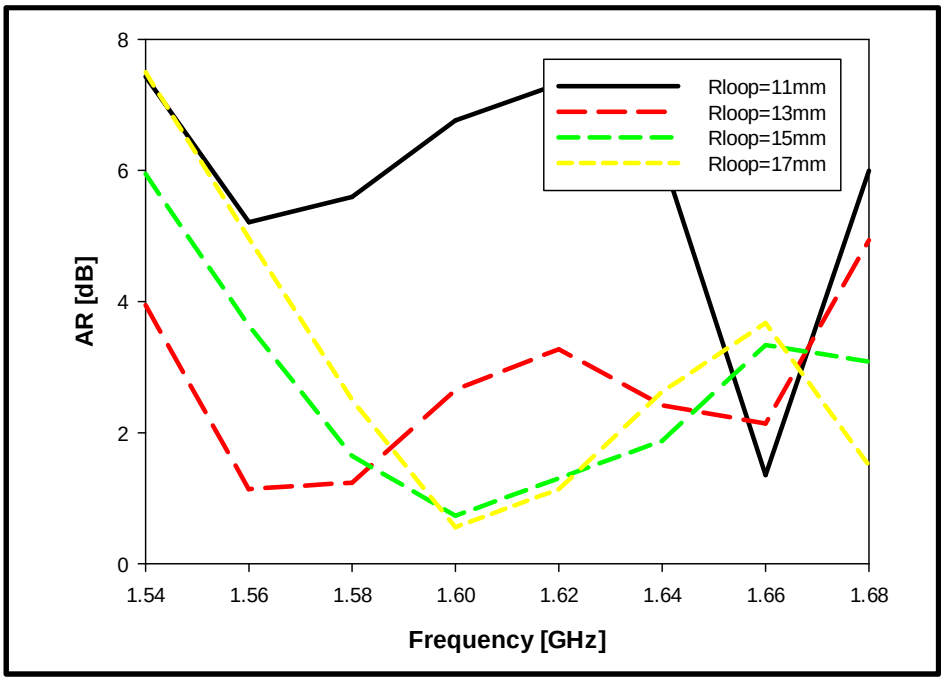

Figure 3.2.15: AR for variable loop radii

It can be noticed from these results that the axial ratio bandwidth varies as a bell shape that change from lower frequency end to an optimum value and then increases, and reduced again towards the high frequency end. The same behaviour can be seen for S_{11} but with less effect since as it is mainly controlled by the feeding stub. These results are illustrated further in Table 3.2.4 and Table 3.2.5.

$R_{loop}[mm]$	$f_2[\mathrm{GHz}]$	$f_1[\mathrm{GHz}]$	$f_{resonance}[\mathrm{GHz}]$	BW [%]
11	1.6671	1.6532	1.66	0.84
13	1.6112	1.5467	1.56	4.13
15	1.6554	1.5664	1.6	5.56
17	1.6472	1.5759	1.6	4.46

Table 3.2.4: S_{11} for various loop radii

$R_{loop}[mm]$	$f_2[\mathrm{GHz}]$	$f_1[\mathrm{GHz}]$	$f_{resonance}[\mathrm{GHz}]$	BW [%]
11	1.7202	1.5583	1.678	9.64
13	1.7194	1.5018	1.6	13.60
15	1.7214	1.4673	1.6	15.88
17	1.7289	1.518	1.6	13.80

Table 3.2.5: AR for various loop radii

On the other hand, the gap between the two layers needs to be set as it controls the mutual coupling between the antenna and the AMC patches. However, since practically, the gap is replaced with rohacell foam sheet of $\varepsilon_r = 1.07$, it has to be an integer number. Therefore, the gap has been varied from $0 - 3\mathrm{mm}$ and the resultant S_{11} and AR curves are presented in Figure 3.2.16 and Figure 3.2.17, respectively.

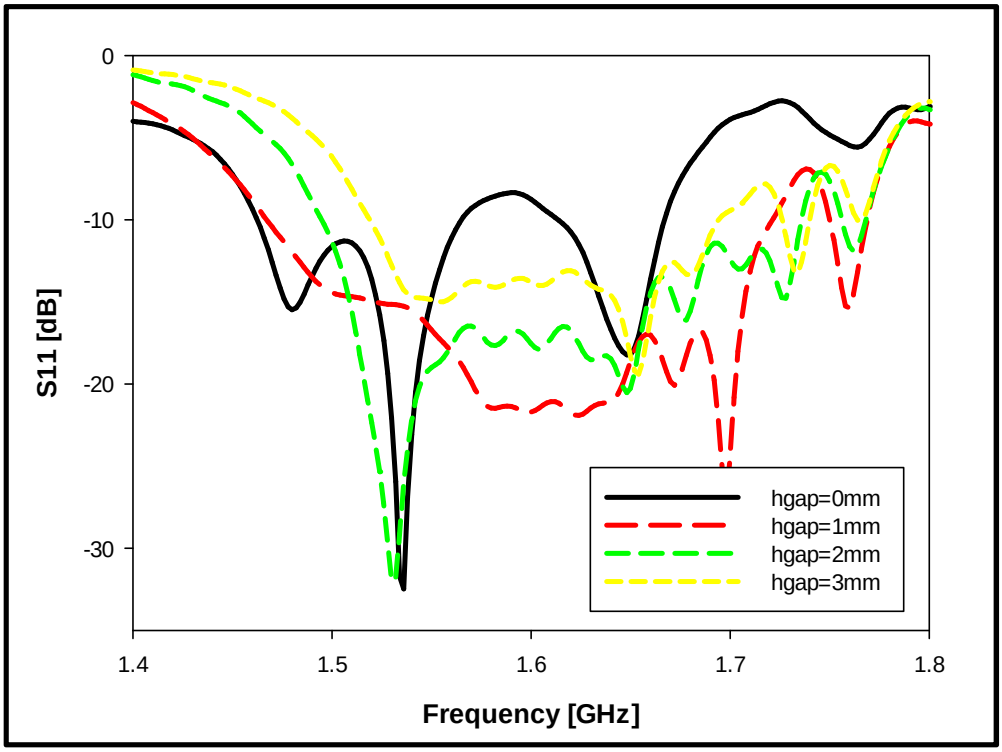

Figure 3.2.16: S_{11} for various gaps between the two layers

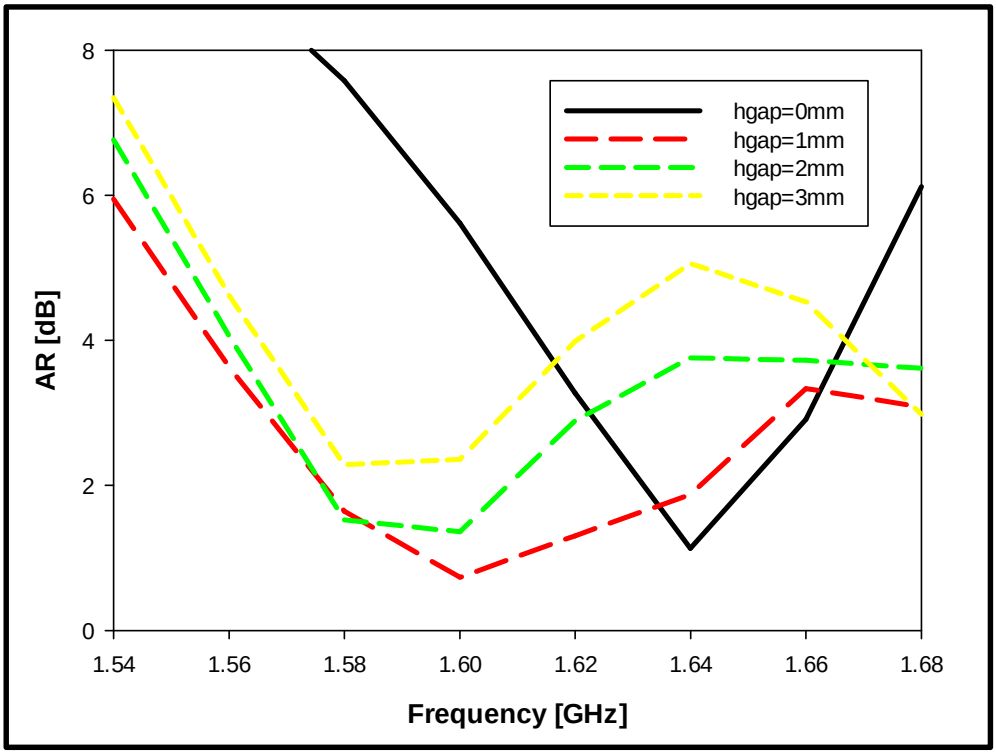

Figure 3.2.17: AR for various gaps between the two layers for a given radius

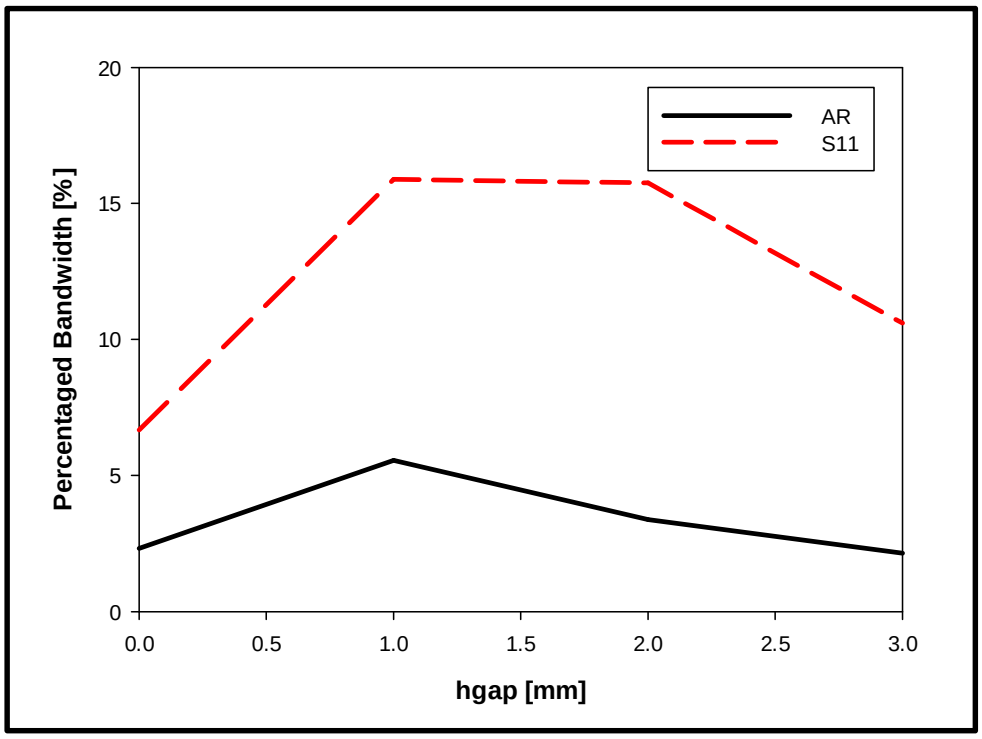

Figure 3.2.18: AR and S_{11} bandwidths for variable h_{gap} values

It can be seen that changing the gap alters the overall results as expected. Again, the S_{11} and AR bandwidths are changing with a bell shape with the worst results for the no-gap case since the mutual coupling is considerably stronger between the two

layers. A tabulated summary can be seen in Table 3.2.6 and Table 3.2.7. It is worth to note that changing the gap has also altered the frequency range from the intended L_1 GPS band.

$h_{gap}[mm]$	f_2[GHz]	f_1[GHz]	$f_{resonance}$[GHz]	BW [%]
0	1.565	1.4625	1.536	6.67
1	1.7214	1.4673	1.6	15.88
2	1.7358	1.4948	1.53	15.75
3	1.6942	1.519	1.654	10.60

Table 3.2.6: S_{11} for various h_{gap} values

$h_{gap}[mm]$	f_2[GHz]	f_1[GHz]	$f_{resonance}$[GHz]	BW [%]
0	1.6606	1.6225	1.64	2.32
1	1.6554	1.5664	1.60	5.56
2	1.6225	1.5684	1.60	3.38
3	1.6079	1.5739	1.58	2.15

Table 3.2.7: AR for various h_{gap} values

There are other parameters that affect the results slightly such as $w_1, l_1,\ x_s$ and y_s. These parameters can be used to fine tune the design to the intended frequency range. The optimum parameters are given in Table 3.2.8.

Parameter	Value [mm]
x_s	90
y_s	58.5
l_1	41.7
l_2	5
l_3	0.8
w_1	11
w_2	4.6
l_w	3.3
R_l	15

Table 3.2.8: Parameter values for the CPW-fed open loop antenna

It should be noted that the gap of the loop is $\sim 16^o$ and therefore, the electrical length of the loop circumference is about $0.47\lambda_o$ or $0.98\lambda_g$. This antenna has been placed on a 4×4 AMC ground plane as demonstrated in Figure 3.2.19.

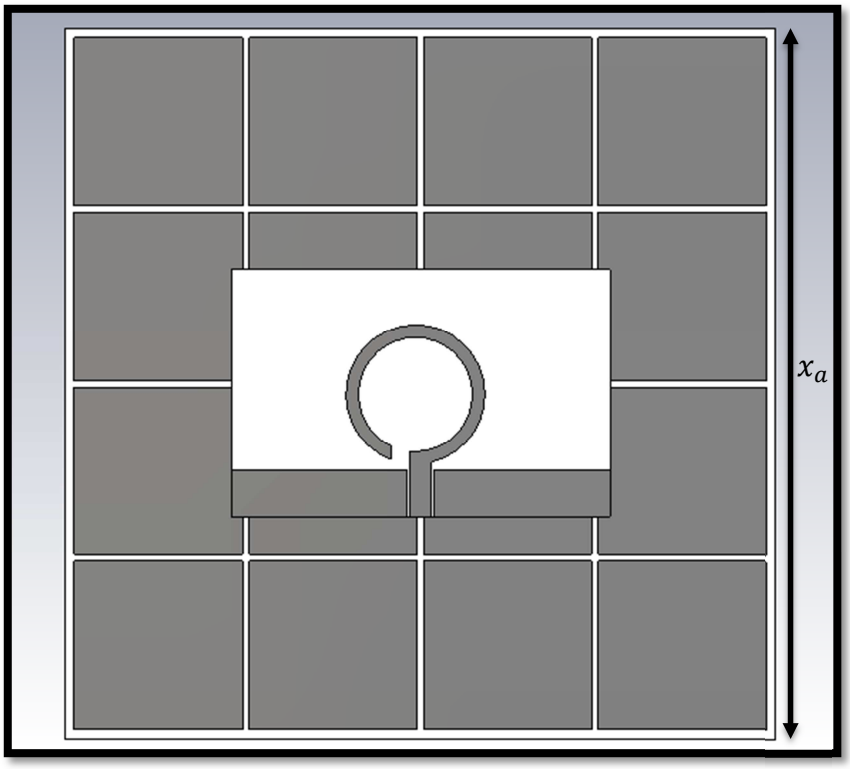

Figure 3.2.19: CPW fed open loop antenna on square patch AMC (Top view)

The optimum gap between the layers has been determined as $h_{gap} = 1\text{mm}$. Therefore, the overall antenna height has been calculated as $h_{tot} = 2.4 + 1 + 1.6 = 5\text{mm}$, which corresponds to a thickness of $\lambda_o/38.2$ as shown in Figure 3.2.20. An overall ground plane size of $x_a = 169\text{mm}$ has been employed, which corresponds to $0.885\lambda_o$.

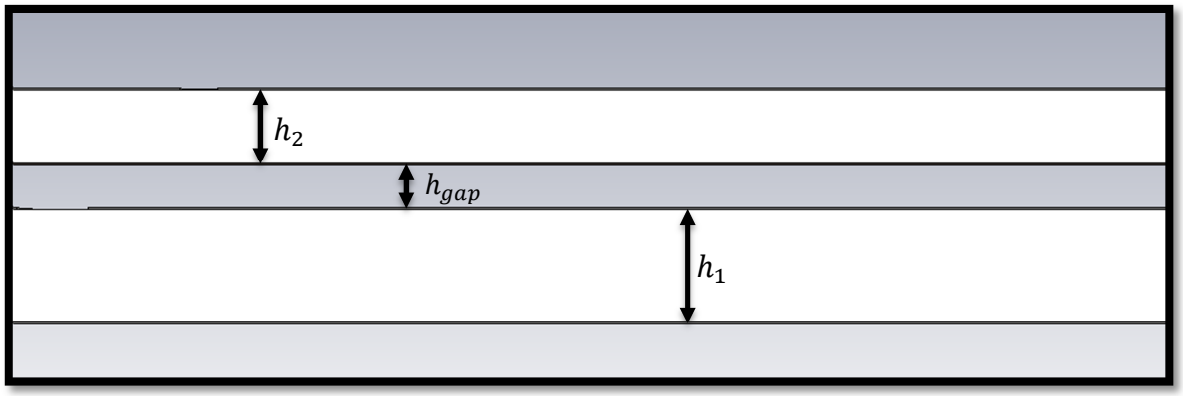

Figure 3.2.20: CPW-fed open loop antenna on square patch AMC (side view)

3.2.3 *Results and Discussion*

A prototype of the designed antenna has been fabricated and measured in the laboratory as shown in Figure 3.2.21 and Figure 3.2.22.

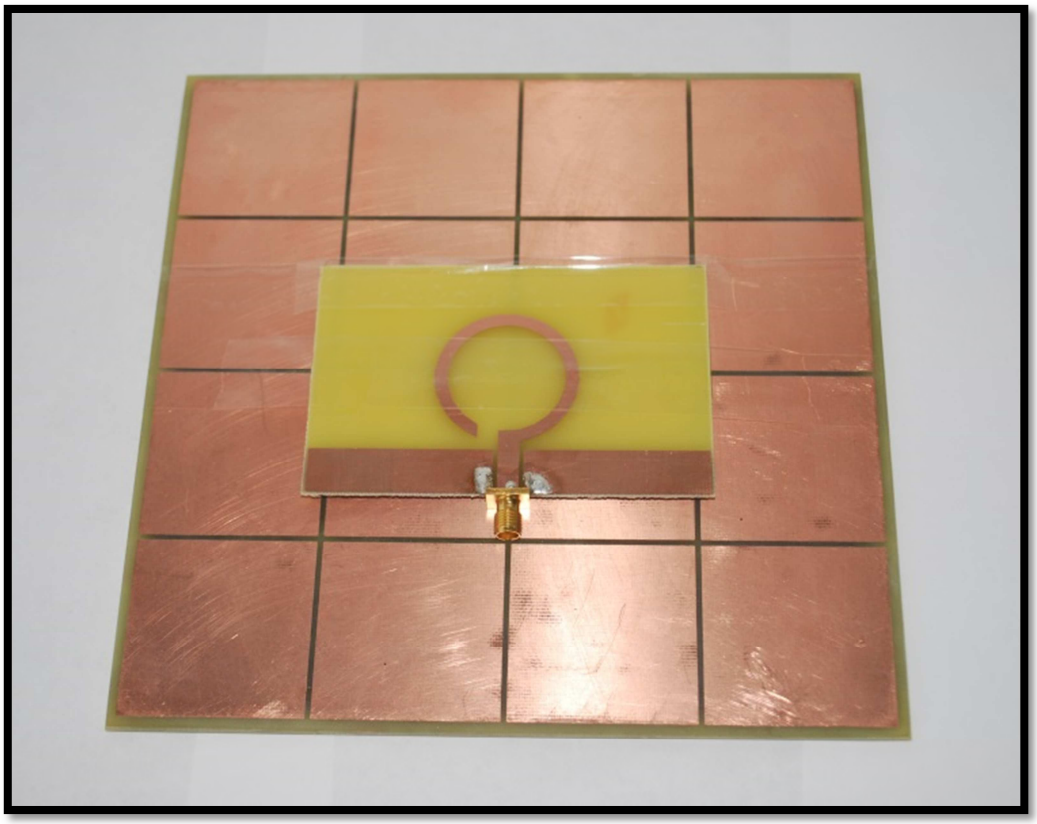

Figure 3.2.21: Fabricated CPW-fed open loop antenna on a square AMC

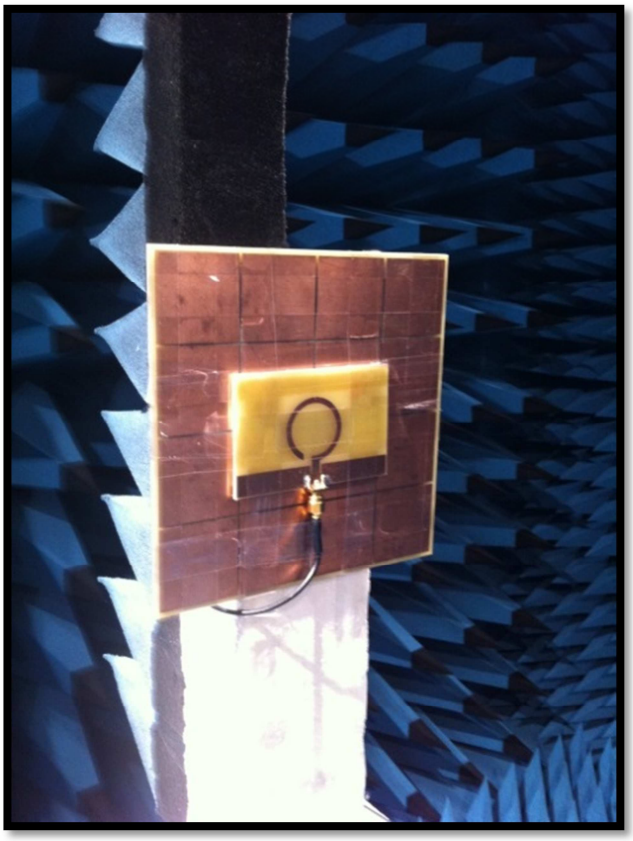

Figure 3.2.22: Fabricated CPW-fed open loop antenna on a square AMC in the anechoic chamber

The simulated and measured reflection coefficients are shown in Figure 3.2.23 with good agreement. The simulated -10dB S_{11} bandwidth range is $1.47 - 1.7\text{GHz}$ cantered at 1.6GHz, which corresponds to 15.9%. On the other hand, the measured bandwidth range is $1.5 - 1.69\text{GHz}$, centered at 1.56GHz, which corresponds to $\sim 12\%$. These results indicate that the antenna is well matched to the source at the desired frequency range.

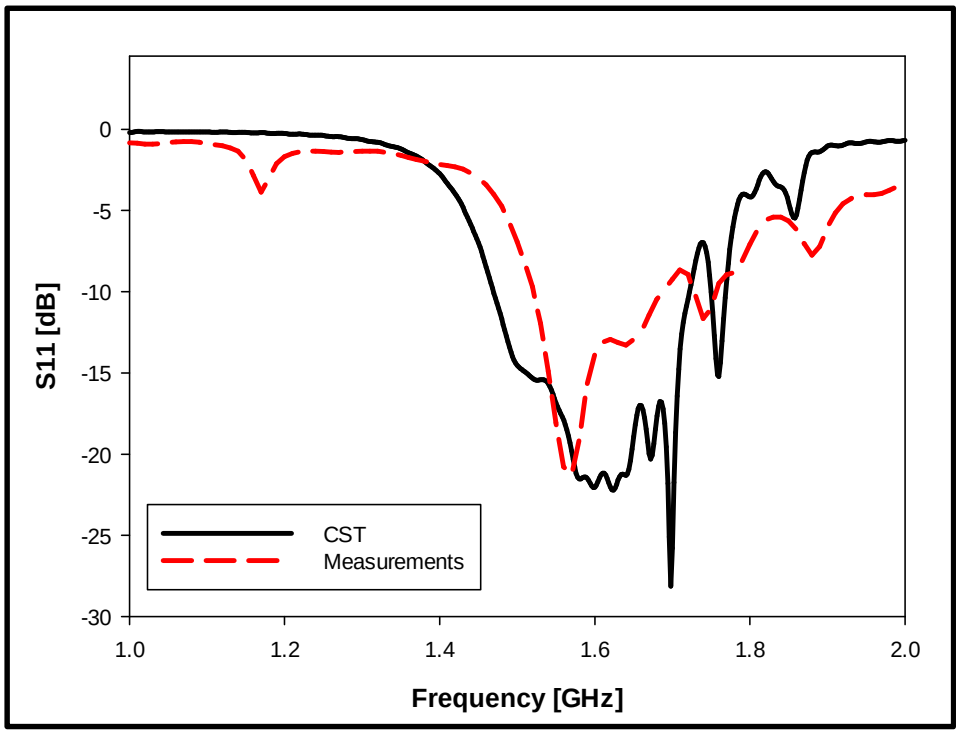

Figure 3.2.23: S_{11} for the CPW-fed open loop antenna on square AMC

A simulated 3dB AR bandwidth of 7.9% has been achieved using l_2 of 7mm. However, due to the unavailability of a large SMA PCB mount connector in the laboratory, the design has been altered slightly and the final value of l_2 has been chosen as 5mm. The simulated and measured AR results agree with each other as illustrated in Figure 3.2.24. Additionally, the simulated 3dB AR bandwidth range is $1.57 - 1.66\text{GHz}$, centred at 1.6GHz, which corresponds to a percentage bandwidth of 5.55%. On the other hand, the measured bandwidth range is $1.57 - 1.66\text{GHz}$, which is centred at 1.58GHz and corresponds to 5.7% with a slight tipping of the 3dB border at the middle.

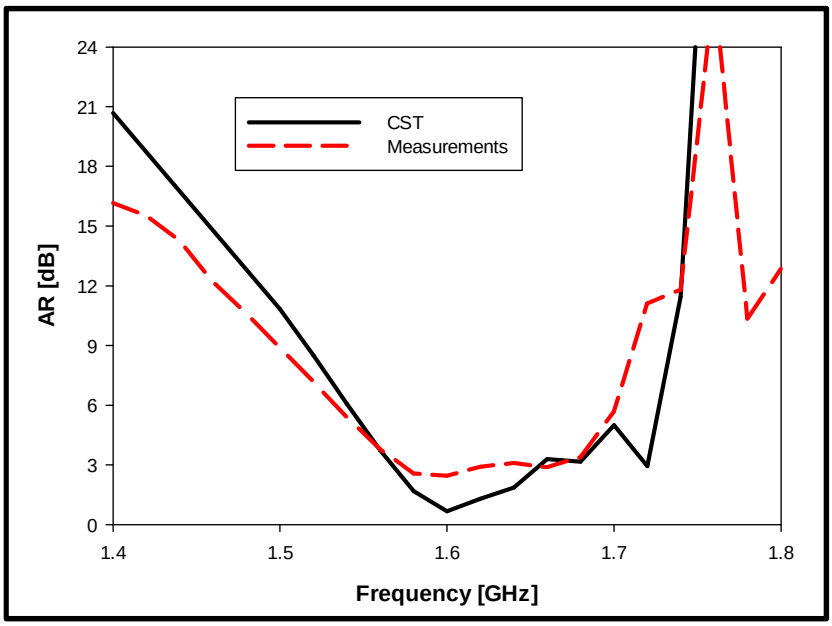

Figure 3.2.24: AR for the CPW-fed open loop antenna on a square AMC

This antenna offers a useful bore-sight gain at the minimum AR point. It can be noticed from Figure 3.2.25 that the CST-simulated gain has been found as ~8dBi. The gain has been cross validated with HFSS, which showed a gain of ~6dBi.

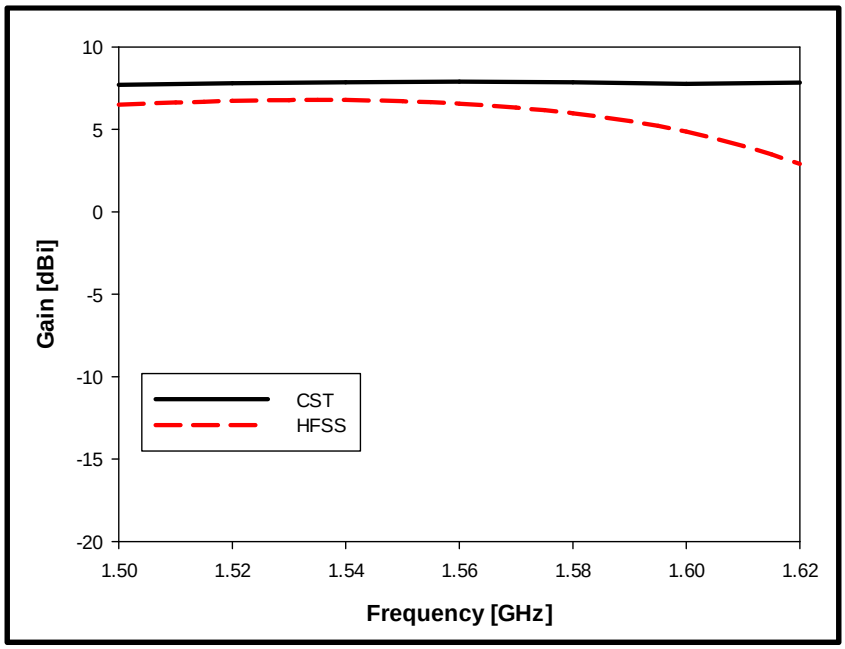

Figure 3.2.25: Gain of the CPW-fed open loop antenna on square AMC

This antenna is Right Handed Circularly Polarized (RHCP). This is because at bore-sight, the E_R is at least 15dB larger than E_L as can be seen in Figure 3.2.26 and Figure 3.2.27.

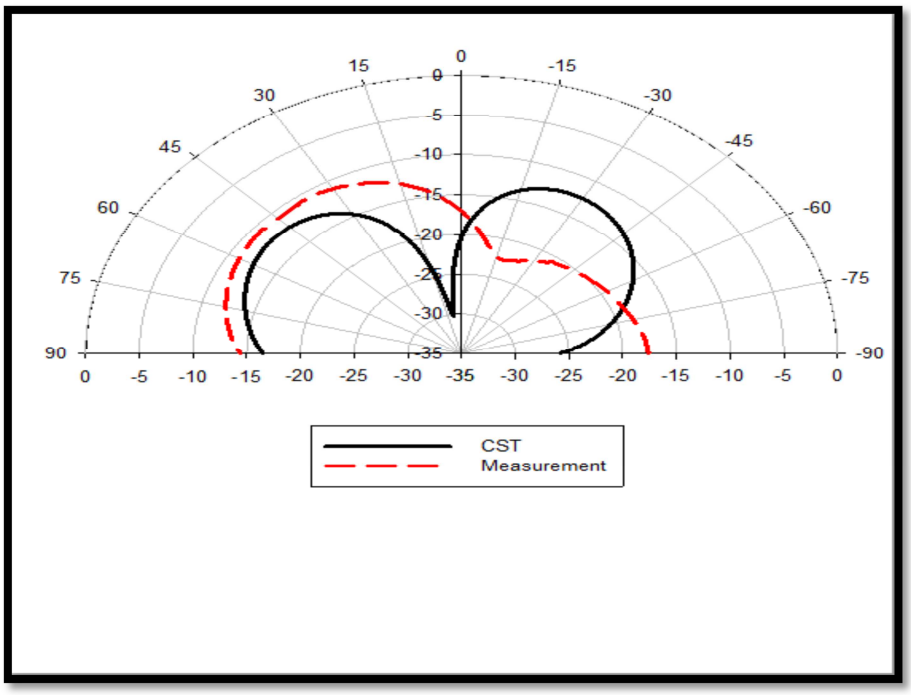

Figure 3.2.26: E_L for the CPW-fed open loop antenna on square AMC

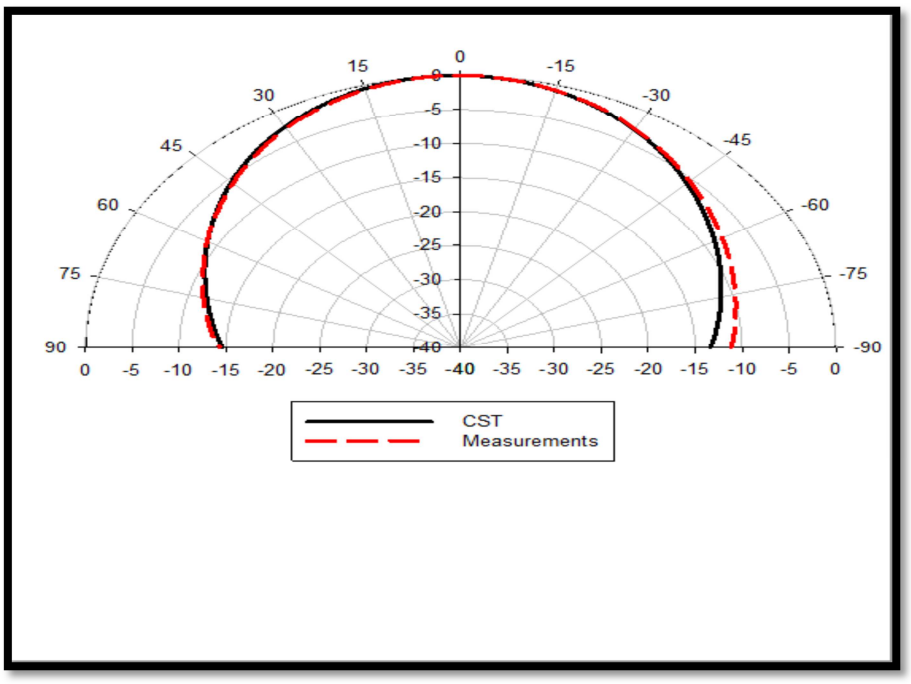

Figure 3.2.27: E_R for the CPW-fed open loop antenna on square AMC

As a summary, this antenna has provided a good axial ratio at the desired frequency range with a good matching and an improved gain. The overall height has been reduced by 80%, that is, from $\lambda_o/21.2$ in [112] to $\lambda_o/38$ as in this design. However, the ground plane size has increased slightly from $0.84\lambda_o$ to $0.88\lambda_o$. As a further step, an effort has been made to change the feeding mechanism to a more robust one, which is the probe feed. This might help in making the antenna as a single block as discussed in the next section.

3.3 Circularly Polarised Open Loop Antenna Fed by a Vertical Probe

3.3.1 *Unit Cell Design Procedures*

Vertical probes are well known as antenna feeding mechanism. In this design, the second dielectric layer, the superstrate, has been attached directly to the AMC to make the antenna more robust as shown in Figure 3.3.1. Therefore, the size of the square patch AMC has to be optimized since the superstrate affects the phase reflection of the AMC. Using the method described earlier for the CPW-fed antenna, a new square patch until cell has been designed as shown in Figure 3.3.2. The optimized values of the parameters are given by $w = 38.4\text{mm}$, $g = 1.9\text{mm}$ and $x = w + g = 40.3\text{mm}$, which corresponds to $\lambda_o\backslash 4.74$. The square patch is printed on a dielectric substrate FR4 of $\varepsilon_r \approx 4.3$ and thickness of $h_1 = 2.4\text{mm}$.

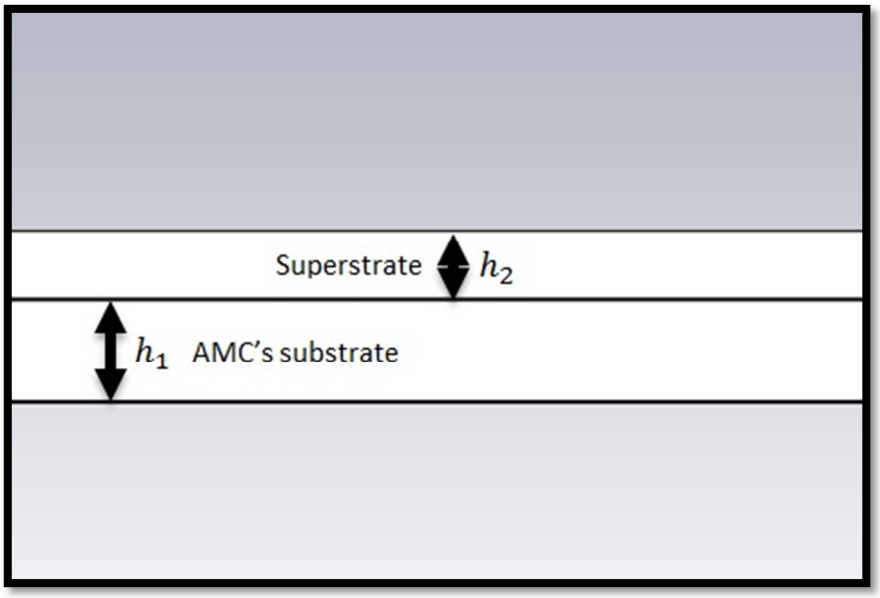

Figure 3.3.1: Side view of the proposed probe-fed antenna

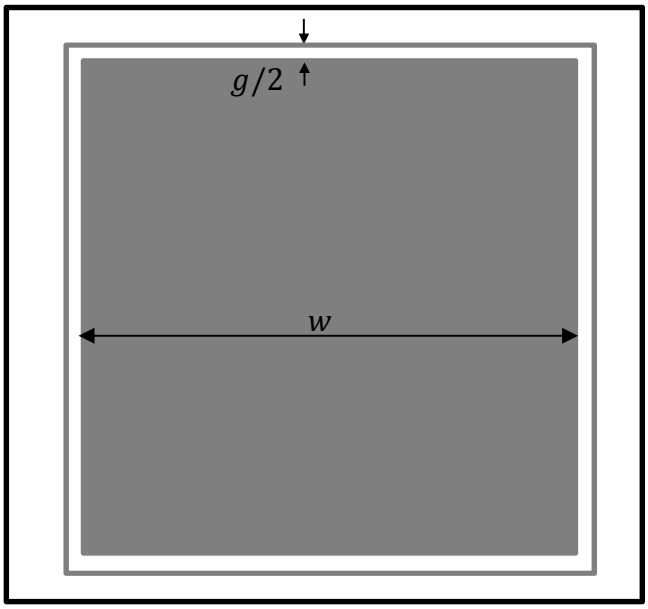

Figure 3.3.2: Unit cell for the probe fed open loop antenna backed by square patch AMC

The reflection phase of the unit cell is presented in Figure 3.3.3.

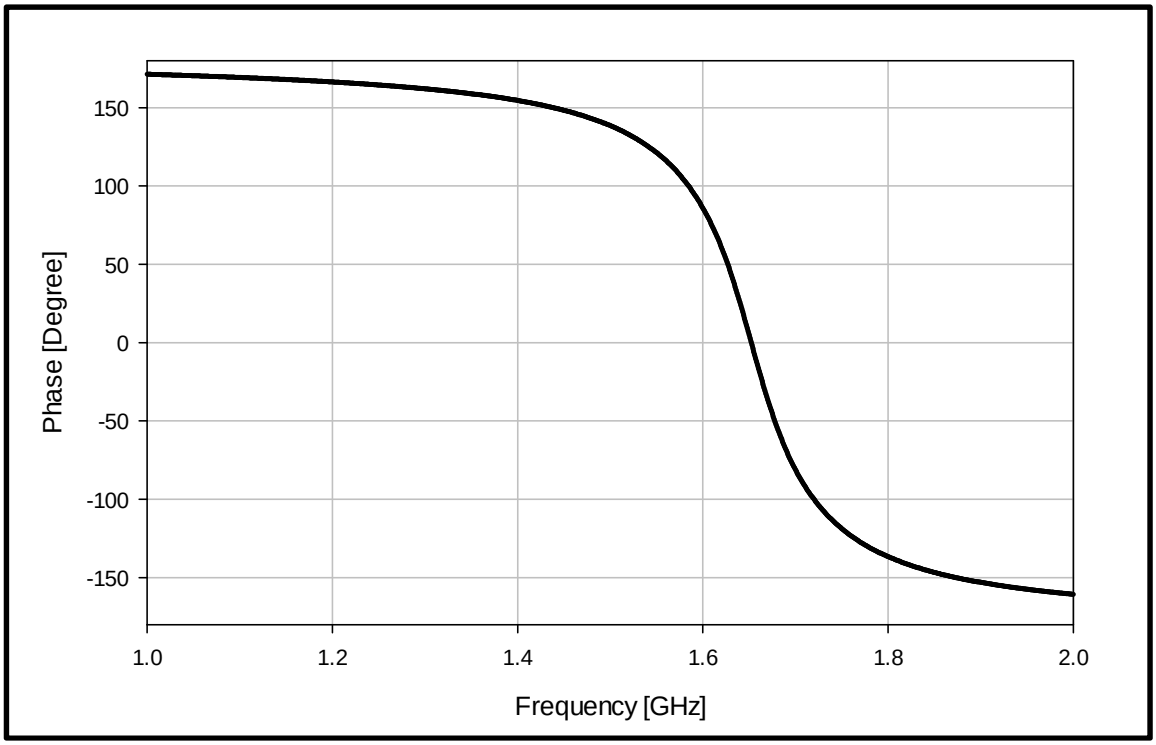

Figure 3.3.3: Reflection phase for the unit cell of a probe fed open loop antenna backed by square AMC

For this unit cell, the 0 ± 90^{o} bandwidth range is $1.6 - 1.7\text{GHz}$ centred at 1.65GHz with a percentage bandwidth of 6.8%. There are few references, which state that the desired reflection phase for low profile antennas is 90 ± 45^{o} [37]. Therefore the

90 ± 45^o bandwidth of the unit cell has been calculated as $1.5 - 1.63\text{GHz}$ centred at 1.6GHz with a percentage bandwidth of 7.3%.

3.3.2 *Open Loop Antenna Design*

An open loop antenna has been printed on an FR4 substrate with $\varepsilon_r \approx 4.3$ and thickness h_2. The schematic of the open loop is given in Figure 3.3.4.

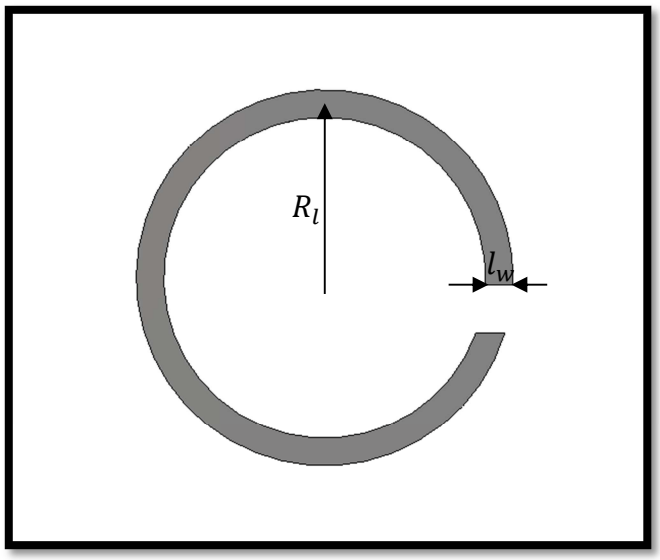

Figure 3.3.4: The dimensions of the probe-fed open loop antenna

The same procedures used earlier to design an open loop antenna have been repeated here. First, the loop size has been selected so that the circumference is approximately one wavelength. Then, it has been optimized to improve the results. The loop width, l_w, has been chosen as $l_w = 4R_p$, where R_p is the radius of the feeding probe as discussed in [96]. The radius of the loop has been selected as $R_l = 16.5\text{mm}$. The optimized gap width is 16^o. Therefore, the loop circumference has been calculated as $0.52\lambda_o$ or $1.07\lambda_g$. The radius of the feeding probe has been selected as $R_p = 0.65\text{mm}$ since such a radius is available in the laboratory and can be placed in the gap between the patches without the need of further modifications. Then, the superstrate has been placed on top of the AMC substrate. The optimum thickness for the superstrate has been found as $h_2 = 1.6\text{mm}$. Therefore, the overall thickness has been calculated as $h_{tot} = 4\text{mm}$, which corresponds to $\lambda_o/47.8$, i.e. it is 125% thinner than the one in [112] and 25% thinner than the antenna designed in section 3.2, which was $\lambda_o/38.2$. The antenna has been placed on a 4×4 square patch AMC layer as illustrated in Figure 3.3.5, where the ground plane size has been

found as $x_l = 168.6\text{mm}$, which corresponds to $0.88\lambda_o$. It should be mentioned that superstrate is hidden in Figure 3.3.5 for a clearer view of the antenna.

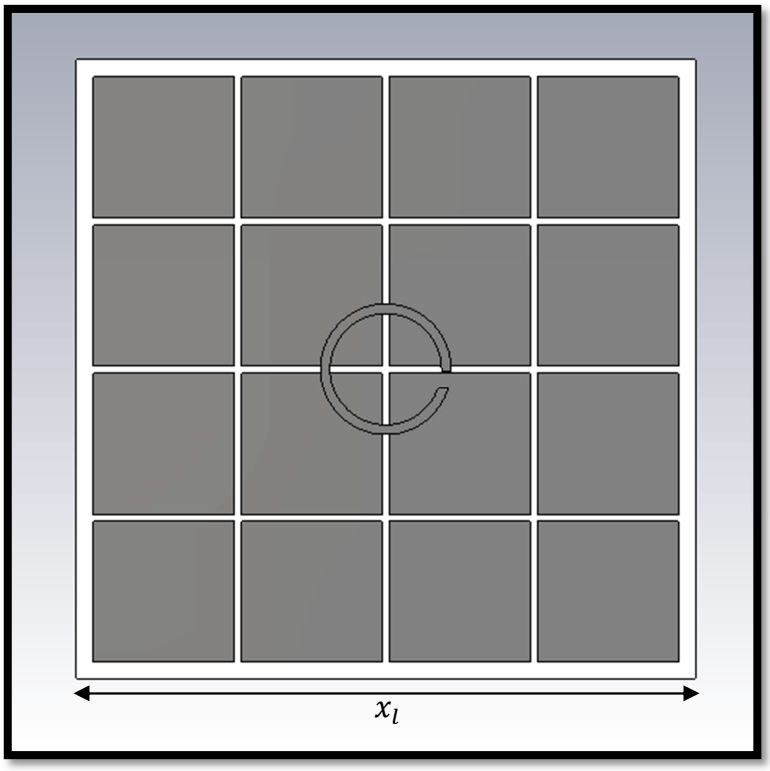

Figure 3.3.5: Probe-fed open loop antenna backed by square patch AMC

3.3.3 *Results and Discussion*

A prototype has been fabricated and measured as shown in Figure 3.3.6.

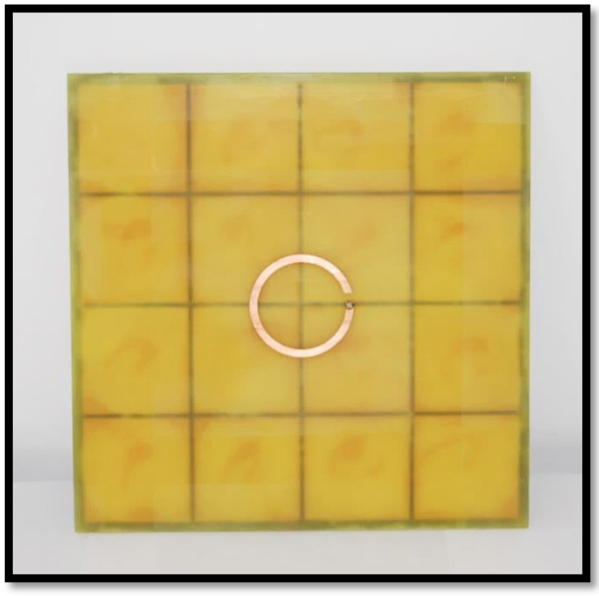

Figure 3.3.6: Prototype of the probe-fed open loop antenna backed by a square patch

First, A comparison of the reflection coefficient and the axial ratio for the same structure, with and without AMC are illustrated in Figure 3.3.7 and Figure 3.3.8, where it can be seen clearly that introducing AMC enhanced the matching and provided axial ratio less than 3dB.

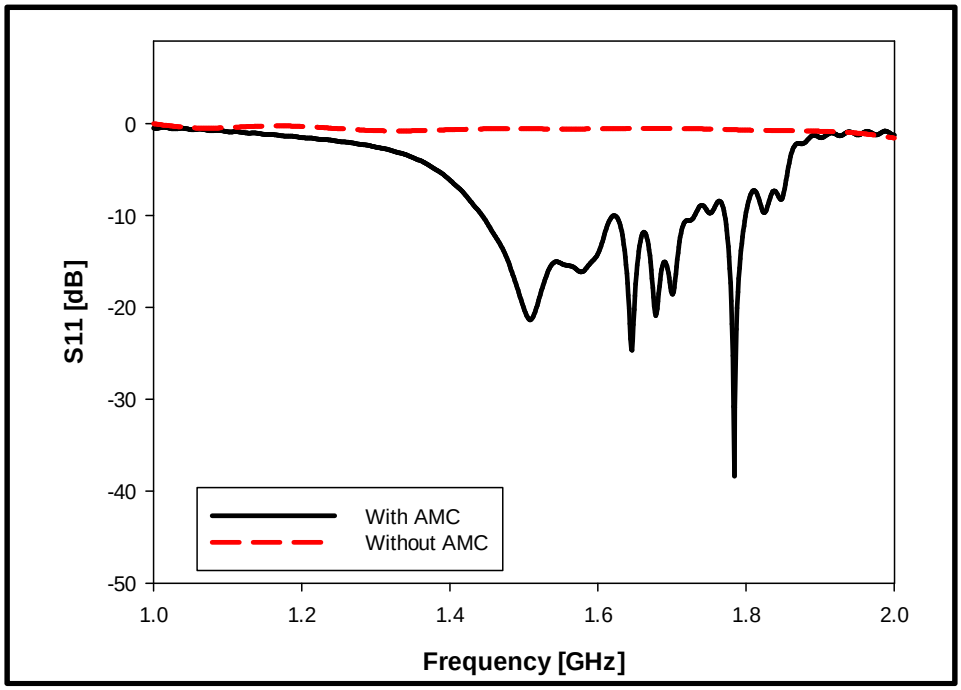

Figure 3.3.7: Reflection coefficient of the probe-fed antenna, with and without AMC

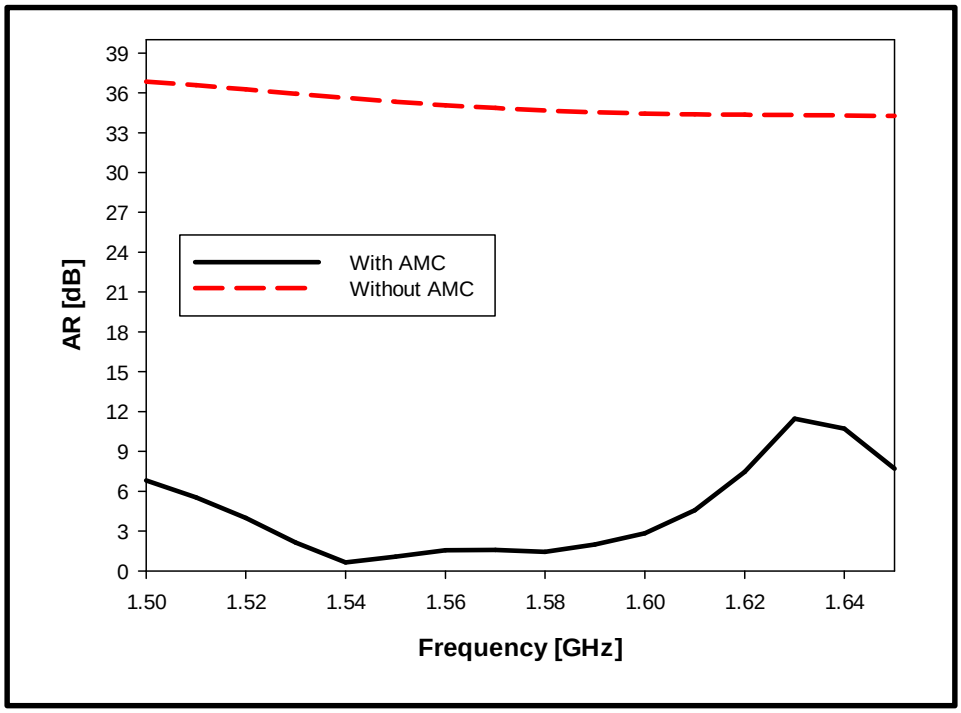

Figure 3.3.8: Axial ratio of the probe-fed antenna, with and without AMC

The simulated and measured reflection coefficient S_{11} is shown in Figure 3.3.9. The simulated -10dB bandwidth range is $1.44 - 1.73\text{GHz}$ and centred at 1.5GHz with a bandwidth of 19%. On the other hand, the measured S_{11} bandwidth range extends from 1.44 to 1.76GHz and centred at 1.54GHz with a percentage bandwidth of 20.6%. The axial ratio of antenna is presented in Figure 3.3.10, with a 3dB bandwidth of 4.9% compared to a measured bandwidth of 4.54%.

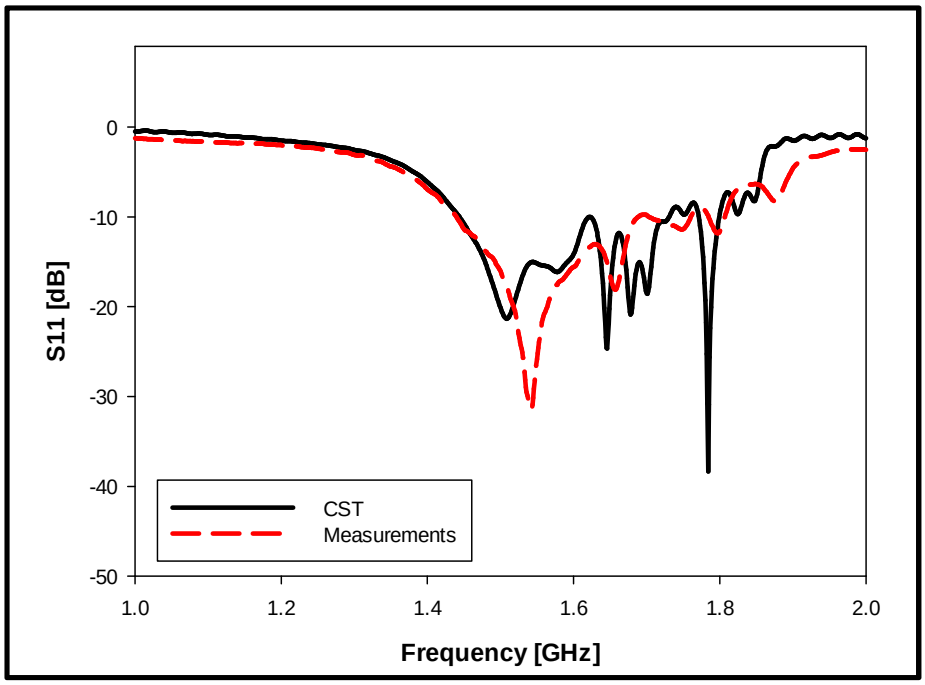

Figure 3.3.9: S_{11} for the probe-fed open loop antenna backed by square AMC

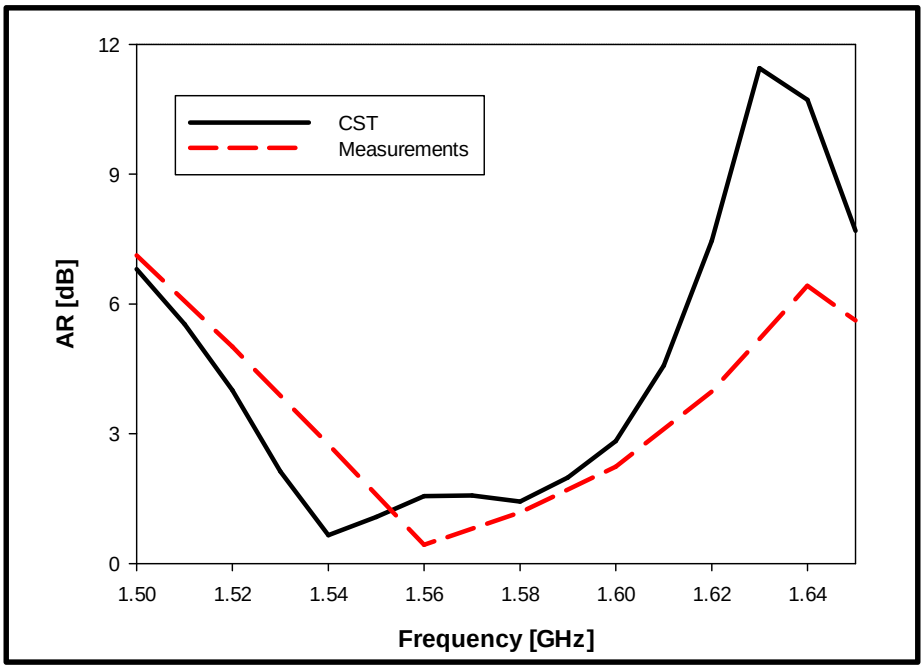

Figure 3.3.10: AR for the probe-fed open loop antenna backed by square AMC

The beamwidth of the antenna has been found and it is given in Figure 3.3.11, where it can be a seen a close agreement between the simulated and the measured results. The 3dB bandwidth is for an angle of $\sim 25^{o}$.

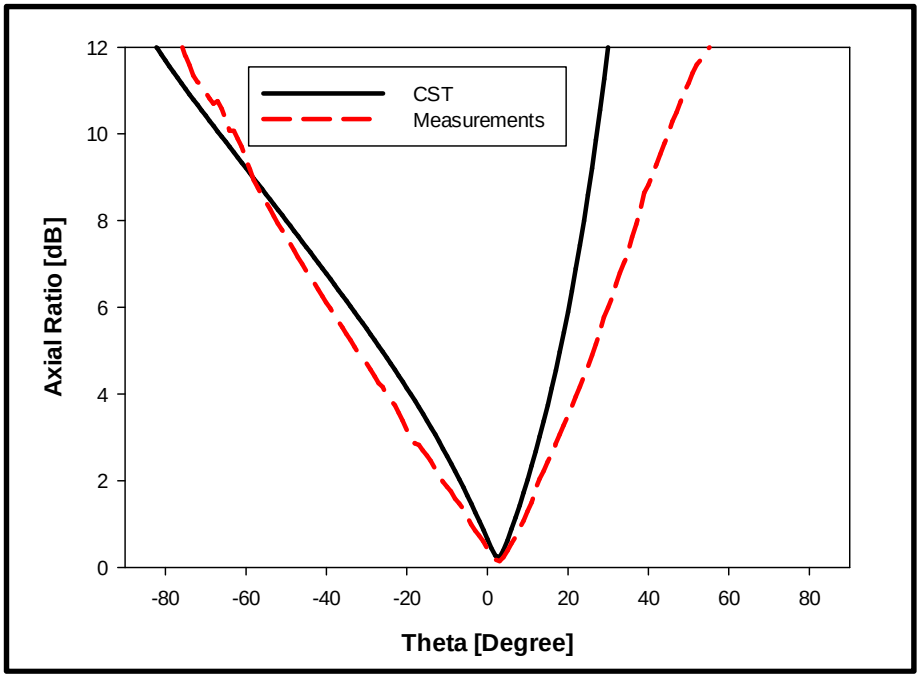

Figure 3.3.11: Beamwidth for the probe-fed open loop antenna backed by square AMC

This antenna provides useful gain as shown in Figure 3.3.12. The CST simulated gain at the minimum AR is about 5dBi. However, the gain from HFSS is ~1.5dBi.

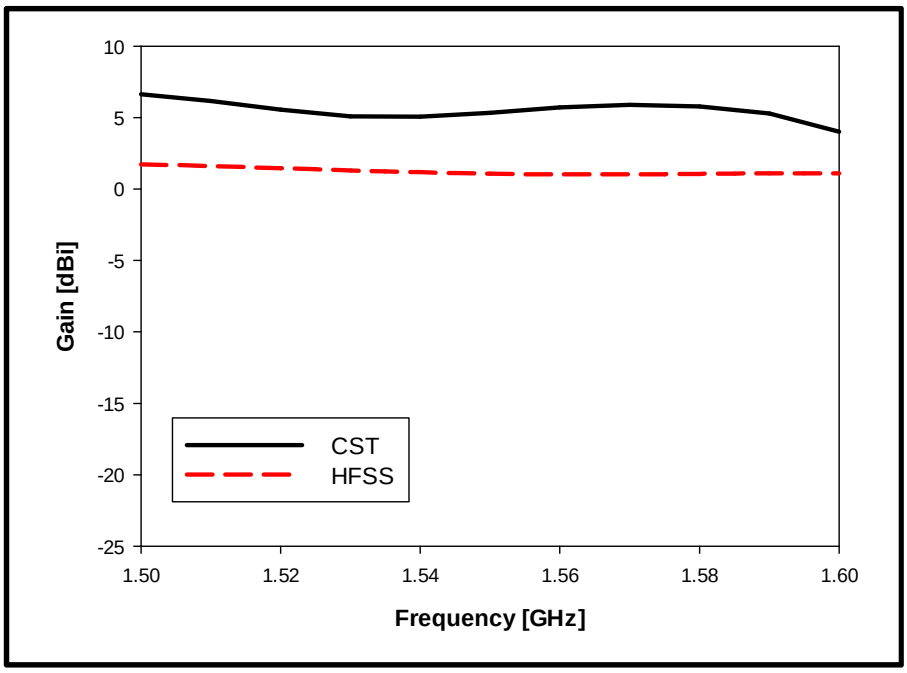

Figure 3.3.12: Gain of the probe-fed open loop antenna backed by square AMC

The antenna is Right Handed Circularly Polarised, since E_R is greater than E_L by ~30dB at bore-sight as can be seen in Figure 3.3.13 and Figure 3.3.14.

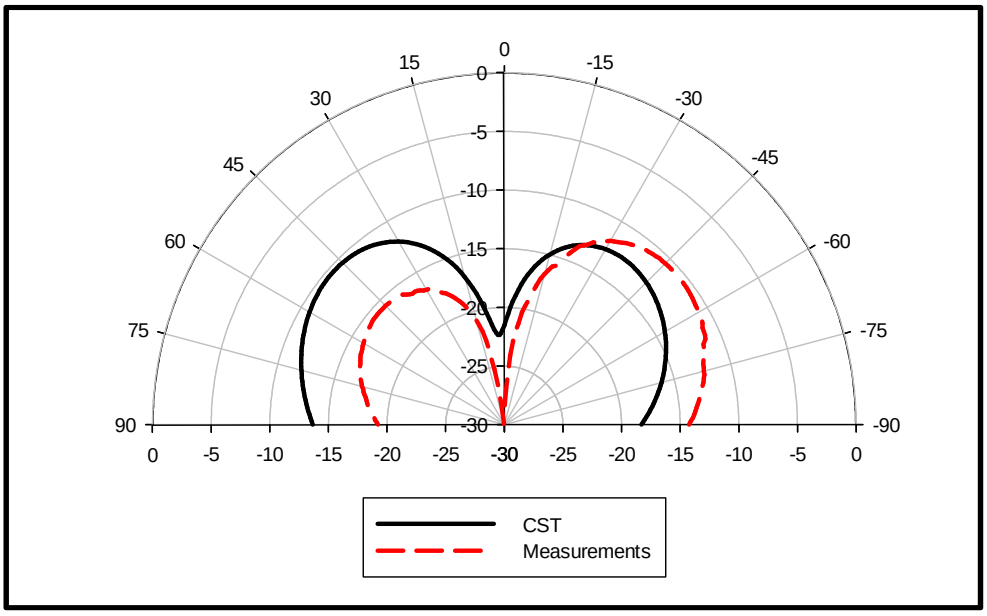

Figure 3.3.13: E_L of the probe-fed open loop antenna backed by square AMC

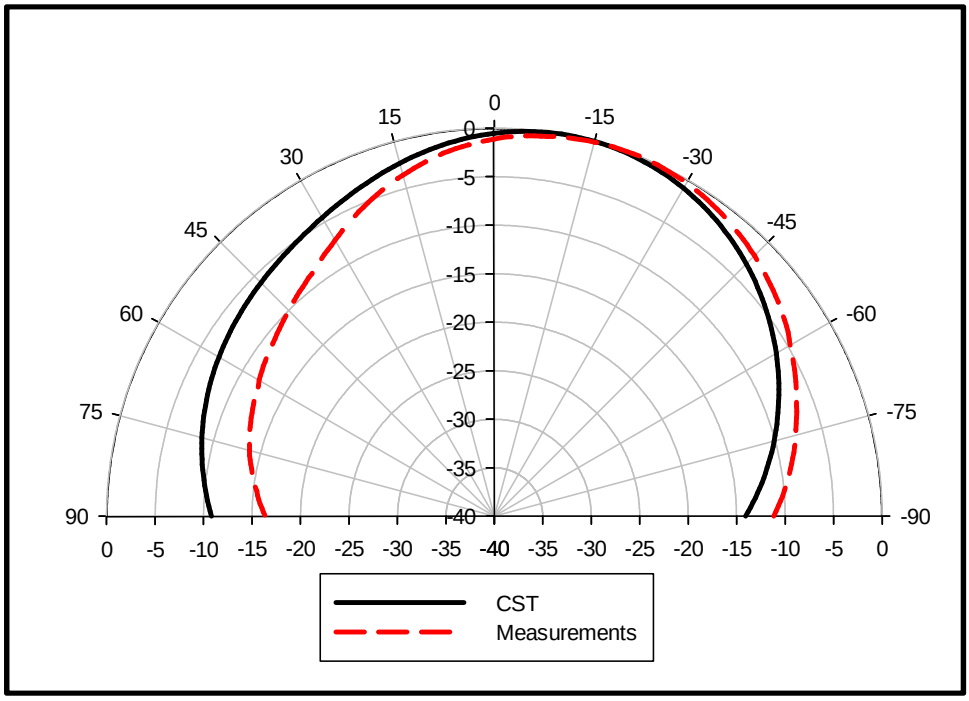

Figure 3.3.14: E_R of the probe-fed open loop antenna backed by square AMC

This antenna has provided CP radiation throughout the GPS L_1 bandwidth with good matching and useful gain. The main improvement in this design in lowering the thickness to $\lambda_o/47.8$. However, the ground plane size is still $0.88\lambda_o$. An effort has made to decrease the size of the ground plane with the same AMC. The AMC grid

has been changed to be 3×4 with a rotation of the antenna as shown in Figure 3.3.15. The overall height of this antenna is still 4mm but the size of the ground plane has changed to be $x_l = 168.6\text{mm}$ and $y_l = 128.3\text{mm}$.

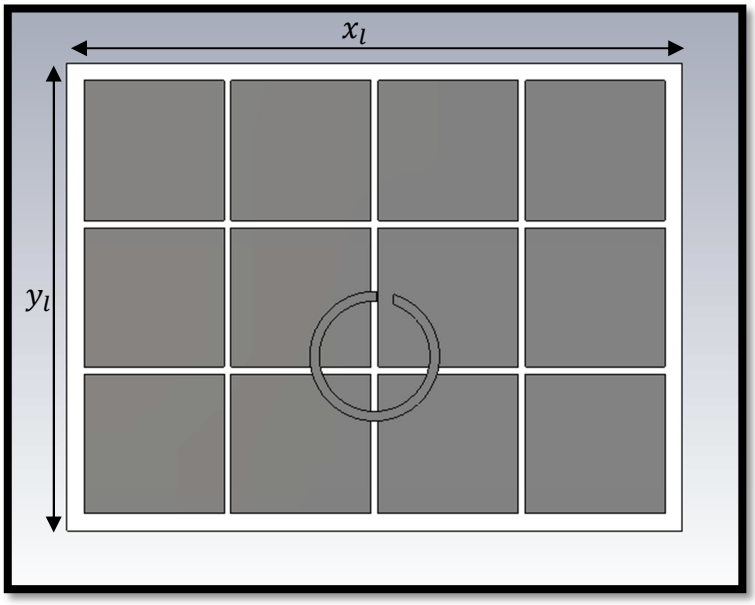

Figure 3.3.15: Reduced size probe-fed open loop antenna backed by square patch AMC

The reflection coefficient is given in Figure 3.3.16, where the -10dB simulated bandwidth has been calculated as 15.63%. The axial ratio of the antenna is shown in Figure 3.3.17, where a 3dB bandwidth of 2.5% has been achieved.

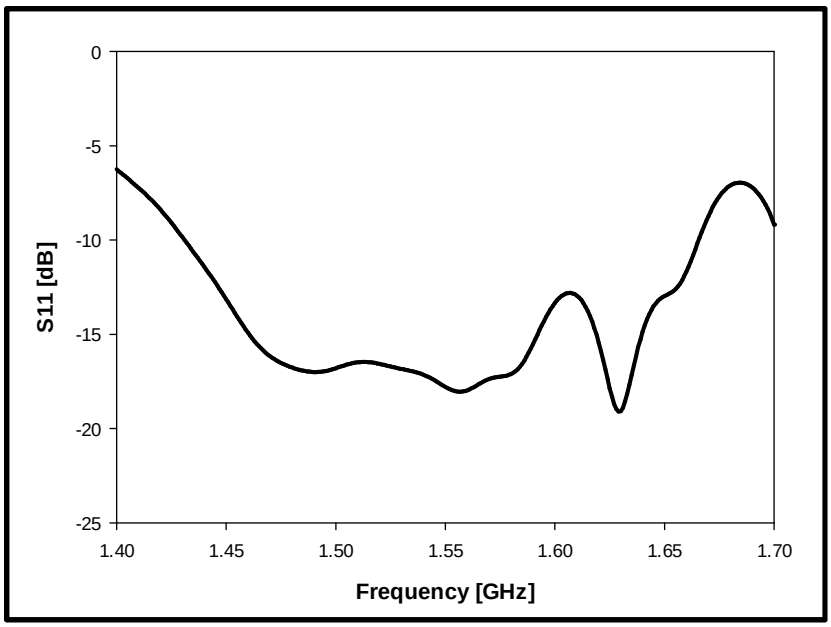

Figure 3.3.16: S_{11} for the reduced size probe-fed open loop antenna backed by square patch AMC

It can be seen that the frequency range is not at the desired L_1 GPS frequency range and the axial ratio is close to 3dB, which means it is difficult to be measured. Therefore, it has been decided to design a novel AMC with reduced size.

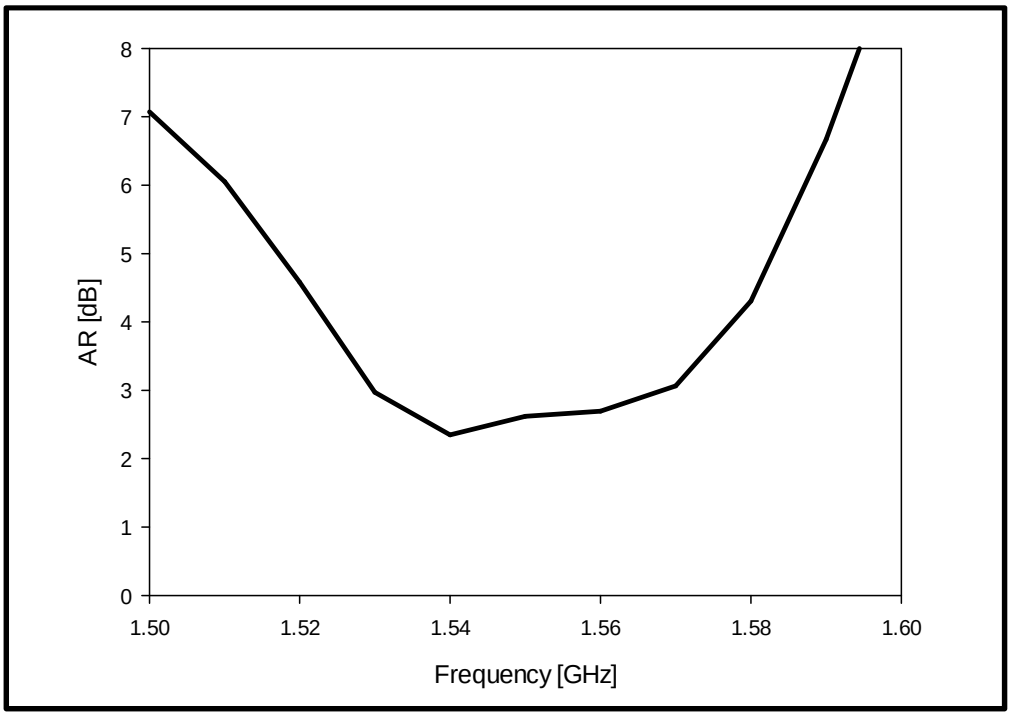

Figure 3.3.17: AR for the reduced size probe-fed open loop antenna backed by square patch AMC

A summary of the designed antennas in this chapter is given in Table 3.3.1.

	Unit Cell -90° to 90°	Antenna Parameters	S_{11}	AR	Gain
CPW-Fed open loop antenna backed by square AMC	1.5168-1.6193 @ 1.5681 (6.54%)	Htotal=2.4+1+1.6=5mm (λo/38) Xtotal=169mm (0.88λo) Rloop=15mm Circumference=0.98λg, Xsupersrate=90mm, ysuperstrate=58.5mm	Sim: 1.4684-1.7224 @1.6 (15.88%) Meas: 1.52144-1.68746 @ 1.56 (10.64%)	Sim: 1.5672-1.656 @ 1.6 (5.6%) Meas: 1.57362-1.66352 @ 1.58 (5.69%)	Sim: 8dBi Meas: 10dBi Antenna: RHCP
Probe-fed open loop antenna backed by square AMC	1.596-1.7085 @ 1.6523 (6.8%)	Htotal=2.4+1.6=4mm (λo/48) (125% thinner than reported reference) Xtotal=168.6mm (0.88λo) Rloop=16.5mm Circumference=1.07λg, Loop width=2.6mm	Sim: 1.4438-1.7305 @1.5075 (19%) Meas: 1.44076-1.75879 @ 1.54339 (20.6%)	Sim: 1.5254-1.601 @ 1.54 (4.9%) Meas: 1.53761-1.60841 @ 1.56 (4.54%)	Sim: 5dBi Meas: 8dBi Antenna: RHCP

Table 3.3.1: Summary of designs in Chapter 3

3.4 Conclusion

In conclusion, two circularly polarised antenna, backed by square patch AMC have been designed, fabricated and measured. The first one is fed by a Co-Planar Waveguide (CPW) and the second is fed using a vertical probe. For the first design, the antenna achieved axial ratio of 5.6% bandwidth in conjunction with a good matching and a useful gain. The overall height is 80% thinner than that report in [112]. However, The ground plane size has increased slightly from $0.84\lambda_o$ to $0.88\lambda_o$. For the second design, an axial ratio of 4.5% has been measured with a good matching and gain. The main improvement in this design in lowering the thickness to $\lambda_o/47.8$ and became more robust. However, it was not possible to reduce the ground plane size further. Therefore, it has been decided to design a new AMC to decrease the size of the ground plane, which is discussed in next chapter.

CHAPTER 4

Circularly Polarized Antenna backed by A Novel Artificial Magnetic Conductor (AMC) Ground Plane

4.1 Introduction

In this chapter, a novel AMC is proposed that can be used as a ground plane for a circularly polarised open loop antenna. The aim is to reduce the ground plane size for the antenna designed in the previous chapter with the same, or a reduced, thickness. In the AMC design, there are three main parameters to be considered; the dielectric permittivity, the unit cell's width, and the substrate's thickness. The permittivity is inversely proportional to the bandwidth of operation. Therefore, it shouldn't be considerably high in order to maintain a useful operation bandwidth. Additionally, higher permittivity increases the cost and fabrication complexity. As mentioned earlier, the width and thickness contribute to the inductance and capacitance of the HIS. A designer may have a considerably thin AMC substrate in conjunction with a wide unit cell. Alternately, a smaller unit cell may be used with a thicker AMC substrate. As a result, a trade-off needs to be considered between the size and the thickness depending on the application. There are numerous unit cells' designs without reactive components that have been reported in the literature as summarised in Table 4.1.1.

No	ε_r	h	w	Reference
1	2.2	$\lambda_o/21.4$	$\lambda_o/6.12$	[109]
2	10.4	$\lambda_o/18.75$	$\lambda_o/9.04$	[43]
3	2.98	$\lambda_o/7.5$	$\lambda_o/1.46$	[50]
4	13	$\lambda_o/65$	$\lambda_o/6.44$	[50]
5	36	$\lambda_o/37.4$	$\lambda_o/8.00$	[50]
6	6.15	$\lambda_o/38.7$	$\lambda_o/8.9$	[49]
7	3.28	$\lambda_o/67.87$	$\lambda_o/4.49$	[47]
8	2.2	$\lambda_o/14.7$	$\lambda_o/6.07$	[39]
9	11.9	$\lambda_o/16.6$	$\lambda_o/33.3$	[113]
10	4.4	$\lambda_o/79.6$	$\lambda_o/4.74$	Chapter 3

Table 4.1.1: Summary of various AMC cells reported in the literature

From these data, it can be seen that, the thickness of the AMC substrate designed in Chapter 3 is smaller than those reported in the literature. On the other hand, there are designs with smaller unit cells but with a significantly higher dielectric permittivity, which affects the operational bandwidth. One of the objectives of this chapter is to investigate the effect of symmetrical and asymmetrical AMC unit cells' shapes on the performance of circularly polarised antennas. Once more, an FR4 substrate has been considered with a relative permittivity of $\varepsilon_r \approx 4.3$.

In order to introduce flexibility in the design process, a larger number of design parameters is needed. For instance, introducing squares and rectangles is a known approach to increase the variables in the AMC design. These can provide alternative capacitance and inductance so that the same performance can be achieved with a smaller, or thinner, unit cell size compared to the planar square patch AMC. Two novel AMC unit cells are presented: The first is asymmetrical and the second is symmetrical. Both of them will be used along with a circularly polarised open loop antenna.

4.2 Circularly Polarized Open Loop Antenna, Fed by a Co-Planar Waveguide, backed by a Novel Asymmetrical AMC

4.2.1 *Unit Cell Design Procedures*

Based on the design criteria illustrated in the previous section, a novel asymmetrical AMC until cell has been designed. This facilitates the investigation of the symmetry effects on the radiation properties. A top view of the unit cell is shown in Figure 4.2.1. It has been designed to operate at the L_1 GPS frequency band. The design consists of two hollow rectangles separated by a rectangular strip. There are some parameters, which can be used to alter the frequency range widely and there are others that can be used for fine tuning of the final design.

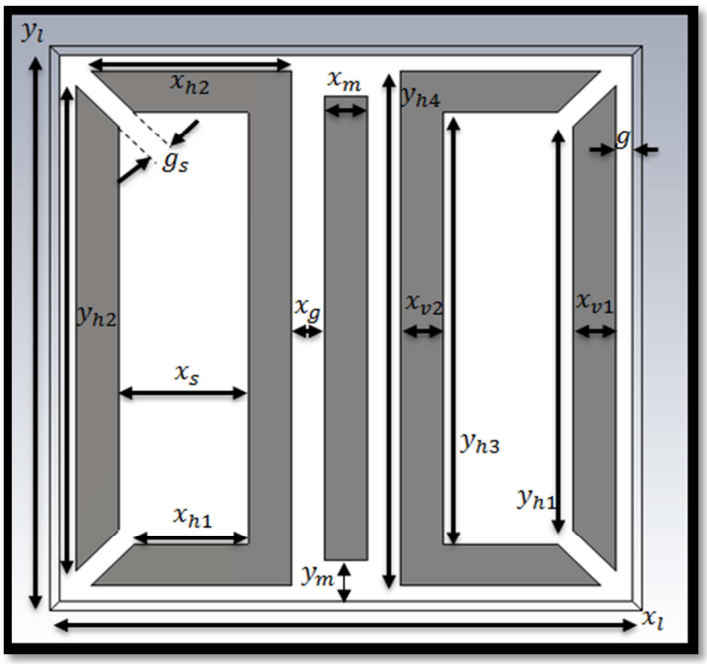

Figure 4.2.1: Asymmetrical unit cell design

Each hollow rectangle has an important two side gaps g_s that can alter the 0°-phase to the required frequency considerably as can be seen in Figure 4.2.2. For example, when $g_s = 0$, the system has a particular capacitance and inductance and the 0°-phase is obtained at 1.69GHz with a $\pm 90^o$ bandwidth of 13.6%. The variation of the gap g_s results in changing the capacitance and the frequency point of the 0°-phase is changed to 1.42GHz with a lower bandwidth of 6.5%. Further increment in the gap reduces the capacitance, which results in shifting the 0°-phase to a higher frequency since the resonance frequency is inversely proportional to the capacitance.

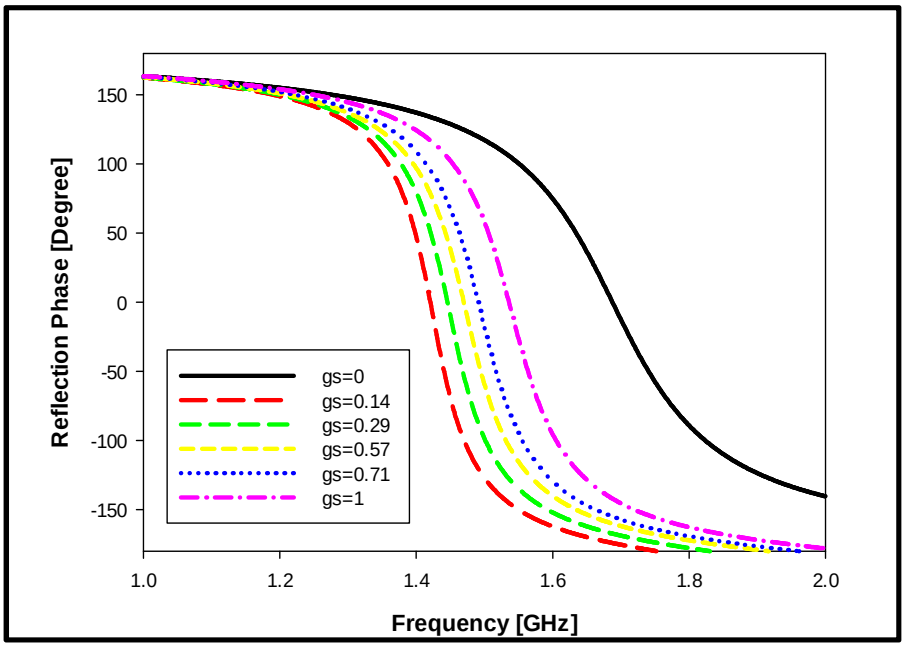

Figure 4.2.2: Reflection phase for different g_s values

The effects of other key parameters such as y_m and x_s have been investigated as can be seen in Figure 4.2.3 and Figure 4.2.4 respectively. When $y_m = 0$, the middle strip is connected to the middle strip of the adjacent cells and therefore, the 0°-phase is obtained at 1.76GHz. However, when y_m exceeds 0, capacitance starts to build between the strips of the adjacent cell, which results in altering the 0°-phase frequency point to 1.45GHz. Then, as the y_m is increased, the capacitance is decreased, which results in a higher resonance frequency. On the other hand, increasing x_s provides a lower resonance frequency. For instance, changing x_s from 4mm to 10mm can shift the frequency from 1.59GHz to 1.32GHz. The thickness of the substrate is the major inductance contributor in the structure. As illustrated in

Figure 4.2.5, when the thickness is increased from 2.4 to $5.6\,\mathrm{mm}$, the resonance frequency is reduced in conjunction with an increment in the bandwidth.

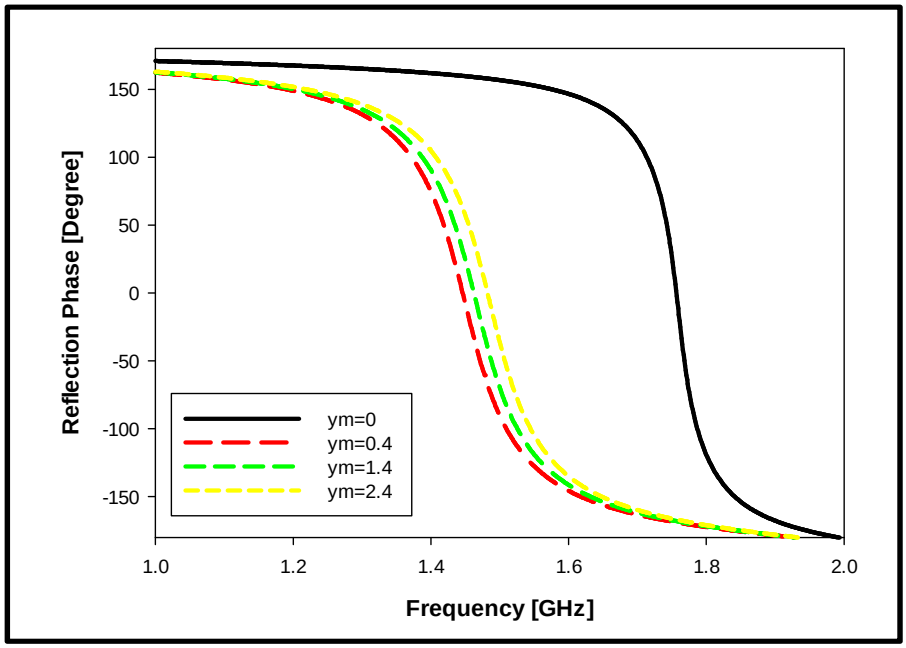

Figure 4.2.3: Reflection phase for different y_m values

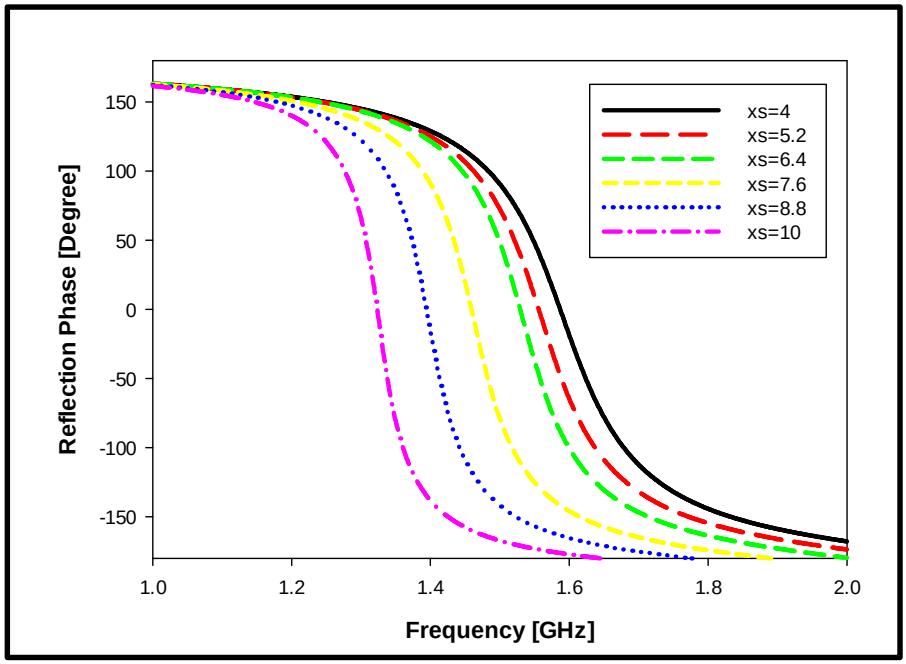

Figure 4.2.4: Reflection phase for different x_s values

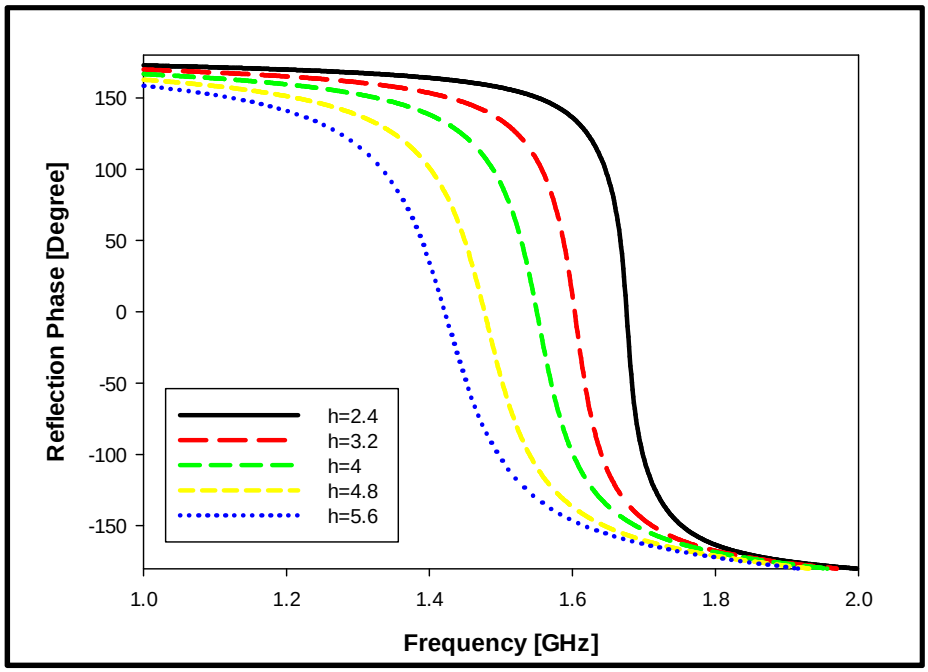

Figure 4.2.5: Reflection phase for different substrates' thicknesses

Finally, using iterative design procedure, the optimum unit cell has been found and the design parameters are given in Table 4.2.1.

Parameter	Value [mm]
x_l, y_l	31.6
x_{v1}	2.4
x_{v2}	2.4
x_{h1}	6.3
x_{h2}	11.1
x_g	1.8
x_m	2.4
x_s	7.2
y_{h1}	23.4
y_{h2}	28.1
y_{h3}	25
y_{h4}	29.8
y_m	2.4
g	0.9
g_s	1.2

Table 4.2.1: Parameter values of the asymmetrical novel AMC

The unit cell's reflection phase is shown in Figure 4.2.6.

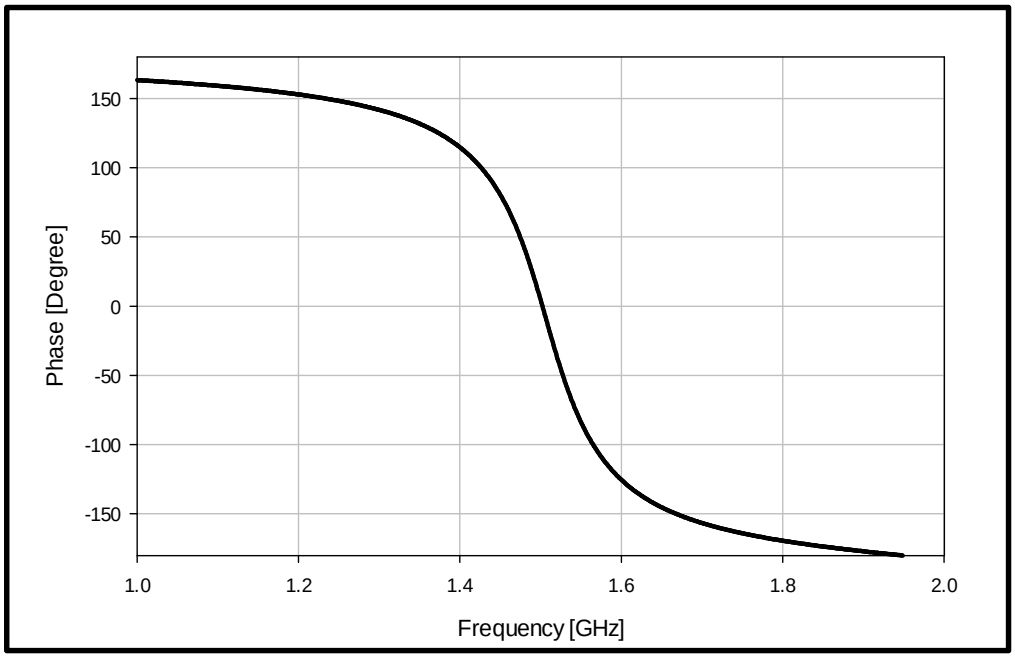

Figure 4.2.6: Reflection Phase for the asymmetrical novel unit cell

The patch has been printed on an FR4 substrate with $\varepsilon_r \approx 4.3$ and a thickness of $h_1 = 4.8\text{mm}$, which corresponds to $\lambda_0/39.8$ at 1.57GHz. The 0 ± 90^o bandwidth for this patch extends from 1.44GHz to 1.56GHz and centred at 1.5GHz with a percentage bandwidth of $\sim 7.7\%$. The unit cell size is 31.6mm, which corresponds to $\lambda_o/6.1$. To test the antenna, a dipole has been placed at a height of $\sim 1\text{mm}$ above a 4×4 unit cells' grid as shown in Figure 4.2.7 and the resultant reflection coefficient, S_{11}, is presented in Figure 4.2.8, where it can be observed that the antenna offers a poor matching at the intended frequency range. A further investigation has been carried out, where it has been found that the matching can be improved noticeably if the antenna is rotated by an angle of 45^o as shown in Figure 4.2.9 and Figure 4.2.10. Such results indicate that the asymmetrical shape of the unit cell play an important role even with a simple dipole.

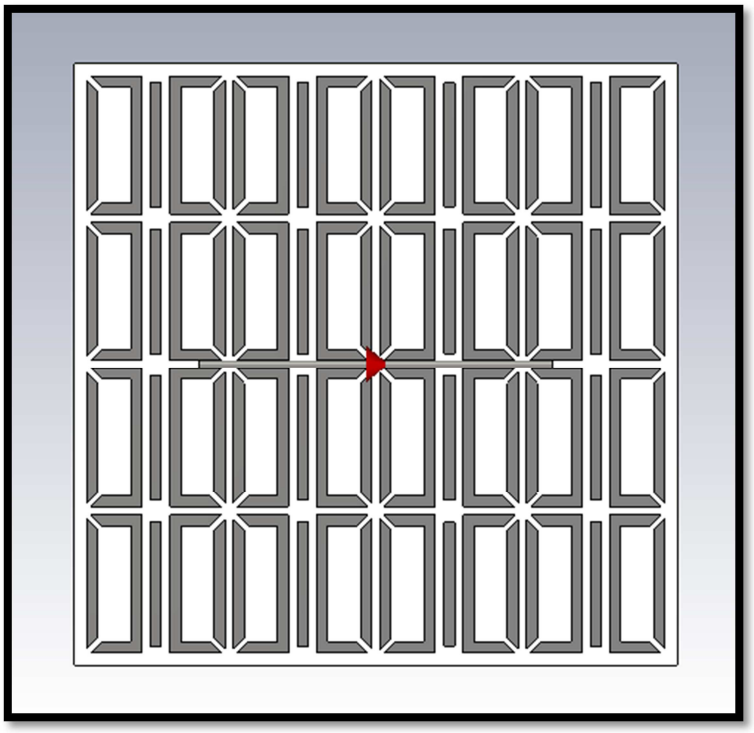

Figure 4.2.7: A dipole antenna above the novel asymmetrical AMC

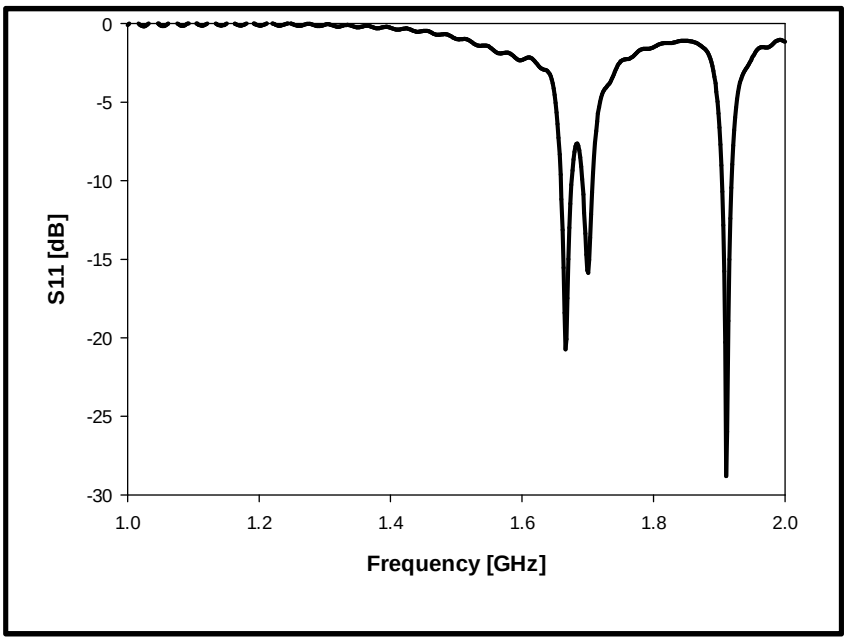

Figure 4.2.8: S_{11} for a dipole antenna placed above the an asymmetrical AMC

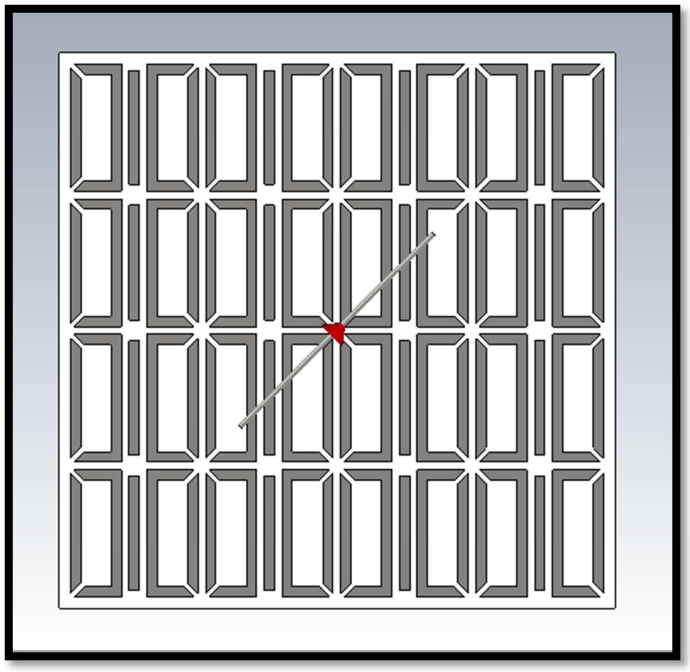

Figure 4.2.9: A rotated dipole antenna above an asymmetrical novel AMC

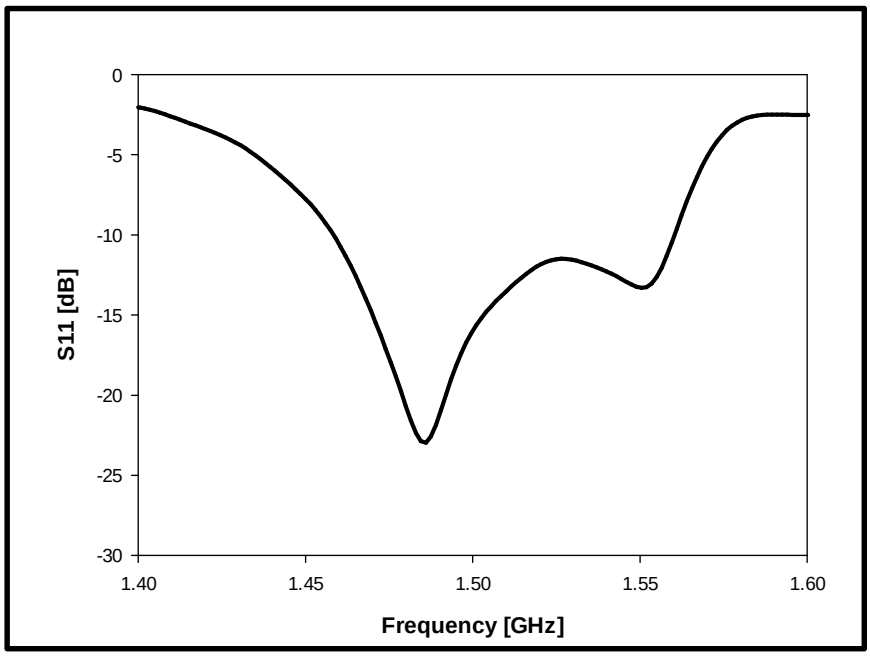

Figure 4.2.10: S_{11} for the rotated dipole above an asymmetrical novel AMC

4.2.2 *Open Loop Antenna Design and Results*

The next step was placing the CPW-fed antenna designed in Chapter 3 at a height of 1mm above a 4×4 grid of the asymmetrical AMC as shown in Figure 4.2.11. The overall structure size is $130 \times 130\text{mm}$, which corresponds to $0.68\lambda_o \times 0.68\lambda_o$ and the

thickness is 7.4mm, which corresponds to $\lambda_o/25.8$. The ground plane size is 23% smaller than the square patch AMC. However, the antenna is 54% thicker.

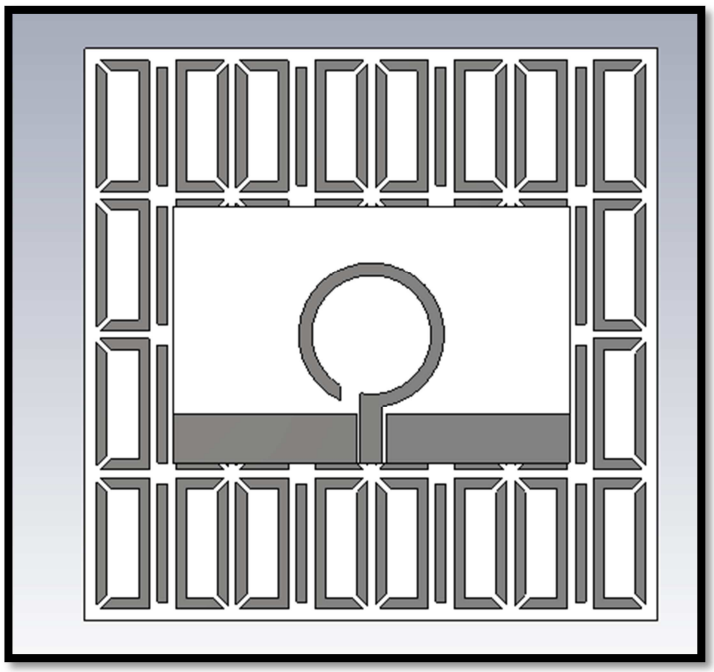

Figure 4.2.11: CPW-fed open loop antenna on the asymmetrical AMC

The reflection coefficient and the axial ratio have been investigated and given in Figure 4.2.12 and Figure 4.2.13.

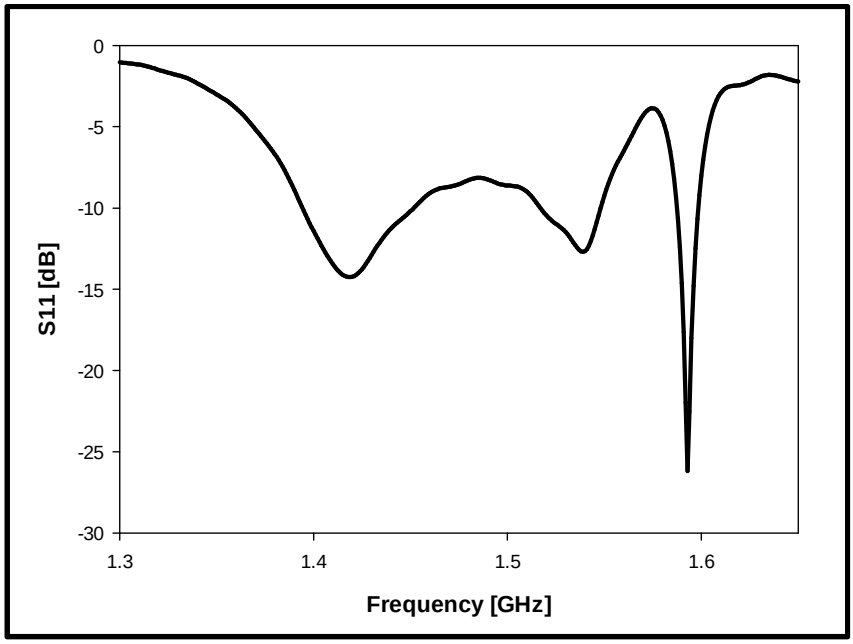

Figure 4.2.12: S_{11} for the CPW-fed antenna backed by the asymmetrical novel AMC

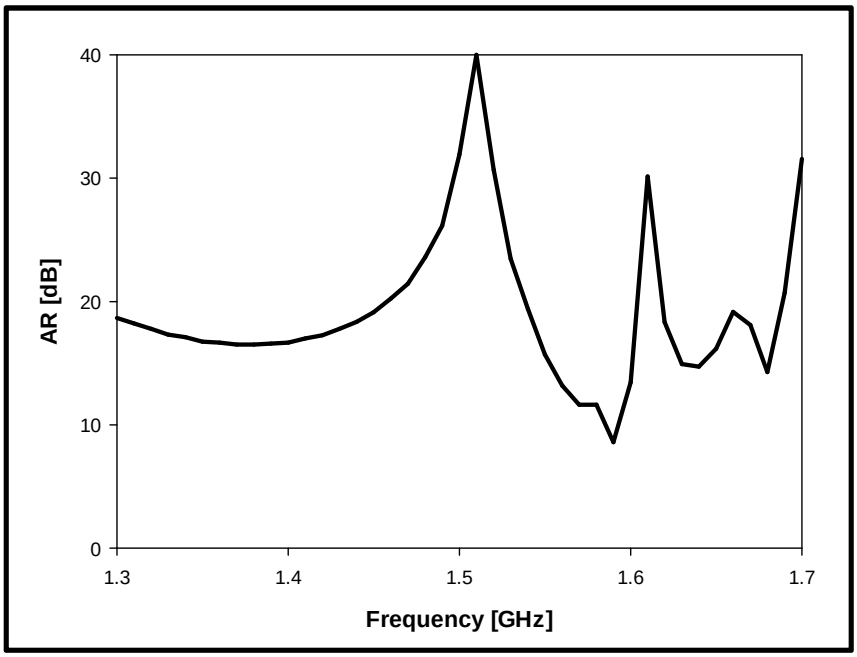

Figure 4.2.13: AR for the CPW-fed antenna backed by asymmetry novel AMC

It can be seen from these results that matching has not been achieved at the desired frequency range and the axial ratio is greater than 3dB. These results were expected to some extent based on the outcome of the dipole test. Although considerable attempts have been made to improve the performance, no improvement has been noticed. The structure's asymmetry may be preventing the correct suppression of the surface waves, and accordingly causing interference with the open loop antenna. Therefore, a new symmetrical AMC needs to be designed as discussed in the next section.

4.3 Circularly Polarized Open Loop Antenna, Fed by a Co-Planar Waveguide, backed by a Novel Symmetrical AMC

4.3.1 *Unit Cell Design Procedures*

In this section, a novel symmetrical AMC unit cell is introduced to reduce the ground plane size and to avoid the asymmetry limitation explained earlier. In order to maintain the same reflection phase while reducing the size, an effort has been carried out to alter the until cell's shape by introducing a number of squares and rectangles in the patch in a symmetrical way. A top view of the achieved design can be shown in Figure 4.3.1. The patch has been printed on an FR4 substrate that has a thickness of $h_1 = 4\text{mm}$, which corresponds to $\lambda_0/47.8$ at 1.57GHz.

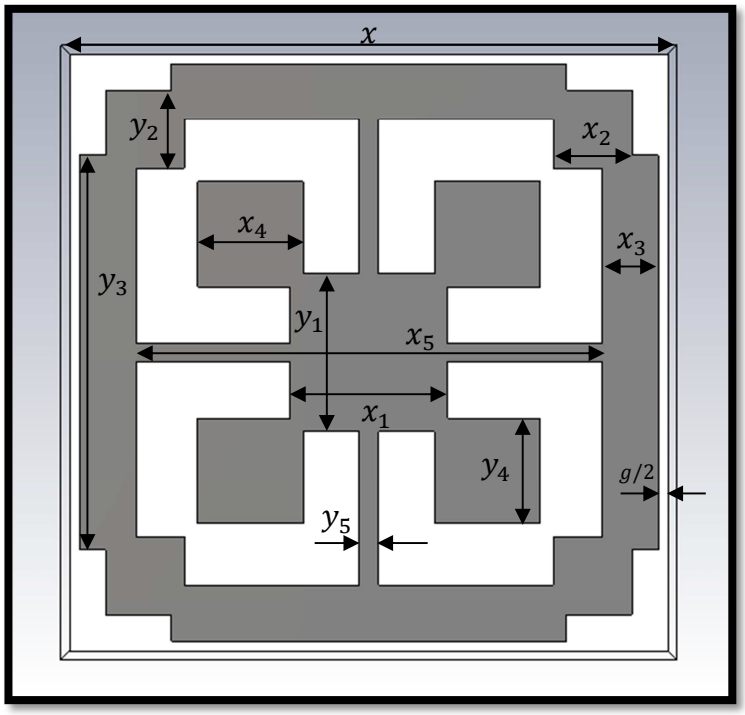

Figure 4.3.1: Top view of the novel AMC structure

In this design, there are few parameters are sensitive and need to be set carefully. On the other hand, there are other less sensitive parameters that can be used for fine tuning. The important parameters are $x_2, x_3, y_3, x_4, x_5, g$ and h and their effects have been investigated. For example, when $x_2 < 2.8\text{mm}$, the 0^o-reflection phase has been achieved at 1.08GHz. On the other hand, when x_2 is greater than 2.8mm, the 0^o-reflection phase is obtained at ~1.48GHz. Then, the 0^o-reflection phase changes slightly when x_2 is increased further; i.e. as x_2 increases, the 0^o-reflection phase frequency point reduces as illustrated in Figure 4.3.2. This is because when x_2 is less than 2.8mm, the side strips are disconnected and, hence, more capacitance is introduced between the strips and the small corner squares as can be seen in Figure 4.3.3. However, when $x_2 \geq 2.8\text{mm}$, the strips are connected as can be seen in the unit cell design.

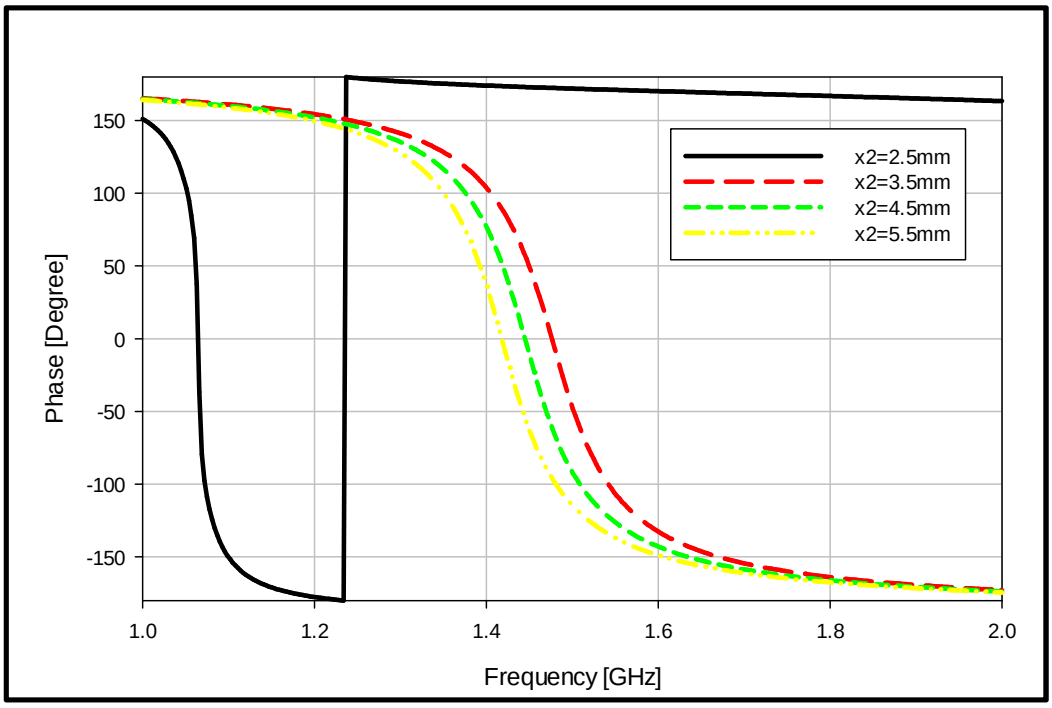

Figure 4.3.2: Effects of x_2 on the reflection phase

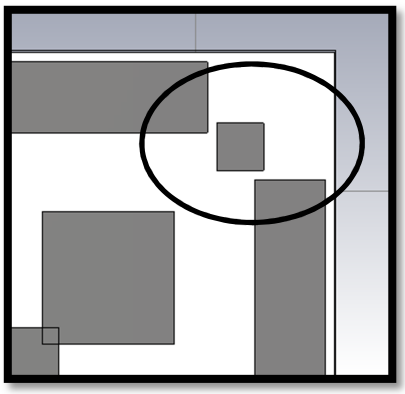

Figure 4.3.3: The novel symmetrical unit cell when $x_2 < 2.8\text{mm}$

The second sensitive parameter is x_3, which can be used to adjust the 0^o-reflection phase to the desired frequency. As can be seen from Figure 4.3.4, x_3 is inversely proportional to the 0^o-reflection frequency point. For example, when $x_3 = 1.5\text{mm}$, the 0^o-reflection point has been achieved at 1.65GHz. Altering the x_3 to 3.5mm changes the 0^o-reflection to 1.29GHz. The bandwidth is almost constant as can be seen in Table 4.3.1.

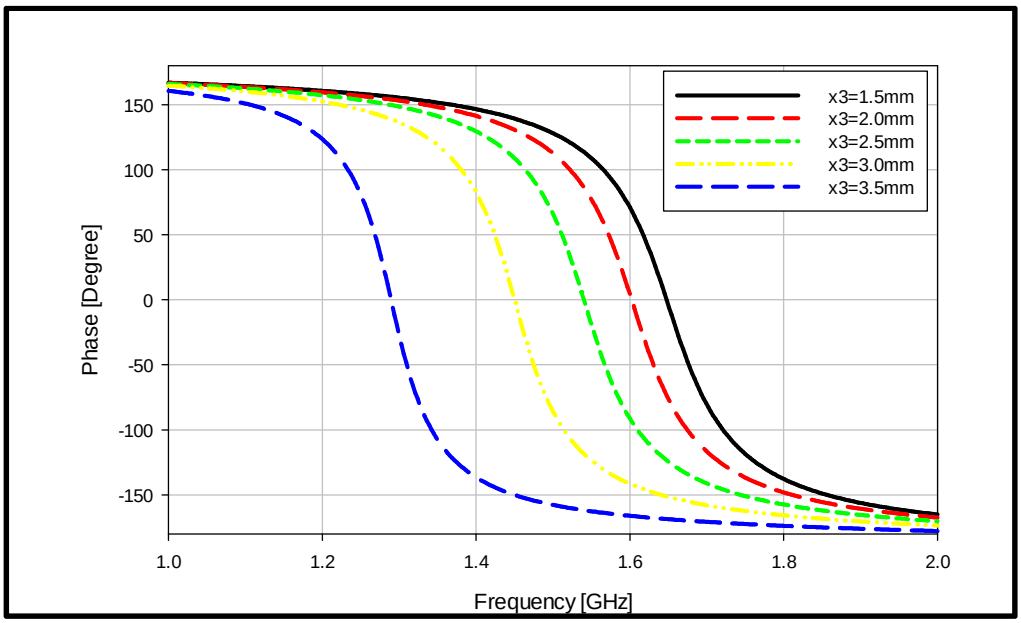

Figure 4.3.4: Effects of x_3 on the reflection phase

$x_3[mm]$	$f_2[\mathrm{GHz}]$	$f_1[\mathrm{GHz}]$	$f_{resonance}[\mathrm{GHz}]$	BW [%]
1.5	1.7094	1.5795	1.6477	7.88
2.0	1.6631	1.5359	1.6023	7.90
2.5	1.5987	1.4769	1.5401	7.90
3.0	1.5038	1.3924	1.4499	7.68
3.5	1.3337	1.2430	1.2895	7.00

Table 4.3.1: The reflection phase and bandwidth for various x_3 values

Another important parameter is y_3, which has a similar behaviour to that of x_2. For instance, when y_3 is less than $19.6\mathrm{mm}$, the side strips are disconnected from the corner squares as can it illustrated in Figure 4.3.5. Therefore, the capacitance is high and the unit cell resonates at a lower frequency. For instance, when $y_3 = 14\mathrm{mm}$, the 0^o-reflection phase frequency point is $1.29\mathrm{GHz}$ with a bandwidth of 2.5%. Increasing y_3 increases the capacitance further and lowers the 0^o-reflection frequency point with a slightly lower bandwidth. On the other hand, when y_3 exceeds $19.6\mathrm{mm}$, the strips are connected to the corner squares, which changes the capacitance dramatically and let the 0^o-reflection phase moves to $1.45\mathrm{GHz}$ for $y_3 = 21\mathrm{mm}$ with a remarkable increase in the bandwidth to 7.7% as can be observed from Figure 4.3.6. Further increments of y_3 reduce the 0^o-reflection phase frequency point marginally, which can be used for fine tuning purposes.

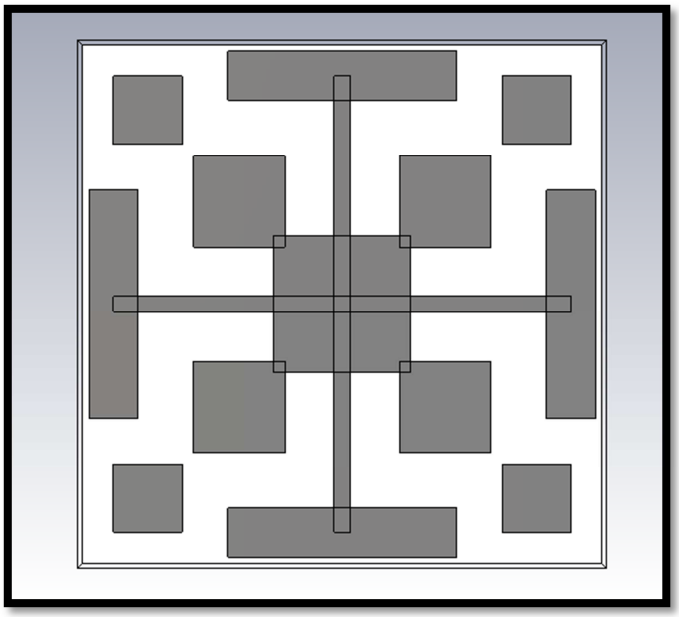

Figure 4.3.5: The symmetrical novel AMC when $y_3 < 19.6\ \mathrm{mm}$

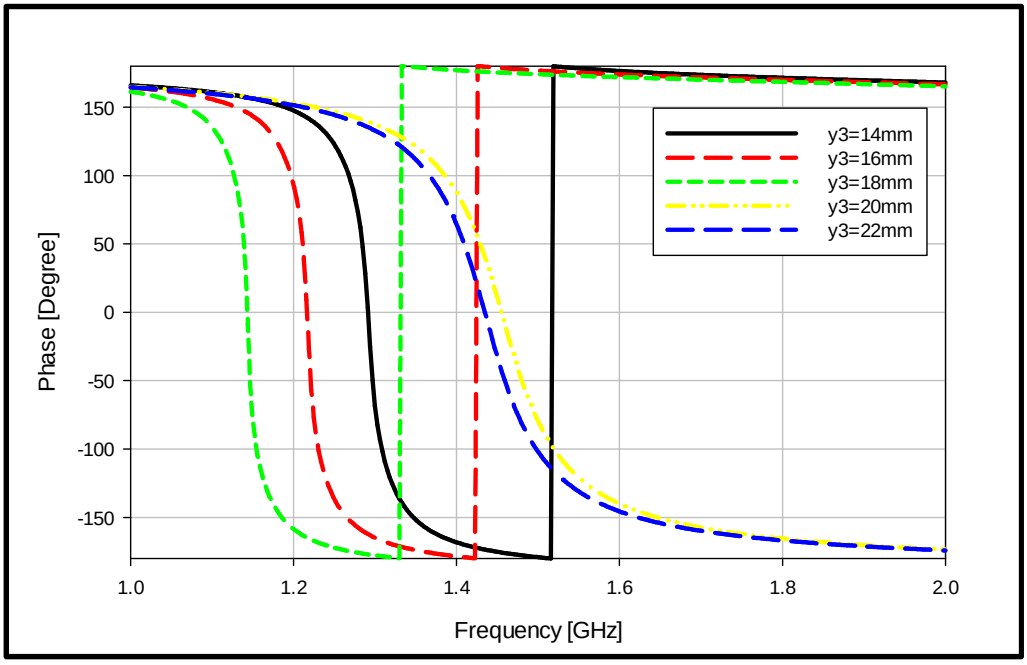

Figure 4.3.6: Effects of y_3 on the reflection phase

The parameters x_4 and x_5 let the AMC resonates at two different frequencies depends if the correspondent square, or rectangle, is connected with the adjacent conductors or not. For example, when x_4 is less than $7\mathrm{mm}$, the AMC resonates at $1.44\mathrm{GHz}$ since the correspondent squares are disconnected from the outer smaller squares as illustrated in Figure 4.3.1. On the contrary, when $x_4 \geq 7\mathrm{mm}$, the squares are connected and the AMC resonates at $1.55\mathrm{GHz}$ as shown in Figure 4.3.7. The reflection phase is illustrated in Figure 4.3.8 for different x_4 values, where it can be

noticed that fine frequency tuning can be obtained by adjusting x_4 when it is bigger than 7mm. Additionally, the AMC resonates at 1.24GHz when x_5 is less than 25mm, i.e. for the case of disconnected centre rectangle strips and at 1.45GHz when $x_5 \geq 25\text{mm}$ with a wider bandwidth when the centre strips are connected to the side strips as shown in Figure 4.3.9.

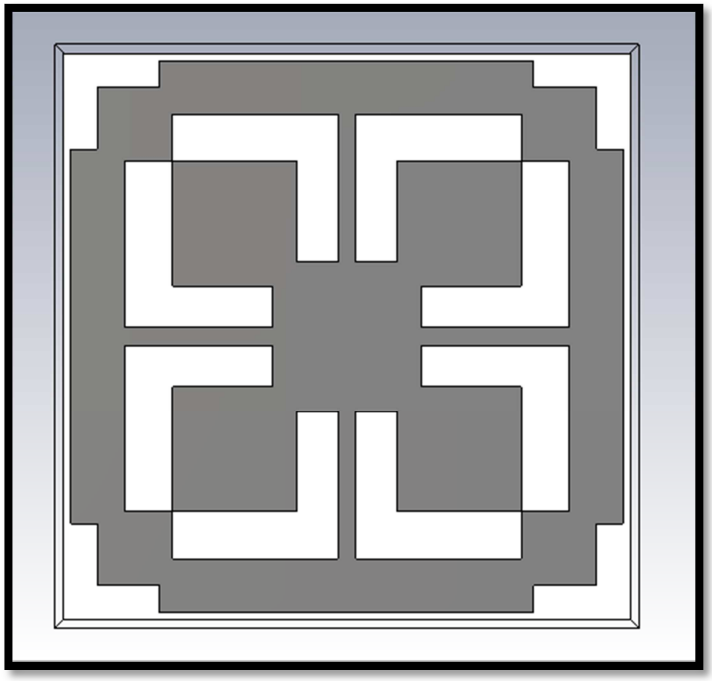

Figure 4.3.7: The novel symmetrical AMC for $x_4 = 7mm$

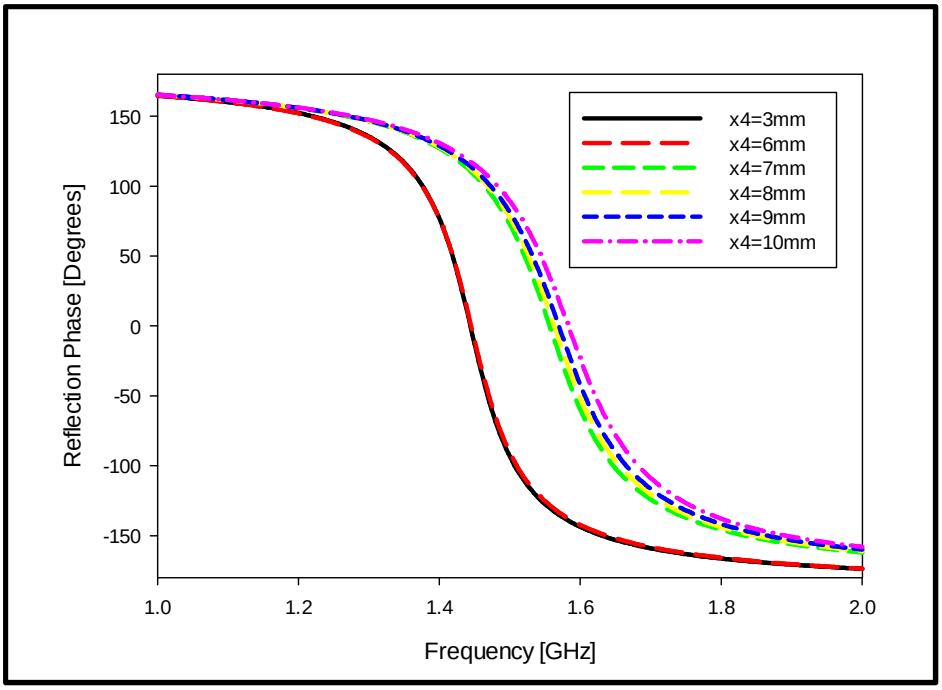

Figure 4.3.8: Effects of x_4 on the reflection phase

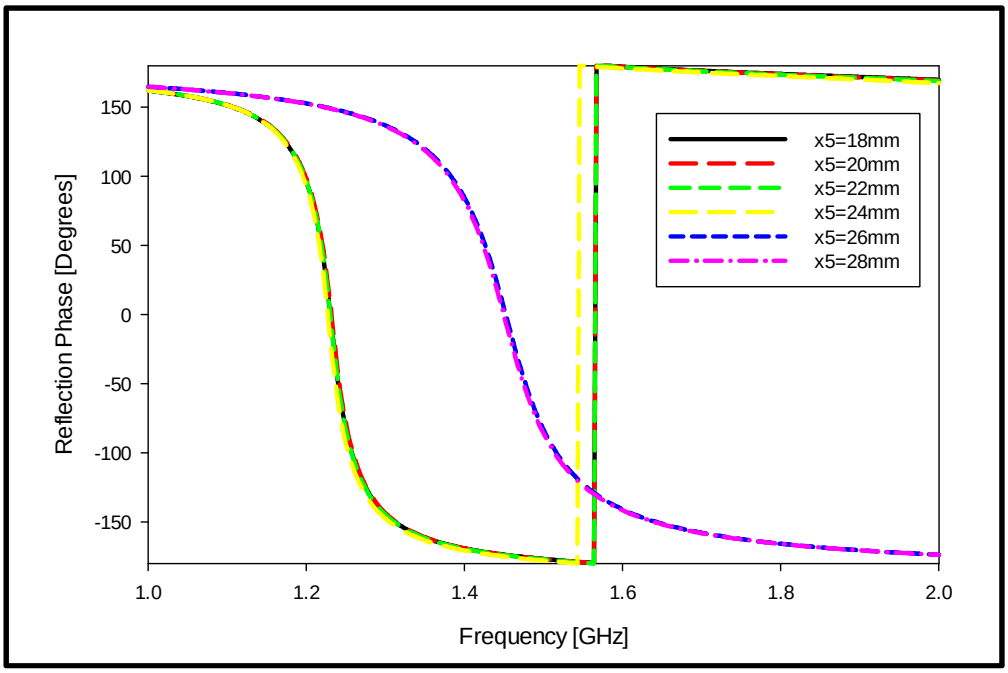

Figure 4.3.9: Effects of x_5 on the reflection phase

The effects of the gap between unit cells, g, and the substrates' thickness, h, have been considered, where it has been observed that g affects the capacitance of the structure as shown in Figure 4.3.10 and Table 4.3.2.

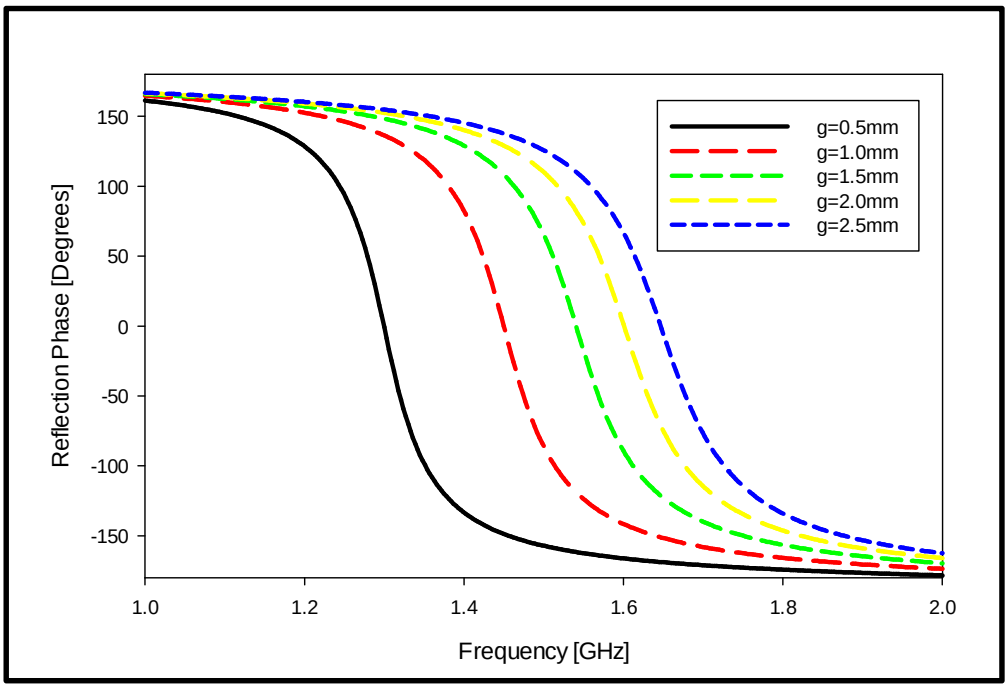

Figure 4.3.10: Effects of g on the reflection phase

$g[mm]$	$f_2[\mathrm{GHz}]$	$f_1[\mathrm{GHz}]$	$f_{resonance}[\mathrm{GHz}]$	BW [%]
0.5	1.3432	1.2535	1.2997	6.9
1.0	1.5038	1.3924	1.4499	7.7
1.5	1.6008	1.4762	1.5408	8.1
2.0	1.6650	1.5316	1.6009	8.3
2.5	1.7138	1.5742	1.6468	8.5

Table 4.3.2: Effects of g on the reflection phase and bandwidth

It can be seen that the 0°-reflection phase moves towards higher frequency when g is increased. Also, the 0 ± 90^{o} bandwidth increases for bigger values of g. Additionally, the thickness has been varied in the range of $0.8 - 5.6\mathrm{mm}$ and the results are shown in Figure 4.3.11 and Table 4.3.3. The 0°-reflection phase frequency point has changed from $1.75\mathrm{GHz}$ to $1.3\mathrm{GHz}$ when the thickness is increased from $0.8\mathrm{mm}$ to $5.6\mathrm{mm}$. On the other hand, the bandwidth has increased dramatically from 0.09% at $0.8\mathrm{mm}$ to $\sim 11\%$ at $5.6\mathrm{mm}$. Therefore, a trade-off is needed between the required bandwidth and the thickness of the substrate.

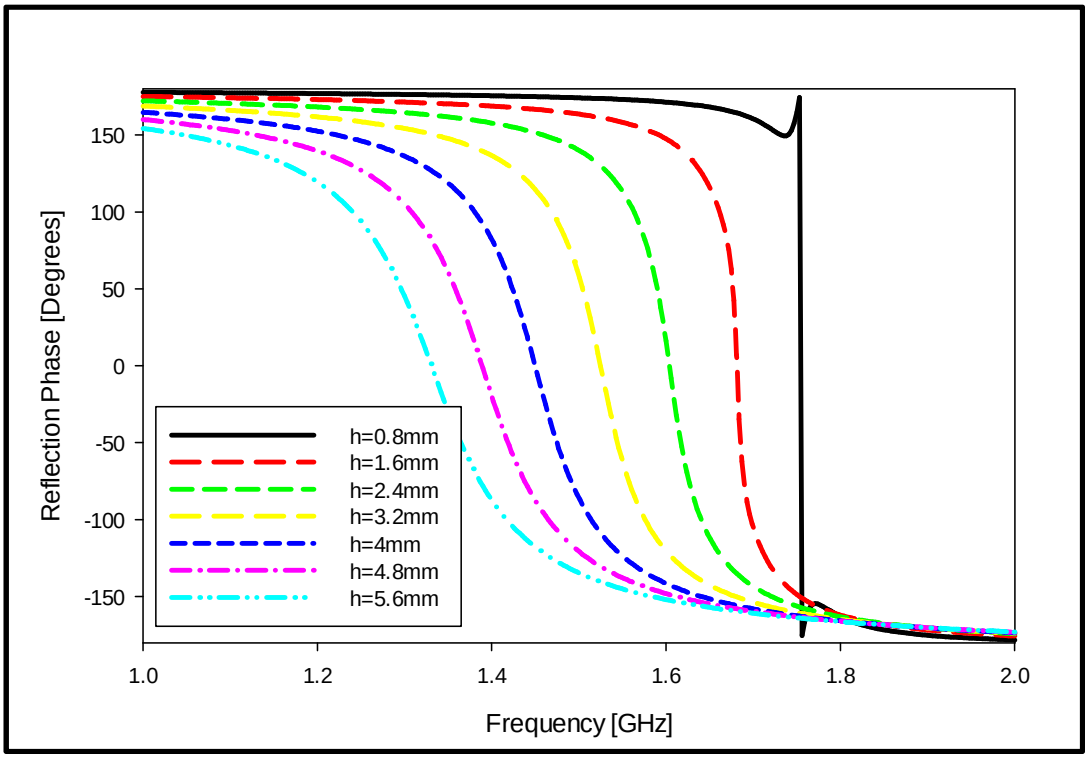

Figure 4.3.11: Effects of h on the reflection phase

$h[mm]$	$f_2[\mathrm{GHz}]$	$f_1[\mathrm{GHz}]$	$f_{resonance}[\mathrm{GHz}]$	BW [%]
0.8	1.7553	1.7537	1.7545	0.09
1.6	1.6936	1.6667	1.6815	1.6
2.4	1.6341	1.5708	1.6040	3.95
3.2	1.5677	1.4787	1.5250	5.84
4.0	1.5038	1.3924	1.4499	7.7
4.8	1.4529	1.3216	1.3890	9.5
5.6	1.4034	1.2554	1.3310	11.1

Table 4.3.3: Effects of h on the reflection phase and bandwidth

The parameters x_1 and y_5 can be used to fine tune the intended frequency range as illustrated in Figure 4.3.12 and Figure 4.3.13.

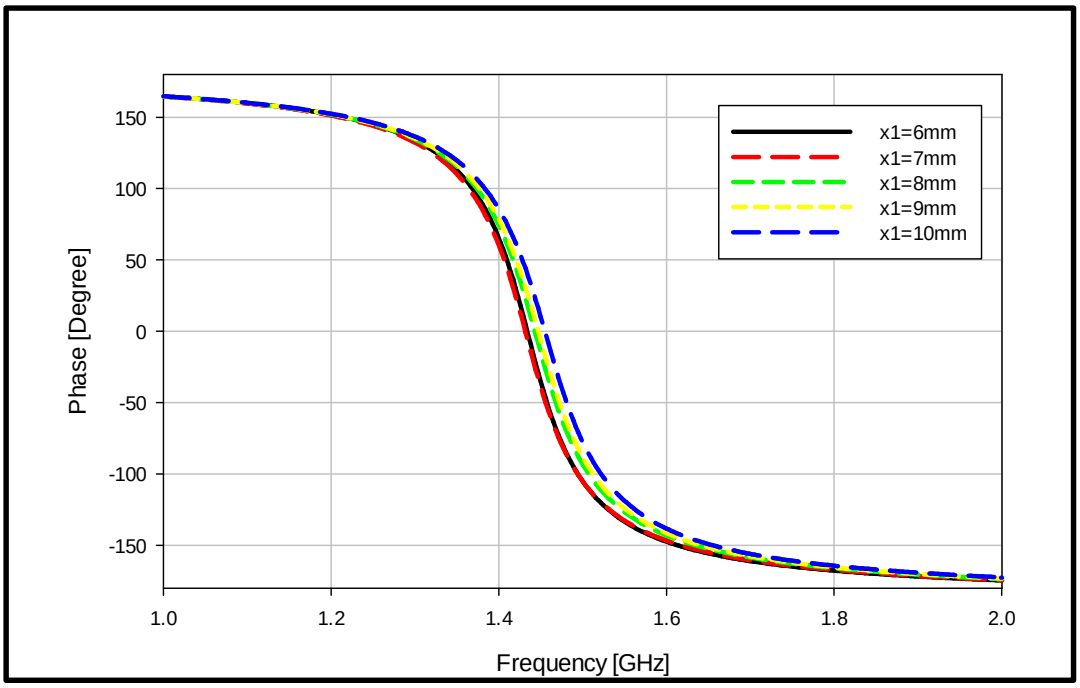

Figure 4.3.12: Effects of x_1 on the reflection phase

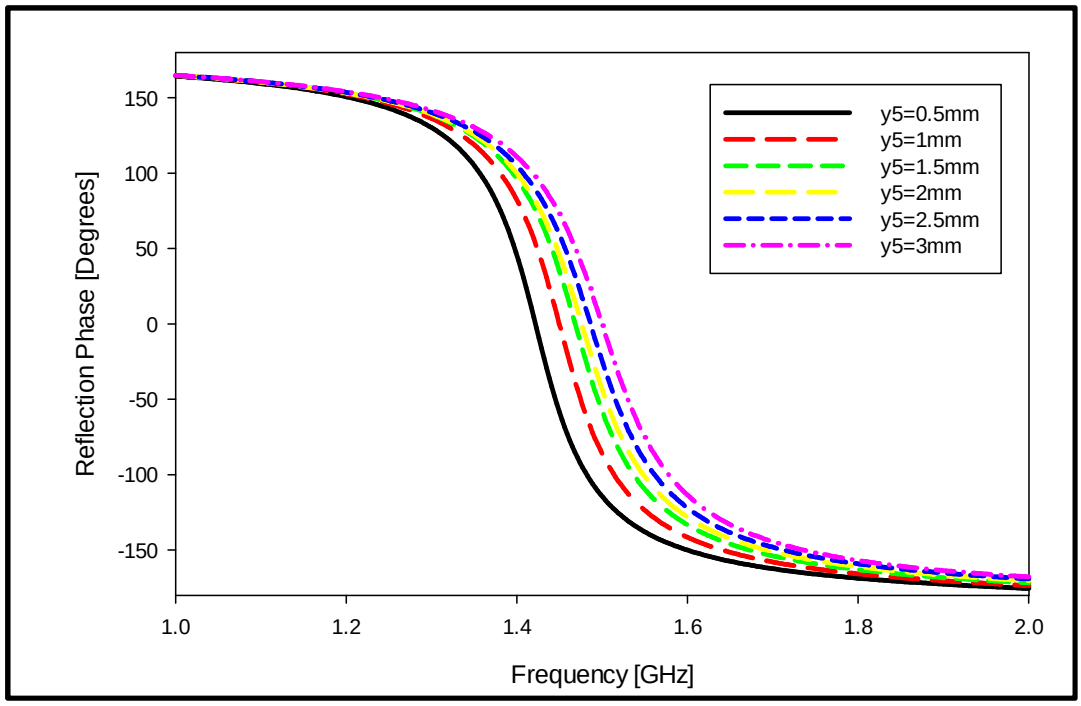

Figure 4.3.13: Effects of y_5 on the reflection phase

Based on these investigations, the optimum values for the design parameters have been selected and are given in Table 4.3.4.

Parameter	Value [mm]
x_1	8.4
x_2	4.2
x_3	3
x_4	5.6
x_5	25
x	31.8
y_1	8.4
y_2	4.2
y_3	21
y_4	5.6
y_5	1
g	1

Table 4.3.4: Parameters values for the novel AMC structure

The design has been simulated and the reflection phase is shown in Figure 4.3.14

.

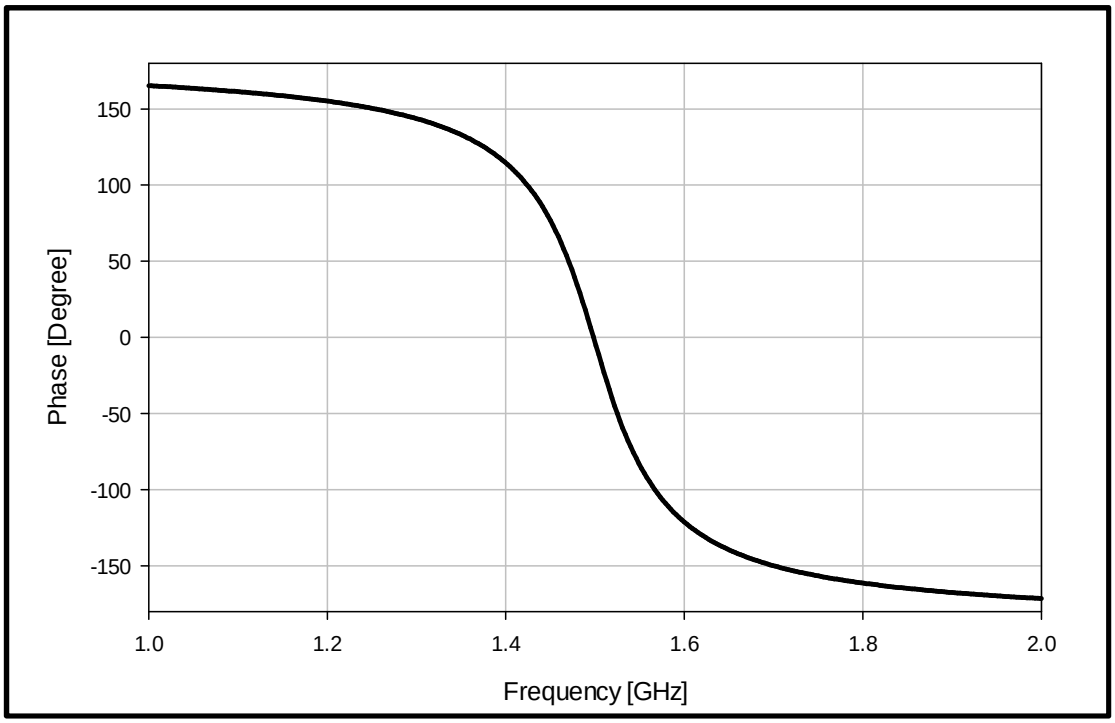

Figure 4.3.14: Phase reflection for the novel Symmetrical AMC structure

As a starting point the novel AMC has been designed so that the 0 ± 90^o reflection phase covers the L_1 GPS bandwidth. However, since the interaction between the antenna and the AMC is strong, the dimensions of the unit cell have been optimized. The 0 ± 90^o bandwidth for this AMC extends from $1.44 - 1.56\text{GHz}$ centred at 1.5GHz with a bandwidth of $\sim 8\%$.

For testing purposes, a dipole antenna has been placed at a height of 2.6mm above a 4×4 grid of the novel symmetrical AMC, i.e. 6.6mm above the PEC ground plane as shown in Figure 4.3.15. The resultant reflection coefficient is given in Figure 4.3.16, from which two points can be observed: The first is the AMC has improved the S_{11} significantly compared to the same the same configuration in the absence of the AMC. The second is that the S_{11} has been improved with a smaller ground plane compared to the square patch and without any rotation comparing to the asymmetrical AMC presented earlier.

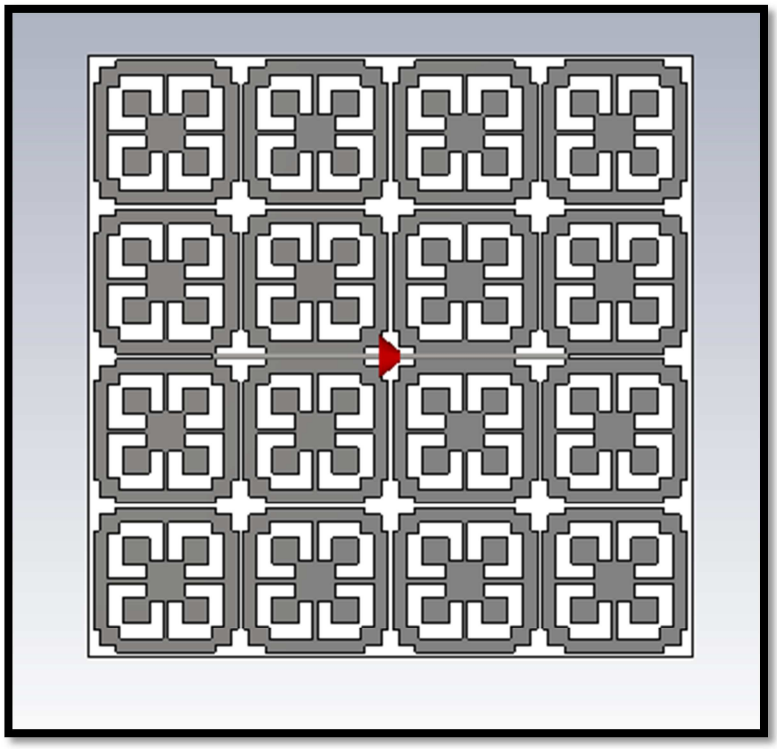

Figure 4.3.15: A dipole antenna above the new symmetrical AMC

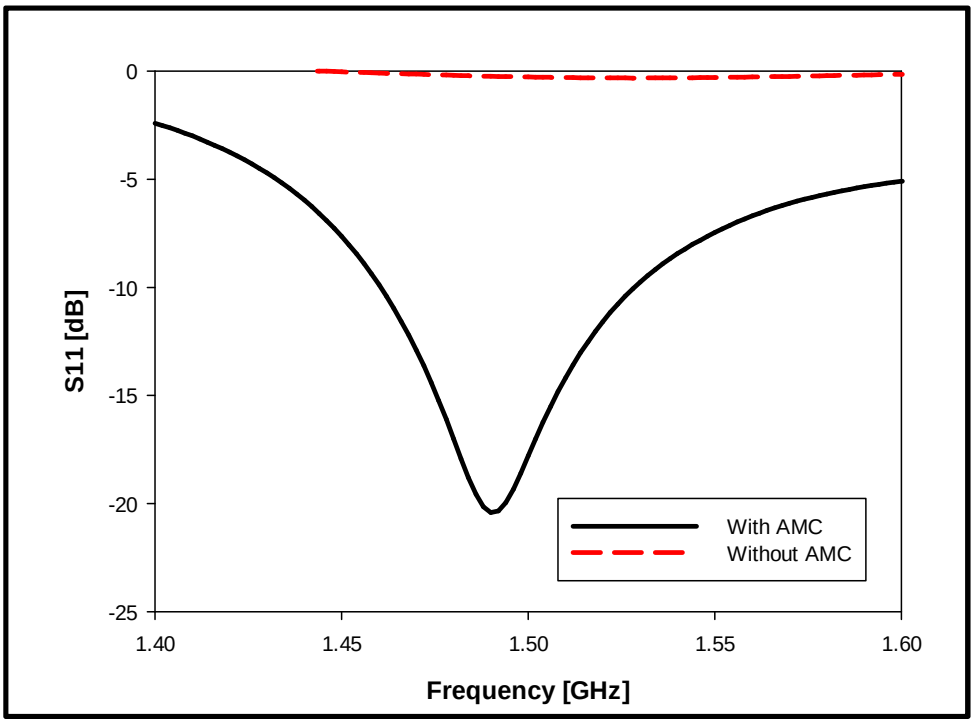

Figure 4.3.16: S_{11} for the dipole antenna above the symmetrical new AMC

4.3.2 *Open Loop Antenna Design and Results*

The open loop antenna has been used in conjunction with a 4×4 grid of the new symmetrical AMC ground plane. The size of the ground plane is 128.2mm, which corresponds to $0.67\lambda_o$ compared to 169mm for the square patch AMC, which gives a reduction of $\sim 24\%$ as illustrated in Figure 4.3.17. However, the thickness for the new AMC is 4mm whereas it was 2.4mm with the square patch AMC.

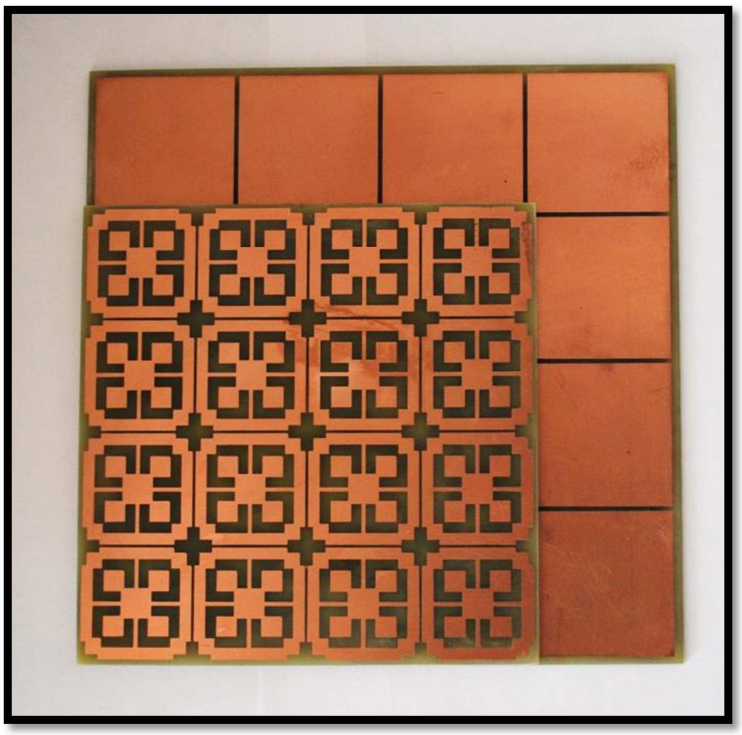

Figure 4.3.17: Prototype for the new ground plane compared to the old one

The same CPW-fed antenna given in Chapter 3 has been placed at height of h_{gap} above the AMC surface as illustrated in Figure 4.3.18 and Figure 4.3.19.

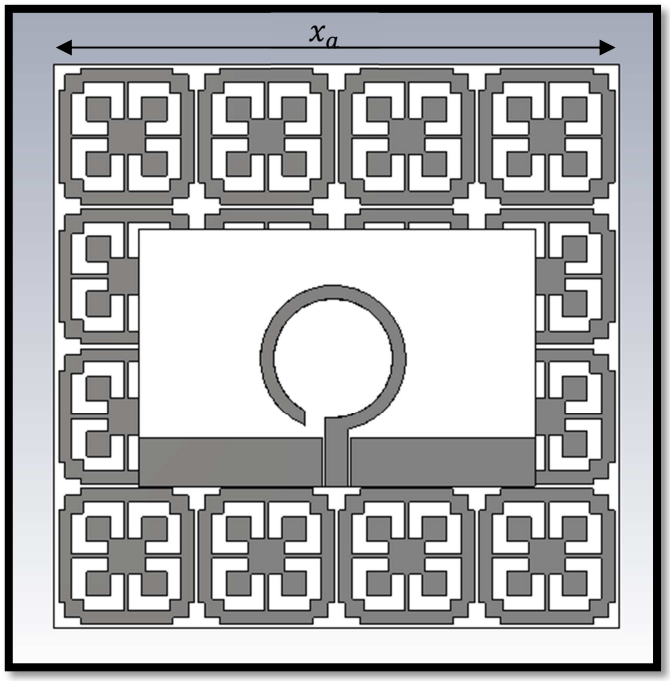

Figure 4.3.18: CPW-fed open loop antenna on a novel AMC ground plane (Top view)

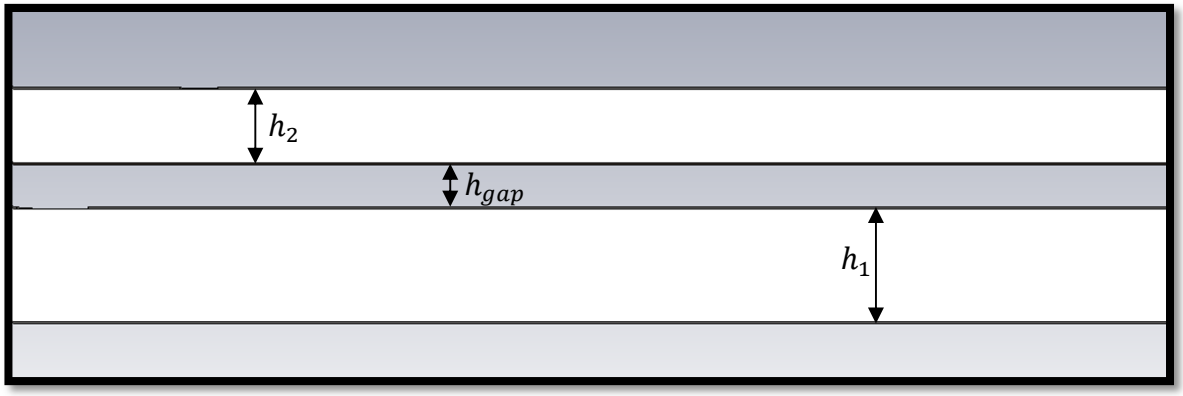

Figure 4.3.19: CPW-fed open loop antenna on a novel AMC ground plane (side view)

As have been discussed in Chapter 3, there are few design parameters that can be tuned to improve the performance such as the gap between the AMC and the antenna, the radius of the loop, the width and the height of the grounded rectangular patch of the CPW feed and the size of the loop's substrate. As an example, the gap between the two layers has been varied from $0 - 3\text{mm}$ and the results are shown in Figure 4.3.20 and Figure 4.3.21.

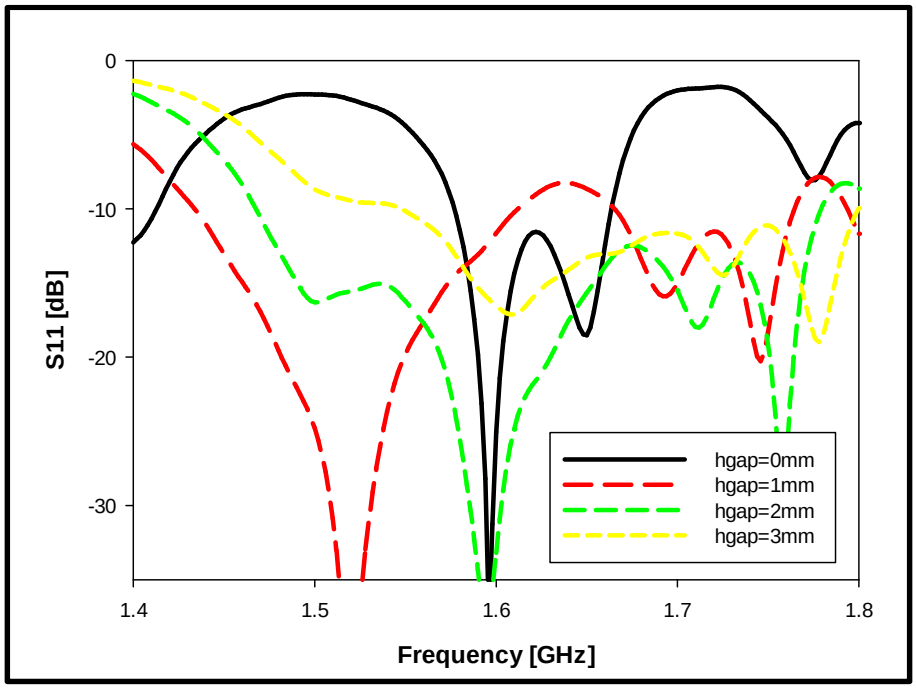

Figure 4.3.20: S_{11} for variable gap values

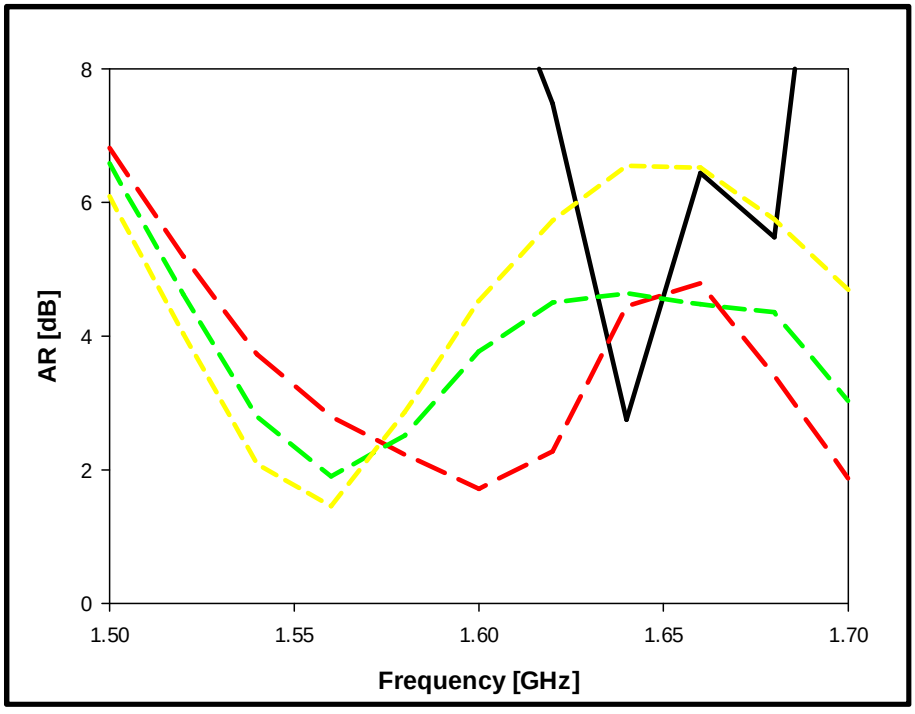

Figure 4.3.21: AR for different gap values

The optimized gap between the antenna and the AMC has been determined as $h_{gap} = 1\text{mm}$. The total thickness of the antenna therefore is $h_{tot} = 6.6\text{mm}$, which corresponds to $\lambda_o/29$. The antenna has been fabricated and measured as shown in Figure 4.3.22 and Figure 4.3.23. A sheet of rohacell foam of $\varepsilon_r = 1.07$ [114] and a thickness of 1mm has been placed between the antenna and the AMC, and a transparent adhesive tape has been used to attach the antenna to the AMC.

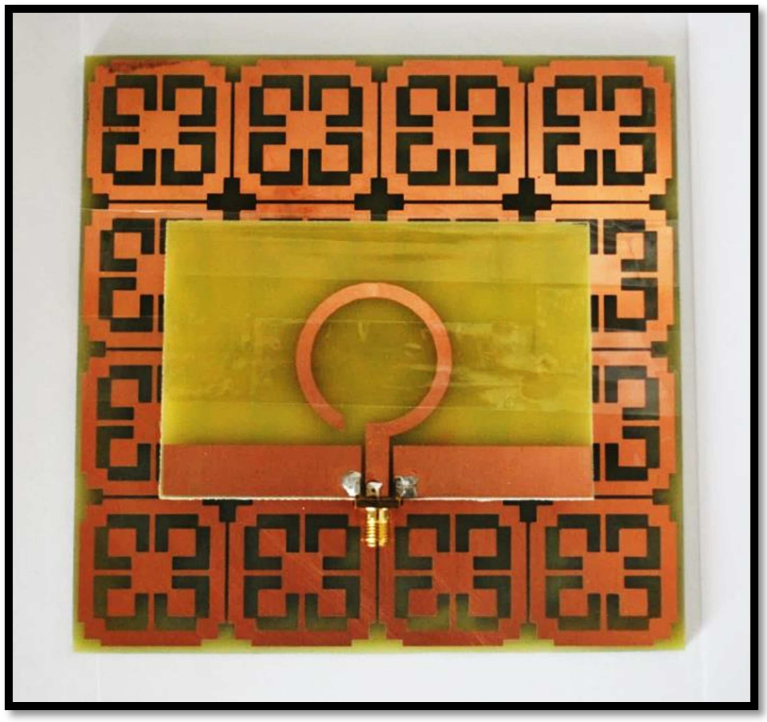

Figure 4.3.22: The fabricated CPW-fed open loop antenna on the new AMC structure

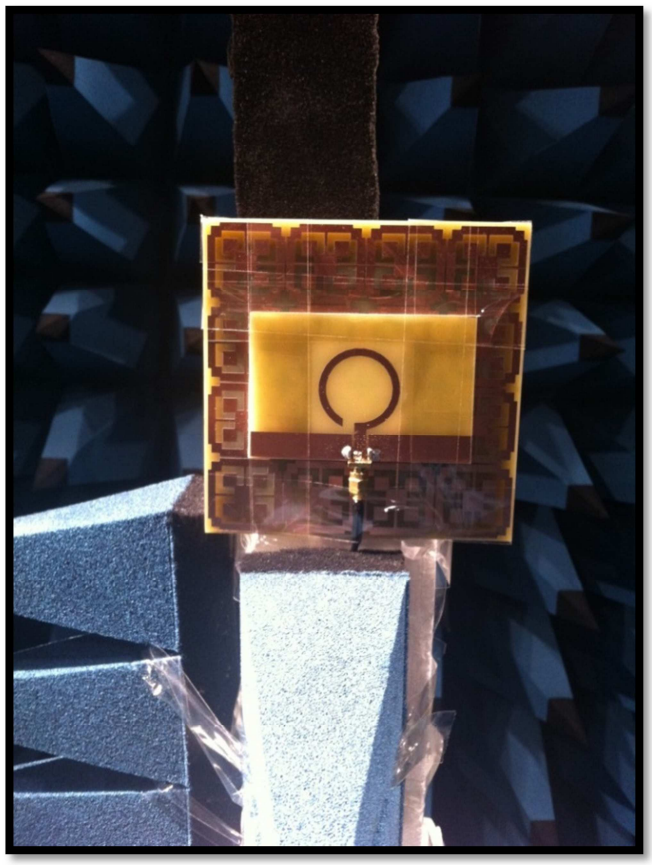

Figure 4.3.23: The fabricated CPW-fed open loop antenna on new AMC structure in the anechoic chamber

The simulated and measured reflection coefficients agree with each other as shown in Figure 4.3.24, where it can be observed that the simulated and measured bandwidths are 20% and 18%, respectively.

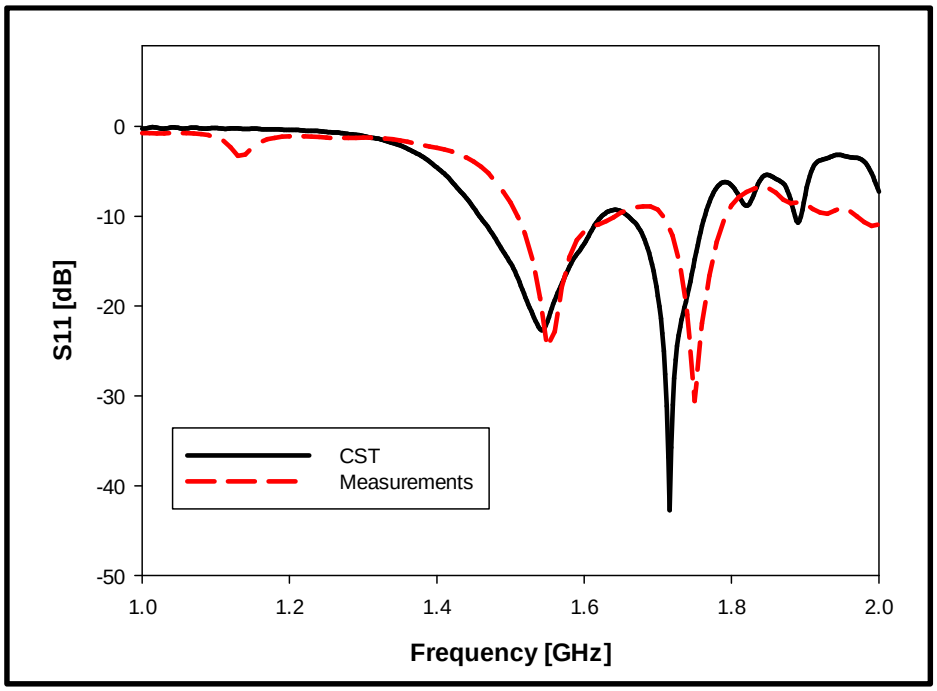

Figure 4.3.24: S11 for the CPW-fed open loop antenna backed by a new AMC

The measured and simulated ARs are given in Figure 4.3.25, where it can be observed that the simulated 3dB bandwidth is ranging from $1.55 - 1.63\text{GHz}$, centred at 1.58GHz with a percentage bandwidth of $\sim 4.9\%$. However, although the measured graph is similar to the simulated counterpart, the measured AR is greater than 3dB. Two assumptions have been made; either the discrepancy due to simulation and design errors or experimental errors. As a further test, the antenna has been simulated using HFSS and the resultant axial ratio is given in Figure 4.3.26, where it can be seen that both CST and HFSS results show this antenna achieves circular polarisation at the intended frequency range. Therefore, it is more likely to be an experimental error. Studying the antenna further yields two sources of experimental errors; thickness of the gap, which is greater than 1mm since the thickness of the connecting cable is greater than 1mm and therefore, the prototype's gap between the antenna and the AMC is greater than what has been used in the simulation. The second is the interference from connecting cable, which had to be placed close to the AMC, and thus interfered with the antenna's radiation.

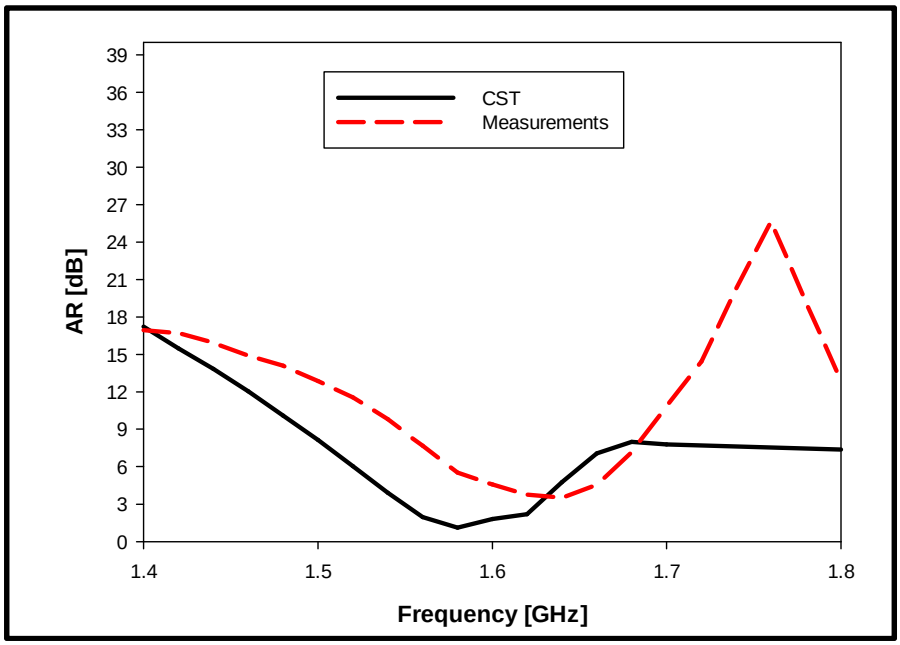

Figure 4.3.25: AR of the CPW-fed open loop antenna backed by a new AMC

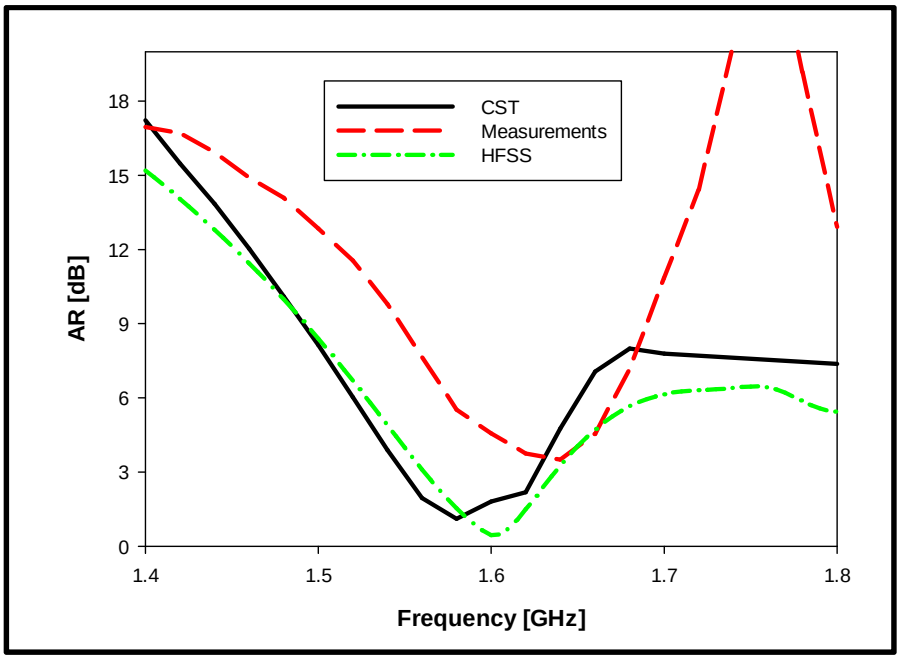

Figure 4.3.26: CST, HFSS and measured axial ratio for the CPW-fed antenna

The CST simulated antenna offers a useful gain of ~7dBi over the desired frequency range as shown in Figure 4.3.27 whereas the HFSS simulated gain is ~5dBi. The radiation pattern is illustrated in Figure 4.3.28 and Figure 4.3.29, where it is evident that this is a right handed circularly polarised (RHCP) antenna since E_R is more than 20dB greater than E_L at bore-sight.

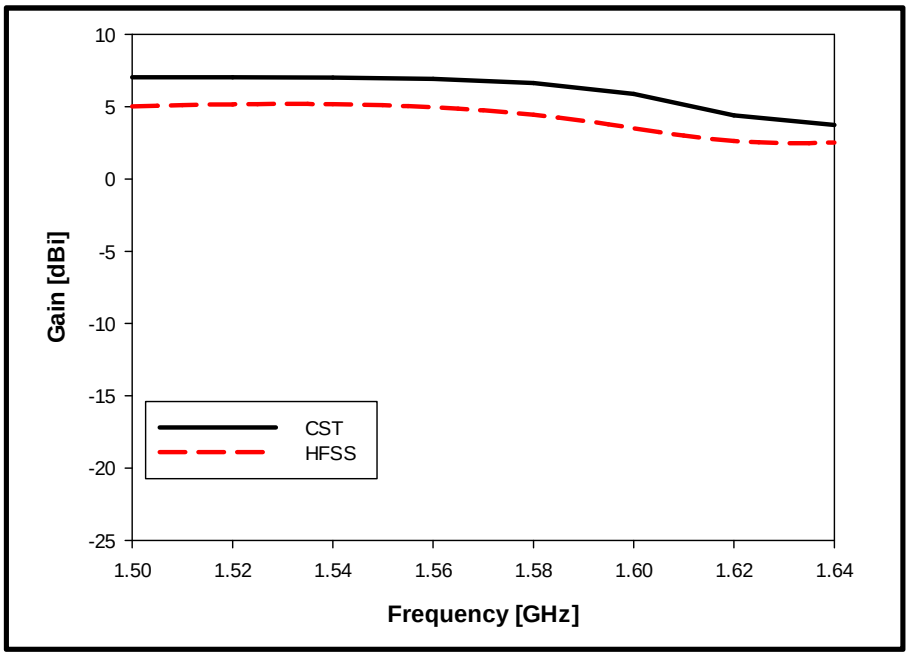

Figure 4.3.27: Gain for the CPW-fed open loop antenna backed by a new AMC

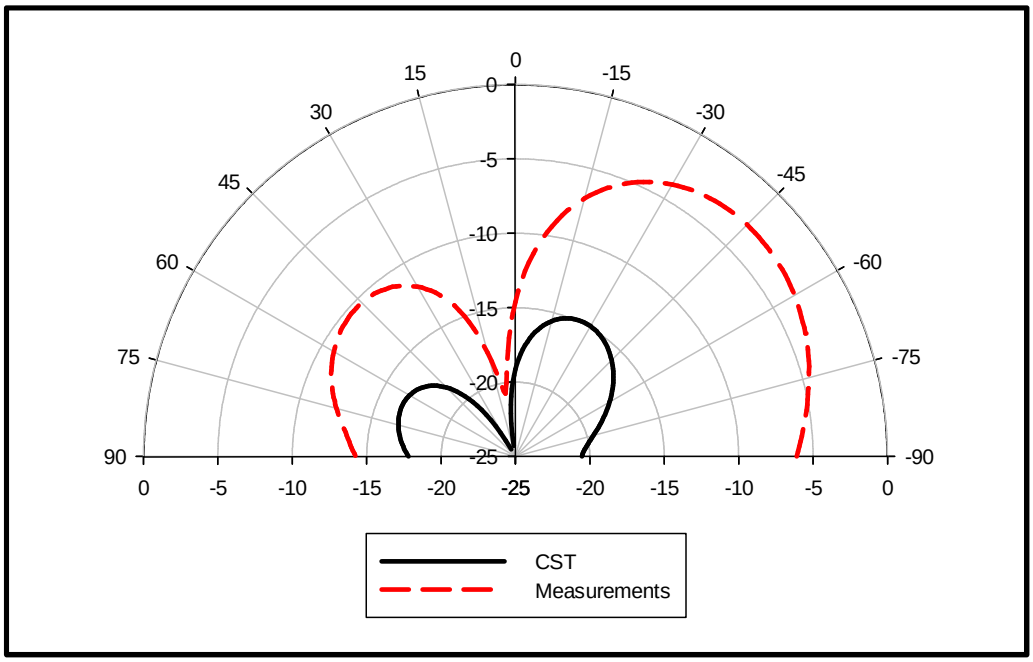

Figure 4.3.28: EL for the CPW-fed open loop antenna backed by a new AMC

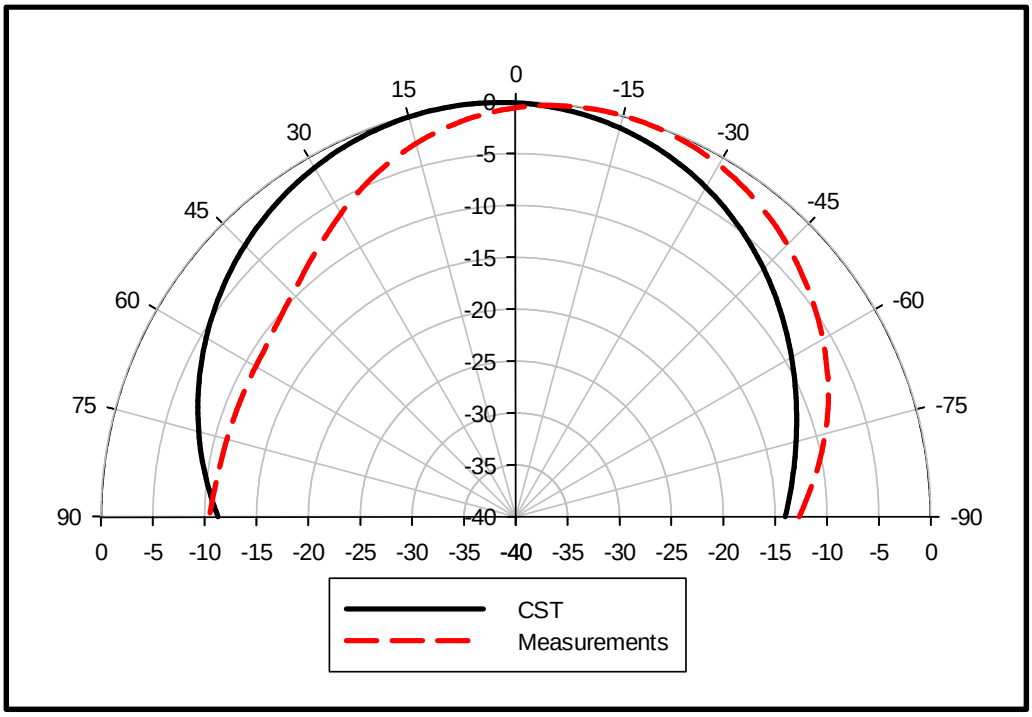

Figure 4.3.29: E_R for the CPW-fed open loop antenna backed by a new AMC

So far, the CPW-fed open loop antenna backed by the new symmetrical AMC has reduced the ground plane size but has shown limitations such as the increase of the overall height to $\lambda_o/29$, from $\lambda_o/38.2$ as for the CPW-fed open loop backed square patch. However, it is thinner than that of $\lambda_o/21.23$ as reported in [112]. The other limitation is the interference of the feeding cable on the radiation and therefore, the difficulty in achieving an axial ratio that is less than 3dB. Therefore, an alternative feeding mechanism has been adopted, which will be investigated in the next section.

4.4 Probe-Fed Open Loop Antenna Backed by a Novel Symmetrical AMC

4.4.1 *Unit Cell Design Procedures*

As demonstrated in the previous section, employing the new symmetrical AMC has reduced the ground plane size by $\sim 24\%$ compared to that designed in Chapter 3. However, the thickness has increased. In this section, the aim is to design a probe fed CP open loop antenna backed by the new symmetrical AMC. The aim is to have same thickness as that of the probe-fed open loop antenna backed by the square patch AMC. To achieve this goal, the design procedures and analysis shown in the previous section have been utilized to redesign the new symmetrical AMC unit cell, shown in Figure 4.4.1, using the same FR4 substrate. Altering the design is needed

because there are two substrate layers; the AMC layer and open loop superstrate layer that need to be attached to each other. Therefore, the 0^o-phase frequency point would be changed. The final optimum dimensions of the unit cell are given in Table 4.4.1.

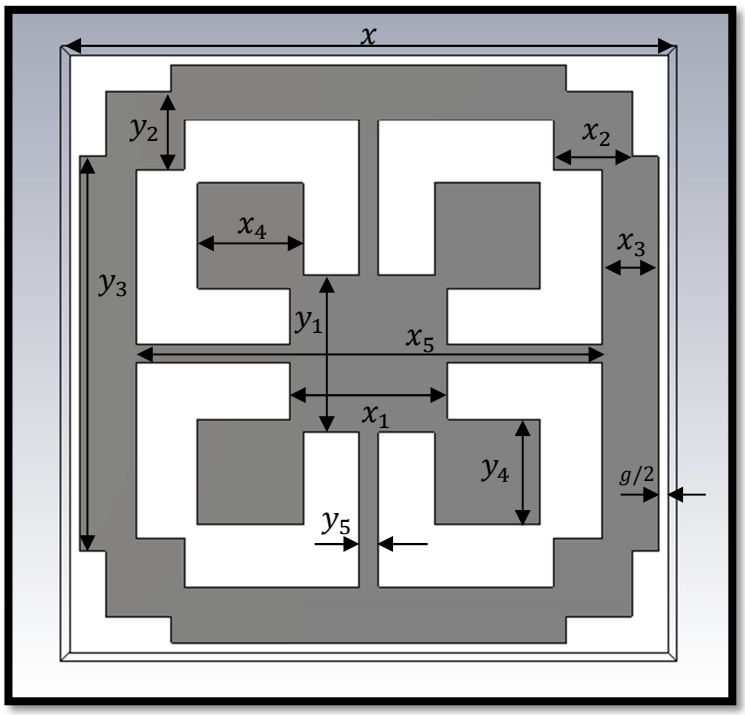

Figure 4.4.1: A new AMC unit cell for the probe-fed open loop antenna

Parameter	Value [mm]
x_1	7.88
x_2	3.92
x_3	2.80
x_4	5.22
x_5	23.40
x	30.00
y_1	7.88
y_2	3.92
y_3	19.6
y_4	5.22
y_5	0.93
g	1

Table 4.4.1: Values for the parameters of the modified new AMC unit cell

The unit cell has been simulated and the phase reflection is shown in Figure 4.4.2. For this unit cell, the 0 ± 90^o bandwidth extends from $1.61 - 1.72\text{GHz}$ and centred at 1.67GHz, with a percentage bandwidth of 6.7%. The 90 ± 45^o bandwidth of the unit cell is given as $1.52 - 1.65\text{GHz}$ centred at 1.61GHz with a percentage bandwidth of 7.8%.

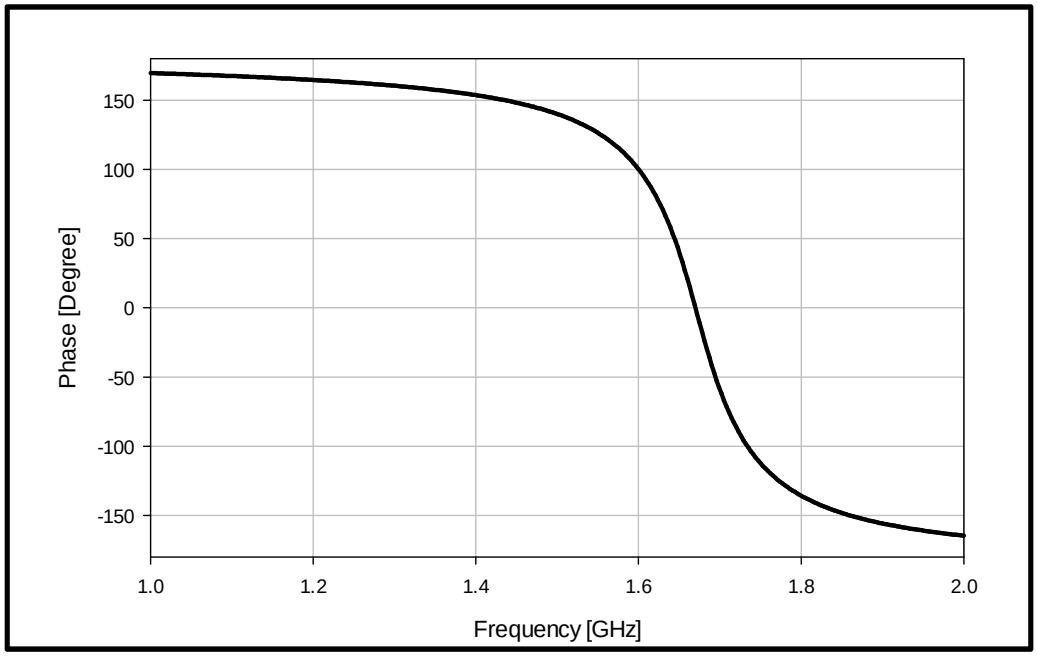

Figure 4.4.2: Phase reflection for the modified new AMC unit cell

4.4.2 *Open Loop Antenna Design and Results*

An open loop antenna has been printed on a dielectric substrate FR4 with a thickness of $h_2 = 0.8\text{mm}$ so that the overall thickness of the antenna is 4mm, which is the same as the probe-fed open loop antenna backed by square patches. The schematic of the open loop is illustrated in Figure 4.4.3. The antenna used in Chapter 4 has been redesigned for best performance with the new AMC. This has been achieved by varying the loop radius R_l, the gap and the loop width l_w using the parametric sweep in CST. The optimum antenna's parameters have been determined as $R_l = 19\text{mm}$, $l_w = 1.63\text{mm}$, and a loop gap of 16^o, which means the loop circumference is $\sim 0.6\lambda_o$ or $\sim 1.2\lambda_g$.

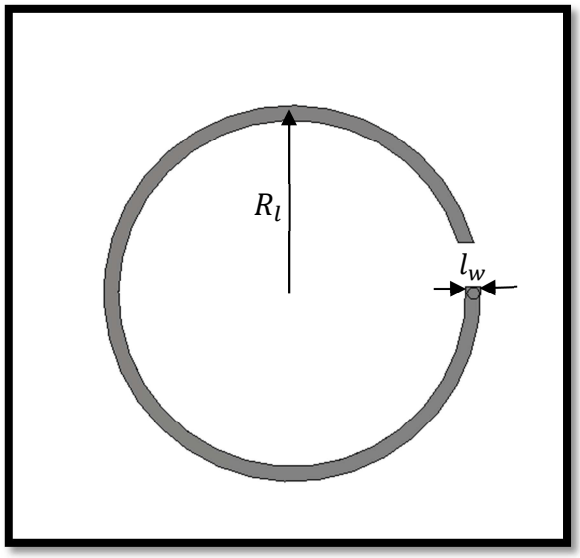

Figure 4.4.3: The new probe-fed open loop antenna

The size of the antenna's layer has been designed to be equal to that of the AMC surface, and the radius of the feeding probe has been chosen as $R_p = 0.65\text{mm}$. The schematic of the antenna is illustrated in Figure 4.4.4.

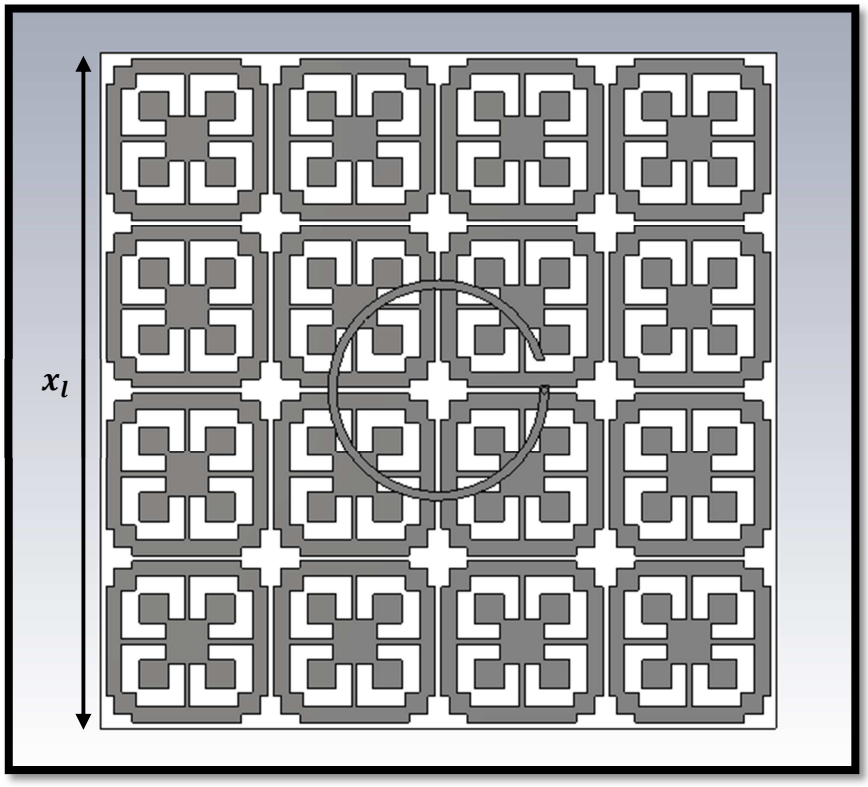

Figure 4.4.4: The probe-fed open loop antenna backed by a novel AMC

The full antenna size is $x_l = 121\text{mm}$, which corresponds to $0.63\lambda_o$, i.e. the size of the ground plane is ~28.2% smaller than square patch AMC, given that both structures

have the same thickness ($h_{tot} = 4\text{mm}$). A prototype has been fabricated and measured as shown in Figure 4.4.5 and Figure 4.4.6.

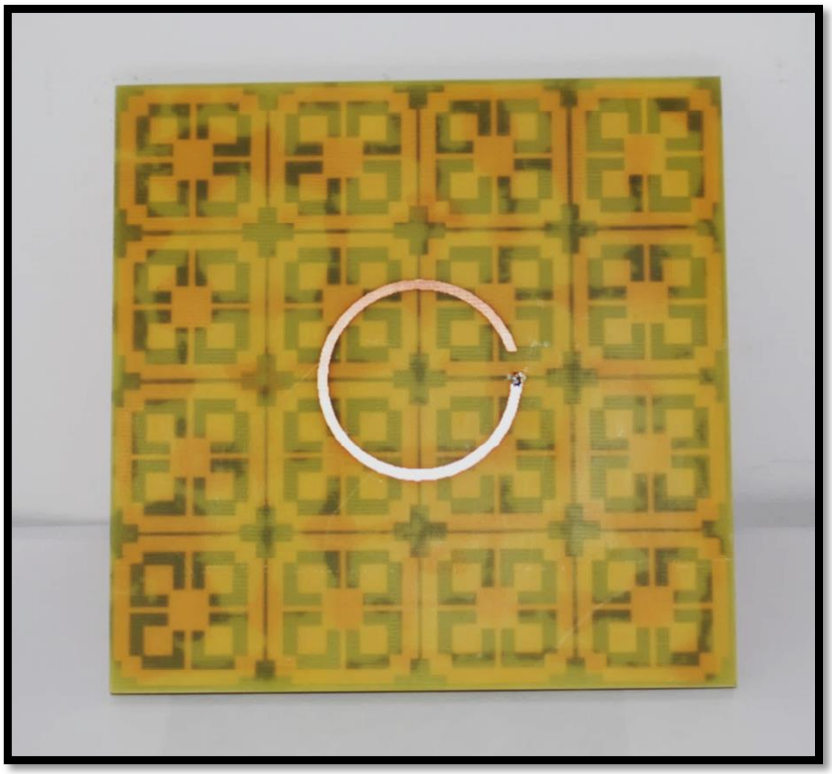

Figure 4.4.5: The manufactured probe-fed open loop antenna backed by a novel AMC

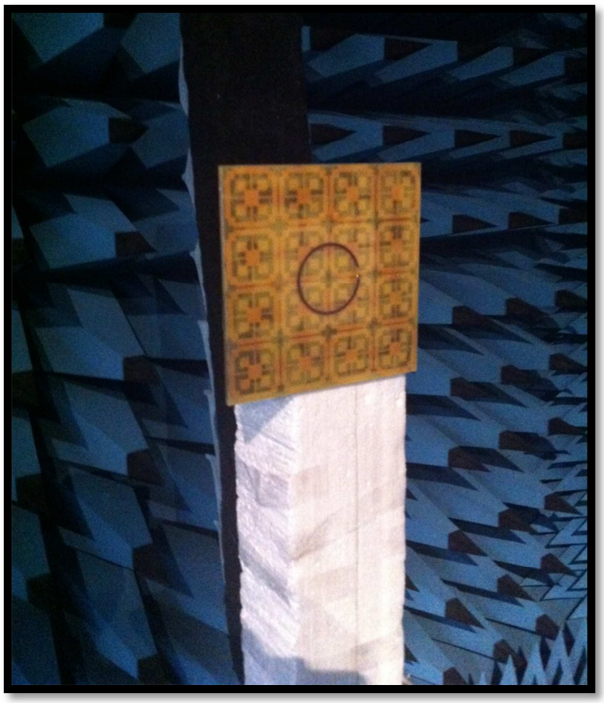

Figure 4.4.6: The manufactured probe-fed open loop antenna backed by a novel AMC in the chamber

A comparison between the last two designed antennas is given in Figure 4.4.7.

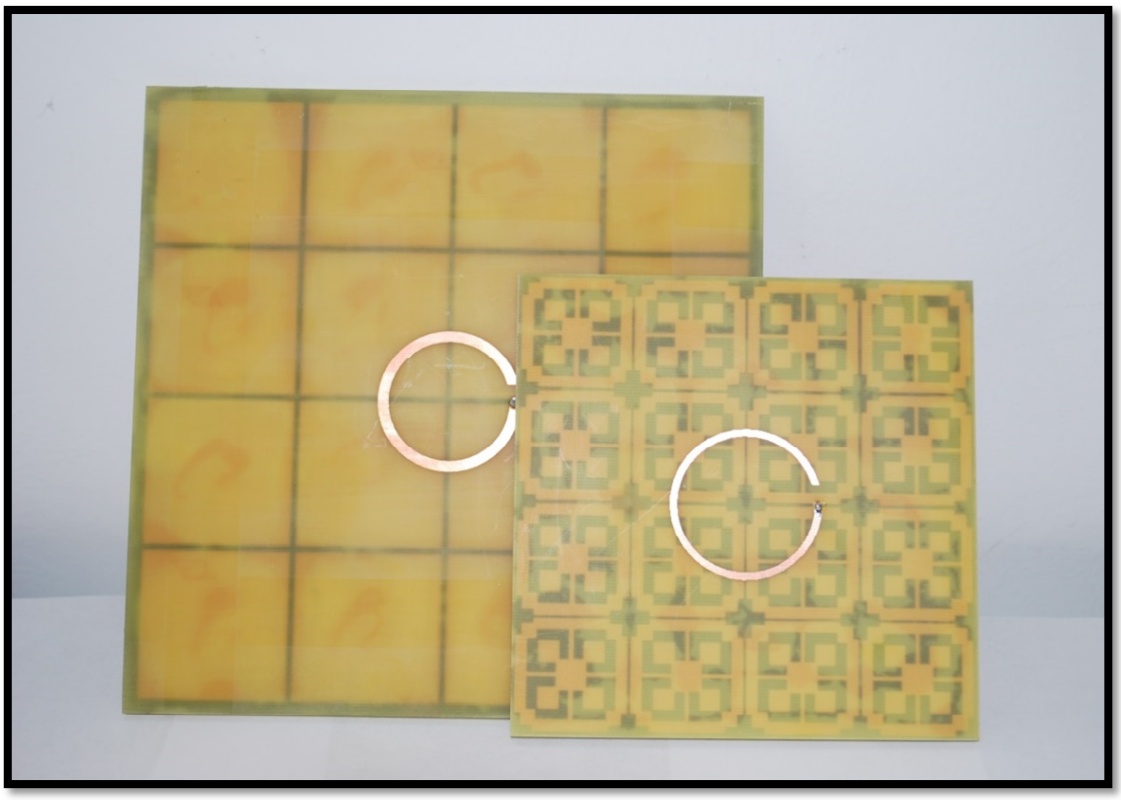

Figure 4.4.7: comparison between the fabricated antennas

Figure 4.4.8 and Figure 4.4.9 present the reflection coefficient and the axial ratio of the CP antenna with and the without the new AMC, where it can be seen clearly that introducing the AMC has improved the matching and provided axial ratio less than 3dB.

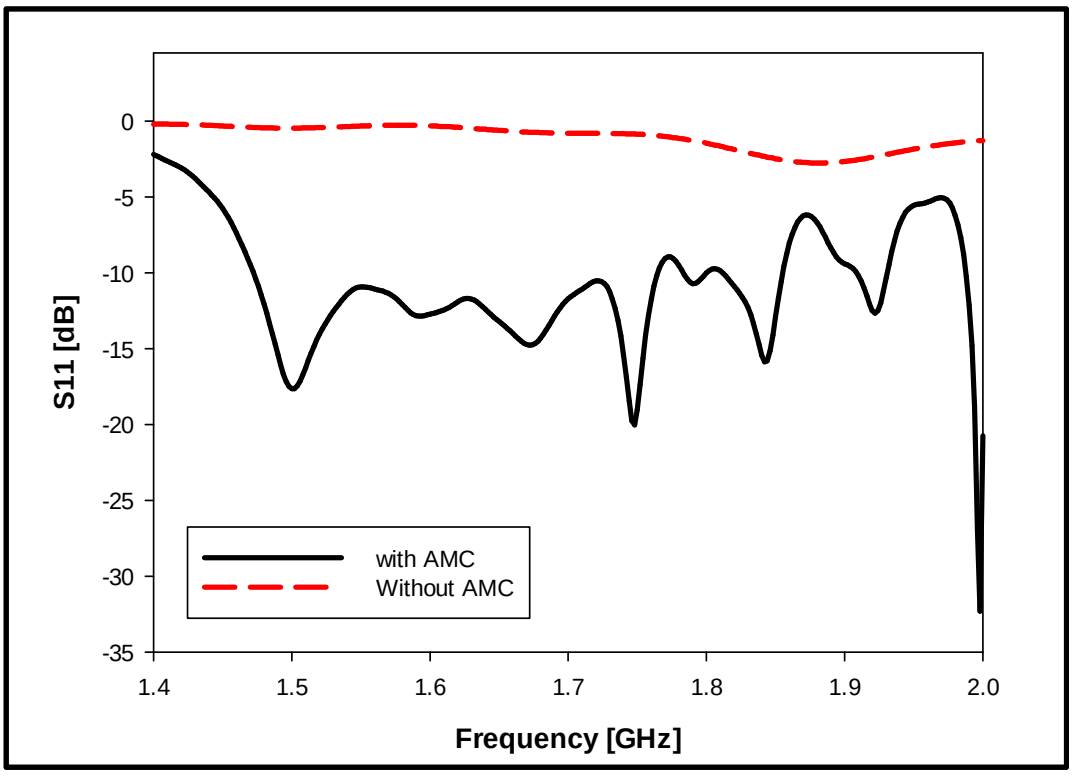

Figure 4.4.8: Reflection coefficient of the CP antenna, with and without the new AMC

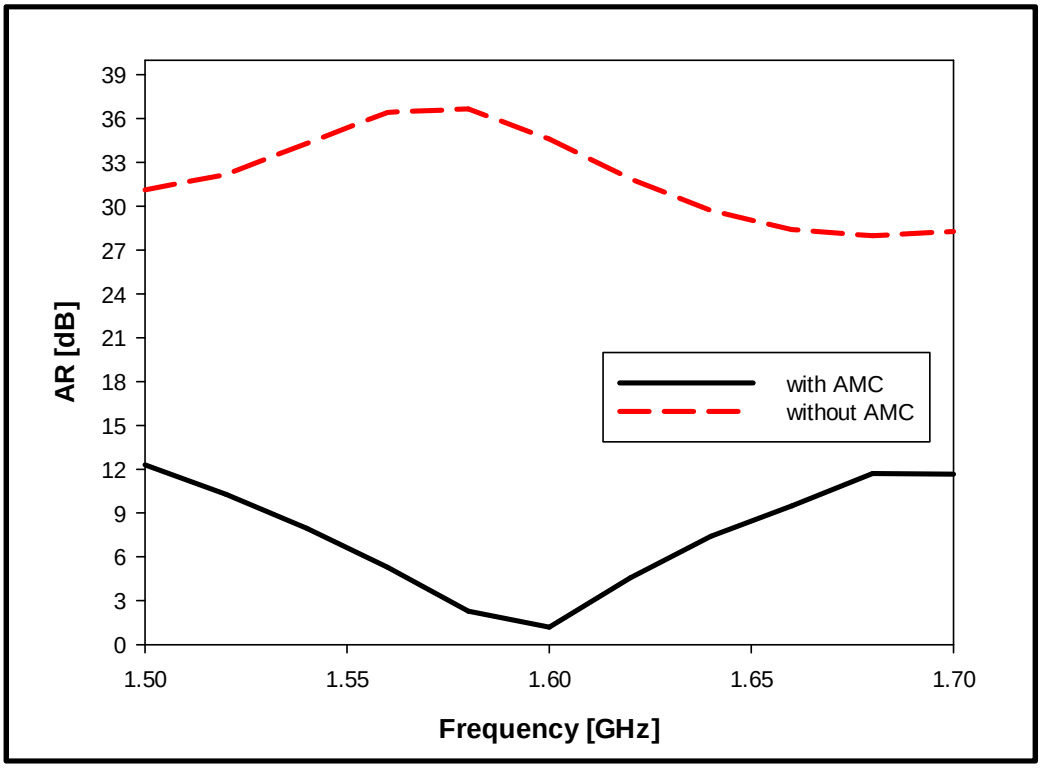

Figure 4.4.9: Axial ratio of the CP antenna, with and without the new AMC

The reflection coefficient is given in Figure 4.4.10, with close agreement between measurements and simulation.

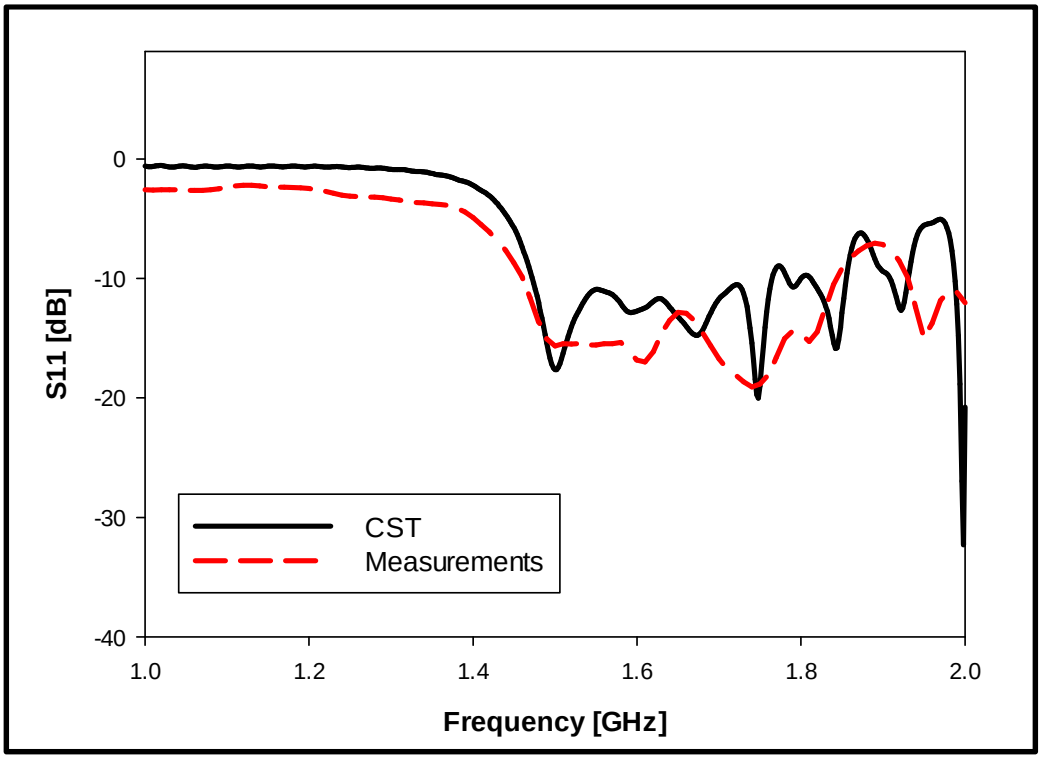

Figure 4.4.10: S_{11} for the probe-fed open loop antenna backed by a new AMC

The simulated -10dB bandwidth is ranging from $1.47-1.76\text{GHz}$ centred at 1.5GHz with a bandwidth of ~19.45%. On the other hand, the measured S_{11} range is $1.46-1.84\text{GHz}$ centred at 1.5GHz with a percentage bandwidth of 25.5%. This good matching can be observed as well by inspecting the input impedance of the antenna as shown in Figure 4.4.11 and Figure 4.4.12. The discrepancy between measured and simulated results can be attributed to fabrication tolerance and experimental errors.

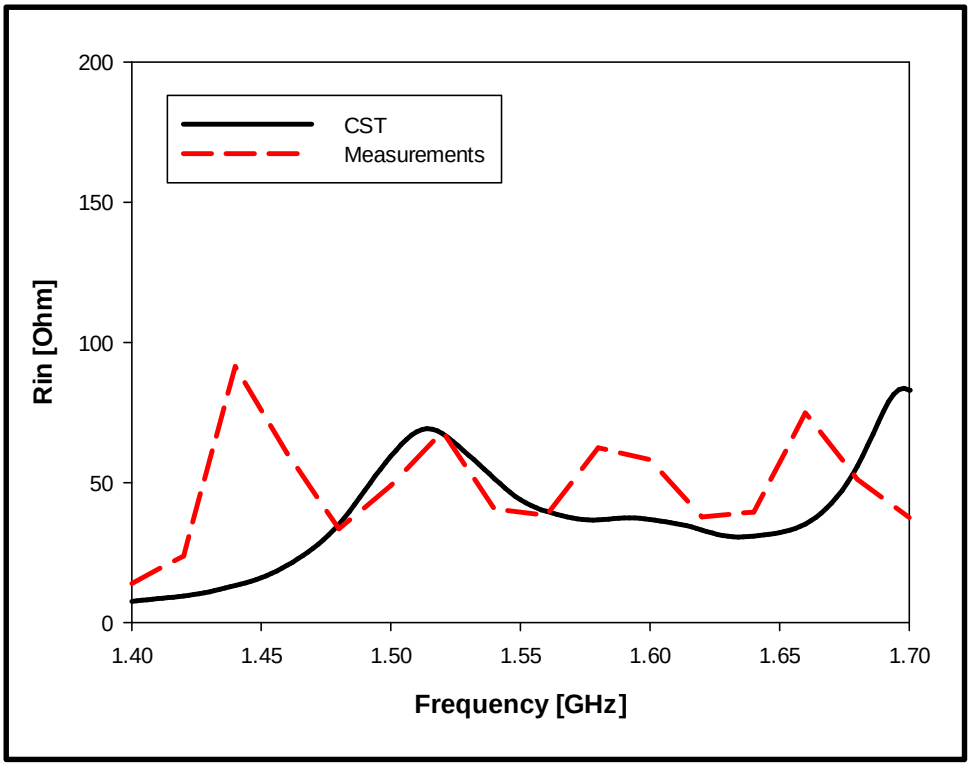

Figure 4.4.11: Input resistance of the probe-fed open loop antenna backed by a new AMC

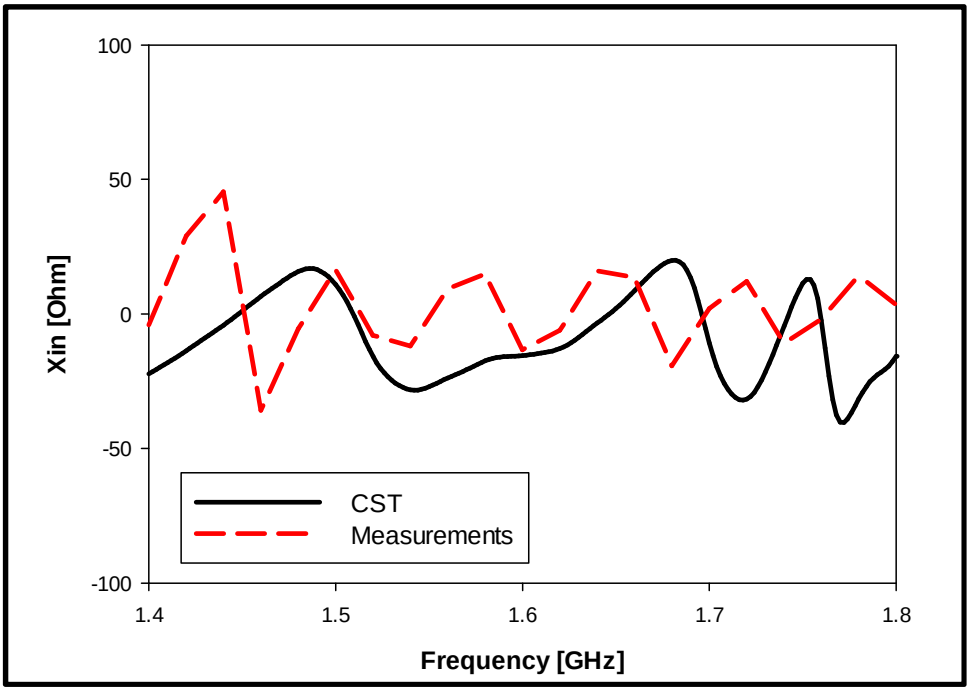

Figure 4.4.12: Input reactance of the probe-fed open loop antenna backed by a new AMC

The axial ratio of antenna is shown in Figure 4.4.13. The simulated 3dB percentage bandwidth is 2.2%, which extends from $1.575 - 1.611\text{GHz}$ and centred at 1.6GHz. The

measured axial ratio range is $1.566 - 1.622\text{GHz}$ centred at 1.6GHz, with a percentage bandwidth of 3.5%. The beamwidth has also been found and it is shown in Figure 4.4.14, where it can be seen that this antenna offers a simulated 3dB axial ratio for an angle of 98^o and a measured bandwidth of 90^o.

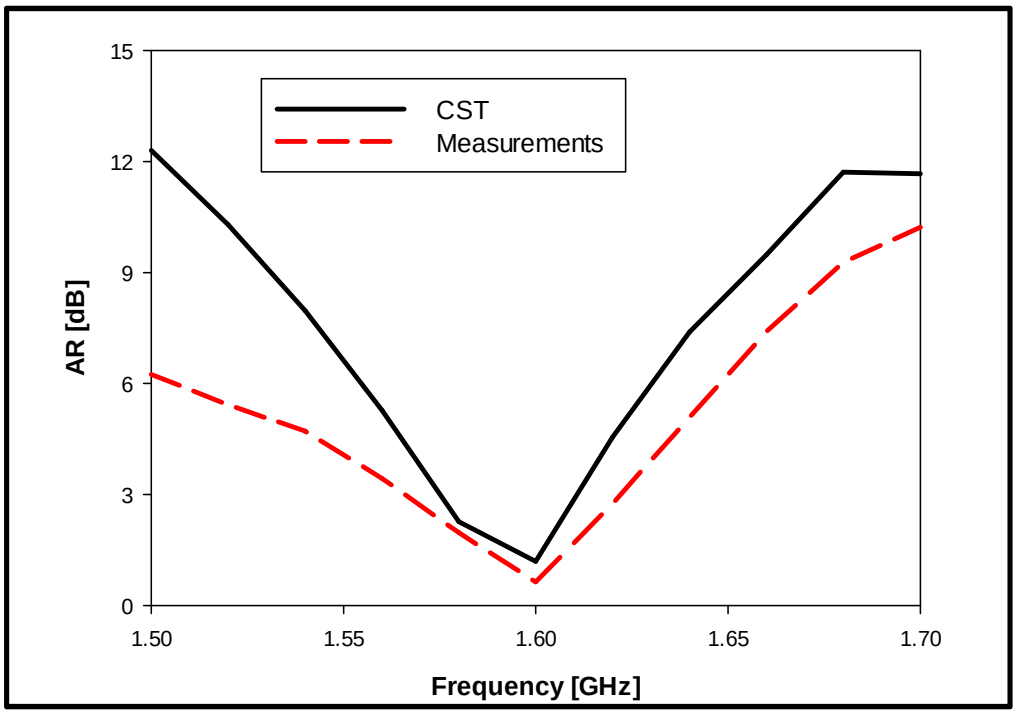

Figure 4.4.13: AR for the probe-fed open loop antenna backed by a new AMC

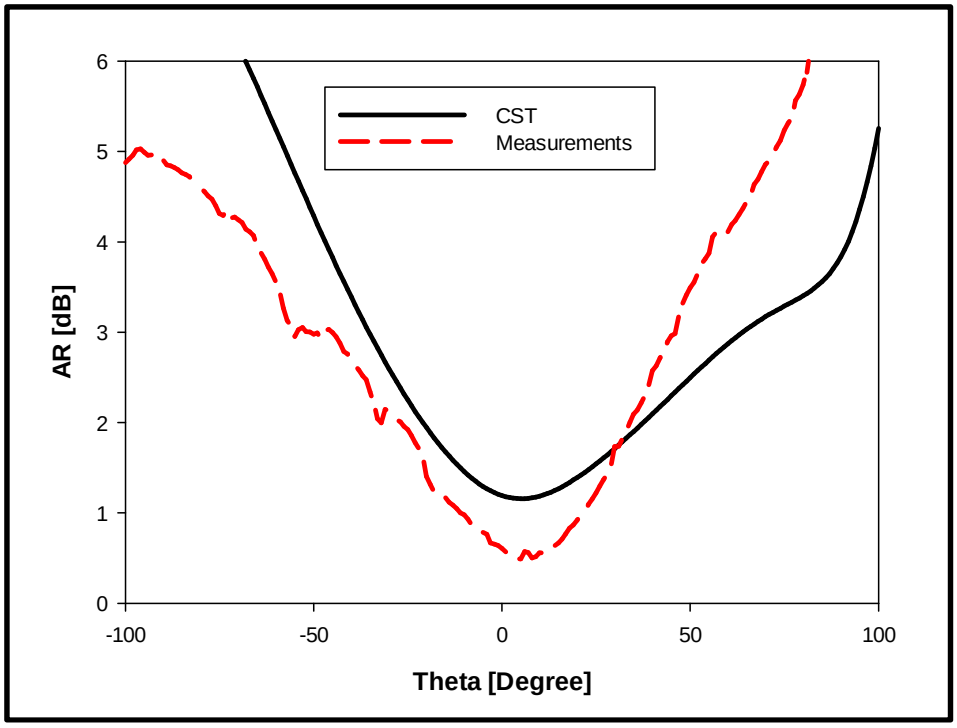

Figure 4.4.14: Beamwidth of the probe-fed open loop antenna backed by a new AMC

The antenna provides a good gain across the CP bandwidth as illustrated in Figure 4.4.15. The CST simulated gain at the minimum AR frequency point is ~7dBi, compared to a HFSS simulated gain of ~4dBi.

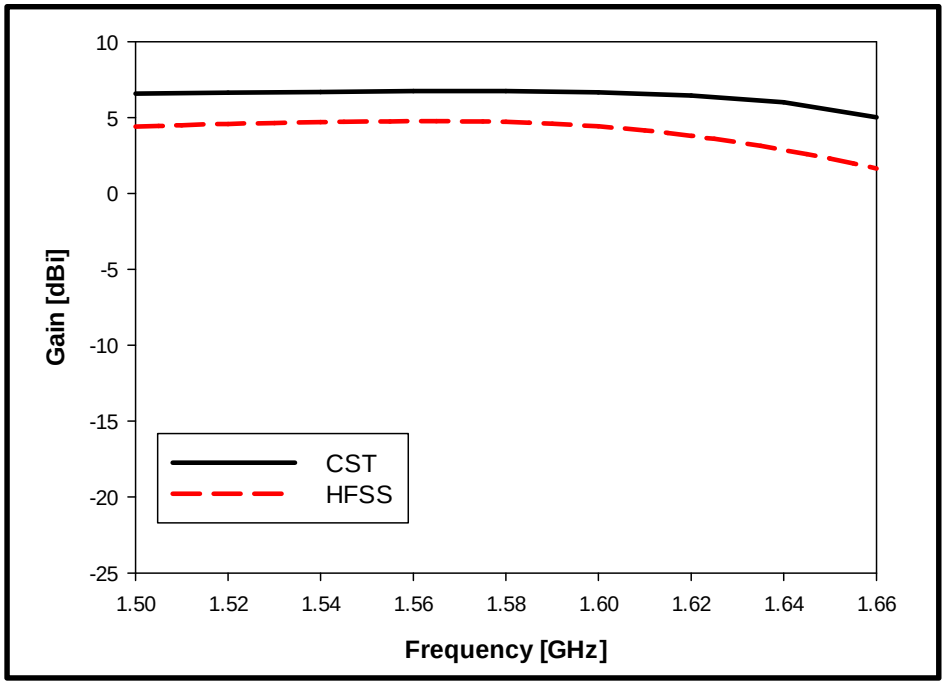

Figure 4.4.15: Gain for the probe-fed open loop antenna backed by a new AMC

The far field patterns are illustrated Figure 4.4.16 and Figure 4.4.17 at the minimum AR frequency points. From these results it can be seen that E_L is ~30dB greater than E_R at bore-sight, which means this is a LHCP antenna.

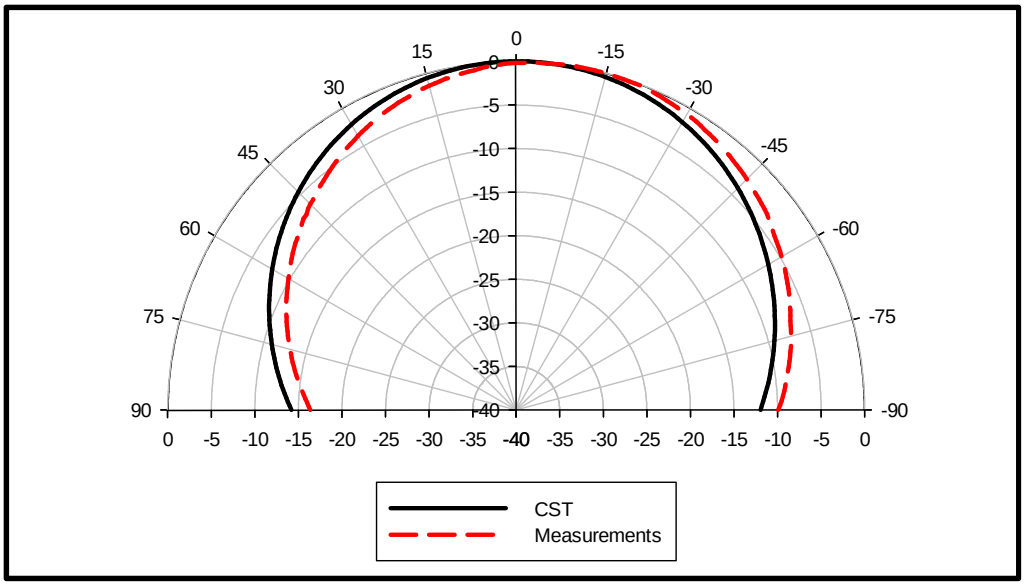

Figure 4.4.16:E_L for the probe-fed open loop antenna backed by a new AMC

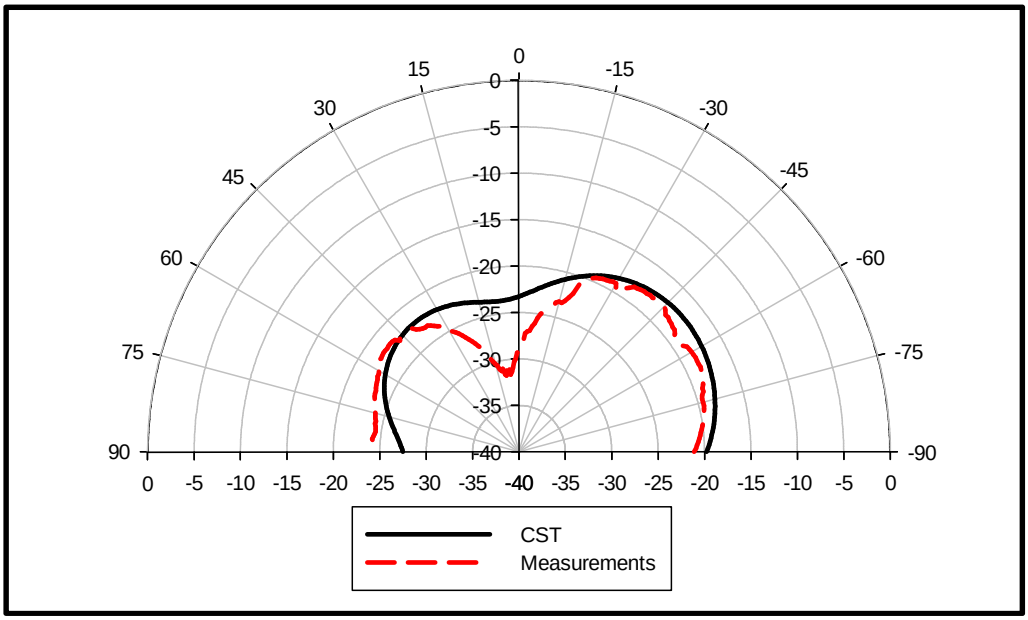

Figure 4.4.17: E_R for the probe-fed open loop antenna backed by a new AMC

A further investigation has been carried out by varying the grid size of the new AMC. First, and as illustrated in Figure 4.4.18, the grid size has been increased to 5×5, which results in a larger ground plane size of 151mm, corresponds to $0.79\lambda_o$.The reflection coefficient and axial ratio are given in Figure 4.4.19 and Figure 4.4.20, where it can be seen that smaller S_{11} bandwidth has been found with axial ratio greater than 3dB.

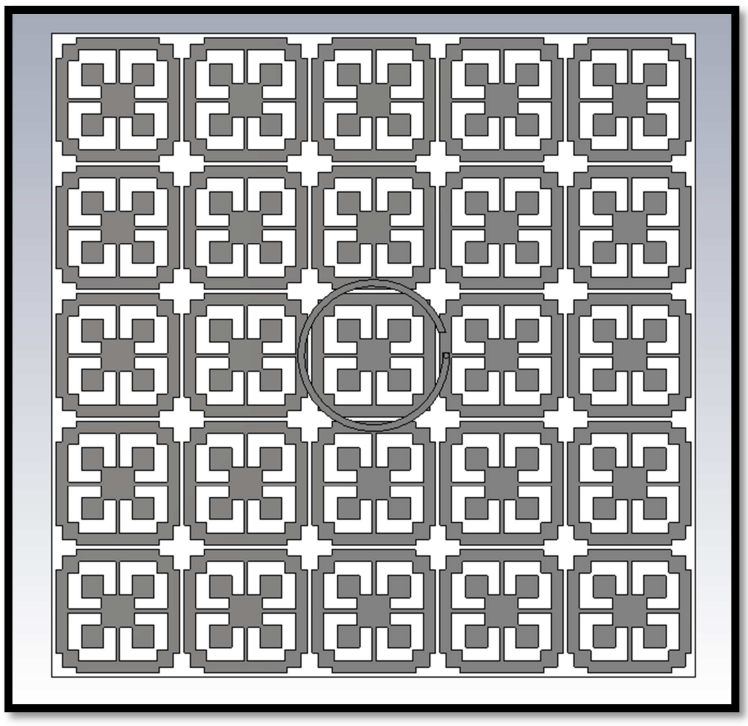

Figure 4.4.18: A 5×5 grid of the probe-fed centred loop, backed by the novel AMC

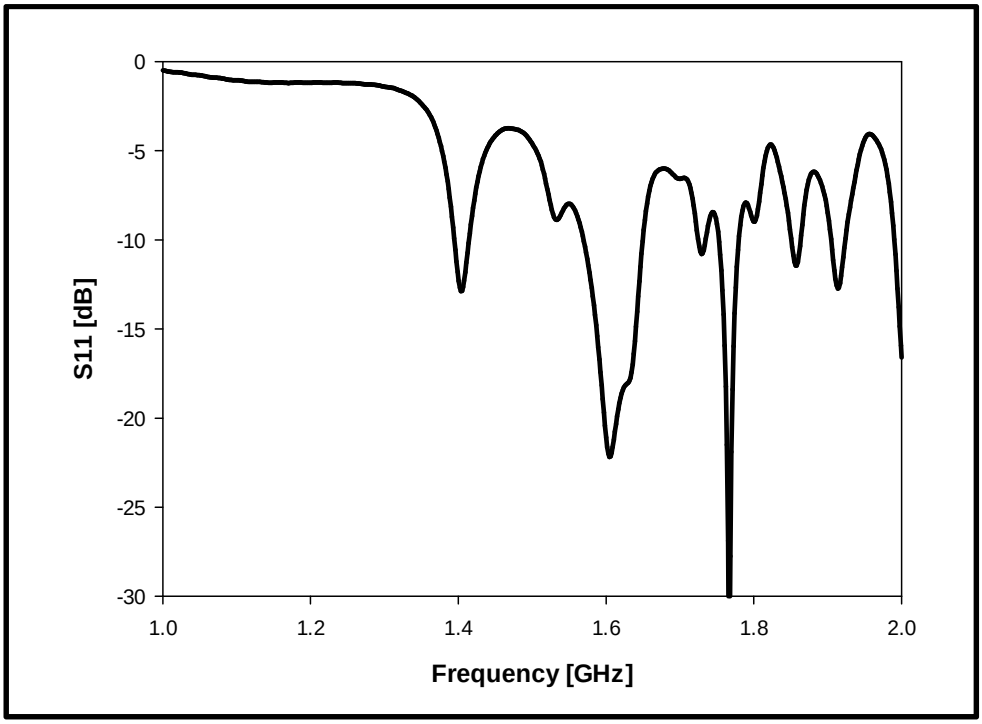

Figure 4.4.19: S_{11} for the 5×5 grid of the probe-fed centred loop, backed by the novel AMC

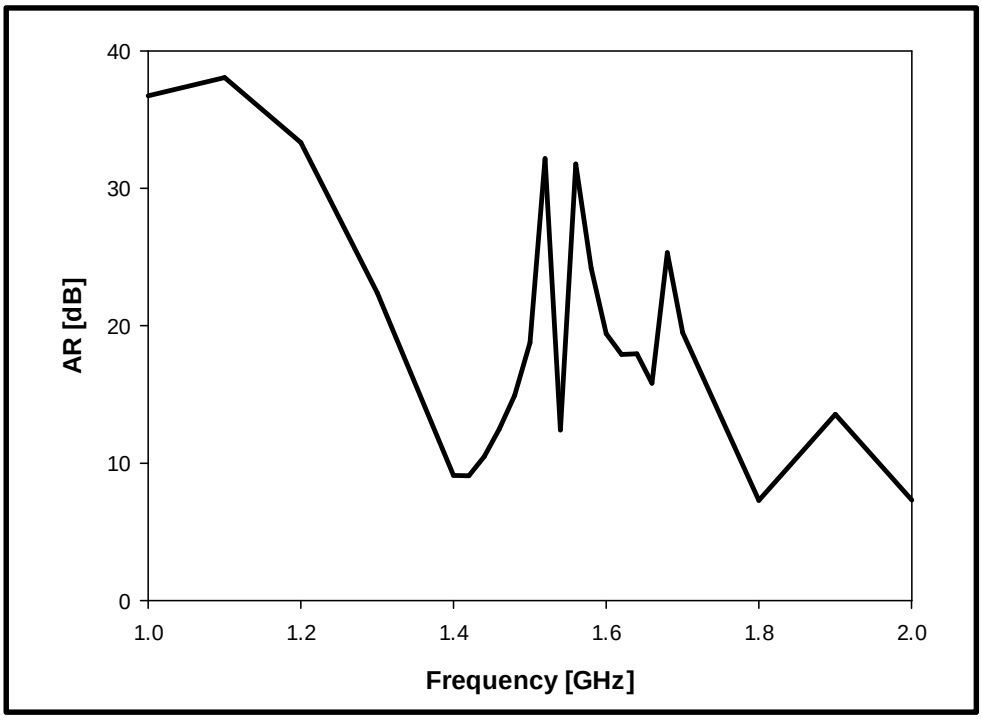

Figure 4.4.20: AR for the 5×5 grid of the probe-fed centred loop, backed by the novel AMC

Due to the strong coupling between the antenna and the AMC, the loop has been displaced as shown in Figure 4.4.21 and the radius has been reduced to 17mm. The resultant reflection coefficient along with input impedance are presented in

Figure 4.4.22, Figure 4.4.23 and Figure 4.4.24, where it can be noticed that wide band impedance matching exists in the desired frequency range. The -10dB S_{11} bandwidth has been calculated from CST as $\sim 29\%$ with a slight dip to the -9dB border in the middle whereas HFSS results showed a bandwidth of $\sim 32\%$.

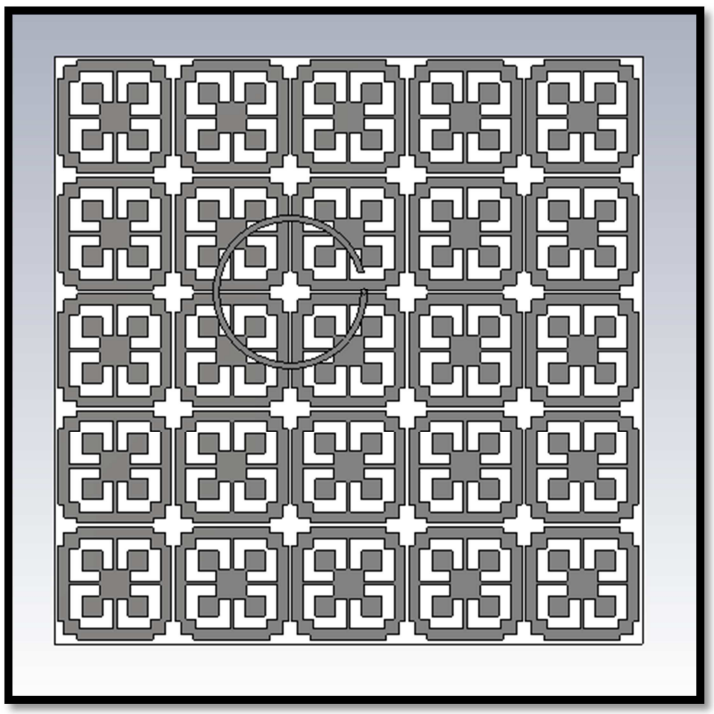

Figure 4.4.21: A 5×5 grid of the probe-fed open loop antenna backed by the novel AMC, with displaced loop

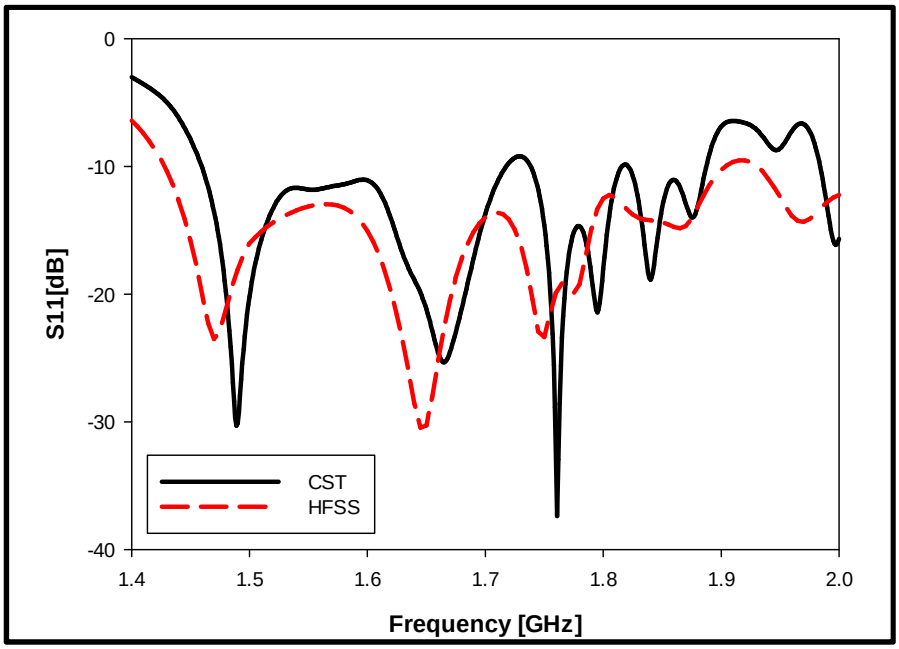

Figure 4.4.22: Reflection coefficient of the 5×5 grid of the probe-fed antenna backed by a novel AMC

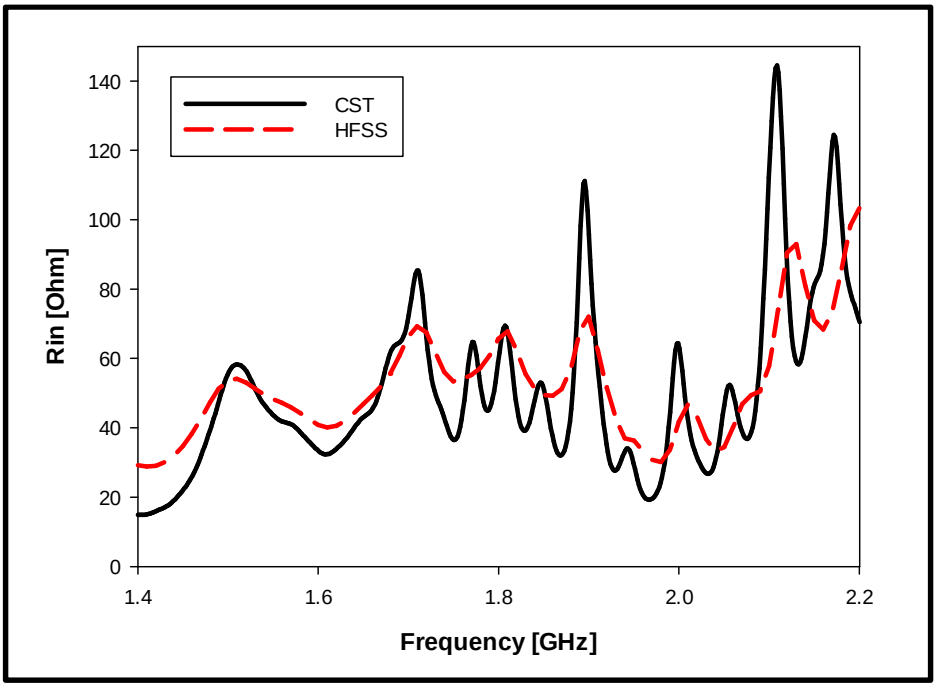

Figure 4.4.23: Input resistance of the 5×5 grid of the probe-fed antenna backed by a novel AMC

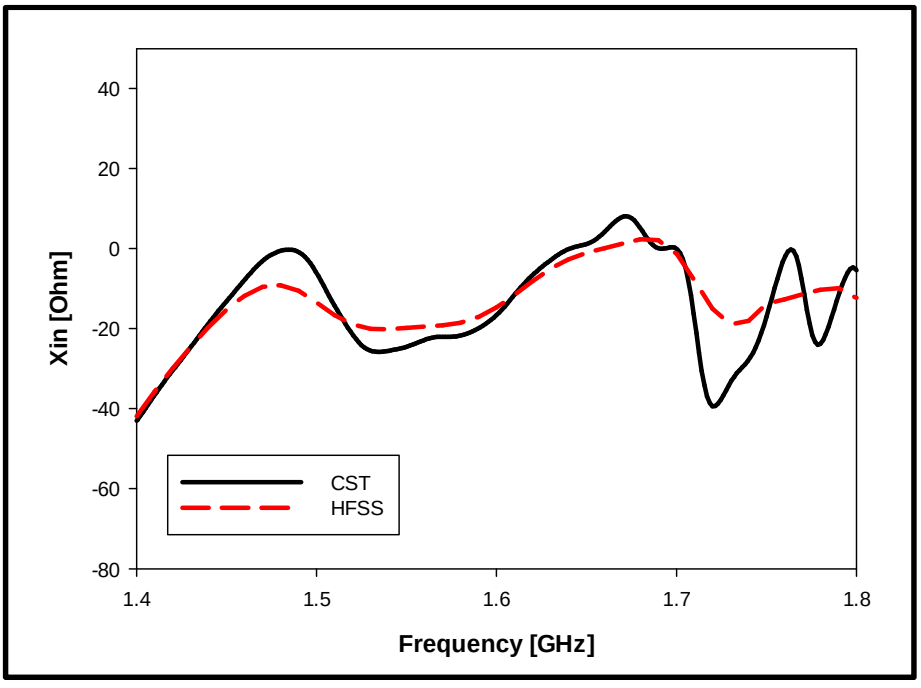

Figure 4.4.24: Input reactance of the 5×5 grid of the probe-fed antenna backed by a novel AMC

The axial ratio is presented in Figure 4.4.25, where it can be seen that a wideband AR bandwidth of $\sim 10\%$ has been achieved in CST that overlaps with the wideband -10dB reflection coefficient. On the other hand, HFSS showed a bandwidth of $\sim 12\%$ with clear two AR minima. Therefore, a significant improvement in the AR bandwidth has been accomplished by increasing the ground plane size to 151mm, which is still

~10% smaller than the square patch AMC. The bore-sight gain is presented in Figure 4.4.26, where it can be seen that the gain is ~7.5dBi at 1.55GHz. However, the gain is dropping below zero at the higher frequency side, which results in effective AR bandwidth with positive gain as ~9.2%

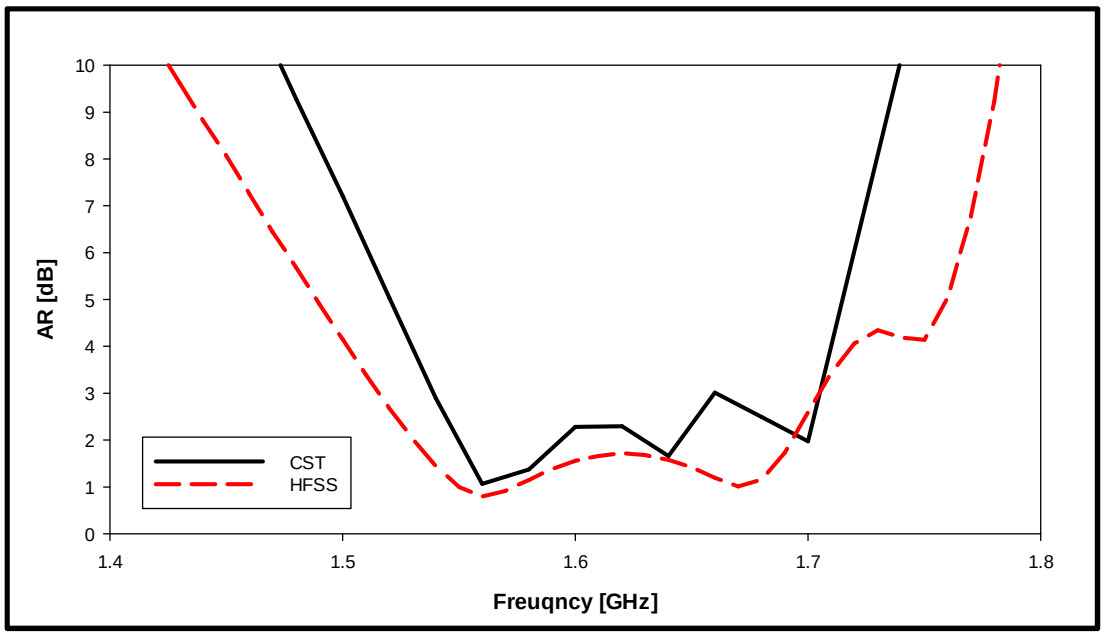

Figure 4.4.25: Axial ratio of the 5 × 5 grid of the probe-fed antenna backed by a novel AMC

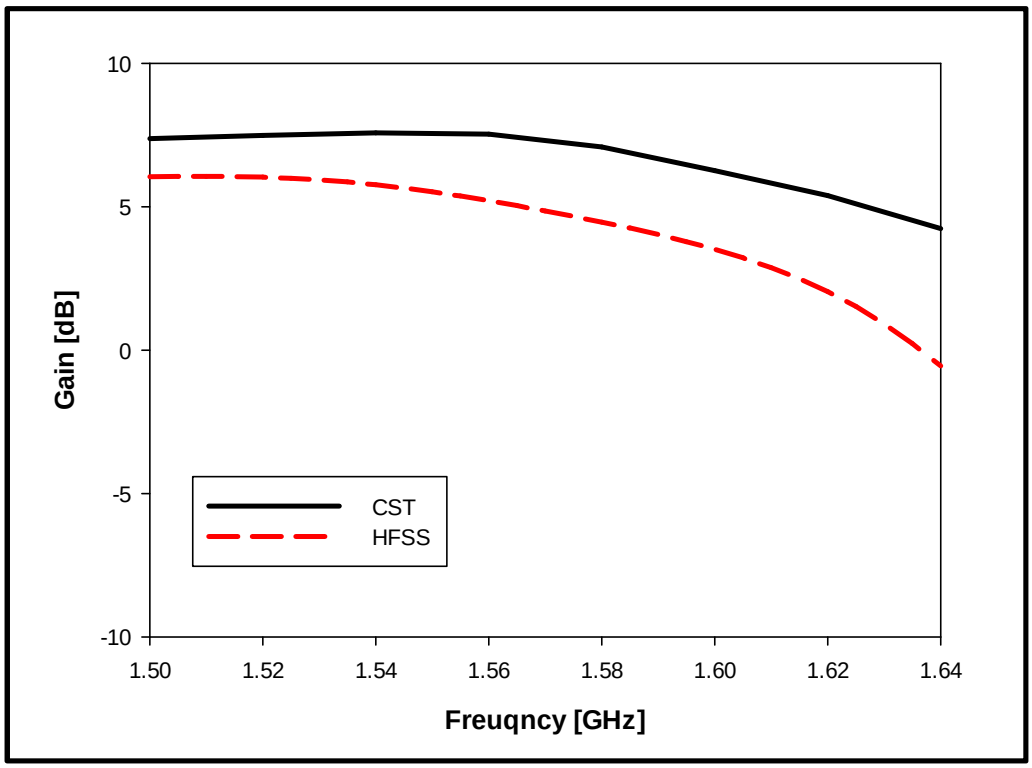

Figure 4.4.26: Gain of the 5 × 5 grid of the probe-fed antenna backed by a novel AMC

The E_L and E_R radiation patterns are presented in Figure 4.4.27 and Figure 4.4.28 where it can be seen that this antenna is Left Handed Circularly Polarised (LHCP) since E_L is ~20dB greater than E_R at bore-sight.

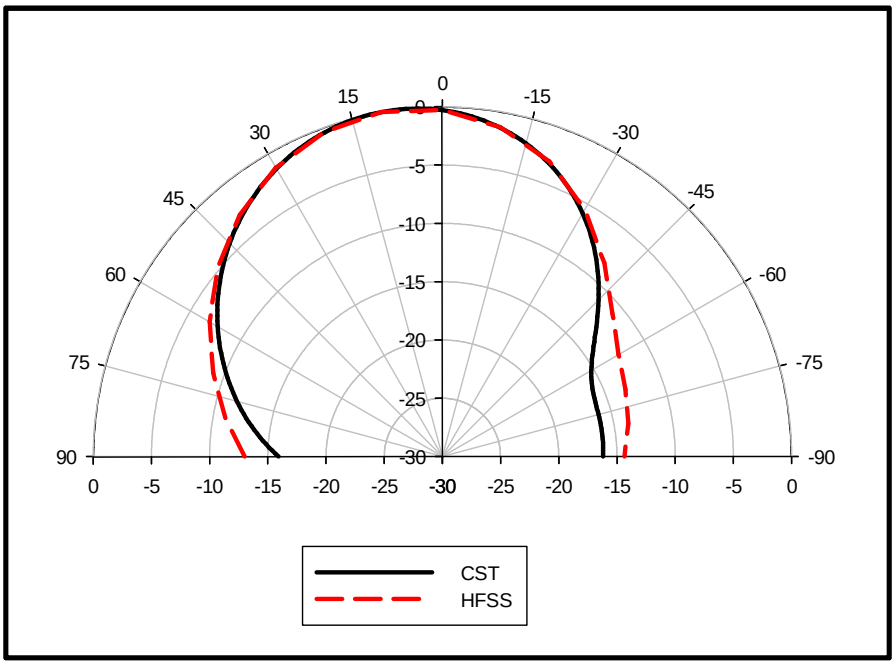

Figure 4.4.27: E_L of the 5×5 grid of the probe-fed antenna backed by a novel AMC

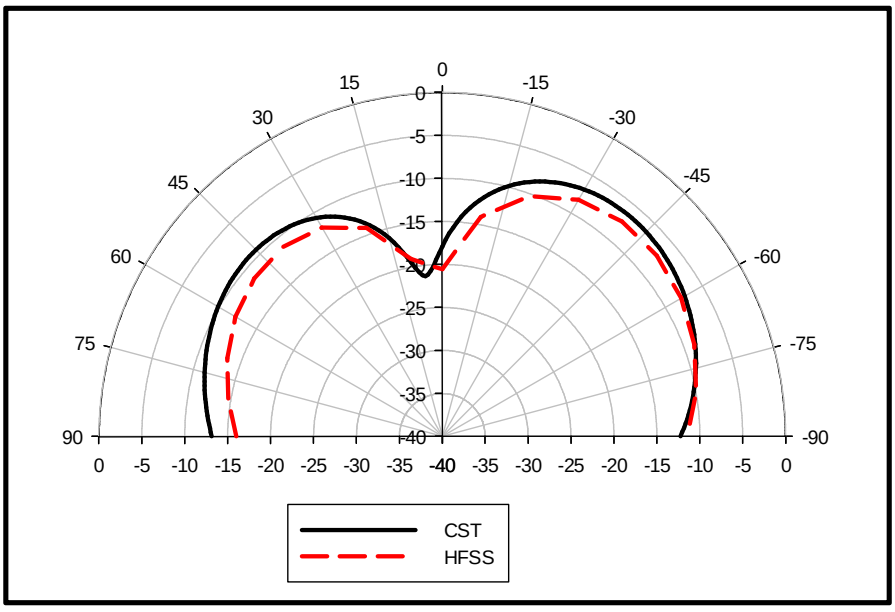

Figure 4.4.28: E_R of the 5×5 grid of the probe-fed antenna backed by a novel AMC

On the other hand, the size of the grid has been decreased to 3×3, which results in total antenna size of 91mm that corresponds to $0.48\lambda_o$. This antenna is miniaturized by 46%, compared to the early designed antenna that is backed by the square AMC. Again, the loop has been located at the centre but deteriorated performance has

been noticed. Therefore, the loop has been displaced as shown in Figure 4.4.29, with optimum loops' radius and width given as 18.9mm and 1.3mm, respectively.

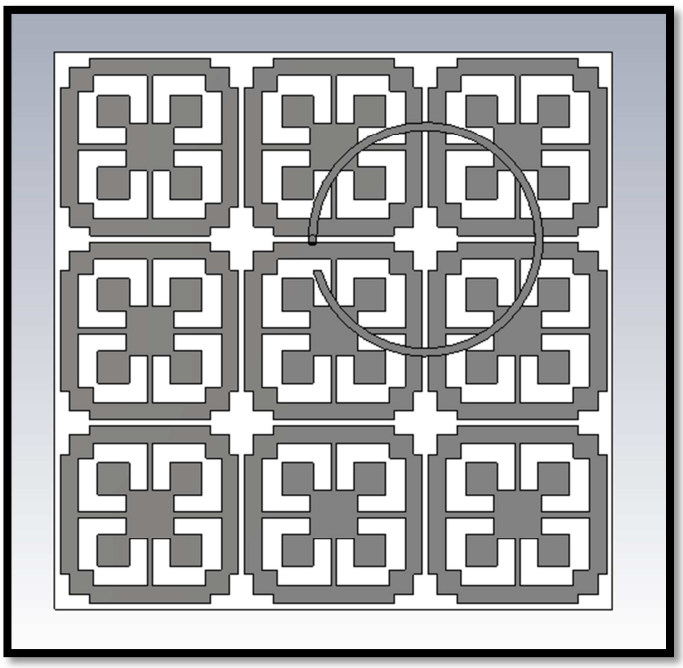

Figure 4.4.29: : A 3×3 grid of the displaced probe-fed open loop antenna backed by the novel AMC

The reflection coefficient is shown in Figure 4.4.30, where, it can be seen that a -10dB bandwidth of 17% has been achieved in CST whereas the bandwidth is 24% in HFSS. This good matching can be observed also at the input impedance result, shown in Figure 4.4.31 and Figure 4.4.32.

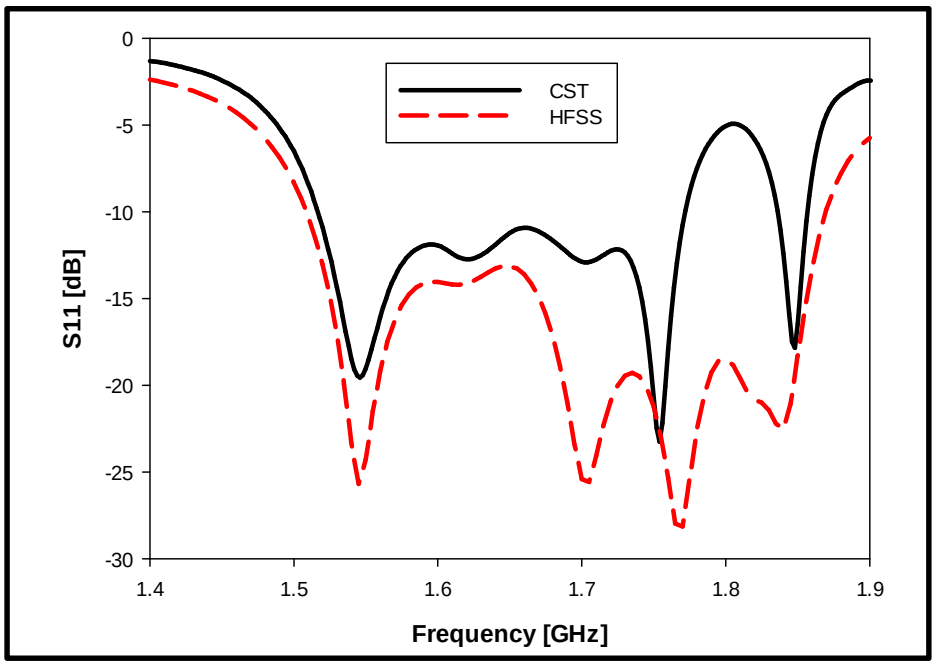

Figure 4.4.30: Reflection coefficient for 3×3 grid antenna

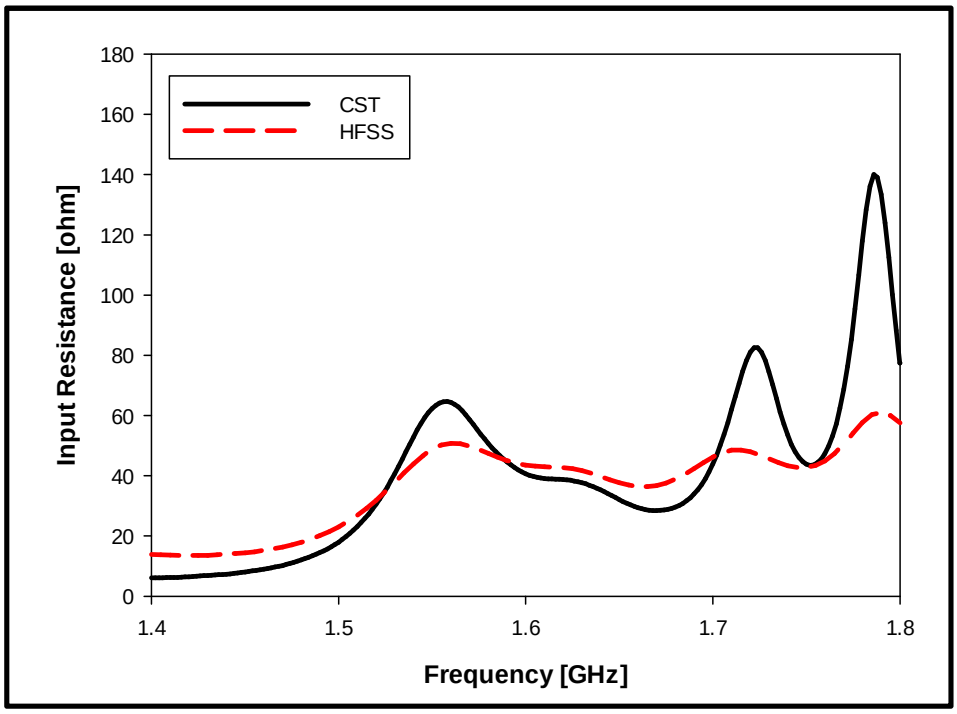

Figure 4.4.31: Input resistance for the 3×3 grid antenna

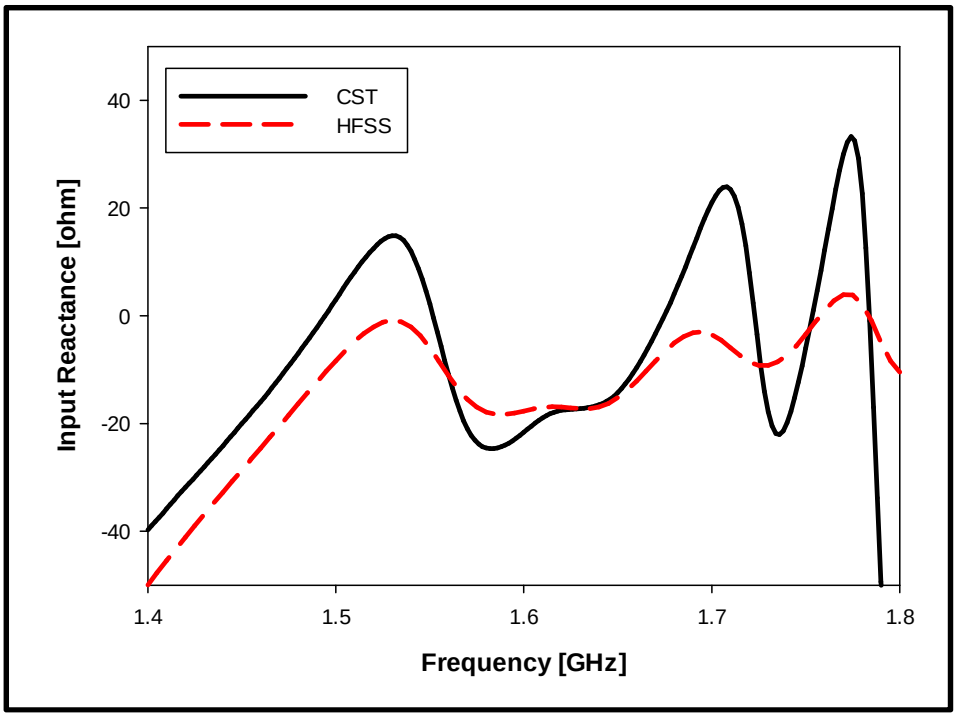

Figure 4.4.32: Input reactance for the 3×3 grid antenna

The axial ratio is shown in Figure 4.4.33, where a 3dB bandwidth of $\sim 2\%$ has been achieved. However, the axial ratio minimum has been shifted to 1.62GHz. This antenna offers a useful gain of ~5dBi at the minimum AR frequency point as shown

in Figure 4.4.34 and is Left Handed Circularly Polarised (LHCP) as shown in Figure 4.4.35, where E_L is ~30dB greater than E_R at bore-sight.

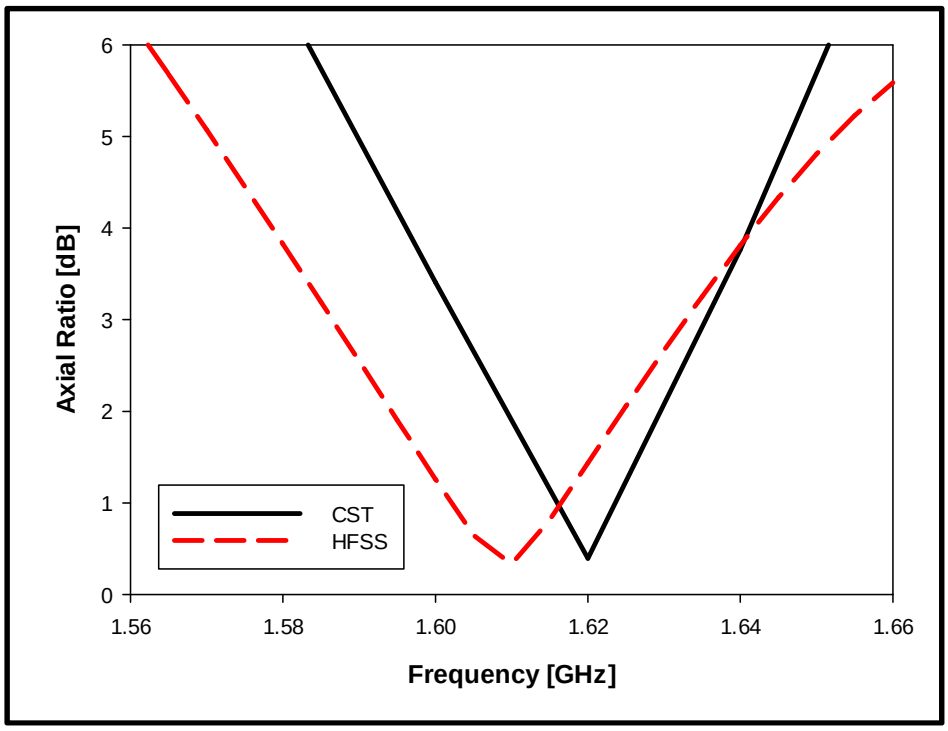

Figure 4.4.33: Axial ratio for the 3 × 3 grid antenna

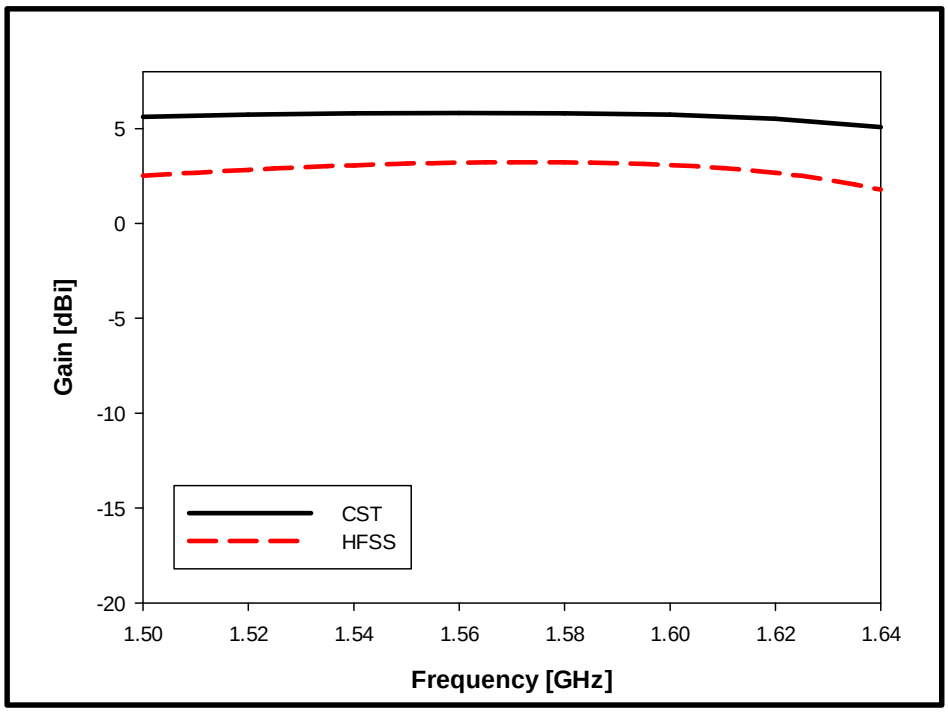

Figure 4.4.34: Gain of the 3 × 3 grid antenna

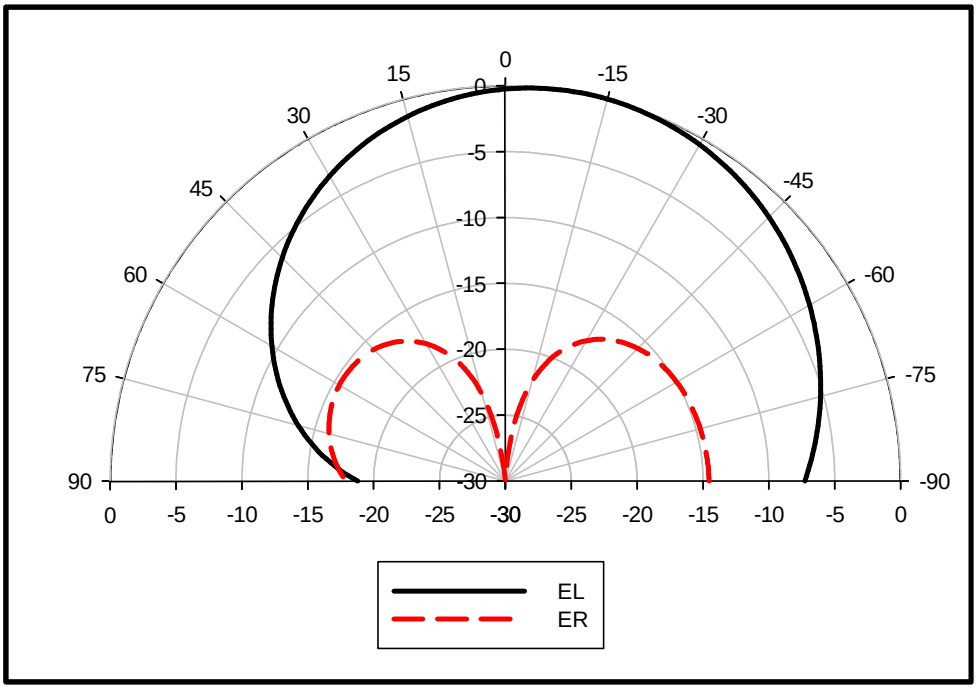

Figure 4.4.35: CST results for the E_L and E_R of the 3×3 grid antenna

To shift the CP operating bandwidth to the desired GPS L_2 band, the unit cell has been modified but the thickness kept the same as 3.2mm and the optimum dimensions are given in Table 4.4.2.

Parameter	Value [mm]
x_1	8.05
x_2	4.02
x_3	2.86
x_4	5.34
x_5	23.92
x	30.66
y_1	8.05
y_2	4.02
y_3	20.03
y_4	5.34
y_5	0.95
g	1.02

Table 4.4.2: Optimum dimensions for the novel AMC for the 3×3 antenna

The optimum loops' radius and width have been found as 19mm and 1.3mm respectively and printed on a FR4 slab of 0.8mm so that the total thickness of the antenna is 4mm, which corresponds to $\lambda_o/48$. The total size of the ground plane has been calculated as 93mm, which corresponds to $0.487\lambda_o$. The new size provides a

reduction of $\sim 45\%$ compared to the probe-fed antenna backed by square patch AMC designed in Chapter 3. The reflection coefficient is shown in Figure 4.4.36 , where, it can be seen a -10dB bandwidth of 17% has been achieved. This good matching can also be observed at the input impedance results, shown in Figure 4.4.37 and Figure 4.4.38. The axial ratio is illustrated in Figure 4.4.39, where a 3dB bandwidth of $\sim 1.8\%$ has been achieved. A useful gain of ~5dBi at the minimum axial ratio has been achieved as shown in Figure 4.4.40. This antenna is Left Handed Circularly Polarised (LHCP) as shown in Figure 4.4.41, where E_L is ~20dB greater than E_R at bore-sight.

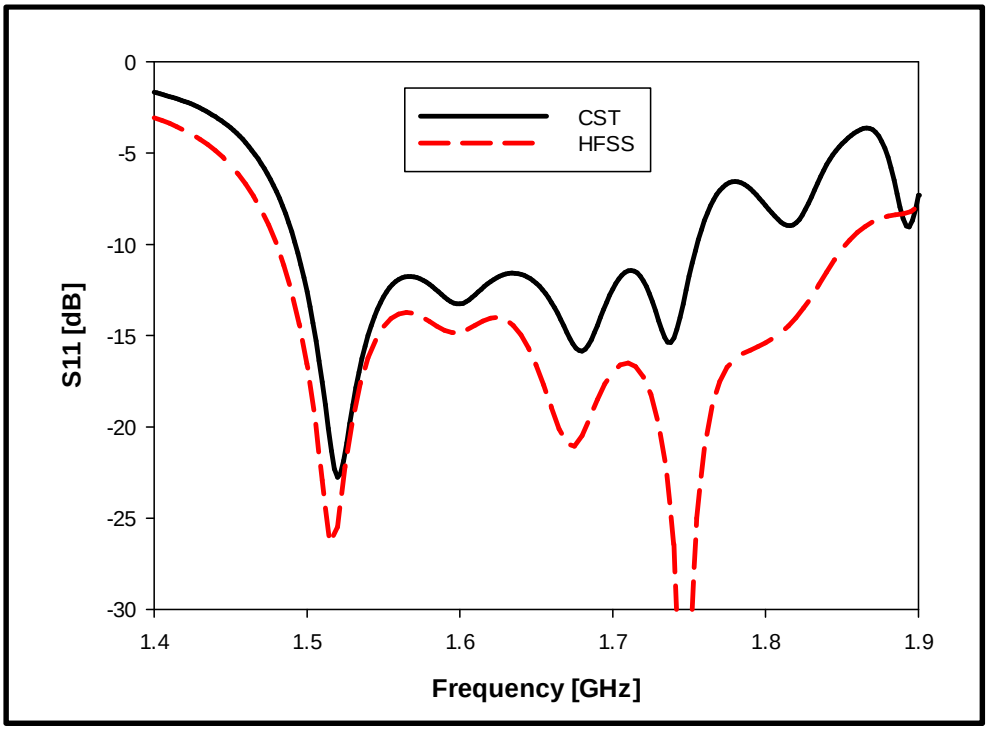

Figure 4.4.36: Reflection coefficient for the modified 3×3 grid antenna

.

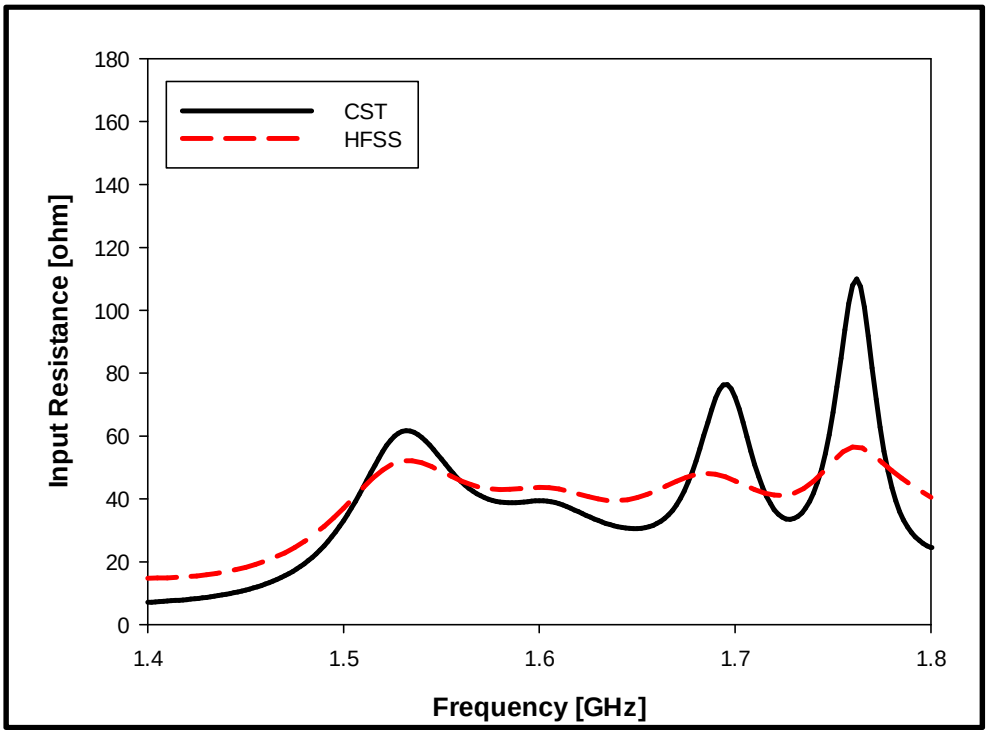

Figure 4.4.37: Input resistance for the modified 3×3 grid antenna

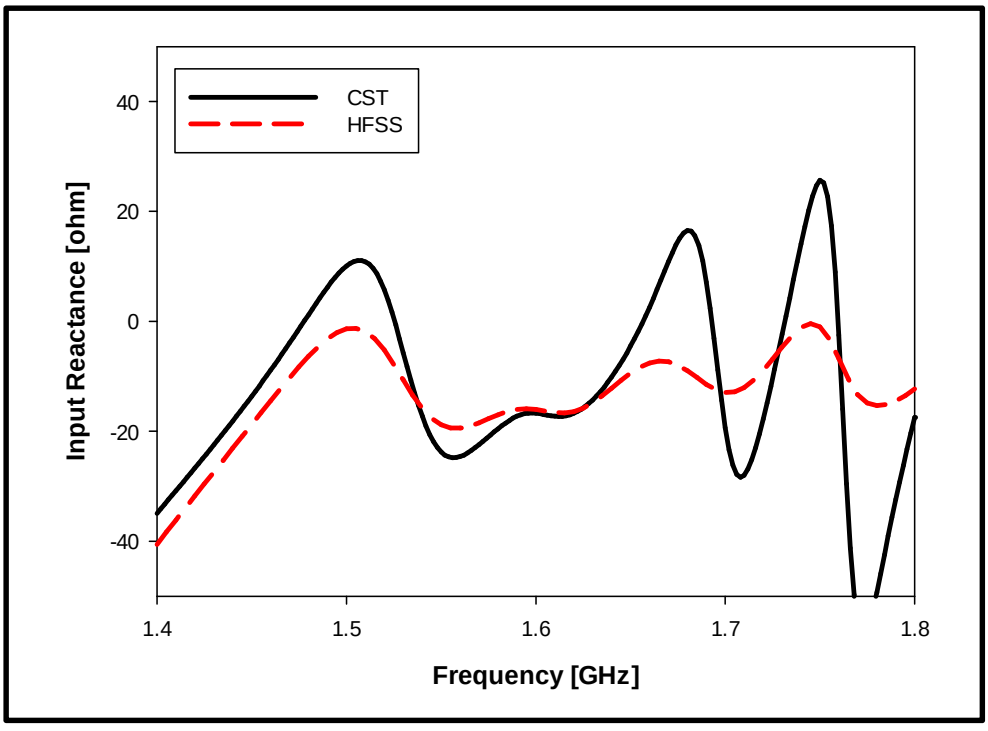

Figure 4.4.38: Input reactance for the modified 3×3 grid antenna

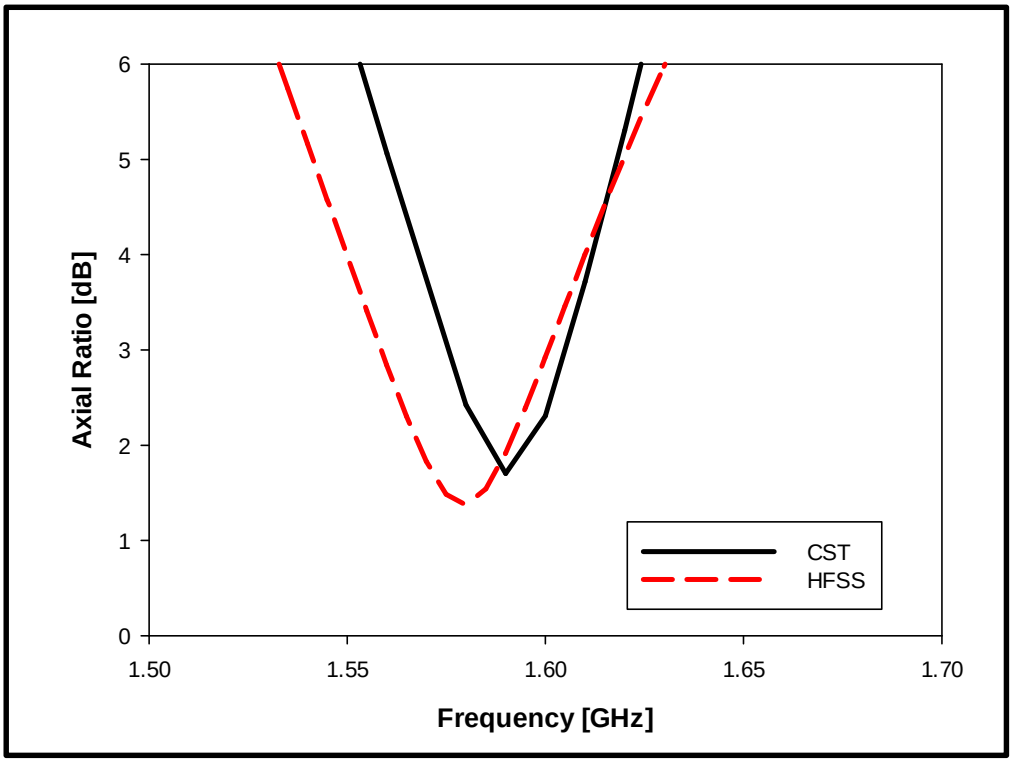

Figure 4.4.39: Axial ratio for the modified 3×3 grid antenna

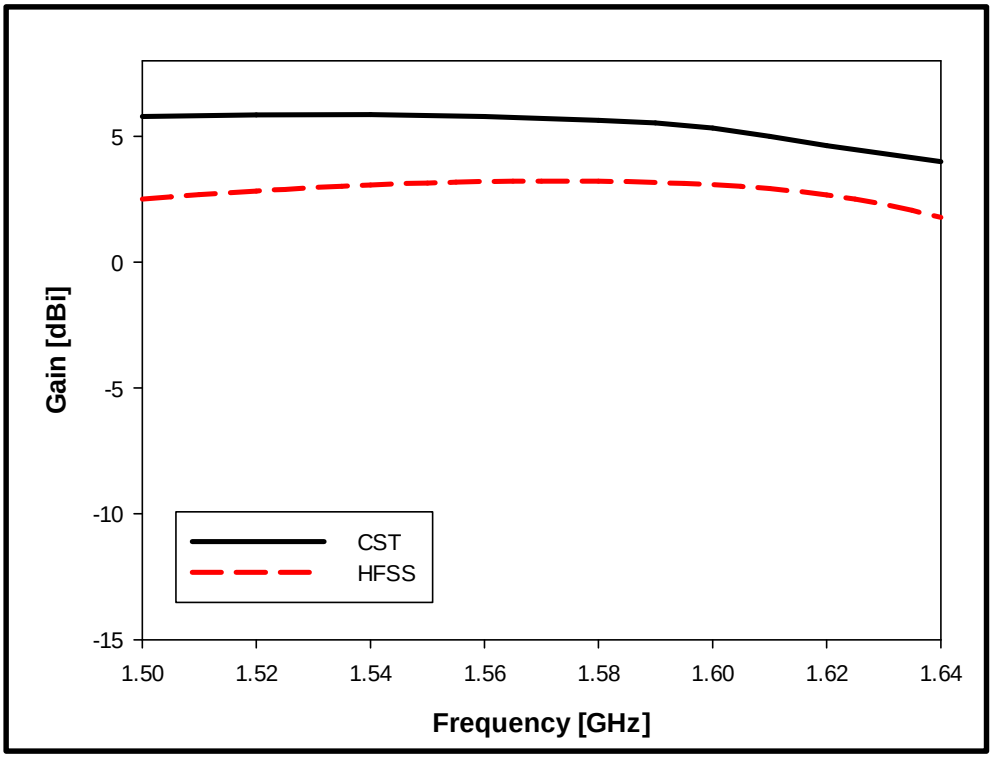

Figure 4.4.40: Gain of the modified 3×3 grid antenna

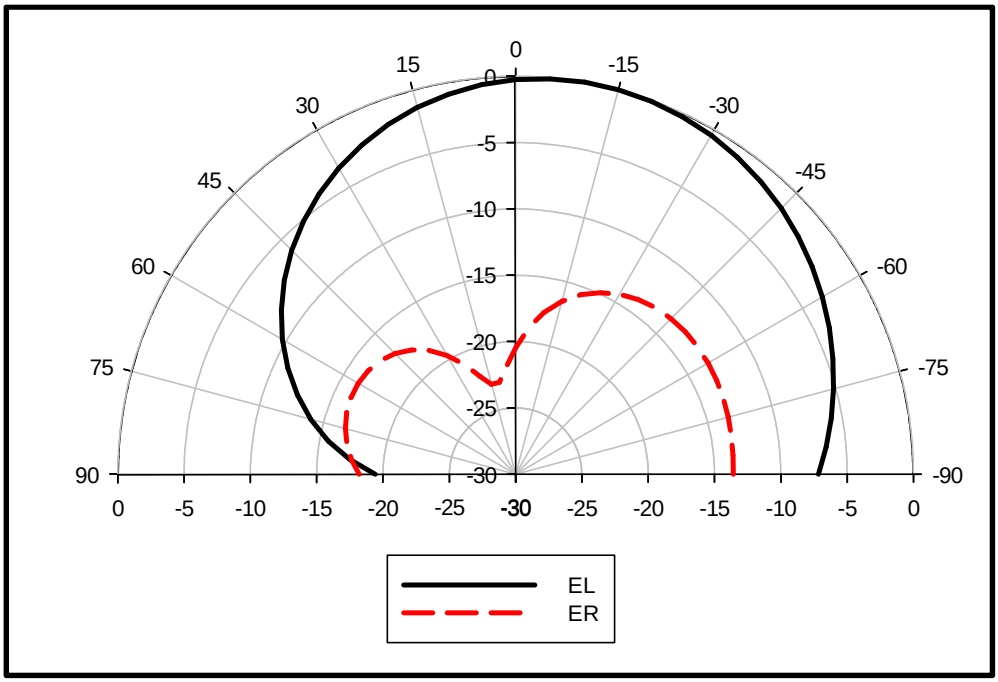

Figure 4.4.41: E_L and E_R of the modified 3×3 grid antenna

A Summary table of the designed antennas in this chapter is presented in Table 4.4.3.

	Unit Cell -90 to 90	Antenna Parameters	S_{11}	AR	Gain
Asymmetrical AMC	1.44-1.56 @ 1.5 (7.7%)	Htotal=4.8+1+1.6= 7.4mm (λo/25.8) Xtotal=130mm (0.68λo), 23% smaller and 54% thicker Rloop=15mm Circumference=0.98λg, 0.77λeff	Dipole (45°): 1.46-1.575 @ 1.48 (7.8%) Loop: Sim: 1.4-1.45 @1.42 (3.5%)	No AR	
New Symmetrical AMC- CPW	1.4366-1.5559 @ 1.4983 (7.96%)	Htotal=4+1+1.6=6.6mm (λo/29) Xtotal=128.2mm (0.67λo) Rloop=15mm Circumference=0.98λg, 0.77λeff	Sim: 1.45722-1.76529 @1.54 (20%) Meas: 1.7909-1.51026 @ 1.54 (18%)	CST: 1.54883-1.62678 @ 1.5798 (4.93%) HFSS: 1.5613-1.6369 @ 1.6 (4.7%)	Sim: 5.6dBi Meas: 6dBi Antenna: RHCP
New Symmetrical AMC- Probe (4×4)	1.6122 - 1.7235 @1.67 (6.66%)	Htotal=3.2+0.8=4mm (λo/48) Xtot=121mm (0.63λo) Rloop=19mm Circumference=1.24λg, 0.974λeff Loop width=1.56mm	Sim: 1.4724-1.7648@1.5035 (19.45%) Meas: 1.46109-1.84353 @ 1.50213 (25.46%)	Sim: 1.5752-1.6108@ 1.6 (2.23%) Meas: 1.566-1.62233 @ 1.6 (3.52%)	Sim: 6.67dBi Meas: 7.09dBi Antenna: LHCP
New Symmetrical AMC- Probe (5×5)	1.6122 - 1.7235 @1.67 (6.66%)	Htotal=3.2+0.8=4mm (λo/48) Xtotal=151mm (0.79λo) Rloop=17mm Circumference=1.1λg, Loop width=1.56mm	CST: 1.46-1.888@1.49 (28.7%) HFSS: 1.42743-1.90417 @ 1.47011 (32%)	CST: 1.53891-1.704@ 1.56 (10.6%) Effective AR with positive gain =9.2% HFSS: 1.51501-1.70432 @ 1.5582 (12.15%) Effective AR=8.9%	CST: 7.2dBi @ 1.57GHz Gain=0 @ 1.68295GHz HFSS: 5.3dBi @ 1.57GHz Gain =0 @1.654 Antenna: LHCP
New Symmetrical AMC- Probe (3×3)	1.6122 - 1.7235 @1.67 (6.66%)	Htotal=3.2+0.8=4mm (λo/48) Xtotal=91mm (0.48λo) Rloop=18.9mm Circumference=1.23λg, Loop width=1.3mm	CST: 1.5167-1.7718 @1.5454 (16.5%) HFSS: 1.5069-1.8684 @ 1.5442 (23.4%)	CST: 1.6027-1.6355@ 1.62 (2.02%) HFSS: 1.5865-1.6328 @ 1.61 (2.9%)	CST: 5dBi
New Symmetrical AMC- Probe (3×3) Scaled	1.6122 - 1.7235 @1.67 (6.66%)	Htotal=3.2+0.8=4mm (λo/48) Xtotal=93mm (0.487λo) Rloop=19mm Circumference=1.23λg, Loop width=1.3mm	Loop: CST: 1.4924-1.7552 @1.52 (17.3%) HFSS: 1.4794-1.8487 @ 1.5147 (24.4%)	CST: 1.5756-1.6049@ 1.59 (1.8%) HFSS: 1.5586-1.6007 @ 1.58 (2.7%)	CST: 5dBi

Table 4.4.3: Summary of designs in Chapter 4

4.5 Conclusion

In this chapter, a novel symmetrical and asymmetrical AMC cells have been designed. It has been shown that the asymmetrical unit cell has not provided a suitable ground plane for circularly polarised antenna. For the symmetrical unit cell, two feeding mechanisms have been used; CPW and probe fed. The probe-fed open loop antenna fed backed by a novel AMC has provided 3dB axial ratio for the entire GPS L_1 bandwidth with a good matching and a useful overlapping gain. Additionally, the height of this antenna has been reduced by $\sim 125\%$ compared to reported designs [112]. Moreover, the size of the ground plane has also been reduced by $\sim 28\%$ compared to the square patch AMC antenna using a 4×4 grid. Moreover, a reduction of 45% has been achieved when a 3×3 grid has been used. Additionally, it has been demonstrated that when designing AMC for low profile CP antennas, the 90 ± 45^{o} reflection phase has been used [37].

CHAPTER 5

Design of a Dual Band AMC

5.1 Introduction

It has been demonstrated in Chapters 3 and 4 that a total antenna thickness of $\sim\lambda_o/48$ can be achieved using an AMC ground plane. A further step is to deploy a dual band AMC ground plane as an alternative to using a thick substrate, cavity, or a foam gap between the antenna and the PEC ground plane to design a low profile dual band circularly polarised antenna. For example, an S-shaped slotted patch has been designed for dual band circularly polarised radiation at L_1 and L_2 GPS frequency bands [115]. The antenna has been excited using a microstrip line printed under a coupling aperture. A foam sheet has been placed between the S-slotted antenna and the coupling aperture resulting in increasing the overall thickness of the antenna to $\sim \lambda_o/11.6$, where λ_o is the free space wavelength at the L_2 GPS band. In another study, a dual band CP operation has been achieved by inserting an air gap between two truncated square patches etched on two substrates of different dielectric constants, which provided a total antenna thickness of $\sim \lambda_o/21.7$ [116]. In addition, two concentric annular-ring patches etched on two FR4 dielectric slabs and separated by an air gap for dual band L_1 and L_2 GPS band have been reported [117]. In that study, dual feed has been incorporated with a 3-dB hybrid to achieve wide axial ratio bands, and the total antenna thickness has been calculated as $\sim \lambda_o/20.8$. On the other hand, a cavity can be used to support a dual band operation, where an annular square slot antenna backed by a cavity has been designed to operate at the L_1 and L_2 GPS bands [118]. The two square slots were etched on opposite sides of an FR4 PCB board, which resulted in a total antenna of $\sim \lambda_o/11.6$.

Although an AMC ground plane facilitates the design of low profile antennas, it has been rarely used for dual band circularly polarised configurations. However, an AMC surface has been incorporated in a 4-layer wideband antenna where a total thickness of $\sim \lambda_o/20.1$ has been reported [46]. The main challenge with the design of a dual band GPS antenna is the closeness of the L_1 and L_2 frequency bands to each other, with a ratio of 1.28 between the two frequencies. In this Chapter, two dual band AMC designs are presented. The first is the conventional double square dual band AMC, and the second is a novel dual band AMC. It will be shown that the proposed AMC reduces the size of the unit cell by $\sim 42\%$ compared to the double square counterpart with the same thickness of $\sim \lambda_o/39$.

5.1.1 *Double Square Unit Cell AMC*

The conventional double square AMC unit cell has been reported for various dual band applications [52, 119, 120]. A top view is illustrated in Figure 5.1.1, where it can be noticed that the unit cell consists of two concentric squares of sizes w and w_2 that are separated by a square slot of width g_2. The total unit cell size is $x = w + g$, and it has been printed on an FR4 substrate with a height of h_1.

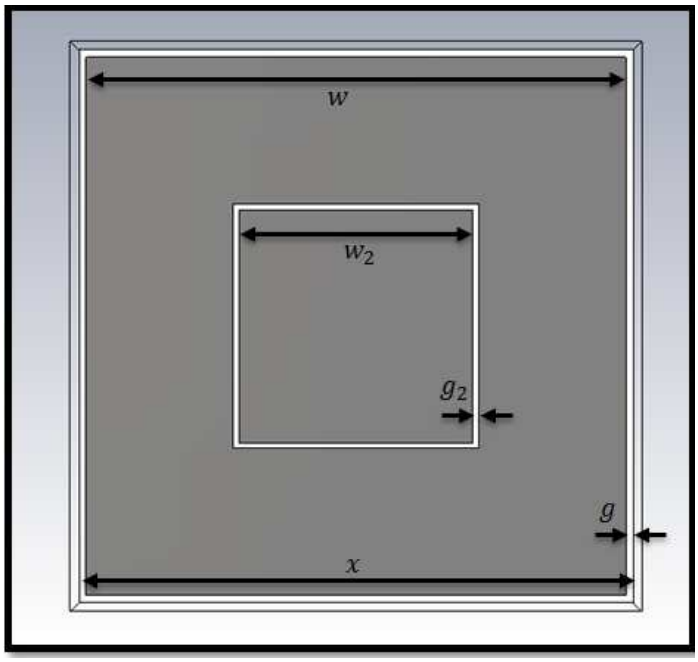

Figure 5.1.1: The double square dual band AMC

Using the design procedure presented in [52], a dual band AMC operates at the L_1 and L_2 bands has been designed and the optimum parameters are presented in Table 5.1.1, where it can be noticed that the respective unit cell thickness and size are $\lambda_o/39$ and $0.48\lambda_o$, where λ_o is the free space wavelength at the first band frequency. The reflection coefficient's phase is shown in Figure 5.1.2, where it can be observed that the 0 ± 90^o bandwidth for the first band is 2.3%, centred at 1.21GHz, and that of the second band is 1.6% centred at 1.59GHz. The 90 ± 45^o bandwidths are 3.5% centred at 1.19GHz for the first band, and 2.2% centred at 1.58GHz for the second band.

Parameter	Value [mm]
w	120
w_1	52
g	3.2
g_1	2.5
h_1	6.4

Table 5.1.1: Optimum dimensions for the double square dual band AMC

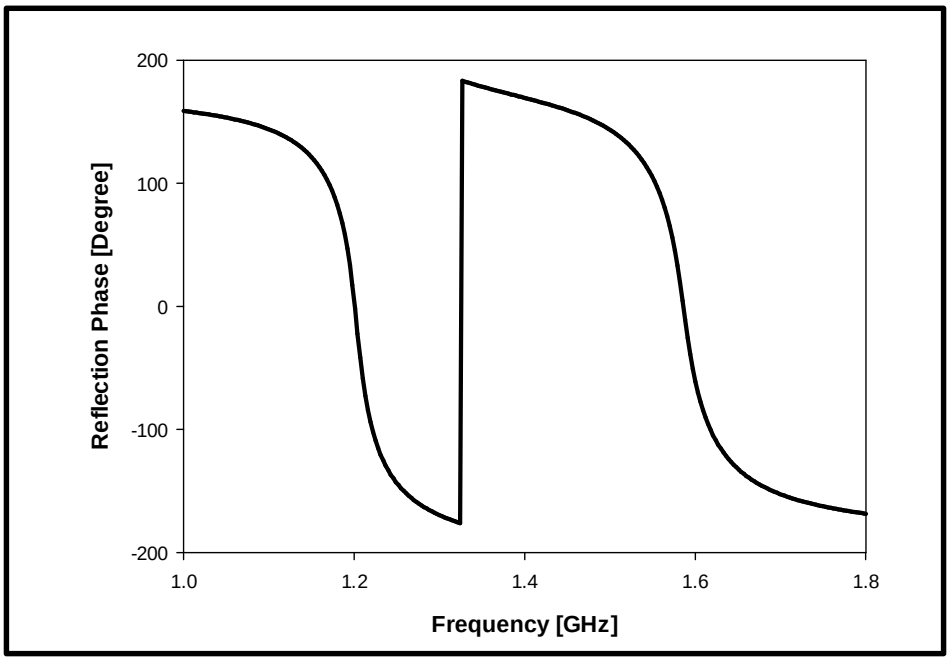

Figure 5.1.2: Reflection phase for the double square AMC

5.1.2 *A New Dual Band AMC*

In this section, a reduced size double band AMC unit cell is introduced as illustrated in Figure 5.1.3. The unit cell consists of a central square patch of size $x_1 \times y_1$, and two crossed rectangle patches of size $x_2 \times y_2$. These rectangular patches cross the central square patch, and connected to the four outer rectangles patches of size $x_3 \times y_3$. Further, the central patch is also connected to four symmetrical distributes each with a size of $x_4 \times y_4$. The advantage of having various square and rectangle patches is to introduce flexibility in the design so that it can be tuned to the desired dual frequencies. Once more, this AMC is printed on a FR4 substrate of thickness h_1.

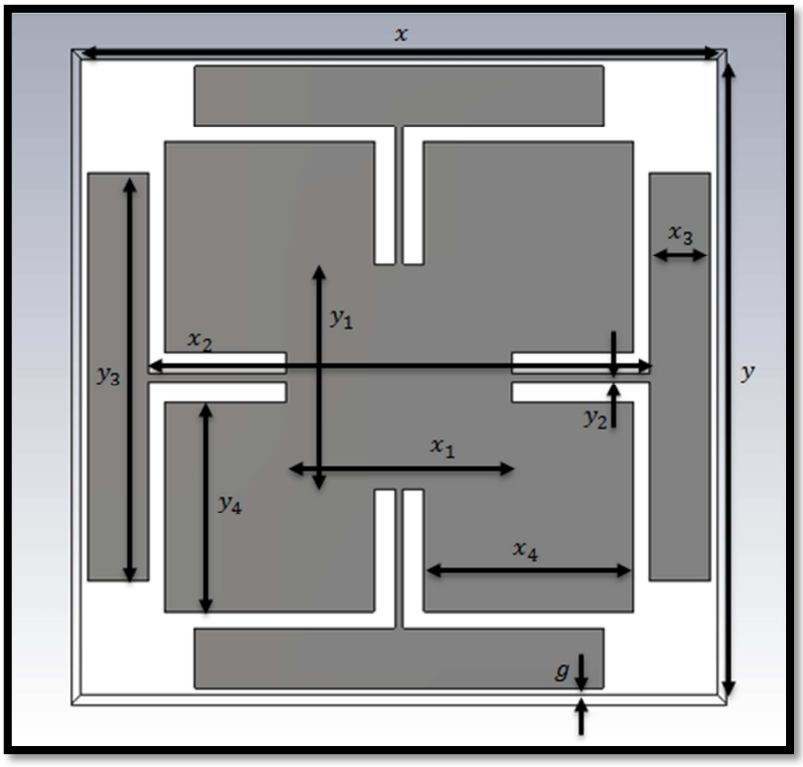

Figure 5.1.3: The dual band symmetrical AMC

The effect of each parameter has been investigated using CST parameter sweep by altering one dimension at a time while the others are kept constant. As an example, for the central square patch, x_1 has been varied and the resultant reflection coefficients are shown in Figure 5.1.4. The effects of x_1 on the 0^o-reflection's phase and the two bands' bandwidths are presented in Figure 5.1.5 and Figure 5.1.6 with numerical data listed in Table 5.1.2.

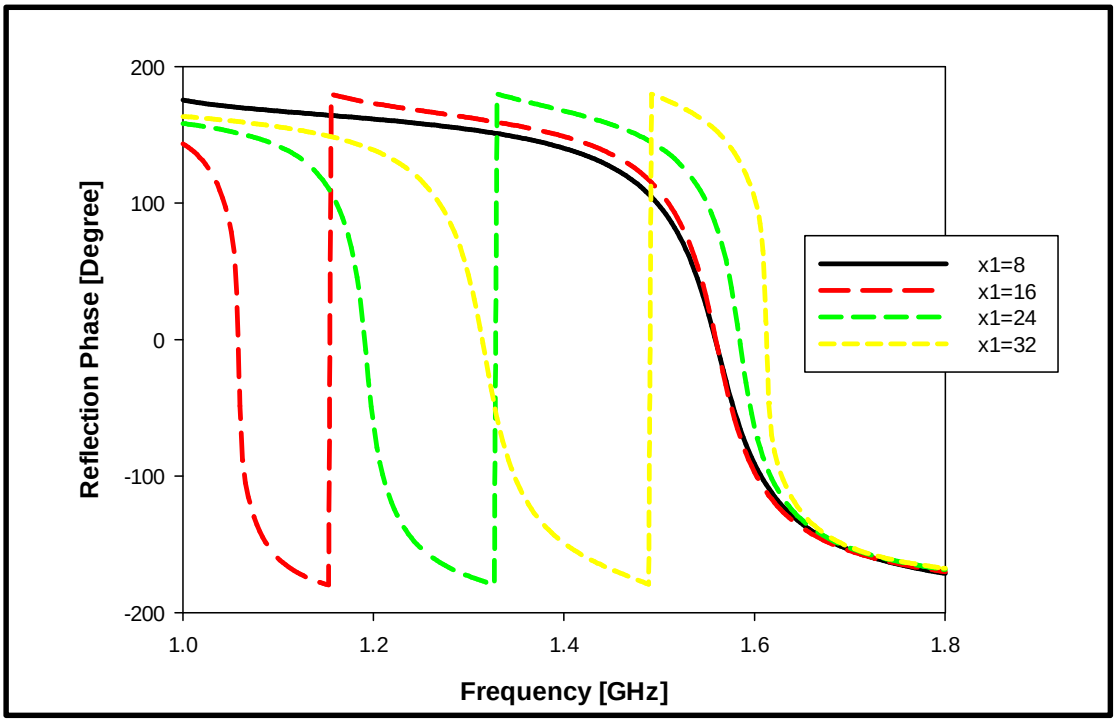

Figure 5.1.4: Reflection phase for the dual band AMC for various x_1 values

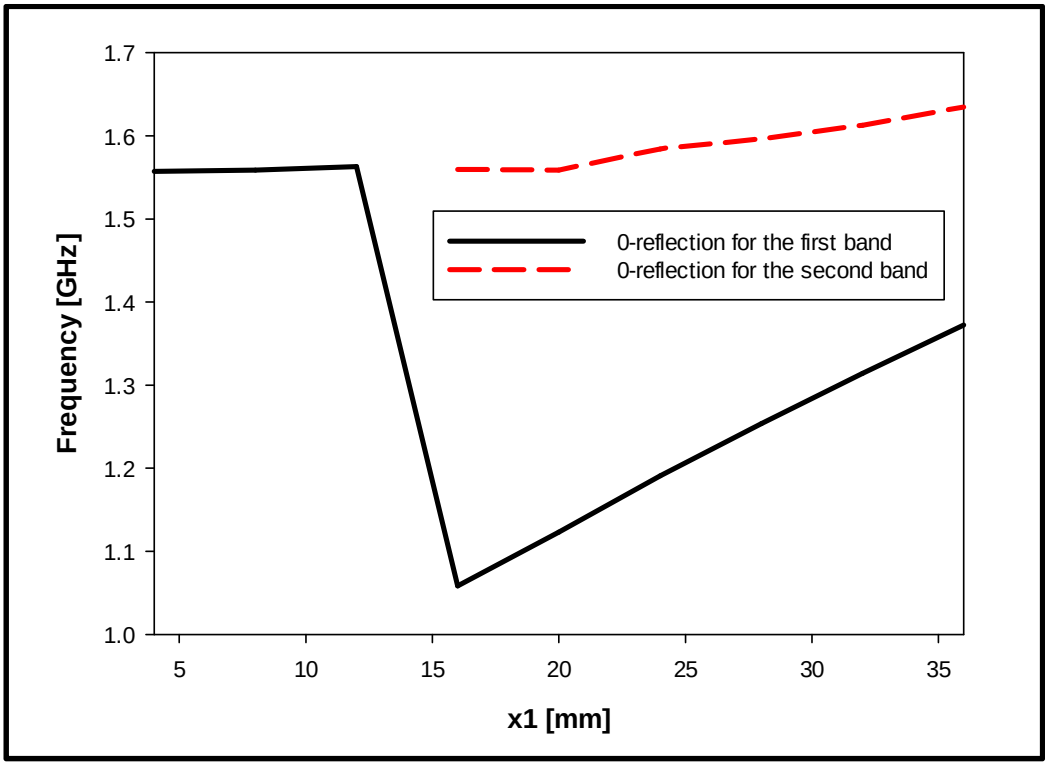

Figure 5.1.5: 0^o-reflection frequencies for the first and second bands for various x_1 values

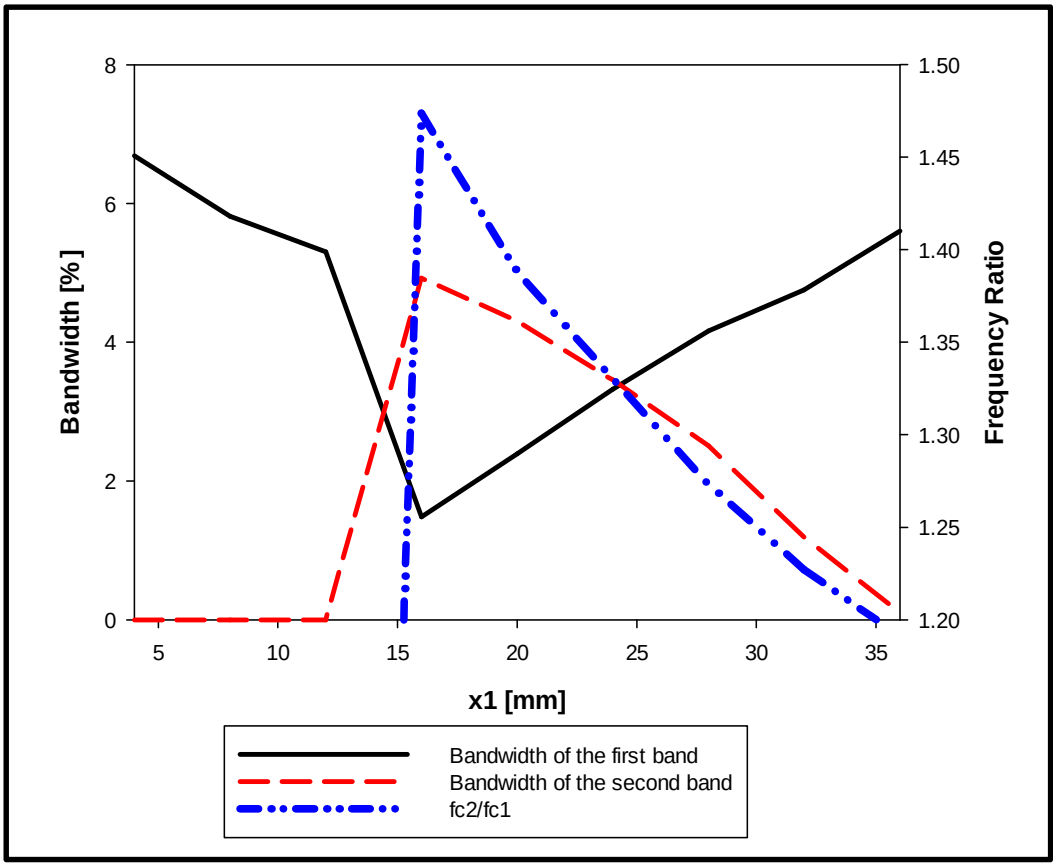

Figure 5.1.6: Bandwidths and frequency ratios for the two bands for various x_1 values

x_1 [mm]	f_2 [GHz]	f_1 [GHz]	f_{c1} [GHz]	BW1 [%]	f_2 [GHz]	f_1 [GHz]	f_{c2} [GHz]	BW2 [%]	f_{c2}/f_{c1}
4	1.601	1.497	1.557	6.686				0.000	0.000
8	1.599	1.509	1.559	5.812				0.000	0.000
12	1.601	1.518	1.563	5.304				0.000	0.000
16	1.063	1.048	1.058	1.484	1.595	1.519	1.560	4.924	1.474
20	1.133	1.106	1.123	2.396	1.591	1.524	1.559	4.305	1.388
24	1.207	1.167	1.191	3.325	1.611	1.556	1.584	3.453	1.330
28	1.276	1.224	1.254	4.164	1.617	1.577	1.596	2.506	1.273
32	1.342	1.280	1.314	4.755	1.624	1.605	1.613	1.191	1.227
36	1.407	1.330	1.372	5.603	1.635	1.634	1.635	0.098	1.191

Table 5.1.2: Effects of varying x_1 on the two bands

It can be observed from these results that varying x_1 results in changing the coupling capacitance between the central patch and the attached square patches. As an example, when $x_1 = 4\text{mm}$, the central patch is not connected to the adjacent four squares and hence only a single band is observed at 1.557GHz. As x_1 is varied, the capacitance is altered and when x_1 approaches 16mm, a dual band operation is

achieved at 1.06GHz and 1.56GHz with respective bandwidths of 1.48% and 4.9% and a frequency ratio of 1.47. Increasing x_1 further shifts the first band significantly to a higher frequency with an increase in the bandwidth and shifts the second band slightly to a higher frequency with a decrease in the bandwidth. A frequency ratio of 1.19 can be obtained when $x_1 = 36\text{mm}$ with a narrow bandwidth for the second band. Reasonable bandwidths of 3.3% and 3.4% for the first and second bands, respectively, can be achieved at $x_1 = 24\text{mm}$. Similar behaviour is observed when varying the size of the four attached squares given by $x_4 \times y_4$ since varying x_4 alters the gap between those patches and the central square.

Another important element in tuning the dual bands is the crossed rectangles crossing the central square patch that are defined by $x_2 \times y_2$. In order to accomplish dual bands at the desired frequencies, they have to be connected to the outer rectangular patches. Otherwise, the unit cell resonates at higher frequencies. On the other hand, varying y_2 can tune the first band as can be observed in Figure 5.1.7. The effect of varying y_2 on the dual frequencies and bandwidths are illustrated in Figure 5.1.8 and Figure 5.1.9 with tabulated data presented in Table 5.1.3.

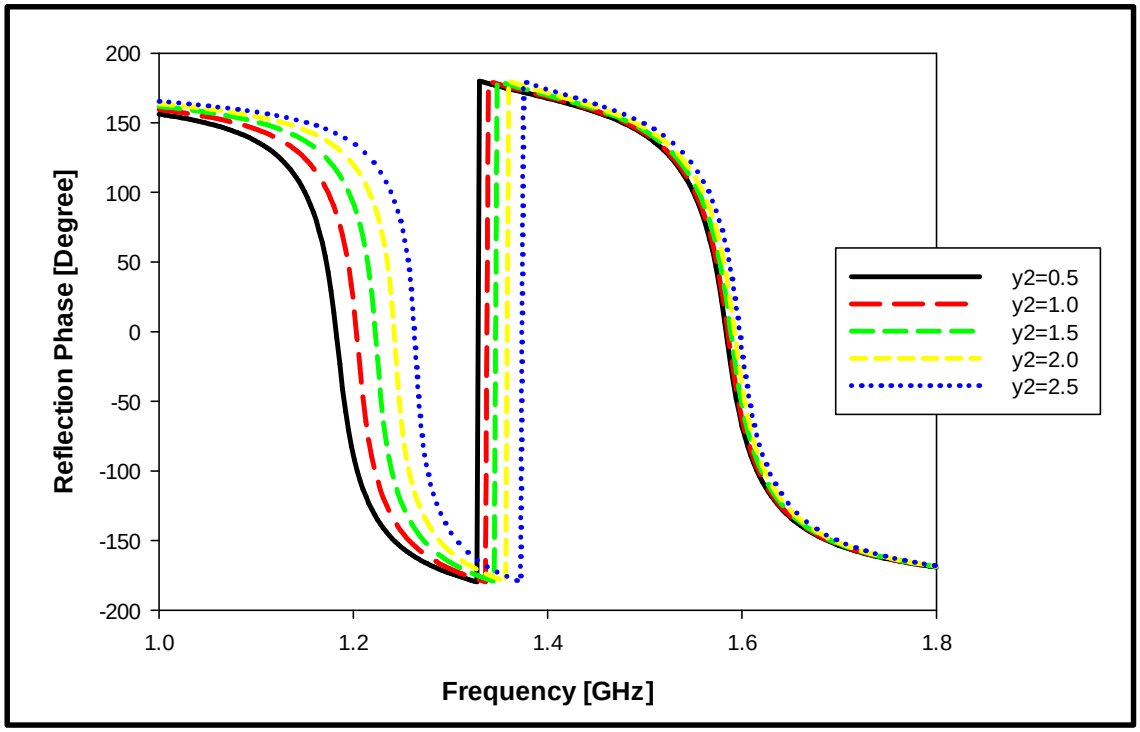

Figure 5.1.7: Reflection phase for the dual band AMC for various y_2 values

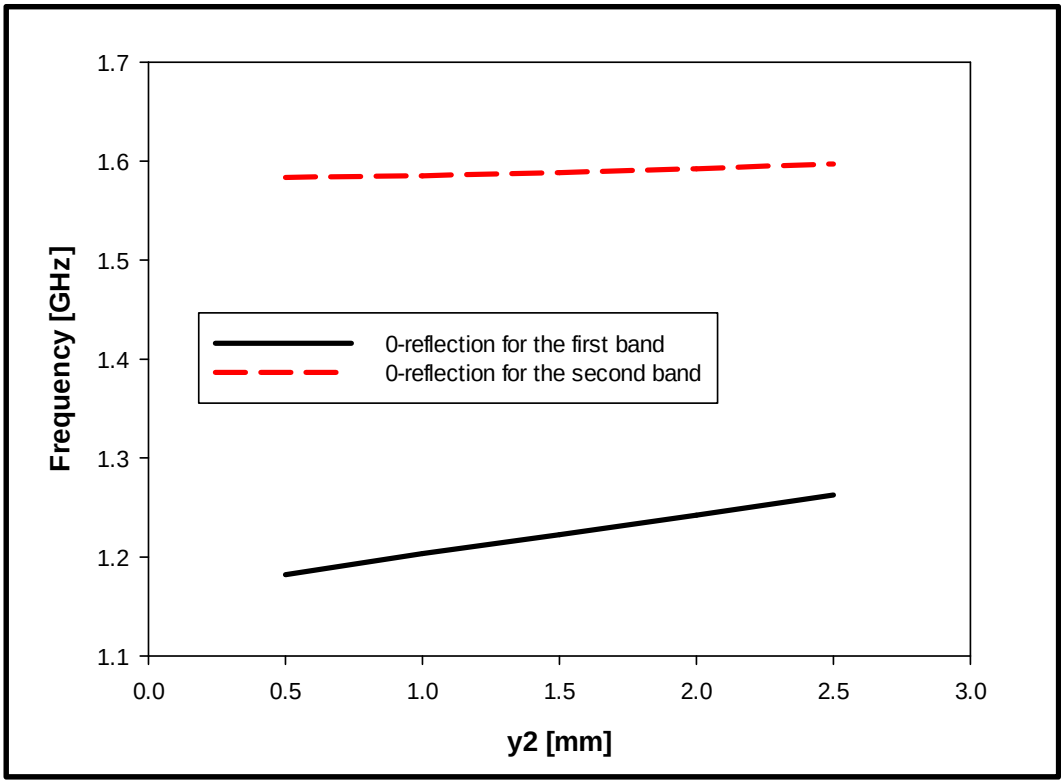

Figure 5.1.8: 0^o-reflection frequencies for the first and second bands for various y_2 values

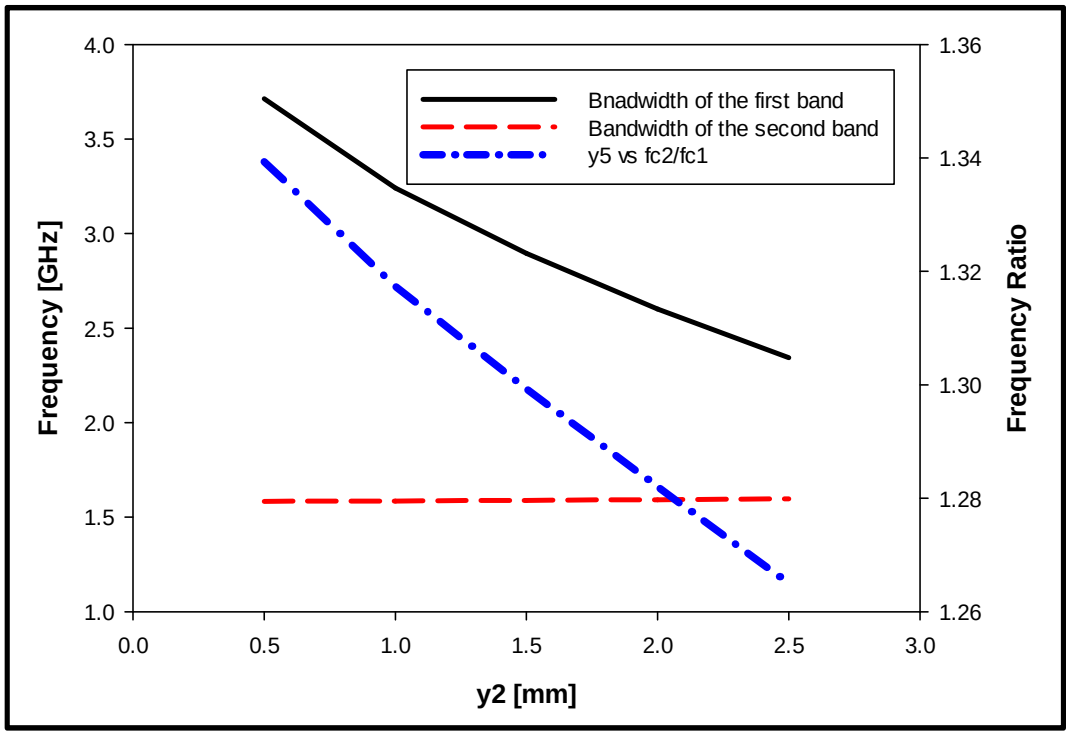

Figure 5.1.9: Bandwidths and frequency ratios for the two bands for various y_2 values

y_2 [mm]	f_2 [GHz]	f_1 [GHz]	f_{c1} [GHz]	BW1 [%]	f_2 [GHz]	f_1 [GHz]	f_{c2} [GHz]	BW2 [%]	f_{c2}/f_{c1}
0.500	1.200	1.157	1.182	3.713	1.610	1.556	1.584	3.385	1.339
1.000	1.219	1.180	1.203	3.241	1.611	1.558	1.585	3.356	1.317
1.500	1.237	1.201	1.223	2.895	1.614	1.562	1.589	3.318	1.299
2.000	1.255	1.222	1.242	2.600	1.618	1.566	1.592	3.240	1.282
2.500	1.274	1.244	1.263	2.344	1.622	1.572	1.597	3.155	1.265

Table 5.1.3: Effect of varying y_2 on the two bands

These results demonstrate that varying y_2 can mainly tune the first band frequency with a marginal effect on the second band. For example, when $y_2 = 0.5\text{mm}$, the AMC resonates at 1.182GHz and 1.584GHz with respective bandwidths of 3.7% and 3.4% and frequency ratio of 1.34. Increasing y_2 to 2.5mm reduces the frequency ratio to 1.265 with a shift of the first band to 1.263GHz and a reduced bandwidth to 2.34%. Therefore, employing y_2 of 1mm is recommended to maintain efficient bandwidth of the first band.

Additional design flexibility is facilitated by tuning the outer rectangles each with a size of $x_3 \times y_3$. For instance x_3 needs to be less than 10.13mm to achieve dual bands. That is because when $x_3 = 10.13\text{mm}$, the outer rectangular patches are connected to the neighbouring square patches and therefore, the AMC resonates at 1.08GHz only. However, when $x_3 < 10.13\text{mm}$, a capacitance is built between the outer rectangular and the adjacent squares and therefore, a dual band AMC is achieved as illustrated in Figure 5.1.10, Figure 5.1.11, Figure 5.1.12 and Table 5.1.4. From these results it can be seen that when $x_3 = 8.375\text{mm}$, the AMC resonates at 1.163GHz and 1.52GHz with respective bandwidths of 3% and 4.29% and frequency ratio of 1.307. As x_3 is decreased, the capacitance is reduced and, hence, both bands shift to higher frequencies. At $x_3 = 4.875\text{mm}$, the AMC resonates at 1.22GHz and 1.65GHz with respective bandwidths of 3.75% and 2.39% and a frequency ratio of 1.35.

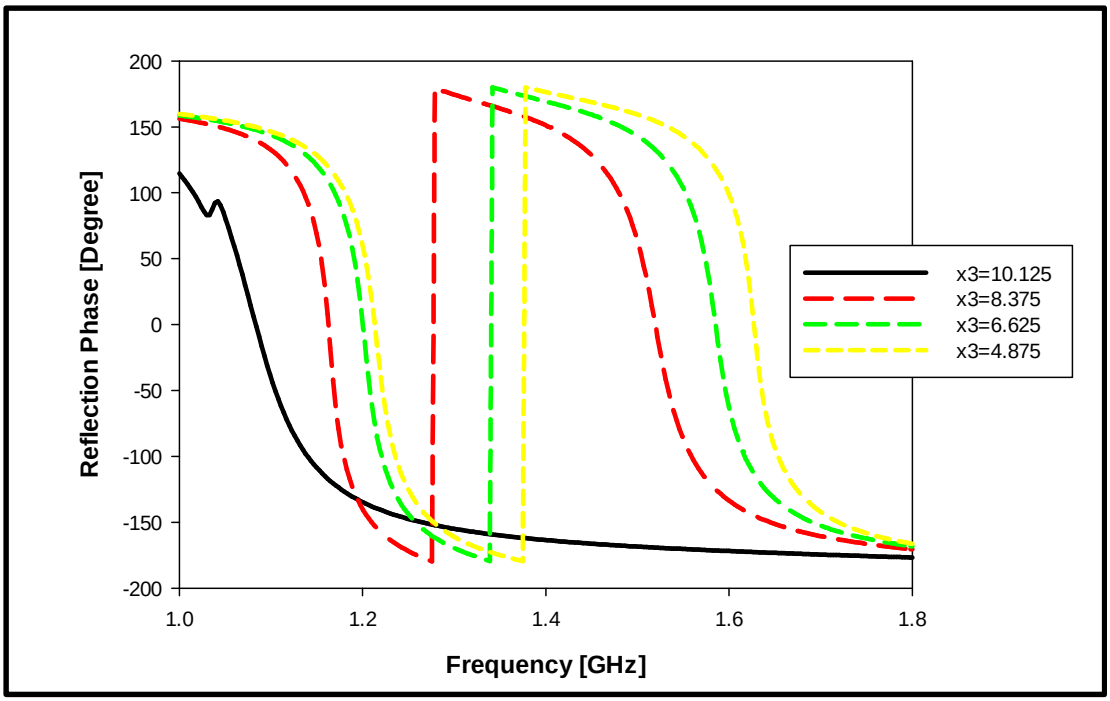

Figure 5.1.10: Reflection phase for the dual band AMC for various x_3 values

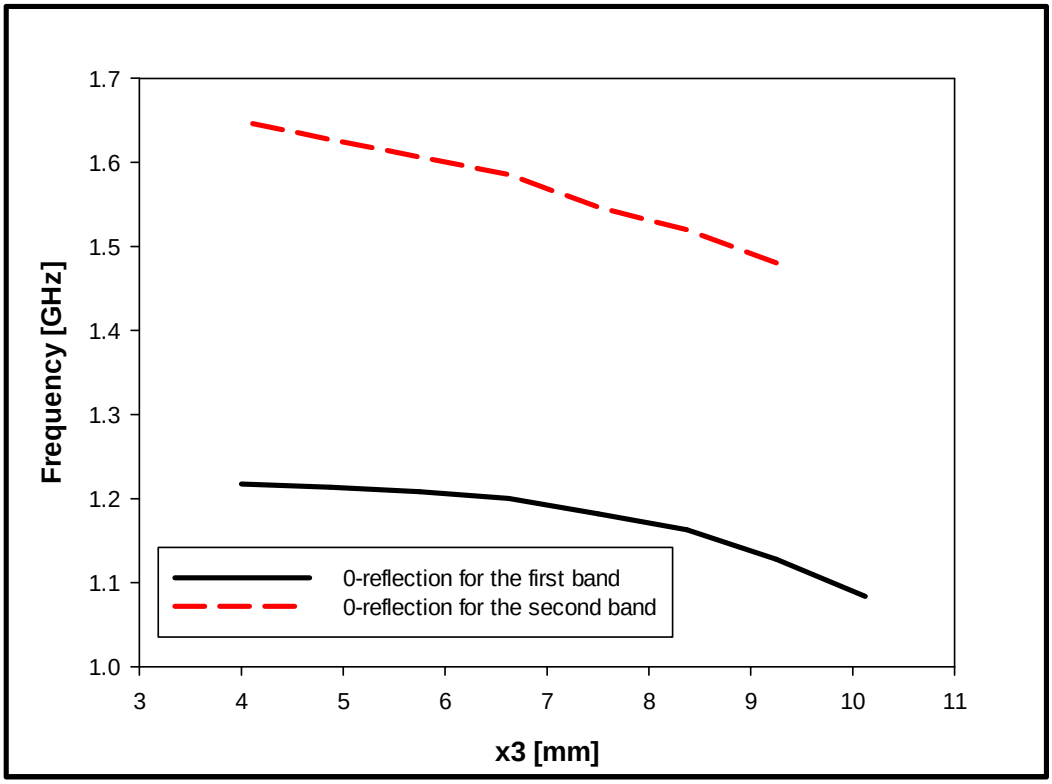

Figure 5.1.11: 0^o-reflection frequencies for the first and second bands for various x_3 values

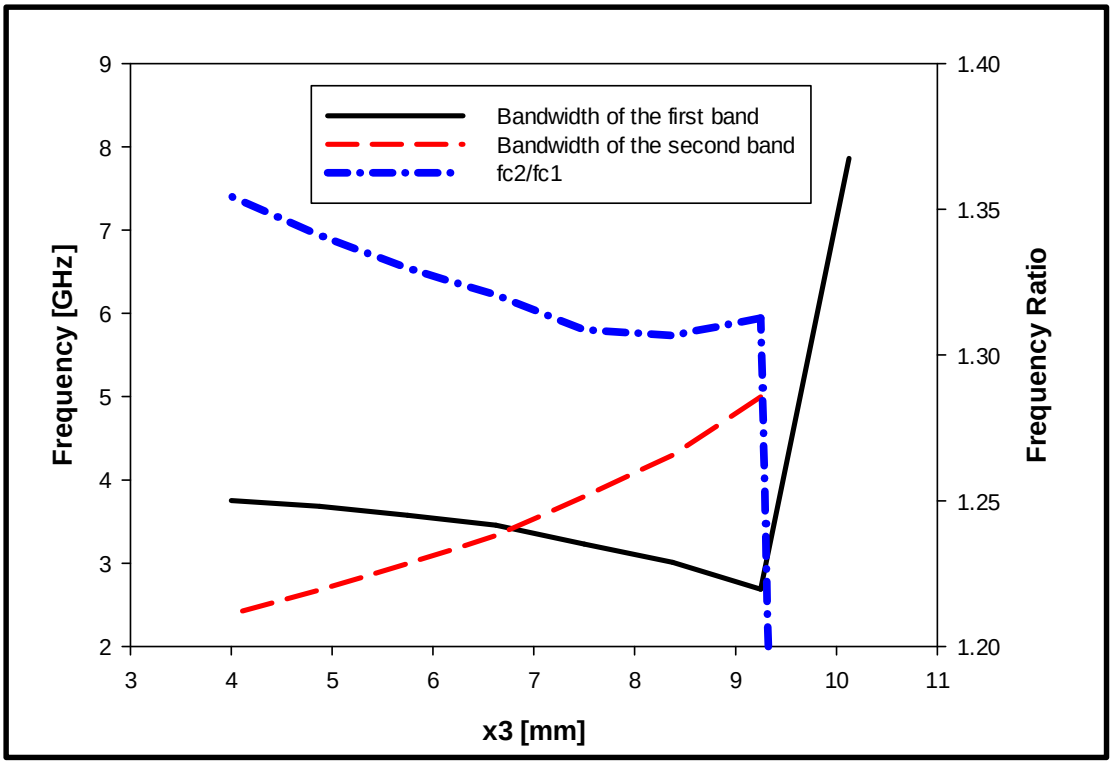

Figure 5.1.12: Bandwidths and frequency ratios for the two bands for various x_3 values

x_3 [mm]	f_2 [GHz]	f_1 [GHz]	f_{c1} [GHz]	BW1 [%]	f_2 [GHz]	f_1 [GHz]	f_{c2} [GHz]	BW2 [%]	f_{c2}/f_{c1}
10.125	1.131	1.045	1.084	7.863				0.000	0.000
9.250	1.139	1.109	1.128	2.686	1.518	1.444	1.481	4.998	1.313
8.375	1.177	1.142	1.163	3.010	1.552	1.487	1.520	4.297	1.307
7.500	1.197	1.159	1.182	3.232	1.576	1.517	1.547	3.802	1.309
6.625	1.218	1.176	1.201	3.457	1.611	1.559	1.585	3.330	1.321
5.750	1.226	1.183	1.208	3.576	1.630	1.582	1.607	2.994	1.330
4.875	1.232	1.188	1.213	3.684	1.648	1.605	1.627	2.679	1.341
4.000	1.237	1.191	1.217	3.754	1.668	1.628	1.649	2.390	1.354

Table 5.1.4: Effect of varying x_3 on the two bands

On the other hand, varying y_3 change the second band significantly with minimum effects on the first band as can be seen in Figure 5.1.13, Figure 5.1.14, Figure 5.1.15 and Table 5.1.5. It can be observed from these results that varying y_3 alters the performance significantly. As an example, when $y_3 = 30\text{mm}$, the AMC resonates at 1.23GHz and 2.17GHz, with respective bandwidths of 2.9% and 4.7% and a frequency ratio of 1.76. Increasing y_3 to 54mm shifts the second band to 1.34GHz with a decrease in the bandwidth to 2.4% and frequency ratio to 1.13. Therefore, a wide

frequency ratio range can be gained by simply varying y_3, which offers considerable design flexibility.

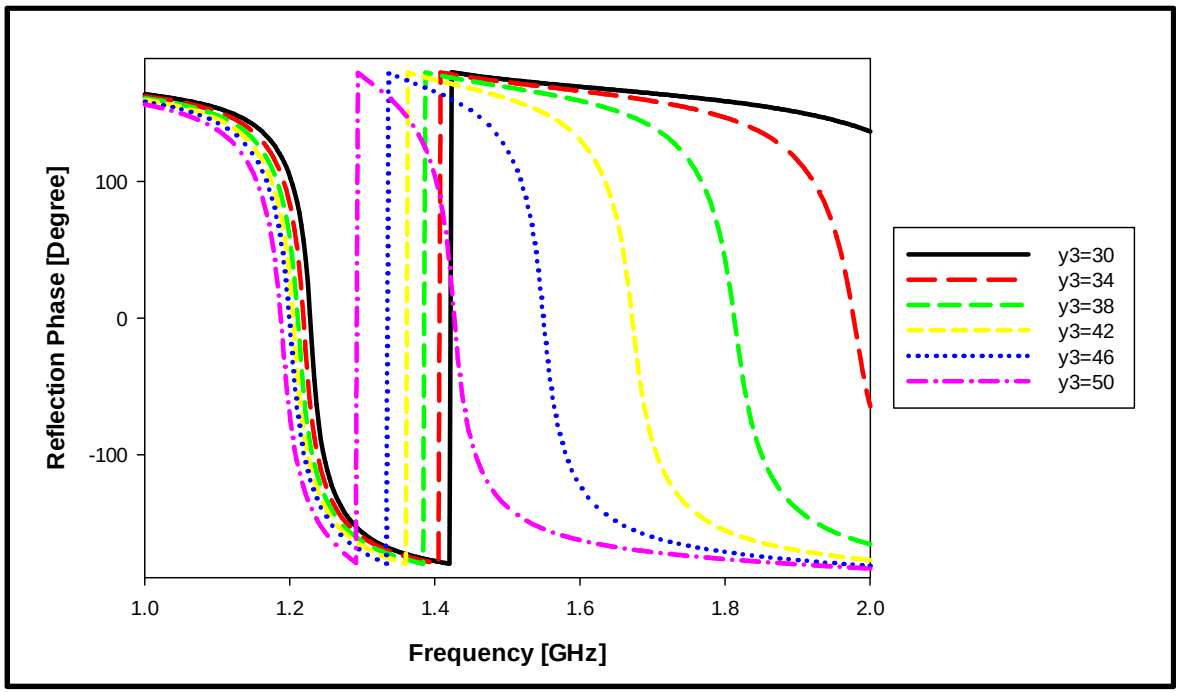

Figure 5.1.13: Reflection phase for the dual band AMC for various y_3 values

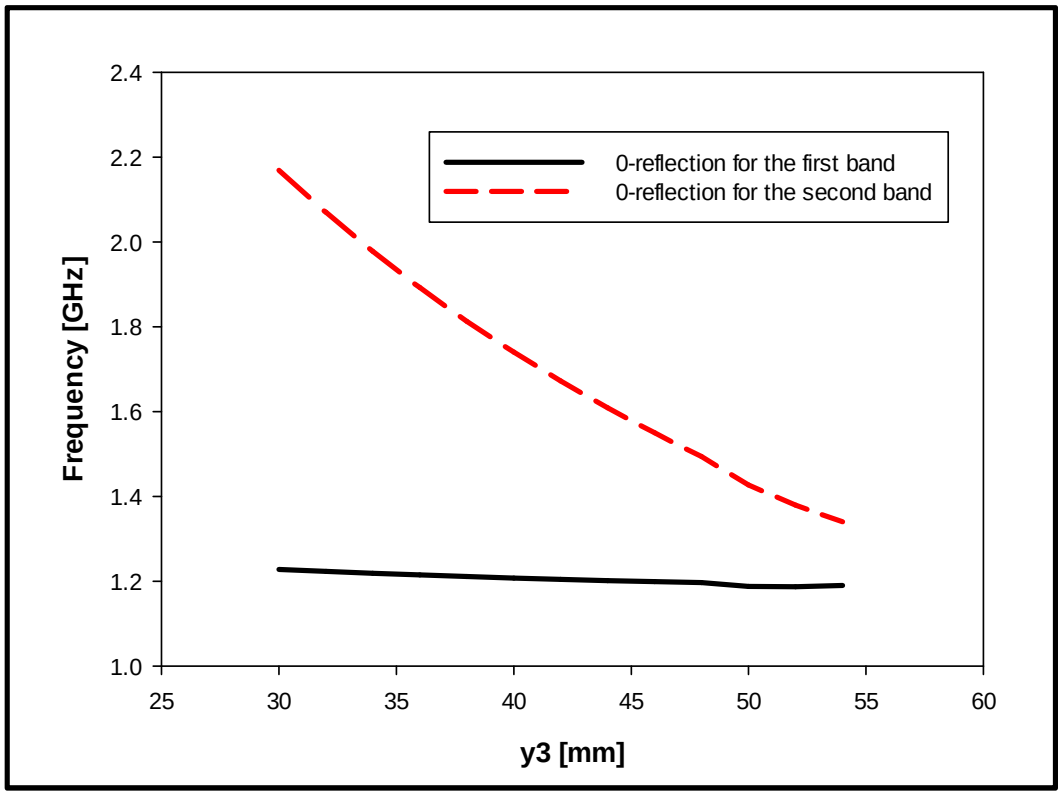

Figure 5.1.14: 0^o-reflection frequencies for the first and second bands for various y_3 values

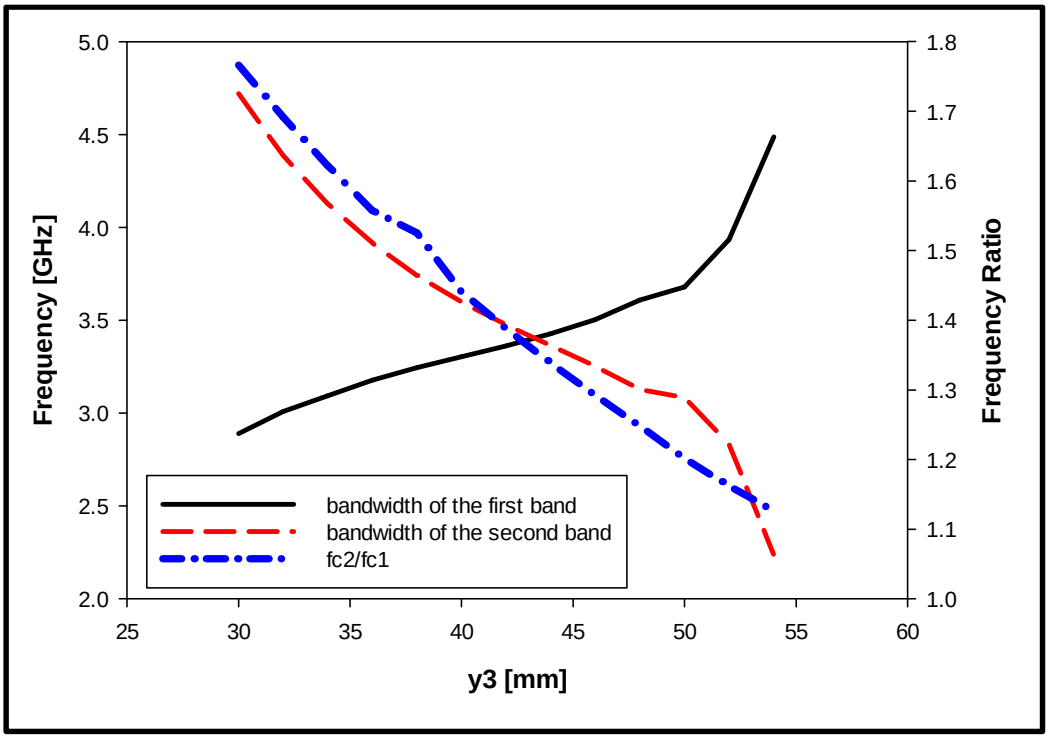

Figure 5.1.15: Bandwidths and frequency ratios for the two bands for various y_3 values

y_3 [mm]	f_2 [GHz]	f_1 [GHz]	f_{c1} [GHz]	BW1 [%]	f_2 [GHz]	f_1 [GHz]	f_{c2} [GHz]	BW2 [%]	f_{c2}/f_{c1}
30.000	1.243	1.208	1.228	2.890	2.214	2.111	2.170	4.720	1.766
32.000	1.239	1.202	1.223	3.008	2.110	2.019	2.070	4.387	1.692
34.000	1.235	1.197	1.219	3.093	2.014	1.932	1.977	4.127	1.622
36.000	1.231	1.193	1.215	3.177	1.926	1.852	1.893	3.915	1.558
38.000	1.228	1.188	1.211	3.245	1.844	1.776	1.813	3.740	1.525
40.000	1.224	1.185	1.208	3.304	1.769	1.707	1.740	3.598	1.441
42.000	1.221	1.181	1.205	3.362	1.700	1.642	1.672	3.475	1.388
44.000	1.219	1.178	1.202	3.428	1.635	1.581	1.609	3.363	1.339
46.000	1.216	1.174	1.199	3.502	1.575	1.524	1.550	3.253	1.292
48.000	1.214	1.171	1.197	3.610	1.518	1.471	1.494	3.127	1.248
50.000	1.205	1.161	1.188	3.679	1.451	1.407	1.427	3.084	1.201
52.000	1.205	1.159	1.187	3.934	1.401	1.362	1.379	2.835	1.162
54.000	1.211	1.157	1.190	4.488	1.359	1.329	1.340	2.239	1.126

Table 5.1.5: Effects of varying y_3 on the two bands

As with any AMC, the substrate thickness has a major contribution on the inductance. In this dual band AMC, the thickness h_1 has been varied and the results are illustrated in Figure 5.1.16, Figure 5.1.17, Figure 5.1.18 and Table 5.1.6. From these results, it can be concluded that varying the thickness of the substrate has a

minimum effect on the resonance frequencies since dual bands have been achieved in all cases. However, the thickness has a major effect on the bandwidths. For example, when $h_1 = 3.2\text{mm}$, the bandwidths of the first and second bands are 0.1%. Increasing the thickness to 6.4mm yields bandwidths of 3.5% and 3.3% for the first and second bands, respectively. A summary of the parameters effects on the frequency ratio is given in Figure 5.1.19, where *s* represents the variable parameter where it can be seen that varying y_3 has the most pronounced impact on the frequency ratio.

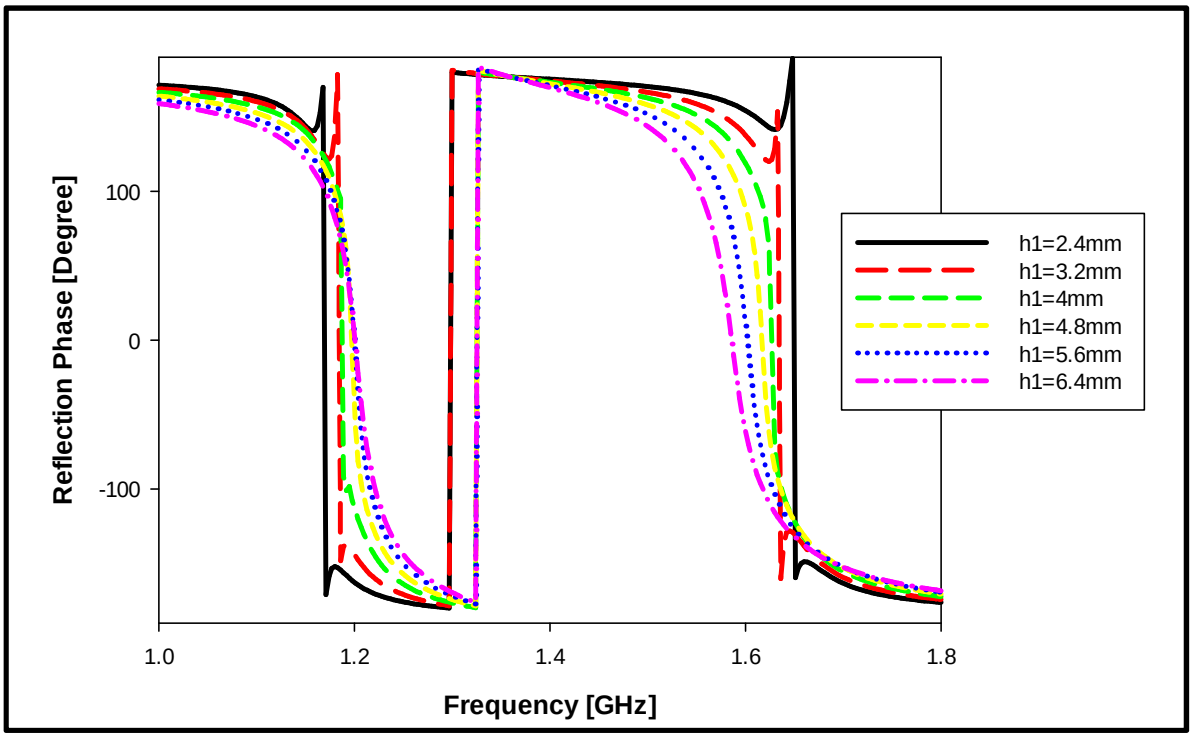

Figure 5.1.16: Reflection phase for the dual band AMC for various h_1 values

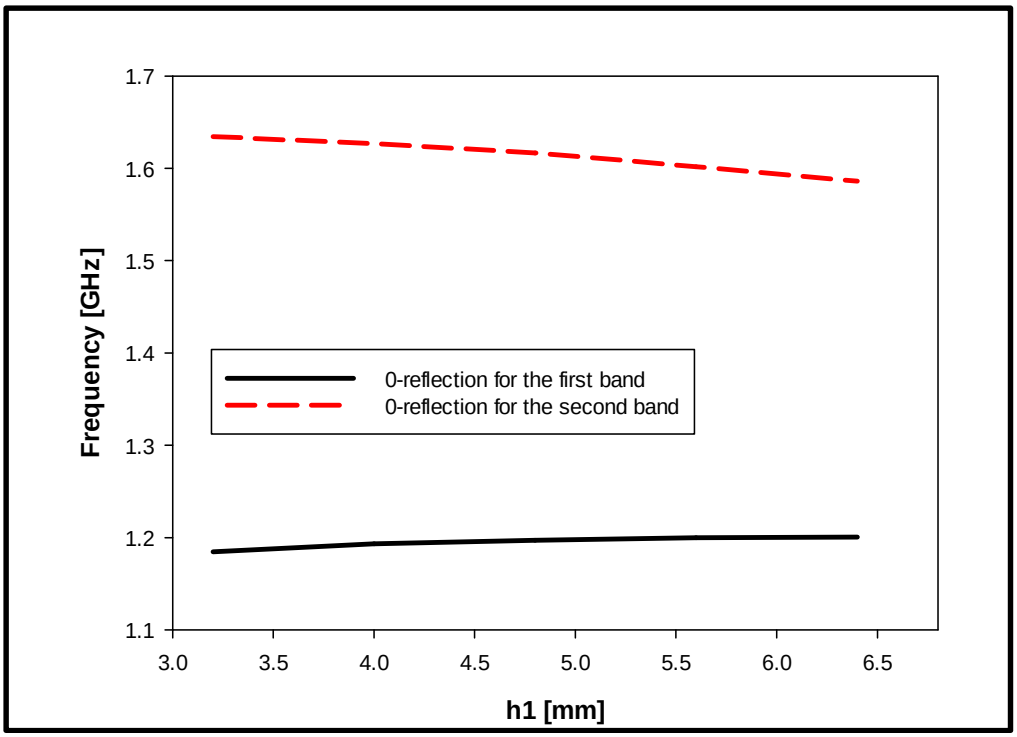

Figure 5.1.17: 0^o-reflection frequencies for the first and second bands for various h_1 values

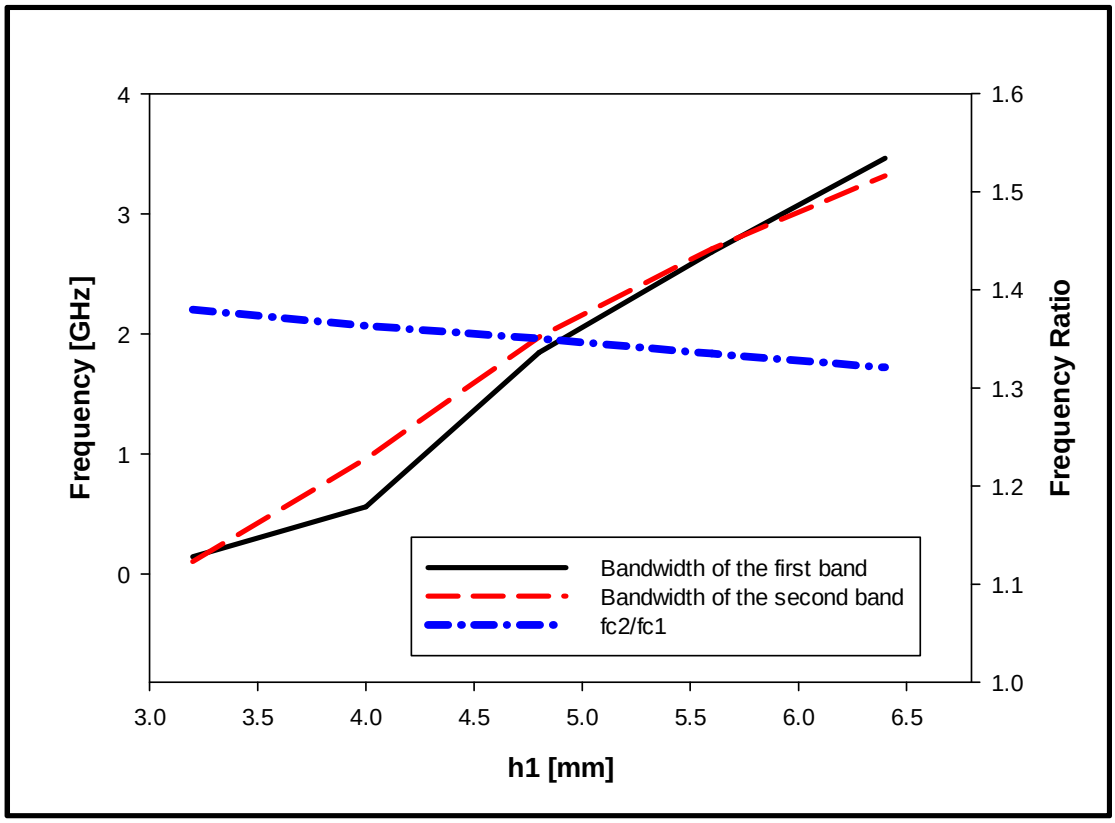

Figure 5.1.18: Bandwidths and frequency ratios for the two bands for various h_1 values

h_1 [mm]	f_2 [GHz]	f_1 [GHz]	f_{c1} [GHz]	BW1 [%]	f_2 [GHz]	f_1 [GHz]	f_{c2} [GHz]	BW2 [%]	f_{c2}/f_{c1}
3.2	1.186	1.184	1.185	0.144	1.635	1.634	1.635	0.104	1.380
4	1.195	1.188	1.193	0.561	1.633	1.618	1.627	0.959	1.363
4.8	1.206	1.184	1.197	1.846	1.632	1.600	1.617	1.973	1.350
5.6	1.213	1.181	1.200	2.683	1.623	1.579	1.602	2.709	1.335
6.4	1.218	1.176	1.201	3.465	1.612	1.559	1.586	3.317	1.321

Table 5.1.6: Effects of varying h_1 on the two bands

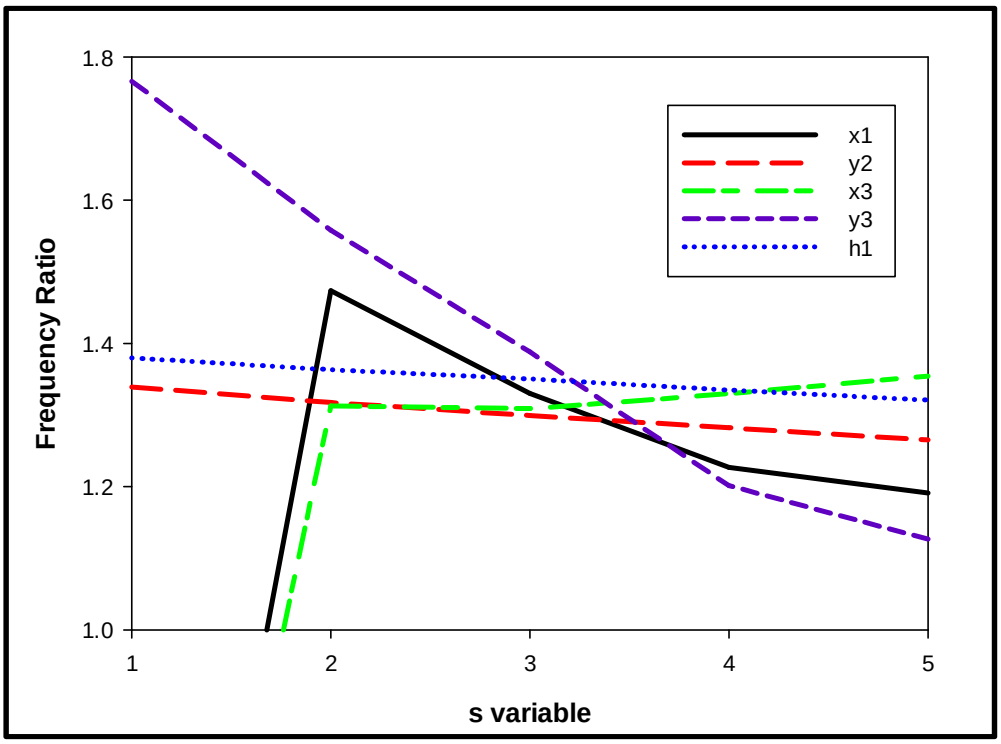

Figure 5.1.19: Effects of the variables of the dual band AMC on the frequency ratio

Finally, using an iterative design procedure, the optimum dimensions of the dual band AMC are given in Table 5.1.7 and the reflection's phase is presented in Figure 5.1.20. The AMC thickness is $\lambda_o/39$ and the unit cell size is $0.28\lambda_o$, where λ_o is the free space wavelength at the first band frequency. This is to be compared to a size of $0.48\lambda_o$ for the double squares AMC with the same thickness. Therefore, the proposed AMC is $\sim 42\%$ smaller than the double squares counterpart with wider bandwidths for both bands. The novel dual band AMC resonates at 1.20GHz and 1.59GHz with respective 0 ± 90^o bandwidths of 3.5% and 3.3%, and respective 90 ± 45^o bandwidths of 5.7% and 3.8%.

Parameter	Value [mm]
x_1	24.62
y_1	24.62
x_2	55
y_2	0.958
x_3	6.6
y_3	44.75
x_4	23
y_4	23
h_1	6.4
g	1.5
x	69.7
y	69.7

Table 5.1.7: Optimum values for the dual band AMC

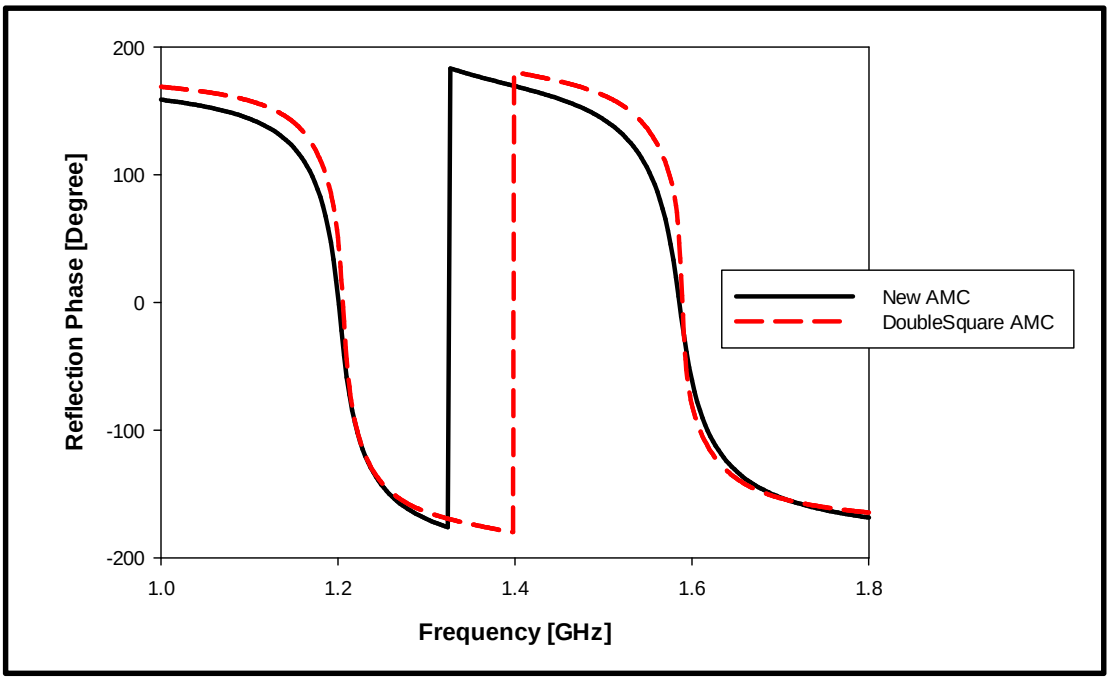

Figure 5.1.20: Reflection phase for the dual band AMC

5.2 Wide band Circularly Polarised Open Loop Antenna Backed by a Dual Band AMC

5.2.1 *Wide band Open Loop Antenna Design*

As mentioned earlier, incorporating a parasitic loop inside the driven loop introduces another AR minima and therefore increases the AR bandwidth considerably [15]. This concept is deployed in this section, where a wide band open loop antenna is

designed and backed by the new dual band AMC. As a starting point, a probe-fed wideband circularly polarised planar open loop antenna associated with a parasitic loop has been designed as shown in Figure 5.2.1, where the open loop has been printed on an FR4 substrate with a thickness of h_1 and a width of x.

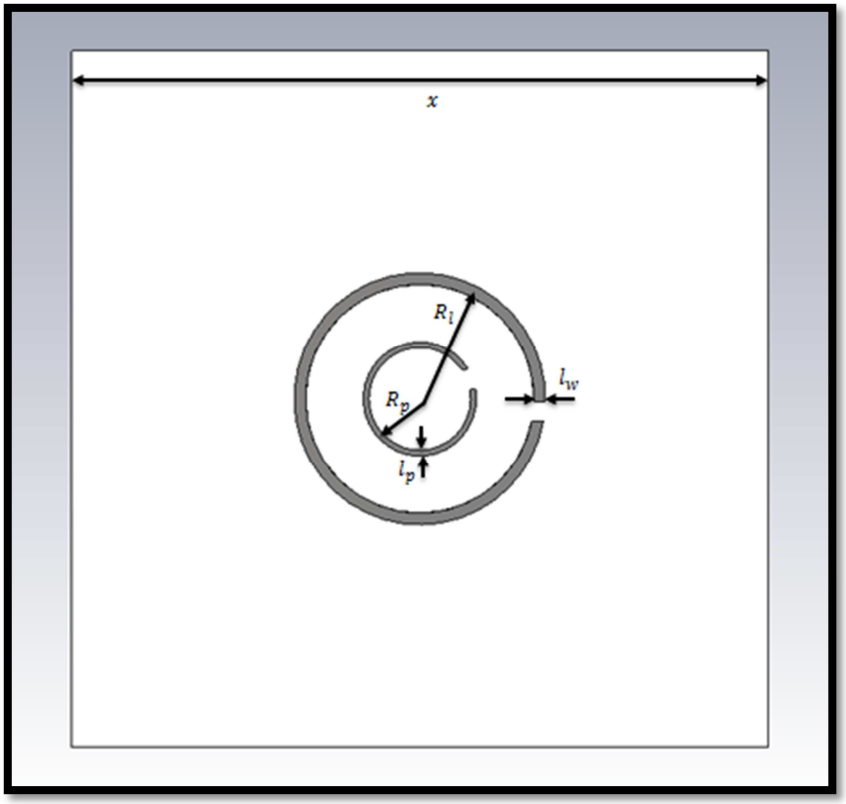

Figure 5.2.1: The wideband open loop antenna

The structure's parameters have been varied and the optimum results for a wide band axial ratio covering the L_1 and L_2 GPS bands are given in Table 5.2.1, where the thickness and the width have been determined as $\lambda_o/8.9$ and λ_o, respectively. The circumference of the open loop has been calculated as $1.13\lambda_{eff}$.

Parameter	Value [mm]
h_1	28
x	249.2
R_l	29
R_p	13
l_w	1.2
l_p	0.6

Table 5.2.1: Optimum values for the wideband open loop antenna

The axial ratio is shown in Figure 5.2.2, where a 3dB AR of 35% has been achieved. The reflection coefficient has been calculated as illustrated in Figure 6.2.3, where it can be observed that a matching bandwidth of 24% has been achieved.

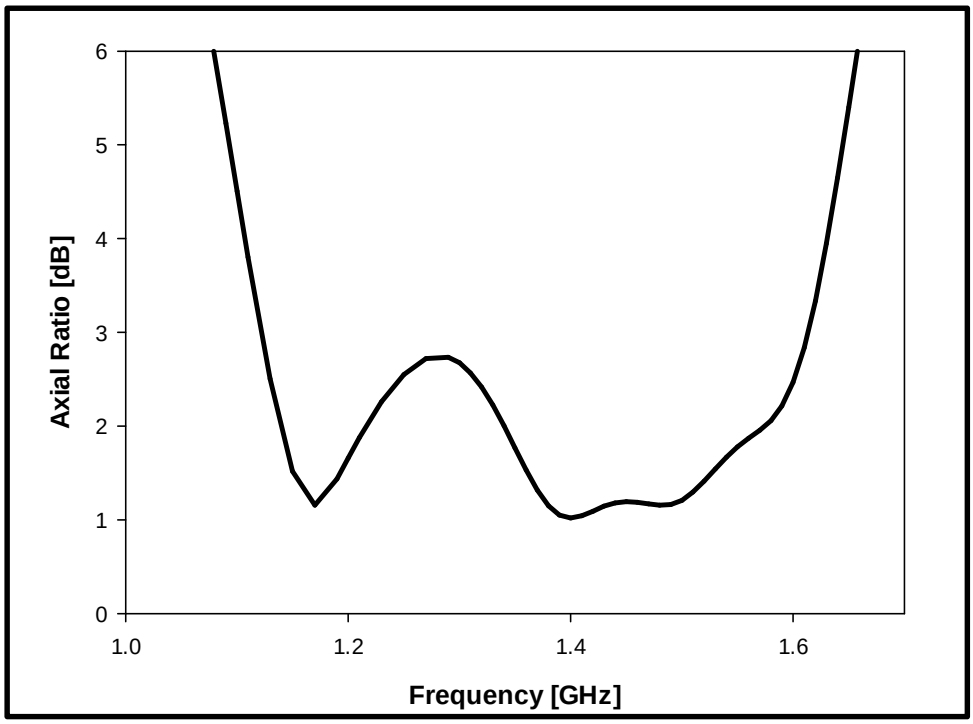

Figure 5.2.2: Axial ratio for the wideband open loop antenna

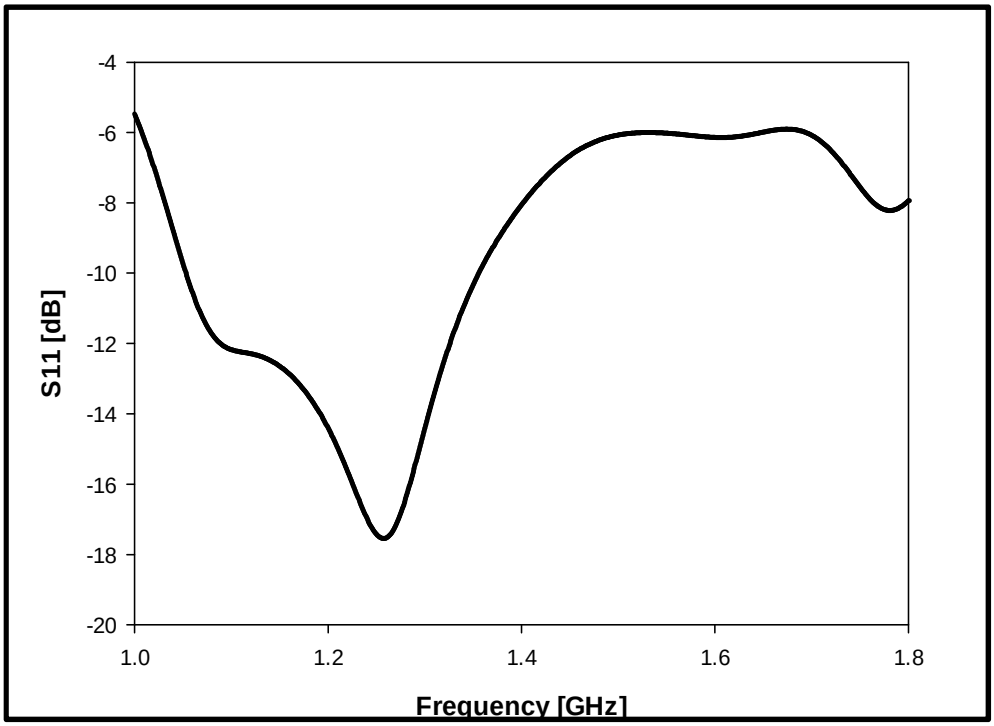

Figure 5.2.3: Reflection coefficient for the wideband open loop antenna

5.2.2 *The Dual Band Antenna*

The next step is to lower the antenna height by incorporating the dual band AMC with the wideband open loop antenna as illustrated in Figure 5.2.4, in which the concentric loops are printed on an FR4 substrate with a thickness of h_2 and placed above a 2×2 grid of the novel dual band AMC. It is worth to mention that the second layer substrate is not shown in Figure 5.2.4 for a clearer display. The dimensions of the driven and parasitic loops have been varied and the optimum values are presented in Table 5.2.2, where the total antenna thickness has been calculated as$\lambda_o/31.25$. Owing to the interaction between the AMC surface and the antenna, the best results have been achieved when the driven and the parasitic loops are shifted to the left by $3mm$.

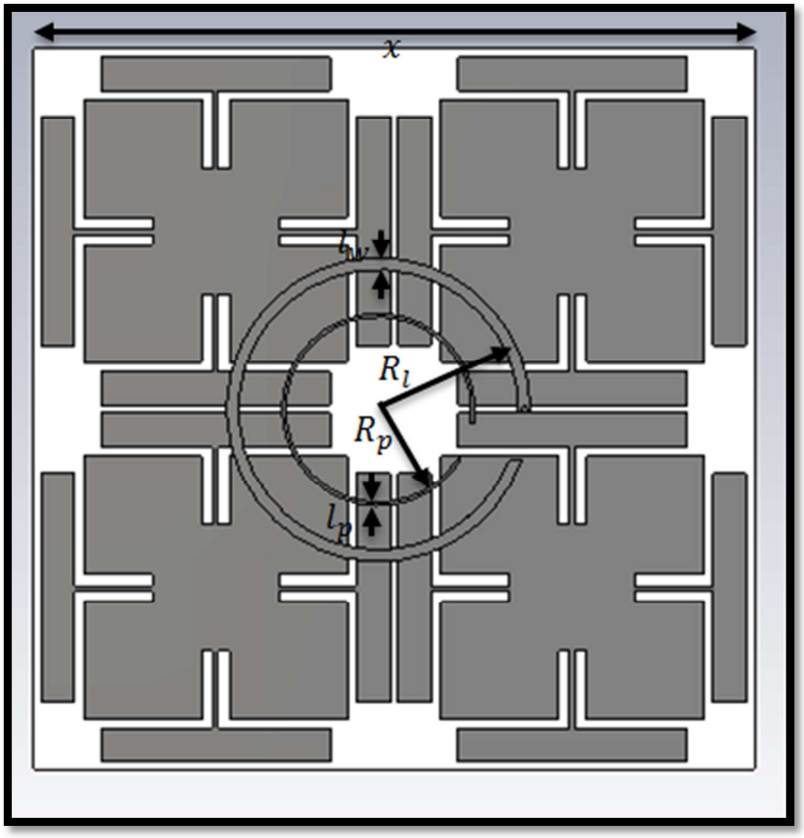

Figure 5.2.4: Wideband open loop antenna on the new dual band AMC

Parameter	Value [mm]
h_1	6.4
h_2	1.6
x	140.9
R_l	28.5
R_p	18.5
l_w	2.3
l_p	0.67

Table 5.2.2: Optimum parameter values for the dual band antenna

The reflection coefficient is presented in Figure 5.2.5, where it is evident that a dual band operation has been achieved at the L_1 and L_2 GPS bands. The -10dB bandwidths have been calculated as 3.2% and 13.4% for the first and second bands, respectively. The axial ratio is illustrated in Figure 5.2.6, where it can be noticed that AR dips exist in the vicinity of the L_1 and L_2 GPS bands. However, the AR is higher than 3dB. This is can be understood as a result of the strong coupling between the AMC and antenna. Such effect has also been reported in [113], where the problem has been resolved by removing the AMC unit cells underneath the antenna. However, this solution is not applicable here since the size of the unit cell is large. The size of the ground plane has been increased by introducing more cells and the thickness of the second layer has been varied but with no improvement. The radiation pattern at the central frequencies of the two bands are presented in Figure 5.2.7 and Figure 5.2.8, where it can be seen that the main beam is shifted for both bands. For the first band, it is shifted to -20^o, whereas it is shifted to 20^o for the second band. The bore-sight gain is presented in Figure 5.2.9, where it can be noticed that the results show improvement in the gain to some extent. At 1.2GHz, the gain is $\sim$2dB whereas at 1.57GHz, the gain is $\sim$0.6dB with a negative gain at $\sim 1.6\text{GHz}$. Further investigation is required to improve the CP performance by considering alternative circularly polarised wideband or dual band antennas. Other measures include designing smaller AMC unit cells that can be removed in the middle to reduce the coupling between the AMC and antenna.

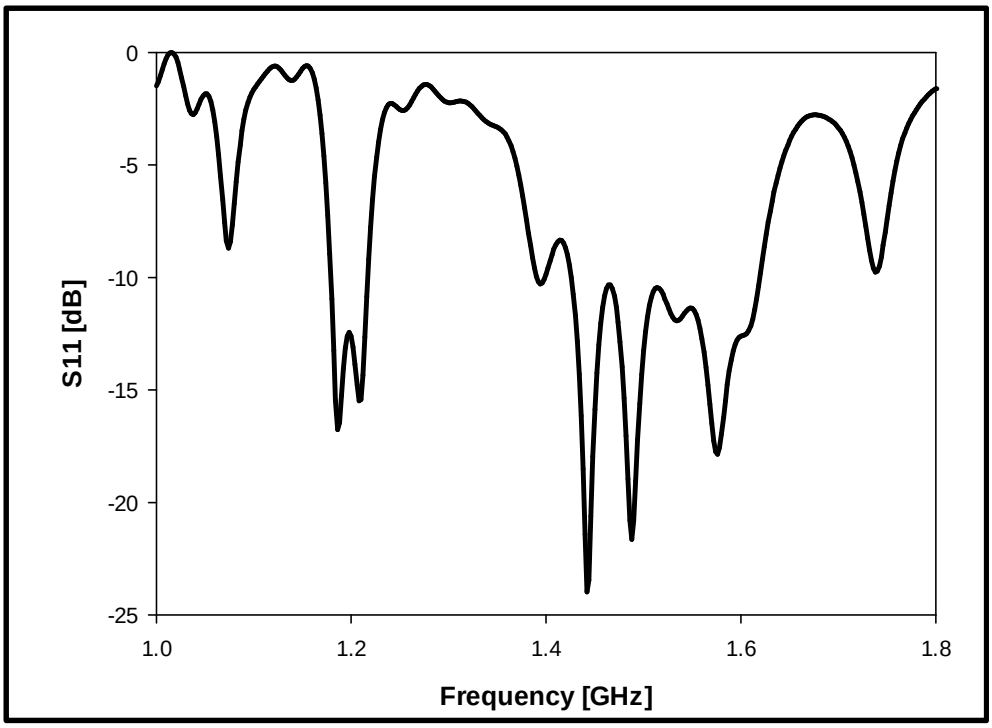

Figure 5.2.5: Reflection coefficient for the dual band antenna

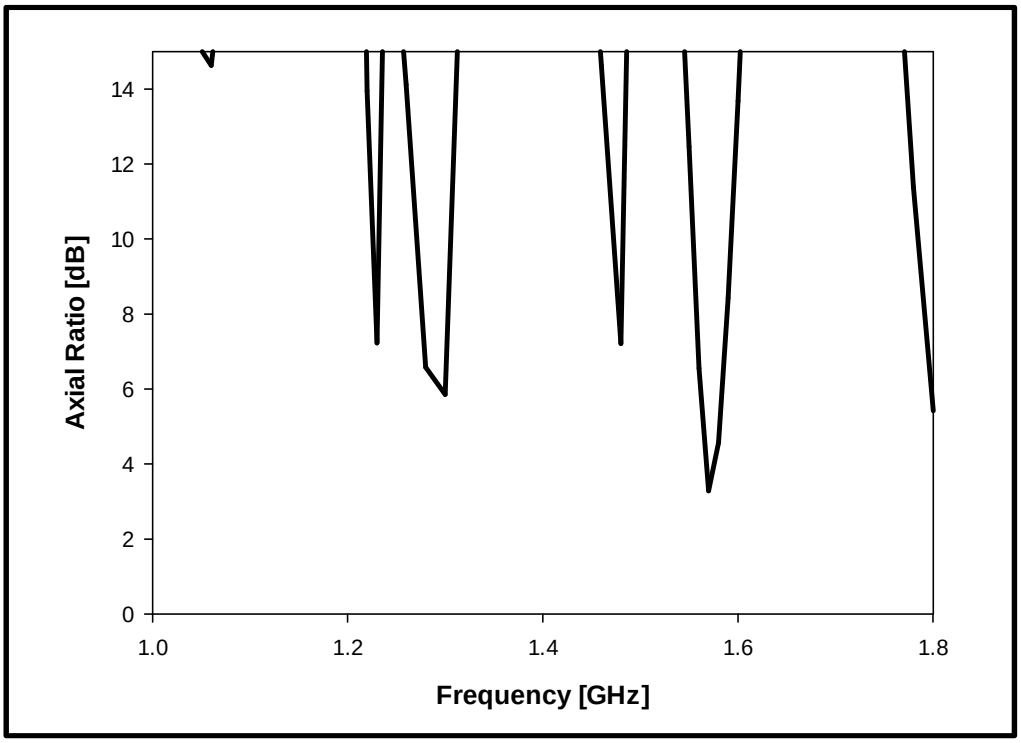

Figure 5.2.6: Axial ratio for the dual band antenna

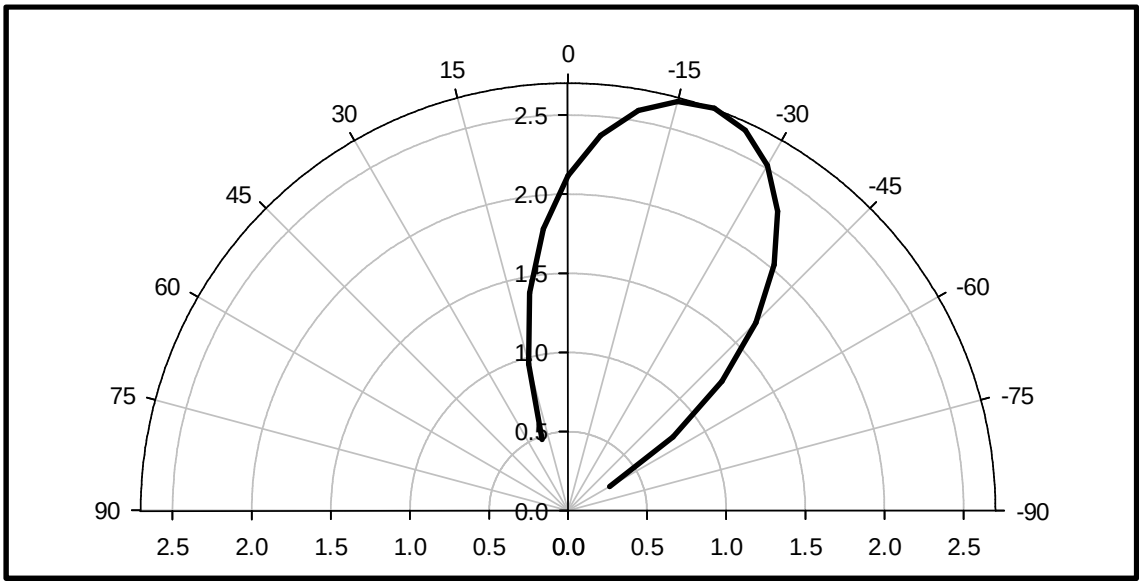

Figure 5.2.7: Radiation pattern for the dual band antenna @ 1.2GHz at $phi = 0^o$

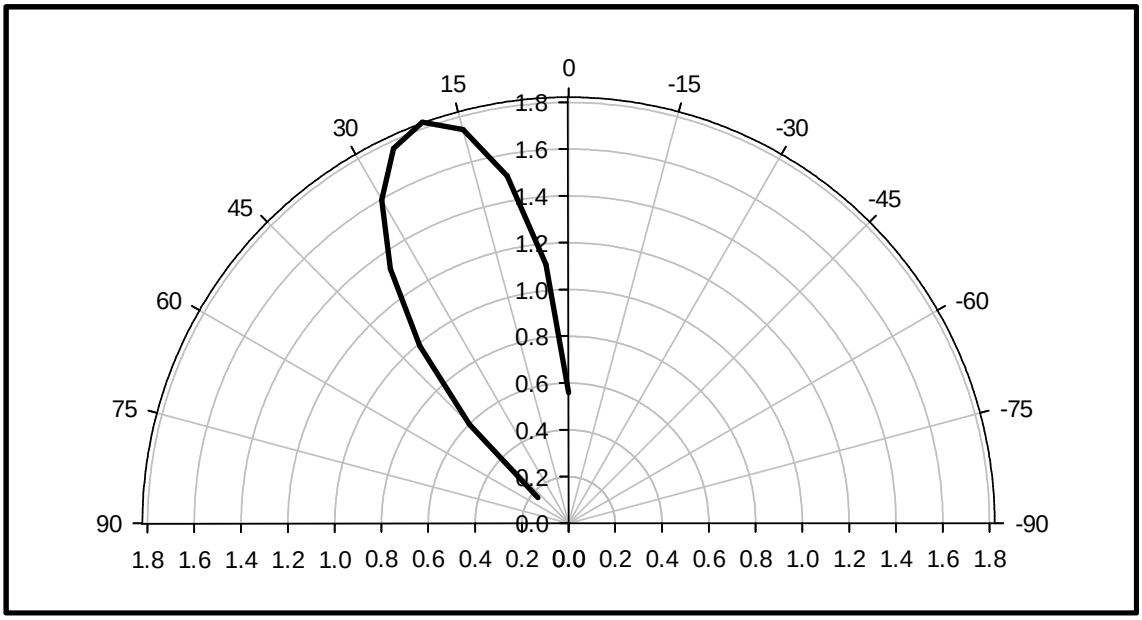

Figure 5.2.8: Radiation pattern for the dual band antenna @ 1.57GHz at $phi = 0^o$

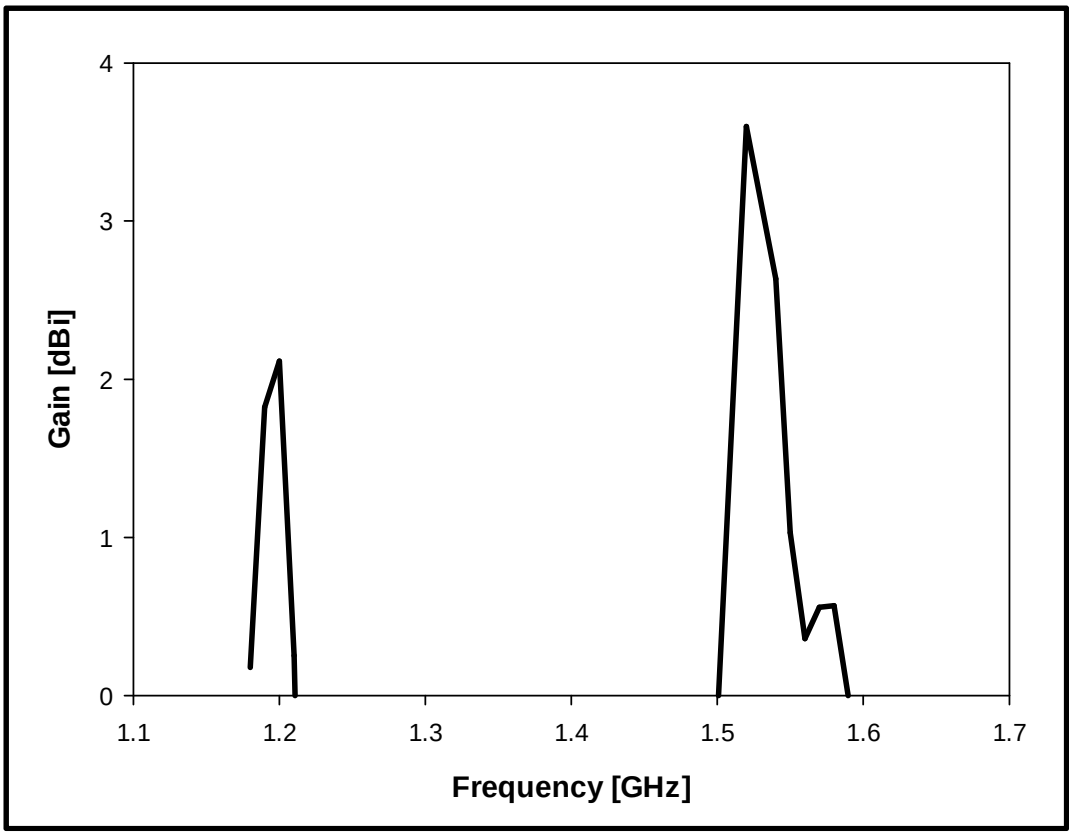

Figure 5.2.9: Gain of the dual band antenna at bore-sight

5.3 Conclusion

In this chapter, two dual band AMC surfaces have been designed for L_1 and L_2 GPS bands. The first is a conventional double square AMC, while the second is a novel dual band AMC. It has been shown that using the same thickness, the proposed dual band AMC is $\sim 42\%$ smaller than the double squares counterpart. Introducing the AMC has improved the reflection coefficient, hence -10dB S_{11} bandwidths of 3.2% and 13.4% have been achieved with a decrease in the total antenna thickness from 28mm to 8mm. However, due to the strong coupling between the AMC and the antenna, results showed an AR of more than 3dB in the two bands. Therefore, further investigations are needed to achieve a low profile dual band CP antenna.

CHAPTER 6

Conclusions and Future Work

6.1 Summary and Conclusion

This thesis focuses on the design of low profile circularly polarised antennas that can be adopted for GPS applications. The first chapter described the concepts of low profile antennas and circularly polarised radiation. Additionally, it reviewed the possible techniques used in the literature to ignite and measure CP waves. Two types of antennas have been used in this thesis; the first is a Dielectric Resonator Antenna (DRA) and the second is a planar loop antenna backed by Artificial Magnetic Conductor (AMC) ground plane. In Chapter two, several designs of singly fed Elliptical DRAs have been presented using conformal strip excitation for simplicity. In the first design, it has been demonstrated that a single strip excitation can be employed to generate circularly polarised radiation with an axial ratio 3dB bandwidth of 4.8%. Additionally, a wide band CP radiation has been accomplished using a half open loop antenna associated with a parasitic inner loop, where a 3dB simulated axial ratio bandwidth of 11.7% has been achieved. Further, a singly fed dual band circularly polarised EDRA has been designed at 2GHz and 3.5GHz. In that design, dual band operation has been achieved using a half open loop with a matching stub to excite the required DRA modes. Good agreement between simulated and measured results has been achieved. Finally, a low profile EDRA has been proposed using $\varepsilon_r = 25$. As expected, increasing the dielectric constant reduces the DRA size. However, there is a limit in the increment as the antenna's performance degrades considerably when ε_r exceeds 25. Therefore, Artificial Magnetic Conductor (AMC) has been used as an alternative approach to design a low profile CP antenna.

In Chapter three, circularly polarised antennas that are backed by square patch AMC have been designed, fabricated and measured. An open circular loop antenna has been employed to achieve the CP radiation. Initially, the loop has been fed using a Co-Planar Waveguide (CPW) and an axial ratio bandwidth of 5.6% has been achieved in conjunction with a good matching and a useful gain. The overall antenna height is 80% thinner than that reported in [112]. However, The ground plane size has increased slightly from $0.84\lambda_o$ to $0.88\lambda_o$. Next, and as an alternative simpler feeding mechanism, a vertical probe has been considered to feed the CP antenna. An axial ratio of 4.5% has been measured with a good matching and gain.

Employing the feeding probe has provided a more robust design and reduced the structure's thickness to $\sim\lambda_o/48$.

In order to reduce the ground plane size, a novel smaller AMC unit cell has been designed in Chapter four. Once more, the open loop has been considered with two feeding mechanisms; CPW and vertical probe. The probe-fed antenna backed by the novel AMC surface has provided a measured 3dB axial ratio bandwidth of 3.5% with a good matching and a useful overlapping gain. Additionally, the antenna height has been reduced by $\sim 125\%$ compared to reported designs [112]. Moreover, the ground plane size has also been reduced by $\sim 28\%$ compared to the square patch AMC antenna using a similar number of 4×4 unit cells. On the other hand, it has been shown that for a grid of 5×5 novel AMC unit cells, which is $\sim 10\%$ smaller than the square patch AMC designed in Chapter three, an axial ratio bandwidth of $\sim 10\%$ can be achieved. In addition, decreasing the ground plane size to a 3×3 grid has produced an axial ratio of $\sim 1.7\%$ with a reduction of 45% in size compared to the square patch probe fed antenna designed in Chapter three.

In Chapter five, two dual band AMC unit cells have been designed for the L_1 and L_2 GPS bands. The first is a conventional double squares AMC, while the second is a novel dual band AMC. It has been demonstrated that the proposed dual band AMC unit cell is $\sim 42\%$ smaller than the double squares counterpart with the same thickness. Introducing the novel AMC has improved the reflection coefficient, where bandwidths of 3.2% and 13.4% have been achieved for the first and second bands, respectively. As expected, the total antenna thickness has been reduced from 28mm to 8mm when an AMC surface has been employed. However, owing to the strong coupling between the AMC and the antenna, axial ratios of more than 3dB have been achieved in both bands. Further investigations are required to design a smaller dual band AMCs.

6.2 Future Works

In addition to the presented work, there are several investigations that need to be conducted in order to enhance the performance. As an example, other CP antennas can be employed with the novel AMC, such as the helix antenna, to investigate the possibility of widening the AR bandwidth. In addition, a different type of wideband/dual bands circularly polarised antenna can be incorporated with the dual band AMC to achieve dual band CP radiation at the intended L_1-L_2 GPS frequencies. Suitable configurations may incorporate annular slot antenna reported in [118] or annular ring patch antenna reported in [117]. In addition, it has been shown that increasing the dielectric constant can achieve low profile DRA. However, this has been achieved with a significantly narrower bandwidth. An alternative approach is to incorporate the AMC as a ground plane for the DRA. Theoretically, the DRA height should be reduced without increasing the dielectric constant and, therefore, a reasonable bandwidth can be maintained.

In the conventional AMC structure, the design relies on the physical size and shape to resonate at a particular frequency. In addition, it requires periodicity to work effectively, which increases the size. Recently, an FSS structure associated with lumped reactive element has been reported so that resonance relies on the lumped elements rather than the physical size [53], where a unit cell size of $\lambda_o/115$ has been achieved using lumped capacitor and inductor. So far, the entire antennas reported with these active AMCs have been Linearly Polarised antennas (LP). A further promising investigation is to employ the active AMC with a circularly polarised antenna, which can have a larger periodicity than 4×4 but with a considerably smaller ground plane.

REFERENCES

[1] C. A. Balanis, *Antenna Theory: Analysis and Design*, Third ed. New Jersey: John Wiley & Sons, Inc., 2005.

[2] J. L. Volakis, *Antenna Engineering Handbook*, Fourth ed.: McGraw-Hill, Inc., 2007.

[3] W. L. Stutzman and G. A. Thiele, *Antenna Theory and Design*, Second ed.: John Wiley & Sons, Inc., 1998.

[4] J. D. Kraus and D. A. Fleisch, *Electromagnetics with Applications*, Fifth ed.: The McGraw Hill Companies, Inc., 1999.

[5] S. S. Gao, Q. Luo, and F. Zhu, *Circularly Polarised Antennas*: John Wiley & Sons, Ltd, 2014.

[6] Y. Huang and K. Boyle, *Antennas: From Theory to Practice*: John Wiley & Sons, Ltd., 2008.

[7] J. R. James and P. S. Hall, *Handbook of Microstrip Antennas*. London: Peter Peregrinus Ltd., 1989.

[8] J. Huang, "Circularly Polarised Conical Patterns from Circular Microstrip Antennas," *IEEE Transaction on Antennas and Propagation,* vol. AP-32, 1984.

[9] J. Huang, "A Technique for an Array to Generate Circular Polarizations with Linealry Polarized Elements " *IEEE Transaction on Antennas and Propagation,* vol. AP-34, 1986.

[10] C. A. Balanis, *Modern Antenna Handbook*: John Wiley & Sons, Inc., 2008.

[11] C.-Y. Huang, J.-Y. Wu, and K.-L. Wong, "Cross-Slot-Coupled Microstrip Antenna and Dielectric Resonator Antenna for Circular Polarization," *IEEE Transaction on Antennas and Propagation,* vol. 47, pp. 605-609, 1999.

[12] J. D. Kraus, "Helical Beam Antennas for Wide-Band Applications," *Proceedings of the I.R.E.,* 1948.

[13] H. Nakano, S. Okuzawa, K. Ohishi, H. Mimaki, and Y. Yamauchi, "A Curl Antenna," *IEEE Transaction on Antennas and Propagation,* vol. 41, pp. 1570-1575, 1993.

[14] H. Nakano, H. Yoshida, and Y. Wu, "C-Figured Loop Antennas," *Electronic Letters,* vol. 31, pp. 693-694, 1995.

[15] R. Li, G. DeJean, J. Laskar, and M. M. Tentzeris, "Investigation of Circularly Polarized Loop Antennas With a Parasitic Element for Bandwidth Enhancement," *IEEE Transaction on Antennas and Propagation,* vol. 53, pp. 3930-3939, 2005.

[16] R. K. Mongia and P. Bhartia, "Dielectric Resonator Antennas—A Review and General Design Relations for Resonant Frequency and Bandwidth," *International Journal of Microwave and Millimeter-Wave Computer-Aided Engineering,* vol. 4, pp. 230-247, 1994.

[17] K. M. Luk and K. W. Leung, *Dielectric Resonator Antennas*. Baldock, Hertfordshire, England: Research Studies Press Ltd., 2003.

[18] S. A. Long, M. W. McAllister, and L. Shen, "The Resonant Cylindrical Dielectric Cavity Antenna," *IEEE Transaction on Antennas and Propagation,* vol. 31, pp. 406-412, 1983.

[19] A. Petosa and A. Ittipiboon, "Dielectric Resonator Antennas: A Historical Review and the Current State of the Art," *IEEE Antennas and Propagation Magazine,* vol. 52, pp. 91-116, 2010.
[20] M. W. McAllister, S. A. Long, and G. L. Conway, "Rectangular Dielectric Resonator Antenna," *Electronics Letters,* vol. 19, pp. 218-219, 1983.
[21] M. W. McAllister and S. A. Long, "Resonant Hemispherical Dielectric Antenna," *Electronics Letters* vol. 20, pp. 657-659, 1984.
[22] V. Hamsakutty, A. V. Praveen Kumar, J. Yohannan, and K. T. Mathew, "Coaxial Fed Hexagonal Dielectric Resonator Antenna," in *Asia-Pacific Microwave Conference*. vol. 4, 2005.
[23] A. A. Kishk, A. Ittipiboon, Y. M. M. Antar, and M. Cuhaci, "Slot Excitation of the Dielectric Disk Radiator," *IEEE Transaction on Antennas and Propagation,* vol. 43, 1995.
[24] R. K. Mongia, A. Ittibipoon, and M. Cuhaci, "Low Profile Dielectric Resonator Antennas Using a Very High Permittivity Material," *Electronic Letters,* vol. 30, 1994.
[25] H. Y. Lo, K. W. Leung, K. M. Luk, and E. K. N. Yung, "Low Profile Equilateral-Triangular Dielectric Resonator Antenna of Very High Permittivity," *Electronic Letters,* vol. 35, pp. 2164-2165, 1999.
[26] H. Wu, X. Wu, C. Hua, and N. Yang, "A Dual Frequency Rectangular Dielectric Resonator Antenna Fed by a Coaxial Probe," *Progress In Electromagnetics Research Symposium Proceedings,* pp. 211-213, 2011.
[27] Y. Ge and K. P. Esselle, "A Dielectric Resonator Antenna for UWB Applications," in *IEEE Antennas and Propagation Society International Symposium* Charleston, SC, 2009, pp. 1-4.
[28] K. P. Esselle, "Circularly Polarised Higher-Order Rectangular Dielectric-Resonator Antenna," *Electronic Letters,* vol. 32, 1996.
[29] L. C. Y. Chu, D. Guha, and Y. M. M. Antar, "Comb-Shaped Circularly Polarised Dielectric Resonator Antenna," *Electronic Letters,* vol. 42, 2006.
[30] M. I. Sulaiman and S. K. Khamas, "A Singly Fed Rectangular Dielectric Resonator Antenna With a Wideband Circular Polarization," *IEEE Antennas and Wireless Propagation Letters,* vol. 9, pp. 615-618, 2010.
[31] M. I. Sulaiman and S. K. Khamas, "Correction to “A Singly Fed Rectangular Dielectric Resonator Antenna With a Wideband Circular Polarization”," *IEEE Antennas and Wireless Propagation Letters,* vol. 9, p. 1286, 2010.
[32] M. Haneishi and H. Takazawa, "Broadband Circularly Polarised Planar Array Composed of a Pair of Dielectric Resonator Antennas," *Electronics Letters,* vol. 21, pp. 437-438, 1985.
[33] K.-W. Khoo, Y.-X. Guo, and L. C. Ong, "Wideband Circularly Polarized Dielectric Resonator Antenna," *IEEE Transaction on Antennas and Propagation,* vol. 55, pp. 1929-1932, 2007.
[34] K. W. Leung, W. C. Wong, K. M. Luk, and E. K. N. Yung, "Circular-Polarised Dielectric Resonator Antenna Excited by Dual Conformal Strips," *Electronics Letters,* vol. 36, pp. 484-486, 2000.
[35] H. K. Ng and K. W. Leung, "Circular-Polarized Hemispherical Dielectric Resonator Antenna Excited by Dual Conformal-Strip," in *IEEE International Symposium on Antennas and Propagation* San Antonio, 2002, pp. 442-445.
[36] D. Sievenpiper, L. Zhang, R. F. J. Broas, N. G. Alexopolous, and E. Yablonovitch, "High-Impedance Electromagnetic Surfaces with a Forbidden

Frequency Band," *IEEE Transaction on Antennas and Propagation,* vol. 47, pp. 2059-2074, 1999.

[37] F. Yang and Y. Rahmat-Samii, "Reflection Phase Characterizations of the EBG Ground Plane for Low Profile Wire Antenna Applications," *IEEE Transaction on Antennas and Propagation,* vol. 51, pp. 2691-2703, 2003.

[38] K.-P. Ma, K. Hirose, F.-R. Yang, Y. Qian, and T. Itoh, "Realisation of Magnetic Conducting Surface using Novel Photonic Bandgap Structure," *Electronics Letters,* vol. 34, pp. 2041-2042, 1998.

[39] Y. Zhang, J. v. Hagen, M. Younis, C. Fischer, and W. Wiesbeck, "Planar Artificial Magnetic Conductors and Patch Antennas," *IEEE Transaction on Antennas and Propagation,* vol. 51, pp. 2704-2712, 2003.

[40] A. P. Feresidis, G. Goussetis, S. Wang, and J. Y. C. Vardaxoglou, "Artificial Magnetic Conductor Surfaces and Their Application to Low-Profile High-Gain Planar Antennas," *IEEE Transaction on Antennas and Propagation,* vol. 53, pp. 209-215, 2005.

[41] F.-R. Yang, K.-P. Ma, Y. Qian, and T. Itoh, "A Uniplanar Compact Photonic-Bandgap (UC-PBG) Structure and Its Applications for Microwave Circuits," *IEEE Transaction on Microwave Theory and Techniques,* vol. 47, pp. 1509-1514, 1999.

[42] S. Clavijo, R. E. Díaz, and W. E. McKinzie, "Design Methodology for Sievenpiper High-Impedance Surfaces: An Artificial Magnetic Conductor for Positive Gain Electrically Small Antennas," *IEEE Transaction on Antennas and Propagation,* vol. 51, pp. 2678-2690, 2003.

[43] D. J. Kern, D. H. Werner, and P. L. Werner, "Optimization of Multi-band AMC Surfaces with Magnetic Loading " *IEEE International Symposium of Antennas and Propoagation Society,* vol. 1, pp. 823-826, 2004.

[44] L. Yousefi, B. Mohajer-Iravani, and O. M. Ramahi, "Enhanced Bandwidth Artificial Magnetic Ground Plane for Low-Profile Antennas," *IEEE Antennas and Wireless Propagation Letters,* vol. 6, pp. 289-292, 2007.

[45] S. M. Amjadi and M. Soleimani, "A Novel Compact Artificial Magnetic Conductor Based on Multiple Non-grounded Vias," *PIERS Online,* vol. 2, pp. 672-675, 2006.

[46] J.-M. Baracco, L. Salghetti-Drioli, and P. d. Maagt, "AMC Low Profile Wideband Reference Antenna for GPS and GALILEO Systems," *IEEE Transaction on Antennas and Propagation,* vol. 56, pp. 2540-2547, 2008.

[47] M. E. d. Cos, Y. Álvarez, R. C. Hadarig, and F. Las-Heras, "Novel SHF-Band Uniplanar Artificial Magnetic Conductor," *IEEE Antennas and Wireless Propagation Letters,* vol. 9, pp. 44-47, 2010.

[48] M. T. Xie, Q. G. Guo, and K.M.Huang, "Design of a Novel Artificial Magnetic Conductor Plane and Its Application for Low-Profile Dipole," *International Conference on Microwave and Millimeter Wave Technology,* pp. 2085-2087, 2010.

[49] M. K. T. Al-Nuaimi and W. G. Whittow, "Ultra Thin Dipole Antenna Backed by New Planar Artificial Magnetic Conductor," in *Loughborough Antennas & Propagation Conference (LAPC)* Loughborough, England, 2009.

[50] D. J. Kern, D. H. Werner, A. Monorchio, L. Lanuzza, and M. J. Wilhelm, "The Design Synthesis of Multiband Artificial Magnetic Conductors Using High Impedance Frequency Selective Surfaces," *IEEE Transaction on Antennas and Propagation,* vol. 53, pp. 8-17, 2005.

[51] L. Lanuzza, A. Monorchio, D. J. Kern, and D. H. Werner, "A Robust CA-FSS Technique for the Synthesis of Optimal Multiband AMCs with Angular Stability," in *IEEE International Symposium on Antennas and Propagation Society*. vol. 2, 2003, pp. 419-422.
[52] N. A. Abbasi and R. Langley, "A Wideband Printed Monopole Antenna over Dual-band AMC," in *2010 Loughborough Antennas & Propagation Conference* Loughborough, UK, 2010.
[53] H. Liu, K. L. Ford, and R. J. Langley, "Miniaturised bandpass frequency selective surface with lumped components," *Electronic Letters,* vol. 44, 2008.
[54] H. L. Liu, K. L. Ford, and R. J. Langley, "Design Methodology for a Miniaturized Frequency Selective Surface Using Lumped Reactive Components," *IEEE Transaction on Antennas and Propagation,* vol. 57, pp. 2732-2738, 2009.
[55] R. Saad and K. L. Ford, "A Miniaturised Dual Band Artificial Magnetic Conductor using Lumped Components," in *2011 Loughborough Antennas & Propagation Conference* Loughborough, UK, 2001.
[56] R. F. Harrington, "Matrix Method for Field Problems," *Proceeding of IEEE,* vol. 55, February, 1967.
[57] R. Bansal, *Handbook of Engineering Electromagnetics*. New York: Marcel Dekker, Inc, 2004.
[58] "https://www.feko.info."
[59] "http://www.nec2.org/."
[60] M. N. O. Sadiku, *Elements of Electromagnetics*, Fourth ed.: Oxford University Press, 2007.
[61] "http://apsimtech.com/."
[62] "http://www.remcom.com/xf7."
[63] "http://www.ansys.com."
[64] R. Marklein, "The Finite Integration Technique as a General Tool to Compute Acoustic, Electromagnetic, Elastodynamic and Coupled Wave Fields," in *Review of Radio Science 1999-2002* NewYork: IEEE Press, 2002.
[65] "www.cst.com."
[66] F. G. Bogdanov, D. D. Karkashadze, and R. S. Zaridze, "The Method of Auxiliary Sources in Electromagnetic Scattering Problems," in *Generalized Multipole Techniques for Electromagnetic and Light Scattering*, W. T., Ed. North-Holland: Elsevier Science, 1999, pp. 143-172.
[67] J. Lee and S. Nam, "Protecting the Method of Auxiliary Sources (MAS) Solutions From the Interior Resonance Problem," *IEEE Microwave and Wireless Components Letters,* vol. 15, March 2005.
[68] D. Karkashadze and R. Zaridze, "The Method of Auxiliary Sources in Applied Electrodynamics," *URSI Symposium,* pp. 104-106, 1986.
[69] D. I. Kaklamani and H. T. Anastassiu, "Aspects of the Method of Auxiliary Sources (MAS) in Computational Electromagnetics," *IEEE Antennas and Propagation Magazine,* vol. 44, pp. 48-64, 2002.
[70] R. Zaridze, G. Bit-Babik, K. Tavzarashvili, A. Bijamov, D. Kakulia, and G. Ghvedashvili, "The Method of Auxiliary Sources in Scattering and Diffraction Problems," *IEEE Antennas and Propagation Society International Symposium* vol. 4, pp. 738 - 741 2001.
[71] A. J. Petrov, "An Adaptation of Auxiliary Sources Method for Stationary Acoustic Problems," *Wave Motion,* vol. 39, pp. 169–180, 2004.

[72] H. T. Anastassiu, D. G. Lymperopoulos, and D. I. Kaklamani, "Accuracy Analysis and Optimization of the Method of Auxiliary Sources (MAS) for Scattering by a Circular Cylinder," *IEEE Transaction on Antennas and Propagation,* vol. 52, pp. 1541-1547, 2004.

[73] N. P. Agrawall, G. Kumar, and K. P. Ray, "Wideband Planar Monopole Antennas," *IEEE Transaction on Antennas and Propagation,* vol. 46, pp. 294-295, 1998.

[74] H. Schantz, "Planar Elliptical Element Ultra-Wideband Dipole Antennas," *IEEE Antennas and Propagation Society International Symposium,* vol. 3, 2002.

[75] J. Powell and A. Chandrakasan, "Differential and Single Ended Elliptical Antennas for 3.1-10.6 GHz Ultra Wideband Communication," *IEEE Antennas and Propagation Society International Symposium,* vol. 3, pp. 2935-2938, 2004.

[76] B.-T. Lim, "Dielectric Resonator Antennas: Theory and Design," in *Department of Electrical Engineering*. vol. Master of Engineering in Electrical Engineering and Computer Science: Massachusetts Institute of Technology, 1999.

[77] A. A. Kishk, "An Elliptic Dielectric Resonator Antenna Designed for Circular Polarization with Single Feed," *Microwave and Optical Technology Letters,* vol. 37, pp. 454-456, 2003.

[78] J.-J. Chen, Y.-C. Lin, and R.-B. Wu, "A Dual Band Elliptical DRA," *IEEE International Symposium of Antennas and Propoagation Society,* vol. 2, 2004.

[79] M. A. Sharkawy, A. Z. Elsherbeni, and C. E. Smith, "Stacked Elliptical Dielectric Resonator Antennas for Wideband Applications," *IEEE International Symposium of Antennas and Propoagation Society,* vol. 2, pp. 1371-1374, 2004.

[80] A. Tadjalli, A. Sebak, and T. Denidni, "Modes of Elliptical Cylinder Dielectric Resonator and its Resonant Frequencies," in *Antem International Symposium* Ottawa, 2004, pp. 2039-2042.

[81] R. Chair, A. A. Kishk, and K. F. Lee, "Wideband Low Profile EYE Shaped Dielectric Resonator Antennas," *Antennas and Propagation Society International Symposium,* vol. 3A, pp. 582-585, 2005.

[82] S. L. S. Yang, R. Chair, A. A. Kishk, K. F. Lee, and K. M. Luk, "Single-Feed Elliptical Dielectric Resonator Antennas for Circularly Polarized Applications," *Microwave and Optical Technology Letters,* vol. 48, pp. 2340-2345, 2006.

[83] A. Tadjalli and A. Sebak, "Resonance Frequency and Far Field Patterns of Elliptical Dielectric Resonator Antenna: Analytical Approach," *Progress In Electromagnetics Research,* vol. 64, pp. 81-98, 2006.

[84] S.-l. S. Yang, R. Chair, A. A. Kishk, K.-F. Lee, and K.-M. Luk, "Study on Sequential Feeding Networks for Subarrays of Circularly Polarized Elliptical Dielectric ResonatorAntenna," *IEEE Transaction on Antennas and Propagation,* vol. 55, pp. 321-333, 2007.

[85] A. Tadjalli, A. Sebak, and T. Denidni, "Design of Circularly Polarized Slot-Coupled Elliptical Dielectric Resonator Antenna," *Antennas and Propagation Society International Symposium,* pp. 4881-4884, 2007.

[86] E. M. Kejani and M. H. Neshati, "Design Investigation of Circularly Polarized Dielectric Resonator Antenna Array Excited by Dielectric Image Line," in *18th Iranian Conference on Electrical Engineering* Iran, 2010, pp. 75-79.

[87] A. Petosa, *Dielectric Resonator Antenna Handbook*: Artech House, 2007.

[88] D. Kajfez and P. Gullion, *Dielectric Resonators*: Artech House, Inc., 1986.
[89] A. M. Hussein and W. Wurjantara, "Analysis of Elliptic Conductors Using the Point Matching Method with Mathieu Functions," *IEEE Transactions on Magnetics,* vol. 33, pp. 4125-4127, 1997.
[90] M. M. S. Lira, H. M. d. Oliveira, and R. J. d. S. Cintra, "Elliptic-Cylindrical Wavelets: The Mathieu Wavelets," *IEEE Signal Processing Letter,* vol. 11, pp. 52-55, 2004.
[91] Y. Kobayashi and S. Tanaka, "Resonant Modes of a Dielectric Rod Resonator Short Circuited at Both Ends by Parallel Conducting Plates," *IEEE Transaction on Microwave Theory and Techniques,* vol. MTT-28, pp. 1077-1085, 1980.
[92] B. Y. Toh, R. Cahill, and V. F. Fusco, "Understanding and Measuring Circular Polarization," *IEEE Transaction on Education,* vol. 46, pp. 313-318, 2003.
[93] W. H. Kummer and E. S. Gillespie, "Antenna Measurements -1978," *Proceeding of IEEE,* vol. 66, pp. 483-507, 1978.
[94] G. P. Junker, A. A. Kishk, A. W. Glisson, and D. Kajfez, "Effect of An Air Gap Around The Coaxial Probe Exciting A Cylindrical Dielectric Resonator Antenna," *Electronics Letters,* vol. 30, pp. 177-178, 1994.
[95] K. W. Leung, "Conformal Strip Excitation of Dielectric Resonator Antenna," *IEEE Transaction on Antennas and Propagation,* vol. 48, pp. 961-967, 2000.
[96] R.-L. Li, V. F. Fusco, and H. Nakano, "Circularly Polarized Open-Loop Antenna," *IEEE Transaction on Antennas and Propagation,* vol. 51, pp. 2475-2477, 2003.
[97] B. K. Wang, K. Y. Lam, M. S. Leong, and P. S. Kooi, "Elliptical Waveguide Analysis Using Improved Polynomial Approximation," *IEE Proceedings - Microwaves, Antennas and Propagation,* vol. 141, pp. 483-488, 1994.
[98] A. Benomar, N. B. Hacene, H. Megnafi, and P. Vaudon, "Embedded Dual-band Cylindrical Dielectric Resonator Antenna " *International Journal on Communications, Network and System Sciences,* pp. 656-661, 2011.
[99] T.-H. Chang and J.-F. Kiang, "Dual band Split Dielectric Resonator Antenna," *IEEE Transaction on Antennas and Propagation,* vol. 55, pp. 3155-3162, 2007.
[100] L. K. Hady, A. A. Kishk, and D. Kajfez, "Dual Band Dielectric Resonator Antenna for GPS and WLAN Applications," *Asia-Pacific Microwave Conference, APMC,* 2008.
[101] L. K. Hady, A. A. Kishk, and D. Kajfez, "Dual-Band Compact DRA With Circular and Monopole-Like Linear Polarizations as a Concept for GPS and WLAN Applications," *IEEE Transaction on Antennas and Propagation,* vol. 57, pp. 2591-2598, 2009.
[102] J. Patin and S. K. Sharma, "Dual Band Single Feed Dielectric Resonator Antenna With Linear and Circular Polariziations for Ku-Band," *IEEE International Symposium on Antennas and Propagation (APSURSI),* 2011.
[103] Y. Lee, J. Yea, and R. Mittra, "A Dual frequency Circularly Polarized Antenna Design using a Combination of DRA and Microstip Patch," *IEEE Antennas and Propogation Society International Symposium,* vol. 4, pp. 122-125, 2003.
[104] Y. Ding, K. W. Leung, and K. M. Luk, "Circularly-Polarized DRA-Slot Hybrid Antenna for Dualband Applications," *International Conference on Electromagnetics in Advanced Applications, ICEAA,* pp. 880-882, 2007.

[105] X. S. Fang and K. W. Leung, "Linear-/Circular-Polarization Designs of Dual-/Wide-Band Cylindrical Dielectric Resonator Antennas," *IEEE Transaction on Antennas and Propagation,* vol. 60, pp. 2662-2671, 2012.

[106] H. S. Ngan, X. S. Fang, and K. W. Leung, "Design of Dual-Band Circularly Polarized Dielectric Resonator Antenna Using a Higher-Order Mode," *IEEE-APS Topical Conference on Antennas and Propagation in Wireless Communications (APWC),* pp. 424 - 427, 2012.

[107] Z. Meng, L. Bin, and X. Lv, "Cross-Slot-Coupled Wide Dual-Band Circularly Polarized Rectangular Dielectric Resonator Antenna," *IEEE Antennas and Wireless Propagation Letters,* vol. 13, pp. 532 - 535, 2014.

[108] Z. Meng and L. Bin, "Cross-slot-coupled Dual-band Circularly Polarized Rectangular Dielectric Resonator Antenna," http://www.paper.edu.cn.

[109] F. Yang and Y. Rahmat-Samii, "A Low-Profile Circularly Polarised Curl Antenna Over An Electromagnetic BandGap (EBG) Surface," *Microwave and Optical Technology Letters,* vol. 31, pp. 264-267, 2001.

[110] H. S. Farahani, F. Fereidoony, M. Veysi, E. Soufiani, and A. Khaleghi, "A Low-Profile, Wideband Circularly Polarized Curl Antenna Backed by a Polarization Dependent Reflector," *Proceedings of the 5th European Conference on Antennas and Propagation (EUCAP),* pp. 1085-1088, 2011.

[111] F. Yang and Y. Rahmat-Samii, "A Low Profile Single Dipole Antenna Radiating Circularly Polarized Waves," *IEEE Transaction on Antennas and Propagation,* vol. 53, pp. 3083-3086, 2005.

[112] A. M. Mehrabani and L. Shafai, "An Extremely Low-Profile Offset-Fed Curl Antenna Over An AMC Ground," *Microwave and Optical Technology Letters,* vol. 53, pp. 1036-1041, 2011.

[113] X.-Y. Bao, Y.-X. Guo, and Y.-Z. Xiong, "60-GHz AMC-Based Circularly Polarized On-Chip Antenna Using Standard 0.18-microm CMOS Technology," *IEEE Transaction on Antennas and Propagation,* vol. 60, pp. 2234-2241, 2011.

[114] E. P. Ltd., "http://www.emkayplastics.co.uk/tech-data," 07/01/2014.

[115] Nasimuddin, Z. N. Chen, and X. Qing, "Dual-Band Circularly Polarized S-Shaped Slotted Patch Antenna With a Small Frequency-Ratio," *IEEE Transaction on Antennas and Propagation,* vol. 58, pp. 2112-2115, 2010.

[116] Y. Wang, J. Feng, J. Cui, and X. Yang, "A Dual-Band Circularly Polarized Stacked Microstrip Antenna with Single-fed for GPS Applications," in *8th International Symposium on Antennas, Propagation and EM Theory* Kunming, 2008.

[117] X. Sun, Z. Zhang, and Z. Feng, "Dual-Band Circularly Polarized Stacked Annular-Ring Patch Antenna for GPS Application," *IEEE Antennas and Wireless Propagation Letters,* vol. 10, pp. 49-52, 2011.

[118] W.-T. Hsieh, T.-H. Chang, and J.-F. Kiang, "Dual-Band Circularly Polarized Cavity-Backed Annular Slot Antenna for GPS Receiver," *IEEE Transaction on Antennas and Propagation,* vol. 60, 2012.

[119] S. Zhu and R. Langley, "Dual Band Waerable Antenna Over EBG Substrate," *Electronics Letters,* vol. 43, pp. 141-142, 2007.

[120] S. Zhu and R. Langley, "Dual-Band Wearable Textile Antenna on an EBG Substrate," *IEEE Transaction on Antennas and Propagation,* vol. 57, pp. 926 - 935, 2009.